

**The Late Transition Metal-Mediated Activations of the
Molecules Relevant to the Water-Gas Shift Reaction**

Ke Zhang

Shanghai, China

B.S. Chemistry, University of Illinois at Urbana and Champaign, 2016

A Dissertation Presented to the Graduate Faculty of the University of Virginia in
Candidacy for the Degree of Doctor of Philosophy

Department of Chemistry

University of Virginia

October 2022

ABSTRACT

Steam-methane reforming (SMR) reaction and the water-gas shift (WGS) reaction are the major processes for the dihydrogen production in the U.S., which cost enormous amount of energy. As a result, utilization of the products for SMR and WGS processes (H_2 , CO and CO_2) more efficiently could create economic benefits. In the past few decades, many homogenous catalytic processes that use H_2 , CO or CO_2 to produce higher-value chemicals with transition metal catalysts have been developed.

My primary focus of this Dissertation was to study the redox chemistry of a series of capping arene-ligated rhodium complexes during catalysis. Olefin hydrogenation was selected as the model for this study because Rh-catalyzed olefin hydrogenation has been well-developed, and the proposed mechanisms for Rh-catalyzed olefin hydrogenation included the formal oxidation state change on the Rh catalysts. The ligand influence on olefin hydrogenation using four capping arene ligated Rh(I) catalyst precursors $(\text{FP})\text{Rh}(\eta^2\text{-C}_2\text{H}_4)\text{Cl}$ {FP = capping arene ligands, including 6-FP (8,8'-(1,2-phenylene)diquinoline), 6-^{NP}FP (8,8'-(2,3-naphthalene)diquinoline), 5-FP (1,2-bis(N-7-azaindolyl)benzene) and 5-^{NP}FP [2,3-bis(N-7-azaindolyl)naphthalene]} has been studied. Our studies indicate that relative observed rates of catalytic olefin hydrogenation follow the trend $(6\text{-FP})\text{Rh}(\eta^2\text{-C}_2\text{H}_4)\text{Cl} > (5\text{-FP})\text{Rh}(\eta^2\text{-C}_2\text{H}_4)\text{Cl}$. Based on combined experimental and density functional theory modeling studies, we propose that the observed differences in the rate of $(6\text{-FP})\text{Rh}(\eta^2\text{-C}_2\text{H}_4)\text{Cl}$ and $(5\text{-FP})\text{Rh}(\eta^2\text{-C}_2\text{H}_4)\text{Cl}$ -catalyzed olefin hydrogenation are most likely attributed to the difference in the activation energies for the dihydrogen oxidative addition step. We are unable to directly compare the rates of olefin hydrogenation using $(6\text{-}^{\text{NP}}\text{FP})\text{Rh}(\eta^2\text{-C}_2\text{H}_4)\text{Cl}$ and $(5\text{-}^{\text{NP}}\text{FP})\text{Rh}(\eta^2\text{-C}_2\text{H}_4)\text{Cl}$ as the catalyst precursor since (5-

${}^{\text{NP}}\text{FP})\text{Rh}(\eta^2\text{-C}_2\text{H}_4)\text{Cl}$ undergoes relatively rapid formation of an active catalyst that does not coordinate 5- ${}^{\text{NP}}\text{FP}$.

The cobalt-catalyzed styrene hydrogenation has also been studied. A capping arene-ligated cobalt complex (5-FP) CoCl_2 was successfully synthesized. The hydrogenation of styrene was observed when using (5-FP) CoCl_2 as the catalyst and $\text{Zn}(0)$ as an additive. The reaction conditions are further optimized, and the styrene hydrogenation reached 5.5 ± 2.4 turnovers with the best conditions.

Moreover, the capping arene ligated Rh and Ir complexes have also been studied for their catalytic activities on MeI promoted methanol carbonylation. A series of capping arene ligated Rh or Ir carbonyl complexes with the general formula $[(\text{FP})\text{M}^{\text{I}}(\text{CO})_2]\text{BF}_4$ (FP = 5-FP or 6-FP, M = Rh or Ir) were synthesized. The performances of these complexes on MeI promoted methanol carbonylation were examined. The turnovers using $[(\text{FP})\text{M}^{\text{I}}(\text{CO})_2]\text{BF}_4$ (FP = 5-FP or 6-FP, M = Rh or Ir) as the catalyst were not improved when compared to catalysis using $[\text{Rh}(\text{CO})_2(\mu\text{-Cl})_2]$ or $[\text{Ir}(\text{COE})_2(\mu\text{-Cl})_2]$. Mechanistic studies revealed that the $[(5\text{-FP})\text{Rh}(\text{CO})_2]\text{BF}_4$, $[(5\text{-FP})\text{Ir}(\text{CO})_2]\text{BF}_4$ and $[(6\text{-FP})\text{Rh}(\text{CO})_2]\text{BF}_4$ are unstable at 135 °C without MeI. When MeI is present, all four $[(\text{FP})\text{M}^{\text{I}}(\text{CO})_2]\text{BF}_4$ complexes as well as the 5-FP and 6-FP ligands show reactivity with MeI at 135 °C. The decomposition products for $[(5\text{-FP})\text{Rh}(\text{CO})_2]\text{BF}_4$ or $[(5\text{-FP})\text{Ir}(\text{CO})_2]\text{BF}_4$ with MeI at 135 °C are identical to the decomposition product of 5-FP ligand reacting with MeI. Similarly, the decomposition products for $[(6\text{-FP})\text{Rh}(\text{CO})_2]\text{BF}_4$ or $[(6\text{-FP})\text{Ir}(\text{CO})_2]\text{BF}_4$ with MeI at 135 °C are identical to the decomposition product of 6-FP ligand reacting with MeI. The identical decomposition products could suggest that the capping arene ligand falls off from the Rh or Ir complexes.

Thus, the active catalyst for the methanol carbonylation using $[(FP)M^I(CO)_2]BF_4$ and MeI is likely a metal complex without the capping arene ligand, which can explain why no ligand effect is observed for the methanol carbonylation with MeI promoter.

Additionally, carbon dioxide (CO_2) offers the possibility of a C1 synthon because of the low expensive, low toxicity, and high abundance. Thus, the direct carboxylation of hydrocarbons would have many advantages compared to current processes for the carboxylic acids production (e.g. hydroformylation of ethene followed by oxidation). A mechanism for direct carboxylation of benzene under basic condition catalyzed by PCP-ligated $\{(PCP = 2,6-(R_2PCH_2)_2C_6H_3; R = \text{isopropyl, tertbutyl, or phenyl}\}$ palladium complexes has been proposed and analyzed by DFT calculations in order to predict the feasibility of the reaction. A series of PCP Pd complexes have been prepared to study the direct carboxylation of benzene with CO_2 . As CO_2 insertion into the Pd–Ph bond is an important step in the proposed catalytic cycle, the reactivity of the Pd pincer complex with CO_2 is studied. $(iPrPCP)PdPh$ ($iPr PCP = 2,6-(iPr_2PCH_2)_2C_6H_3$) has been prepared and the CO_2 insertion product, $(iPrPCP)PdOBz$ ($OBz = \text{benzoate}$), has been observed by 1H NMR spectroscopy. Under optimized conditions, the yield of the CO_2 insertion product is approximately 70% after 2 h. The next step in the proposed catalytic cycle involves the C–H activation of benzene. The ability of $(iPrPCP)PdOBz$ to activate a C–H bond of benzene has been studied.

ACKNOWLEDGMENTS

During my six-year life as a graduate student, many people provided me with kind help. I would like to say thank you to all of you.

First, I would like to thank my advisor, Professor T. Brent Gunnoe. It was your wonderful classes attracted me into the world of inorganic chemistry. Your first-year inorganic lectures helped me learn so much basic knowledge which is useful for the following graduate studies. It was my pleasure to become a member of your group. I appreciate your knowledge and creativity in chemistry, your leadership and your support. Your advice is always helpful for me to become a better chemist. I also want to thank you, Trecia and Leah to organize the group parties every year, which bring us a lot of fun every time.

I would also like to thank the Gunnoe lab members, it is my pleasure to work with you in the past six years. To Brad, thank you for training me patiently on Schlenk techniques, operating gloveboxes and other instruments. It was your mentorship made my lab skill developed quickly and smoothly. To Junqi, thank you for being a friend and a mentor. You provided me so many supportive suggestions and encouraged me when I had difficulty on my research. To Nichole, thank you for teaching me how to use the VCO reactor, and sharing the reactors and GC-MS with me. To Xiaofan, thank you for being a good friend, and thanks for your contributions as a mentor and as a “LUXURY” team builder. To Shunyan and Weihao, thank you for being my friends, and discussing chemistry with me. To Fanji, thank you for being my friend. I appreciate your broad knowledge on chemistry, your hard working, and your contribution to the group businesses. Thanks to Bala,

Zhongwen, Kaeleigh, Ana, Ryan, Nathan, Chris W., Marc, Hannah, Zoe and Chris R. for the supports in the lab and helpful suggestions on my manuscript.

Thanks to my committee members, Dr. Dean Harman, Dr. Lin Pu and Dr. Charles Machan for your advice and suggestions on my candidacy exam and annual reports. Thanks to Dr. Pu for teaching me the organometallic chemistry as well as the spectrometric chemistry, and to Dr. Machan for teaching me the structural inorganic chemistry. All of these classes are very useful for my graduate studies. Special thanks to Dr. Machan for choosing me to be the teaching assistant for his inorganic class for undergraduates. I really enjoy the well-designed experiments during the classes.

Thanks to Jeff for helped me dealing with the trouble with NMR, and taught me performing complicated NMR experiments. And thanks for Diane for taking single X-ray diffraction and solving the structures for my samples. Thanks to Ess group from Brigham Young University, and Goddard group from Caltech, who collaborated with me and provide me with DFT calculation data.

I would also like to thank my friend outside the lab. To Chen and Pinkang, thanks for being close friends for over 10 years, and I hope we can meet each other again soon in Shanghai. To Kairui and Pingfan, thank you for sharing fun stories and useful experiences from your lives. I hope both of you can have successful careers in the future. To Jialun, you are always humorous and generous, and you are always able to bring fun to others.

Finally, I would like to thank my family members, my parents and grandparents, who provide me with a comfortable environment to grow and learn. Thanks to Yao Shang and Kefeng Li, my high school chemistry teachers, who guided me into the world of chemistry.

And thanks to my wife, Yuying Wu, who gave me significant amount of support and encouragement during the recent eight years.

TABLE OF CONTENTS

1	Introduction	1
1.1	Broad overview and motivation of small molecule activation	1
1.2	Utilization of dihydrogen (H ₂)	1
1.2.1	Properties of H ₂	1
1.2.2	Examples of catalytic H ₂ utilization	4
1.3	Utilization of carbon monoxide (CO)	10
1.3.1	Properties of CO	10
1.3.2	Examples of catalytic CO utilization	12
1.4	Utilization of carbon dioxide (CO ₂)	19
1.4.1	Properties of CO ₂	19
1.4.2	Examples of catalytic CO ₂ utilization	21
1.5	Summary and Conclusions	23
1.6	References	23
2	Capping Arene Ligated Rhodium Catalyzed Olefin Hydrogenation	46
2.1	Introduction	46
2.2	Comparison of olefin hydrogenation rate with various olefins catalyzed by capping arene rhodium complexes	51

2.3 Mechanistic studies	67
2.3.1 Overview of possible catalytic mechanism	67
2.3.2 Kinetic studies of 6FP-A catalyzed styrene hydrogenation	68
2.3.3 Eyring equation determination on catalytic hydrogenation of styrene with 6FP-A	77
2.3.4 Observation and characterization of (6-FP)Rh(Cl)(η^2-styrene)	81
2.3.5 Isotopic studies on styrene hydrogenation catalyzed by (6-FP)Rh(Cl)(η^2-C₂H₄)	88
2.3.6 Kinetic studies on ⁵NPFP-A catalyzed styrene hydrogenation	91
2.3.7 Mechanistic Studies based on Density Functional Theory	102
2.4 Summary and Conclusions	110
2.5 Experimental section	111
2.6 References	116
3 Direct Carboxylation Of Benzene Using Pcp-Pd Complexes As A Catalyst	127
3.1 Introduction	127
3.2 Preliminary conditions screening for Pd catalyzed direct carboxylation of benzene under basic conditions.	134
3.3 Studies of CO₂ insertion using (^RPCP)PdPh complexes	141
3.4 Studies of benzene C–H activation by (^{iPr}PCP)PdOBz	150

3.5	Conclusions	154
3.6	Experimental section	154
3.7	References	172

4 Catalytic Methanol Carbonylation Using Rhodium Or Iridium Catalysts Ligated By “Capping Arene” Ligands 180

4.1	Introduction	180
------------	---------------------	-----

4.2	Synthesis and characterization of [(FP)M^I(CO)₂]BF₄ (FP = 5-FP or 6-FP, M = Rh or Ir) complexes	184
------------	--	-----

4.3	Methanol carbonylation catalyzed by [(FP)M^I(CO)₂]BF₄ (FP = 5-FP or 6-FP, M = Rh or Ir) complexes	186
------------	--	-----

4.4	Mechanistic studies on methanol carbonylation catalyzed by [(FP)Rh(CO)₂]BF₄ complexes	188
------------	--	-----

4.5	Summary and Conclusion	197
------------	-------------------------------	-----

4.6	Experimental section	198
------------	-----------------------------	-----

4.7	References	209
------------	-------------------	-----

5 Catalytic Hydrogenation Of Styrene Catalyzed By A “Capping Arene” Ligated Cobalt Complex 213

5.1	Introduction	213
------------	---------------------	-----

5.2 Synthesis and characterization of (5-FP)CoCl₂	214
5.3 Preliminary NMR-scale studies for (5-FP)CoCl₂-catalyzed styrene hydrogenation	216
5.4 Condition optimization for (5-FP)CoCl₂ catalyzed styrene hydrogenation	218
5.5 Summary and future directions	222
5.6 Experimental section	223
5.7 References	229
6 Summary And Future Directions	233
6.1 Summary	233
6.2 Future Directions	234
6.2.1 Co-catalyzed alkyne partial hydrogenation to produce alkene	234
6.2.2 Development of "capping arene" ligands	235
6.3 References	237

LIST OF FIGURES

Figure 1.2.1 Molecular orbital diagram for H ₂	2
Figure 1.2.2 Possible pathways for H ₂ activation.	3
Figure 1.2.3 The σ -donation and π -back bonding of an η^2 -H ₂ with transition metals (M) 4	
Figure 1.2.4 Proposed catalytic cycle for olefin hydrogenation catalyzed by Wilkinson's catalyst.	5
Figure 1.2.5 Proposed catalytic cycle for olefin hydrogenation catalyzed by the Schrock-Osborn catalyst.....	7
Figure 1.2.6 Proposed Ir(III)/Ir(V) catalytic cycle for Ir catalyzed olefin hydrogenation. 8	
Figure 1.2.7 Calculated mechanism for Rh(H) ₂ (NH ₂ CH ₂ CH ₂ NH ₂)(PH ₃) ₂ catalyzed acetone hydrogenation.	9
Figure 1.2.8 Proposed mechanism for ketone hydrogenation catalyzed by [M(Cp)(CO) ₂ (PR ₃)(OCR ₂)] ⁺ (M = Mo or W).....	10
Figure 1.3.1 Molecular orbital diagram for CO.	11
Figure 1.3.2 σ -donation and π -back bonding of a κ^1 -CO with transition metals (M).....	12
Figure 1.3.3 Proposed mechanism for rhodium and iridium catalyzed methanol carbonylation.....	14
Figure 1.3.4 Examples of ligands studied for Rh catalyzed methanol carbonylation.....	15
Figure 1.3.5 Proposed mechanism for HCo(CO) ₄ catalyzed hydroformylation.	16
Figure 1.3.6 Proposed mechanism for Rh catalyzed hydroformylation.	18
Figure 1.3.7 The bite angles for biphosphine ligands on Rh and the linear:branch (l:b) ratios for catalytic hydroformylation of 1-hexene.	18

Figure 1.3.8 Steric hinderance of biphosphine ligands in square pyramidal transition states of the olefin insertion step.....	19
Figure 1.4.1 MO diagram for CO ₂	20
Figure 1.4.2 Possible binding modes for CO ₂ coordinated to transition metals.	21
Figure 2.2.1 Comparison of olefin hydrogenation catalyzed by four capping arene Rh complexes.	54
Figure 2.2.2 A sample of catalytic hydrogenation of cyclohexene with "capping arene" ligated Rh catalyst.....	55
Figure 2.2.3 Sample ¹ H NMR spectra showing the observed decomposition of (6- ^{NP} FP)Rh(η ² -C ₂ H ₄)Cl (6^{NP}FP-A) during catalytic of styrene hydrogenation.....	56
Figure 2.2.4 Sample ¹ H NMR spectra for the observation of (6- ^{NP} FP)Rh(η ² -C ₂ H ₄)Cl (6^{NP}FP-A) with minimal decomposition at shorter time points during the catalysis of styrene hydrogenation for comparison with Figure 2.2.3	57
Figure 2.2.5 Plot of [cyclohexane] (mM) vs. time (s) for (6-FP)Rh(η ² -C ₂ H ₄)Cl (6FP-A) catalyzed cyclohexene hydrogenation.	58
Figure 2.2.6 Plot of [ethylbenzene] (mM) vs. time (s) for (6-FP)Rh(η ² -C ₂ H ₄)Cl (6FP-A) catalyzed styrene hydrogenation.....	58
Figure 2.2.7 Plot of [2,2-dimethylbutane] (mM) vs. time (s) for (6-FP)Rh(η ² -C ₂ H ₄)Cl (6FP-A) catalyzed 3,3-dimethylbutene hydrogenation.	59
Figure 2.2.8 Plot of [pentane] (mM) vs. time (s) for (6-FP)Rh(η ² -C ₂ H ₄)Cl (6FP-A) catalyzed <i>trans</i> -2-pentene hydrogenation.	59
Figure 2.2.9 Plot of [pentane] (mM) vs. time (s) for (6-FP)Rh(η ² -C ₂ H ₄)Cl (6FP-A) catalyzed <i>cis</i> -2-pentene hydrogenation.	60

Figure 2.2.10 Plot of [cyclohexane] (mM) vs. time (s) for (5-FP)Rh(η^2 -C ₂ H ₄)Cl (5FP-A) catalyzed cyclohexene hydrogenation.	60
Figure 2.2.11 Plot of [ethylbenzene] (mM) vs. time (s) for (5-FP)Rh(η^2 -C ₂ H ₄)Cl (5FP-A) catalyzed styrene hydrogenation.	61
Figure 2.2.12 Plot of [2,2-dimethylbutane] (mM) vs. time (s) for (5-FP)Rh(η^2 -C ₂ H ₄)Cl (5FP-A) catalyzed 3,3-dimethylbutene hydrogenation.	61
Figure 2.2.13 Plot of [pentane] (mM) vs. time (s) for (5-FP)Rh(η^2 -C ₂ H ₄)Cl (5FP-A) catalyzed <i>trans</i> -2-pentene hydrogenation.	62
Figure 2.2.14 Plot of [pentane] (mM) vs. time (s) for (5-FP)Rh(η^2 -C ₂ H ₄)Cl (5FP-A) catalyzed <i>cis</i> -2-pentene hydrogenation.	62
Figure 2.2.15 Plot of [cyclohexane] (mM) vs. time (s) for (6- ^{NP} FP)Rh(η^2 -C ₂ H ₄)Cl (6^{NP}FP-A) catalyzed cyclohexene hydrogenation.	63
Figure 2.2.16 Plot of [ethylbenzene] (mM) vs. time (s) for (6- ^{NP} FP)Rh(η^2 -C ₂ H ₄)Cl (6^{NP}FP-A) catalyzed styrene hydrogenation.	63
Figure 2.2.17 Plot of [2,2-dimethylbutane] (mM) vs. time (s) for (6- ^{NP} FP)Rh(η^2 -C ₂ H ₄)Cl (6^{NP}FP-A) catalyzed 3,3-dimethylbutene hydrogenation.	64
Figure 2.2.18 Plot of [cyclohexane] (mM) vs. time (s) for (5- ^{NP} FP)Rh(η^2 -C ₂ H ₄)Cl (5^{NP}FP-A) catalyzed cyclohexene hydrogenation.	64
Figure 2.2.19 Plot of [ethylbenzene] (mM) vs. time (s) for (5- ^{NP} FP)Rh(η^2 -C ₂ H ₄)Cl (5^{NP}FP-A) catalyzed styrene hydrogenation.	65
Figure 2.2.20 Plot of [2,2-dimethylbutane] (mM) vs. time (s) for (5- ^{NP} FP)Rh(η^2 -C ₂ H ₄)Cl (5^{NP}FP-A) catalyzed 3,3-dimethylbutene hydrogenation.	65

Figure 2.2.21 Plot of [pentane] (mM) vs. time (s) for (5- ^{NP} FP)Rh(η^2 -C ₂ H ₄)Cl (5^{NP}FP-A) catalyzed <i>trans</i> -2-pentene hydrogenation.	66
Figure 2.2.22 Plot of [pentane] (mM) vs. time (s) for (5- ^{NP} FP)Rh(η^2 -C ₂ H ₄)Cl (5^{NP}FP-A) catalyzed <i>cis</i> -2-pentene hydrogenation.	66
Figure 2.3.1 Studies of reaction order for hydrogenation of styrene using (6-FP)Rh(Cl)(η^2 -C ₂ H ₄) (6FP-A).	69
Figure 2.3.2 Scatter plots for [\int (styrene)+ \int (EtPh)/2]/ \int (HMB) vs. time (s) for (6-FP)Rh(η^2 -C ₂ H ₄)Cl (6FP-A) catalyzed styrene hydrogenation.	70
Figure 2.3.3 \int HMB vs. time (s) plot for (6-FP)Rh(η^2 -C ₂ H ₄)Cl (6FP-A) catalyzed styrene hydrogenation.	71
Figure 2.3.4 Plots of [styrene] (mM) vs. time (s) for (6-FP)Rh(η^2 -C ₂ H ₄)Cl (6FP-A) catalyzed styrene hydrogenation with 1 mM 6FP-A , 44 mM styrene, 20 psig H ₂ in CD ₂ Cl ₂ , 45 °C in triplicate.	72
Figure 2.3.5 Plots of [styrene] (mM) vs. time (s) for (6-FP)Rh(η^2 -C ₂ H ₄)Cl (6FP-A) catalyzed styrene hydrogenation with 1 mM 6FP-A , 44 mM styrene, 30 psig H ₂ in CD ₂ Cl ₂ , 45 °C in triplicate.	72
Figure 2.3.6 Plots of [styrene] (mM) vs. time (s) for (6-FP)Rh(η^2 -C ₂ H ₄)Cl (6FP-A) catalyzed styrene hydrogenation 1 mM 6FP-A , 44 mM styrene, 40 psig H ₂ in CD ₂ Cl ₂ , 45 °C in triplicate.	72
Figure 2.3.7 Plots of [styrene] (mM) vs. time (s) for (6-FP)Rh(η^2 -C ₂ H ₄)Cl (6FP-A) catalyzed styrene hydrogenation 1 mM 6FP-A , 44 mM styrene, 50 psig H ₂ in CD ₂ Cl ₂ , 45 °C in triplicate.	73

- Figure 2.3.8** Plots of [styrene] (mM) vs. time (s) for (6-FP)Rh(η^2 -C₂H₄)Cl (**6FP-A**) catalyzed styrene hydrogenation with 4 mM **6FP-A**, 44 mM styrene, 50 psig H₂ in CD₂Cl₂, 45 °C in triplicate..... 73
- Figure 2.3.9** Plots of [styrene] (mM) vs. time (s) for (6-FP)Rh(η^2 -C₂H₄)Cl (**6FP-A**) catalyzed styrene hydrogenation with 2 mM **6FP-A**, 44 mM styrene, 50 psig H₂ in CD₂Cl₂, 45 °C in triplicate..... 73
- Figure 2.3.10** Plots of [styrene] (mM) vs. time (s) for (6-FP)Rh(η^2 -C₂H₄)Cl (**6FP-A**) catalyzed styrene hydrogenation with 1 mM **6FP-A**, 44 mM styrene, 50 psig H₂ in CD₂Cl₂, 45 °C in triplicate..... 74
- Figure 2.3.11** Plots of [styrene] (mM) vs. time (s) for (6-FP)Rh(η^2 -C₂H₄)Cl (**6FP-A**) catalyzed styrene hydrogenation with 0.5 mM **6FP-A**, 44 mM styrene, 50 psig H₂ in CD₂Cl₂, 45 °C in triplicate..... 74
- Figure 2.3.12** Plots of [styrene] (mM) vs. time (s) for (6-FP)Rh(η^2 -C₂H₄)Cl (**6FP-A**) catalyzed styrene hydrogenation with 0.25 mM **6FP-A**, 44 mM styrene, 50 psig H₂ in CD₂Cl₂, 45 °C in triplicate..... 74
- Figure 2.3.13** Plots of [styrene] (mM) vs. time (s) for (6-FP)Rh(η^2 -C₂H₄)Cl (**6FP-A**) catalyzed styrene hydrogenation with 0.5 mM **6FP-A**, 11 mM styrene, 50 psig H₂ in CD₂Cl₂, 45 °C in triplicate..... 75
- Figure 2.3.14** Plots of [styrene] (mM) vs. time (s) for (6-FP)Rh(η^2 -C₂H₄)Cl (**6FP-A**) catalyzed styrene hydrogenation with 0.5 mM **6FP-A**, 44 mM styrene, 50 psig H₂ in CD₂Cl₂, 45 °C in triplicate..... 75

Figure 2.3.15 Plots of [styrene] (mM) vs. time (s) for (6-FP)Rh(η^2 -C ₂ H ₄)Cl (6FP-A) catalyzed styrene hydrogenation with 0.5 mM 6FP-A , 87 mM styrene, 50 psig H ₂ in CD ₂ Cl ₂ , 45 °C in triplicate.....	75
Figure 2.3.16 Plots of [styrene] (mM) vs. time (s) for (6-FP)Rh(η^2 -C ₂ H ₄)Cl (6FP-A) catalyzed styrene hydrogenation with 0.5 mM 6FP-A , 174 mM styrene, 50 psig H ₂ in CD ₂ Cl ₂ , 45 °C in triplicate.....	76
Figure 2.3.17 Plots of [styrene] (mM) vs. time (s) for (6-FP)Rh(η^2 -C ₂ H ₄)Cl (6FP-A) catalyzed styrene hydrogenation with 0.5 mM 6FP-A , 348 mM styrene, 50 psig H ₂ in CD ₂ Cl ₂ , 45 °C in triplicate.....	76
Figure 2.3.18 Eyring plot for the hydrogenation of styrene catalyzed by (6-FP)Rh(η^2 -C ₂ H ₄)Cl (6FP-A).	78
Figure 2.3.19 Plots of [styrene] (mM) vs. time (s) for (6-FP)Rh(η^2 -C ₂ H ₄)Cl (6FP-A) catalyzed styrene hydrogenation. The reaction is performed in triplicate with 1 mM 6FP-A , 44 mM styrene, 50 psig H ₂ in CD ₂ Cl ₂ , 24 °C.	79
Figure 2.3.20 Plots of [styrene] (mM) vs. time (s) for (6-FP)Rh(η^2 -C ₂ H ₄)Cl (6FP-A) catalyzed styrene hydrogenation. The reaction is performed in triplicate with 1 mM 6FP-A , 44 mM styrene, 50 psig H ₂ in CD ₂ Cl ₂ , 34 °C.	80
Figure 2.3.21 Plots of [styrene] (mM) vs. time (s) for (6-FP)Rh(η^2 -C ₂ H ₄)Cl (6FP-A) catalyzed styrene hydrogenation. The reaction is performed in triplicate with 1 mM 6FP-A , 44 mM styrene, 50 psig H ₂ in CD ₂ Cl ₂ , 39 °C.	80
Figure 2.3.22 Plots of [styrene] (mM) vs. time (s) for (6-FP)Rh(η^2 -C ₂ H ₄)Cl (6FP-A) catalyzed styrene hydrogenation. The reaction is performed in triplicate with 1 mM 6FP-A , 44 mM styrene, 50 psig H ₂ in CD ₂ Cl ₂ , 43 °C.	80

- Figure 2.3.23** Plots of [styrene] (mM) vs. time (s) for (6-FP)Rh(η^2 -C₂H₄)Cl (**6FP-A**) catalyzed styrene hydrogenation. The reaction is performed in triplicate with 1 mM **6FP-A**, 44 mM styrene, 50 psig H₂ in CD₂Cl₂, 49 °C. 81
- Figure 2.3.24** Plots of [styrene] (mM) vs. time (s) for (6-FP)Rh(η^2 -C₂H₄)Cl (**6FP-A**) catalyzed styrene hydrogenation. The reaction is performed in triplicate with 1 mM **6FP-A**, 44 mM styrene, 50 psig H₂ in CD₂Cl₂, 54 °C. 81
- Figure 2.3.25** The 2D-Exchange Spectroscopy (2D-EXSY) plot for (6-FP)Rh(Cl)(η^2 -styrene) (**6FP-B**). 83
- Figure 2.3.26** 2D-EXSY peaks used for the exchange rate for the two species observed in CD₂Cl₂ solution of (6-FP)Rh(η^2 -styrene)Cl (**6FP-B**) based on 2D-EXSY. 84
- Figure 2.3.27** DFT calculated structure of (6-FP)Rh(Cl)(η^2 -styrene) (**6FP-B**). 85
- Figure 2.3.28** ORTEP of (6-FP)Rh(Cl)(η^2 -styrene) (**6FP-B**). Ellipsoids are drawn at 50% probability level. Hydrogen atoms and noncoordinating solvents are omitted for clarity. 85
- Figure 2.3.29** ¹H NMR spectroscopy evidence for H/D exchange between styrene and D₂. 89
- Figure 2.3.30** Studies of reaction order for hydrogenation of styrene using (5-^{NP}FP)Rh(Cl)(η^2 -C₂H₄) (**5^{NP}FP-A**) or [Rh(η^2 -C₂H₄)(μ -Cl)]₂. 92
- Figure 2.3.31** Plots of [styrene] (mM) vs. time (s) for (5-^{NP}FP)Rh(η^2 -C₂H₄)Cl (**5^{NP}FP-A**) catalyzed styrene hydrogenation. The reaction was performed in triplicate with 1 mM **5^{NP}FP-A**, 87 mM styrene, 50 psig H₂ in CD₂Cl₂, 45 °C. 93
- Figure 2.3.32** Plots of [styrene] (mM) vs. time (s) for (5-^{NP}FP)Rh(η^2 -C₂H₄)Cl (**5^{NP}FP-A**) catalyzed styrene hydrogenation. The reaction was performed in triplicate with 1 mM **5^{NP}FP-A**, 87 mM styrene, 40 psig H₂ in CD₂Cl₂, 45 °C. 93

- Figure 2.3.33** Plots of [styrene] (mM) vs. time (s) for $(5\text{-}^{\text{NP}}\text{FP})\text{Rh}(\eta^2\text{-C}_2\text{H}_4)\text{Cl}$ (**5^{NP}FP-A**) catalyzed styrene hydrogenation. The reaction was performed in triplicate with 1 mM **5^{NP}FP-A**, 87 mM styrene, 30 psig H_2 in CD_2Cl_2 , 45 °C. 93
- Figure 2.3.34** Plots of [styrene] (mM) vs. time (s) for $(5\text{-}^{\text{NP}}\text{FP})\text{Rh}(\eta^2\text{-C}_2\text{H}_4)\text{Cl}$ (**5^{NP}FP-A**) catalyzed styrene hydrogenation. The reaction was performed in triplicate with 1 mM **5^{NP}FP-A**, 87 mM styrene, 20 psig H_2 in CD_2Cl_2 , 45 °C. 94
- Figure 2.3.35** Plots of [styrene] (mM) vs. time (s) for $(5\text{-}^{\text{NP}}\text{FP})\text{Rh}(\eta^2\text{-C}_2\text{H}_4)\text{Cl}$ (**5^{NP}FP-A**) catalyzed styrene hydrogenation. The reaction was performed in triplicate with 4 mM **5^{NP}FP-A**, 87 mM styrene, 50 psig H_2 in CD_2Cl_2 , 45 °C. 94
- Figure 2.3.36** Plots of [styrene] (mM) vs. time (s) for $(5\text{-}^{\text{NP}}\text{FP})\text{Rh}(\eta^2\text{-C}_2\text{H}_4)\text{Cl}$ (**5^{NP}FP-A**) catalyzed styrene hydrogenation. The reaction was performed in triplicate with 2 mM **5^{NP}FP-A**, 87 mM styrene, 50 psig H_2 in CD_2Cl_2 , 45 °C. 94
- Figure 2.3.37** Plots of [styrene] (mM) vs. time (s) for $(5\text{-}^{\text{NP}}\text{FP})\text{Rh}(\eta^2\text{-C}_2\text{H}_4)\text{Cl}$ (**5^{NP}FP-A**) catalyzed styrene hydrogenation. The reaction was performed in triplicate with 1 mM **5^{NP}FP-A**, 87 mM styrene, 50 psig H_2 in CD_2Cl_2 , 45 °C. 95
- Figure 2.3.38** Plots of [styrene] (mM) vs. time (s) for $(5\text{-}^{\text{NP}}\text{FP})\text{Rh}(\eta^2\text{-C}_2\text{H}_4)\text{Cl}$ (**5^{NP}FP-A**) catalyzed styrene hydrogenation. The reaction was performed in triplicate with 0.5 mM **5^{NP}FP-A**, 87 mM styrene, 50 psig H_2 in CD_2Cl_2 , 45 °C. 95
- Figure 2.3.39** Plots of [styrene], [ethylbenzene] and $[\text{H}_2]$ (mM) vs. time (s) for $[\text{Rh}(\eta^2\text{-C}_2\text{H}_4)_2(\mu\text{-Cl})_2]$ catalyzed styrene hydrogenation. 96
- Figure 2.3.40** Plots of $\ln\{[\text{styrene}][\text{H}_2]_0/[\text{H}_2][\text{styrene}]_0\}$ vs. $\{[\text{styrene}]_0 - [\text{H}_2]_0\}t$ (mM·s) for $[\text{Rh}(\eta^2\text{-C}_2\text{H}_4)_2(\mu\text{-Cl})_2]$ catalyzed styrene hydrogenation. The reaction was performed

in triplicate with 2 mM $[\text{Rh}(\eta^2\text{-C}_2\text{H}_4)_2(\mu\text{-Cl})_2]$, 44 mM styrene, 50 psig H_2 in CD_2Cl_2 ,
45 °C. 97

Figure 2.3.41 Plots of $\ln\{[\text{styrene}][\text{H}_2]_0/[\text{H}_2][\text{styrene}]_0\}$ vs. $\{[\text{styrene}]_0-[\text{H}_2]_0\}t$ (mM·s)
for $[\text{Rh}(\eta^2\text{-C}_2\text{H}_4)_2(\mu\text{-Cl})_2]$ catalyzed styrene hydrogenation. The reaction was performed
in triplicate with 1 mM $[\text{Rh}(\eta^2\text{-C}_2\text{H}_4)_2(\mu\text{-Cl})_2]$, 44 mM styrene, 50 psig H_2 in CD_2Cl_2 ,
45 °C. 98

Figure 2.3.42 Plots of $\ln\{[\text{styrene}][\text{H}_2]_0/[\text{H}_2][\text{styrene}]_0\}$ vs. $\{[\text{styrene}]_0-[\text{H}_2]_0\}t$ (mM·s)
for $[\text{Rh}(\eta^2\text{-C}_2\text{H}_4)_2(\mu\text{-Cl})_2]$ catalyzed styrene hydrogenation. The reaction was performed
in triplicate with 0.5 mM $[\text{Rh}(\eta^2\text{-C}_2\text{H}_4)_2(\mu\text{-Cl})_2]$, 44 mM styrene, 50 psig H_2 in CD_2Cl_2 ,
45 °C. 98

Figure 2.3.43 Plots of $\ln\{[\text{styrene}][\text{H}_2]_0/[\text{H}_2][\text{styrene}]_0\}$ vs. $\{[\text{styrene}]_0-[\text{H}_2]_0\}t$ (mM·s) for
 $[\text{Rh}(\eta^2\text{-C}_2\text{H}_4)_2(\mu\text{-Cl})_2]$ catalyzed styrene hydrogenation. The reaction was performed in
triplicate with 0.25 mM $[\text{Rh}(\eta^2\text{-C}_2\text{H}_4)_2(\mu\text{-Cl})_2]$, 44 mM styrene, 50 psig H_2 in CD_2Cl_2 ,
45 °C. 99

Figure 2.3.44 ^1H NMR evidence for the decomposition of $(5\text{-}^{99}\text{FP})\text{Rh}(\eta^2\text{-C}_2\text{H}_4)\text{Cl}$
 (5^{99}FP-A) during the catalytic styrene hydrogenation. Conditions: (a) 4 mM 5^{99}FP , 87 mM
styrene, 50 psig H_2 , 25 °C, 0 hour in CD_2Cl_2 ; (b) 4 mM 5^{99}FP , 87 mM styrene, 50 psig H_2 ,
45 °C, 1 hour in CD_2Cl_2 ; (c) 4 in CD_2Cl_2 99

Figure 2.3.45 ORTEP of $(5\text{-}^{99}\text{FP})\text{Rh}(\text{Cl})(\eta^2\text{-styrene})$ (5^{99}FP-B). Ellipsoids are drawn at
50% probability level. Hydrogen atoms and noncoordinating solvents are omitted for
clarity. 101

- Figure 2.3.46** Comparison of the ^1H NMR spectra for (1) 4 mM 5^{NP}FP-A , 87 mM styrene, 50 psig H_2 , 25 $^\circ\text{C}$, 0 hour in CD_2Cl_2 (above); (2) crystal of 5^{NP}FP-B in CD_2Cl_2 (below). 101
- Figure 2.3.47** Comparison of the energy diagram for the styrene hydrogenation catalyzed by 6FP-A and 5FP-A 107
- Figure 2.3.48** DFT-optimized transition states (6FP-TS1 and 5FP-TS1) and products (6FP-C and 5FP-C) for H_2 oxidative addition for: $(5\text{-FP})\text{Rh}(\eta^2\text{-styrene})\text{Cl}$ (left) and $(6\text{-FP})\text{Rh}(\eta^2\text{-styrene})\text{Cl}$ (right). 109
- Figure 3.3.1** ^1H NMR (top) and ^{31}P NMR (bottom) evidence for *in situ* formation of new PCP-Pd species through reaction of $(^{\text{tBu}}\text{PCP})\text{PdPh}$ and PhMgBr 142
- Figure 3.3.2** ^1H NMR spectrum of phenyl {2,5-di[(di-*iso*-propyl phosphino)methyl]phenyl palladium} ($^{\text{iPr}}\text{PCP})\text{PdPh}$ in CD_3CN . Unlabeled peaks are from residual solvent (*n*-pentane) in the NMR solvent due to the atmosphere in the glovebox. 144
- Figure 3.3.3** ^{31}P NMR spectrum for phenyl {2,5-di[(di-*iso*-propyl phosphino)methyl]phenyl palladium} ($^{\text{iPr}}\text{PCP})\text{PdPh}$ in CD_3CN 144
- Figure 3.3.4** ORTEP of phenyl{2,5-di[(di-*iso*-propyl phosphino)methyl]phenyl palladium} ($^{\text{iPr}}\text{PCP})\text{PdPh}$. Ellipsoids are drawn at 50% probability level. Hydrogen atoms are omitted for clarity. 145
- Figure 3.3.5** ^1H NMR spectrum of 2,5-di[(di-*iso*-propyl phosphino)methyl]phenyl palladium benzoate ($^{\text{iPr}}\text{PCP})\text{PdOBz}$ in CD_3CN . Unlabeled peaks are from residual solvent (Et_2O and THF) in the NMR solvent due to the atmosphere in the glovebox. 145

Figure 3.3.6 ^{31}P NMR spectrum for 2,5-di[(di- <i>iso</i> -propyl phosphino)methyl]phenyl palladium benzoate ($^{i\text{Pr}}\text{PCP}$)PdOBz in CD_3CN	146
Figure 3.3.7 ORTEP of 2,5-di[(di- <i>iso</i> -propyl phosphino)methyl]phenyl palladium benzoate [$^{i\text{Pr}}\text{PCP}$]PdOBz]. Ellipsoids are drawn at 50% probability level. Hydrogen atoms are omitted for clarity.	146
Figure 3.3.8 ^1H NMR spectra for CO_2 insertion into ($^{i\text{Pr}}\text{PCP}$)PdPh to form ($^{i\text{Pr}}\text{PCP}$)PdOBz.	148
Figure 3.3.9 Observed formation of benzene in the ^1H NMR spectra for ($^{i\text{Pr}}\text{PCP}$)PdPh in 2,2,2-trifluoroethanol.	150
Figure 3.4.1 Changes in the percentage of different isotopic labeled benzene. Conditions: 1 mL benzene, 1 mL benzene- d_6 , 3 mL acetonitrile, 10 mg ($^{i\text{Pr}}\text{PCP}$)PdOBz, 150 °C, 48 hours.	153
Figure 3.4.2 Changes in the percentage of different isotopic labeled benzene. Conditions: 1 mL benzene, 1 mL benzene- d_6 , 3 mL tetrahydrofuran, 10 mg ($^{i\text{Pr}}\text{PCP}$)PdOBz, 150 °C, 48 hours.	153
Figure 3.4.3 Changes in the percentage of different isotopic labeled benzene. Conditions: 1 mL benzene, 1 mL benzene- d_6 , 3 mL toluene, 10 mg ($^{i\text{Pr}}\text{PCP}$)PdOBz, 150 °C, 48 hours.	153
Figure 3.6.1 Calibration curve for quantification of biphenyl using hexamethylbenzene as a standard.	156
Figure 3.6.2 Calibration curve for quantification of benzoic acid using hexamethylbenzene as a standard.	156

- Figure 3.6.3** ^1H NMR spectrum for 1,3-di[(diphenylphosphino)methyl]benzene ($^{\text{Ph}}\text{PCPH}$). Unlabeled peaks are from residual solvent (including Et_2O , THF, DCM, toluene) in the NMR solvent due to the atmosphere in the glovebox. 157
- Figure 3.6.4** ^{31}P NMR spectrum for 1,3-di[(diphenylphosphino)methyl]benzene ($^{\text{Ph}}\text{PCPH}$). 158
- Figure 3.6.5** ^1H NMR spectrum for 1,3-di[(di-*tert*-butylphosphino)methyl]benzene ($^{\text{tBu}}\text{PCPH}$). Unlabeled peaks are from residual solvent (including Et_2O , THF, cyclohexane) in the NMR solvent due to the atmosphere in the glovebox. 159
- Figure 3.6.6** ^{31}P NMR spectrum for 1,3-di[(di-*tert*-butylphosphino)methyl]benzene ($^{\text{tBu}}\text{PCPH}$). 159
- Figure 3.6.7** ^1H NMR spectrum for 1,3-di[(di-*iso*-propylphosphino)methyl]benzene ($^{\text{iPr}}\text{PCPH}$). 160
- Figure 3.6.8** ^{31}P NMR spectrum for 1,3-di[(di-*iso*-propylphosphino)methyl]benzene ($^{\text{iPr}}\text{PCPH}$). 160
- Figure 3.6.9** ^1H NMR spectrum for 2,5-di[(diphenylphosphino)methyl]phenyl palladium trifluoroacetate ($^{\text{Ph}}\text{PCP}$)Pd(TFA). Unlabeled peaks are from residual solvent (including Et_2O , THF, DCM) in the NMR solvent due to the atmosphere in the glovebox. 161
- Figure 3.6.10** ^{31}P NMR spectrum for 2,5-di[(diphenylphosphino)methyl]phenyl palladium trifluoroacetate ($^{\text{Ph}}\text{PCP}$)Pd(TFA). 161
- Figure 3.6.11** ^1H NMR spectrum for 2,5-di[(di-*tert*-butyl phosphino)methyl]phenyl palladium trifluoroacetate [$^{\text{tBu}}\text{PCP}$]Pd(TFA). Unlabeled peaks are from residual solvent (including Et_2O , THF, DCM, n-pentane) in the NMR solvent due to the atmosphere in the glovebox. 162

Figure 3.6.12 ^{31}P NMR spectrum for 2,5-di[(di- <i>tert</i> -butyl phosphino)methyl]phenyl palladium trifluoroacetate ($^{\text{tBu}}\text{PCP}$)Pd(TFA).....	162
Figure 3.6.13 ^{19}F NMR spectrum for 2,5-di[(di- <i>tert</i> -butyl phosphino)methyl]phenyl palladium trifluoroacetate ($^{\text{tBu}}\text{PCP}$)Pd(TFA).....	163
Figure 3.6.14 ^1H NMR spectrum for 2,5-di[(di- <i>tert</i> -butyl phosphino)methyl]phenyl palladium chloroide ($^{\text{tBu}}\text{PCP}$)PdCl.....	164
Figure 3.6.15 ^{31}P NMR spectrum for 2,5-di[(di- <i>tert</i> -butyl phosphino)methyl]phenyl palladium chloroide [$^{\text{tBu}}\text{PCP}$]PdCl].....	164
Figure 3.6.16 ^1H NMR spectrum for 2,5-di[(di- <i>iso</i> -propyl phosphino)methyl]phenyl palladium chloroide ($^{\text{iPr}}\text{PCP}$)PdCl.....	165
Figure 3.6.17 ^{31}P NMR spectrum 2,5-di[(di- <i>iso</i> -propyl phosphino)methyl]phenyl palladium chloroide ($^{\text{iPr}}\text{PCP}$)PdCl.....	165
Figure 3.6.18 ^1H NMR spectrum for phenyl {2,5-di[(di- <i>iso</i> -propyl phosphino)methyl]phenyl palladium} ($^{\text{iPr}}\text{PCP}$)PdPh. Unlabeled peaks are from residual solvent (n-pentane) in the NMR solvent due to the atmosphere in the glovebox.....	166
Figure 3.6.19 ^{31}P NMR spectrum for phenyl {2,5-di[(di- <i>iso</i> -propyl phosphino)methyl]phenyl palladium} ($^{\text{iPr}}\text{PCP}$)PdPh.....	166
Figure 3.6.20 ORTEP of phenyl{2,5-di[(di- <i>iso</i> -propyl phosphino)methyl]phenyl palladium} ($^{\text{iPr}}\text{PCP}$)PdPh. Ellipsoids are drawn at 50% probability level. Hydrogen atoms are omitted for clarity.....	167
Figure 3.6.21 ^1H NMR spectrum for 2,5-di[(di- <i>iso</i> -propyl phosphino)methyl]phenyl palladium benzoate ($^{\text{iPr}}\text{PCP}$)PdOBz. Unlabeled peaks are from residual solvent (Et ₂ O and THF) in the NMR solvent due to the atmosphere in the glovebox.....	168

Figure 3.6.22 ^{31}P NMR spectrum for 2,5-di[(di- <i>iso</i> -propyl phosphino)methyl]phenyl palladium benzoate ($^{i\text{Pr}}\text{PCP}$)PdOBz.....	168
Figure 3.6.23 ORTEP of 2,5-di[(di- <i>iso</i> -propyl phosphino)methyl]phenyl palladium benzoate [$^{i\text{Pr}}\text{PCP}$]PdOBz]. Ellipsoids are drawn at 50% probability level. Hydrogen atoms are omitted for clarity.	169
Figure 3.6.24 Images of high-pressure reaction vessel used (VCO reactor).	170
Figure 4.1.1 Examples of “capping arene” ligands.....	183
Figure 4.2.1 Procedures for the syntheses of [(5-FP)Rh(CO) $_2$]BF $_4$ and [(6-FP)Rh(CO) $_2$]BF $_4$	184
Figure 4.2.2 Procedures for the syntheses of [(5-FP)Ir(CO) $_2$]BF $_4$ and [(6-FP)Ir(CO) $_2$]BF $_4$	185
Figure 4.3.1 Example of GC-MS chromatogram for the quantification of methyl acetate (MeOAc) and acetic acid (HOAc) using cyclohexane as the standard.....	186
Figure 4.3.2 Comparison of methanol carbonylation catalyzed by “capping arene” ligated Ir or Rh complexes.....	187
Figure 4.4.1 Stacked ^1H NMR spectra for the stability of [(5-FP)Rh(CO) $_2$]BF $_4$ at 135 °C in MeOH- d_4 . The top spectrum is the ^1H NMR spectrum of 5-FP ligand for comparison.	189
Figure 4.4.2 Stacked ^1H NMR spectra for the stability of [(6-FP)Rh(CO) $_2$]BF $_4$ at 135 °C in MeOH- d_4 . The top spectrum is the ^1H NMR spectrum of 6-FP ligand for comparison.	190

Figure 4.4.3 Stacked ^1H NMR spectra for the stability of $[(5\text{-FP})\text{Ir}(\text{CO})_2]\text{BF}_4$ at $135\text{ }^\circ\text{C}$ in $\text{MeOH-}d_4$. The top spectrum is the ^1H NMR spectrum of 5-FP ligand for comparison.	190
Figure 4.4.4 Stacked ^1H NMR spectra for the stability of $[(6\text{-FP})\text{Ir}(\text{CO})_2]\text{BF}_4$ at $135\text{ }^\circ\text{C}$ in $\text{MeOH-}d_4$. The top spectrum is the ^1H NMR spectrum of 6-FP ligand for comparison.	191
Figure 4.4.5 Stacked ^1H NMR spectra for the stability of 6-FP ligand at $135\text{ }^\circ\text{C}$ in $\text{MeOH-}d_4$	191
Figure 4.4.6 Stacked ^1H NMR spectra for the stability of 5-FP ligand at $135\text{ }^\circ\text{C}$ in $\text{MeOH-}d_4$	192
Figure 4.4.7 Stacked ^1H NMR spectra for the reaction $[(5\text{-FP})\text{Rh}(\text{CO})_2]\text{BF}_4$ in the presence of MeI at $135\text{ }^\circ\text{C}$	193
Figure 4.4.8 Stacked ^1H NMR spectra for the reaction $[(6\text{-FP})\text{Rh}(\text{CO})_2]\text{BF}_4$ in the presence of MeI at $135\text{ }^\circ\text{C}$	194
Figure 4.4.9 Stacked ^1H NMR spectra for the reaction $[(5\text{-FP})\text{Ir}(\text{CO})_2]\text{BF}_4$ in the presence of MeI at $135\text{ }^\circ\text{C}$	194
Figure 4.4.10 Stacked ^1H NMR spectra for the reaction $[(6\text{-FP})\text{Ir}(\text{CO})_2]\text{BF}_4$ in the presence of MeI at $135\text{ }^\circ\text{C}$	195
Figure 4.4.11 Stacked ^1H NMR spectra for the reaction 6-FP ligand in the presence of MeI at $135\text{ }^\circ\text{C}$	195
Figure 4.4.12 Stacked ^1H NMR spectra for the reaction 5-FP ligand in the presence of MeI at $135\text{ }^\circ\text{C}$	196

Figure 4.4.13 Comparison of the products for the reaction of [(5-FP)Ir(CO) ₂]BF ₄ , [(5-FP)Rh(CO) ₂]BF ₄ or 5-FP ligand with methyl iodide at 135 °C after 6 hours. The decomposition products show identical ¹ H NMR resonances for the three samples....	196
Figure 4.4.14 Comparison of the products for the reaction of [(6-FP)Ir(CO) ₂]BF ₄ , [(6-FP)Rh(CO) ₂]BF ₄ or 6-FP ligand with methyl iodide at 135 °C after 6 hours. The decomposition products show identical ¹ H NMR resonances for the three samples....	197
Figure 4.6.1 Calibration curve for the quantification of methyl acetate (MeOAc) versus cyclohexane (internal standard, CyH).....	200
Figure 4.6.2 Calibration curve for the quantification of acetic acid (HOAc) versus cyclohexane (internal standard, CyH).....	200
Figure 4.6.3 ¹ H NMR spectrum for [(5-FP)Rh(CO) ₂]BF ₄ in methylene chloride- <i>d</i> ₂	201
Figure 4.6.4 ¹³ C NMR spectrum for [(5-FP)Rh(CO) ₂]BF ₄ in methylene chloride- <i>d</i> ₂ . ..	202
Figure 4.6.5 FTIR spectrum of [(5-FP)Rh(CO) ₂]BF ₄	202
Figure 4.6.6 ¹ H NMR spectrum for [(6-FP)Rh(CO) ₂]BF ₄ in methylene chloride- <i>d</i> ₂	203
Figure 4.6.7 ¹³ C NMR spectrum for [(6-FP)Rh(CO) ₂]BF ₄ in methylene chloride- <i>d</i> ₂ . ..	203
Figure 4.6.8 FTIR spectrum of [(6-FP)Rh(CO) ₂]BF ₄	204
Figure 4.6.9 ¹ H NMR spectrum for [(5-FP)Ir(CO) ₂]BF ₄ in methylene chloride- <i>d</i> ₂	205
Figure 4.6.10 ¹³ C NMR spectrum for [(5-FP)Ir(CO) ₂]BF ₄ in methylene chloride- <i>d</i> ₂ . ..	205
Figure 4.6.11 FTIR spectrum of [(5-FP)Ir(CO) ₂]BF ₄	206
Figure 4.6.12 ¹ H NMR spectrum for [(6-FP)Ir(CO) ₂]BF ₄ in methylene chloride- <i>d</i> ₂	207
Figure 4.6.13 ¹³ C NMR spectrum for [(6-FP)Ir(CO) ₂]BF ₄ in methylene chloride- <i>d</i> ₂ . ..	207
Figure 4.6.14 FTIR spectrum of [(6-FP)Ir(CO) ₂]BF ₄	208
Figure 4.6.15 Images of high-pressure reaction vessel used (VCO reactor).	209

Figure 5.1.1 Examples of cobalt catalysts for olefin hydrogenation.	213
Figure 5.1.2 Generic examples of capping arene ligated metal complexes.	214
Figure 5.2.1 ORTEP of (5-FP)CoCl ₂ (1). Ellipsoids are drawn at 50% probability level. Hydrogen atoms are omitted for clarity.	214
Figure 5.2.2 ¹ H NMR spectrum of (5-FP)CoCl ₂ (1) in DCM- <i>d</i> ₂	216
Figure 5.2.3 ¹³ C NMR spectrum of (5-FP)CoCl ₂ (1) in DCM- <i>d</i> ₂	216
Figure 5.3.1 ¹ H NMR spectrum of styrene hydrogenation catalyzed by (5-FP)CoCl ₂ . ..	217
Figure 5.4.1 Turnovers of ethylbenzene vs. time (h) plot for catalytic styrene hydrogenation.	219
Figure 5.4.2 Images of a VCO reactor.	220
Figure 5.4.3 Turnovers of ethylbenzene vs. time (h) plot for (5-FP)CoCl ₂ catalyzed styrene hydrogenation.	220
Figure 5.4.4 Turnovers of ethylbenzene vs. time (h) plot for (5-FP)CoCl ₂ catalyzed styrene hydrogenation.	221
Figure 5.5.1 Possible substrates for (5-FP)CoCl ₂ (1) catalyzed olefin hydrogenation. ..	223
Figure 5.6.1 Calibration curve for the quantification of ethylbenzene (EtPh) against hexamethylbenzene (internal standard, HMB).	225
Figure 5.6.2 Calibration curve for the quantification of styrene against hexamethylbenzene (internal standard, HMB).	225
Figure 5.6.3 ¹ H NMR spectrum for (5-FP)CoCl ₂ (1) in DCM- <i>d</i> ₂	226
Figure 5.6.4 ¹³ C NMR spectrum for (5-FP)CoCl ₂ (1) in DCM- <i>d</i> ₂	227
Figure 5.6.5 ORTEP of (5-FP)CoCl ₂ (1). Ellipsoids are drawn at 50% probability level. Hydrogen atoms are omitted for clarity.	227

Figure 6.2.1 Reported cobalt catalysts for alkyne partial hydrogenation. ⁸⁻¹¹	235
Figure 6.2.2 Proposed target substrates for the studies on Co catalyzed alkyne partial hydrogenation	235
Figure 6.2.3 Proposed new capping arene ligands.....	236

LIST OF SCHEMES

Scheme 1.1.1 Steam-methane reforming and the water-gas shift reaction.	1
Scheme 2.1.1. Examples of capping arene ligands.	48
Scheme 2.1.2 General mechanisms for homogenous Rh-catalyzed olefin hydrogenation reactions.	50
Scheme 2.1.3 Trend of ligand impact on rate of catalytic olefin hydrogenation using capping arene ligated Rh complexes as catalyst precursors.	51
Scheme 2.2.1 Examples of (capping arene)Rh(η^2 -C ₂ H ₄)Cl complexes used in this study.	52
Scheme 2.2.2 Synthetic routes for capping arene ligands used in this study.	52
Scheme 2.2.3 General synthetic routes for capping arene ligated Rh complexes used in this study.	53
Scheme 2.3.1 Two proposed mechanisms for FP-Rh catalyzed olefin hydrogenation.	68
Scheme 2.3.2 Synthesis of (6-FP)Rh(Cl)(η^2 -styrene) (6FP-B).....	82
Scheme 2.3.3 Possible conformational isomers of (6-FP)Rh(Cl)(η^2 -styrene) (6FP-B) and proposed exchange pathways.....	87
Scheme 2.3.4 Isotopic study for (6-FP)Rh(Cl)(η^2 -C ₂ H ₄) (6FP-A) catalyzed styrene hydrogenation.	89
Scheme 2.3.5 Proposed mechanism that explains deuterium incorporation into ethylbenzene during styrene hydrogenation using (6-FP)Rh(Cl)(η^2 -C ₂ H ₄) (6FP-A) as catalyst precursor and D ₂	90
Scheme 2.3.6 DFT free energies at 318 K for conversion of styrene to ethylbenzene using (5-FP)Rh(η^2 -C ₂ H ₄)Cl (5FP-A) as catalyst precursor. Free energies are in kcal/mol.	104

Scheme 2.3.7 DFT free energies at 318 K for conversion of styrene to ethylbenzene via the (6-FP)Rh(η^2 -C ₂ H ₄)Cl (6FP-A) catalyst. Free energies are in kcal/mol.....	105
Scheme 3.1.1 The two-step carboxylic acid synthesis by hydroformylation followed by oxidation.	127
Scheme 3.1.2 Proposed reaction for carboxylic acid synthesis.....	128
Scheme 3.1.3 Direct carboxylation of acidic heteroaromatic C–H bond by NHC-Au(I)-OH catalysts.	129
Scheme 3.1.4 Carboxylation of benzene by a Rh catalyst assisted by aluminum based methylating reagents.	129
Scheme 3.1.5 Comparison of direct carboxylation of benzene and CO ₂ hydrogenation.	130
Scheme 3.1.6 Proposed mechanism for direct carboxylation of arenes under basic conditions.....	131
Scheme 3.1.7 Reported direct carboxylation of benzene catalyzed by Pd(OAc) ₂ under acidic conditions. ³²	131
Scheme 3.2.1 Synthetic routes for (^t BuPCP)Pd(TFA) and (^{Ph} PCP)Pd(TFA).	136
Scheme 3.2.2 Synthetic routes for (ⁱ PrPCP)Pd(OBz).	137
Scheme 3.3.1 Synthesis of (ⁱ PrPCP)PdPh.	143
Scheme 3.3.2 Synthesis of (ⁱ PrPCP)PdOBz (OBz = benzoate).	143
Scheme 4.1.1 Proposed mechanism for rhodium or iridium catalyzed methanol carbonylation.....	181
Scheme 4.4.1 Reported reaction between quinoline or 7-azaindole and methyl iodide. ^{26, 27}	197

Scheme 5.2.1 Synthesis of (5-FP)CoCl ₂ (1).....	214
--	-----

LIST OF TABLES

Table 1.4.1 Examples of catalytic carboxylation reaction with various substrates.....	22
Table 2.3.1 The set temperature, observed chemical shifts for the MeOH- <i>d</i> ₄ standard and the calibrated temperature used for the Eyring equation determination.	79
Table 2.3.2 Rh–C _{cap} distances and C _{cap} –C _{cap} bond distance for (5-FP)Rh(η^2 -C ₂ H ₄)Cl (5FP-A) and (6-FP)Rh(η^2 -C ₂ H ₄)Cl (6FP-A).....	110
Table 2.5.1 Crystal Structure Data for (6-FP)Rh(Cl)(η^2 -styrene) (6FP-B) and (5- ^{NP} FP)Rh(Cl)(η^2 -styrene) (5^{NP}FP-B).	115
Table 3.1.1 Proposed mechanism and DFT calculations for Pd(OAc) ₂ and (^{Me} PCP)PdPh.	133
Table 3.1.2 DFT calculations for the effect of base on overall free energy.	133
Table 3.2.1 Yields of benzoic acid and biphenyl for screenings on Pd(OAc) ₂ catalyzed benzene direct carboxylation under basic conditions	135
Table 3.2.2. Yield of benzoic acid and biphenyl for screenings of (^R PCP)Pd(TFA) catalyzed benzene direct carboxylation under basic conditions.	137
Table 3.2.3 Yields of benzoic acid and biphenyl for screenings on bidentate assisted Pd(II) catalyzed benzene direct carboxylation under basic condition.	140
Table 3.3.1 NMR scale studies on CO ₂ insertion into (^{iPr} PCP)PdPh.	148
Table 3.3.2 Studies on CO ₂ insertion into (^{iPr} PCP)PdPh with high pressure of CO ₂	149
Table 3.4.1 Investigation of (^{iPr} PCP)PdOBz mediated benzene C–H activation.	151
Table 4.1.1 Second-order rate constants (<i>k</i> ₁ , 25 °C) for the oxidative addition of MeI to PN–Rh(I) complexes.....	182

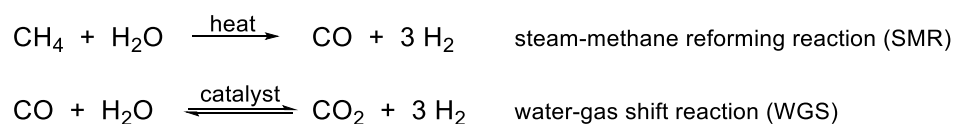
Table 4.2.1 ^{13}C NMR resonances of coordinated CO in $[(\text{FP})\text{M}^{\text{I}}(\text{CO})_2]\text{BF}_4$ (FP = 5-FP or 6-FP, M = Rh or Ir).....	185
Table 4.3.1 Condition optimization of MeI promoted methanol carbonylation catalyzed by $[(5\text{-FP})\text{Ir}(\text{CO})_2]\text{BF}_4$	186
Table 5.3.1 Turnovers of ethylbenzene from (5-FP) CoCl_2 catalyzed styrene hydrogenation with additives. ^A	218
Table 5.4.1 Comparison of the turnovers for (5-FP) CoCl_2 catalyzed olefin hydrogenation with reported cobalt catalyzed olefin hydrogenation reactions. ¹⁵⁻¹⁷	222

1 Introduction

1.1 Broad overview and motivation of small molecule activation

Steam-methane reforming (SMR) reaction and the water-gas shift (WGS) reaction (**Scheme 1.1.1**), processes that produce dihydrogen (H_2), carbon monoxide (CO) and carbon dioxide (CO_2) from methane and water, are responsible for 95% of H_2 (*c.a.* 9.5 million metric tons annually) production in the United States.¹⁻⁵ The products of SMR and the WGS reactions (H_2 and CO) have broad applications in industry, including for the production of ammonia, carboxylic acids, aldehydes, and other fine chemicals.^{4, 6-14}

Scheme 1.1.1 Steam-methane reforming and the water-gas shift reaction.



In the past few decades, chemists have spent enormous efforts to enhance the efficiency of utilizing the products of SMR and the WGS reaction. One of the approaches to reach a faster conversion rate is to use transition metal catalysts to activate H_2 , CO and CO_2 , thus increasing the reaction rate. In the next few chapters, some examples for the utilization of H_2 , CO, and CO_2 by transition metal catalysts are introduced.

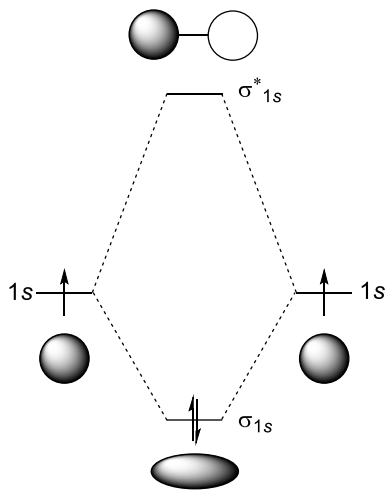
1.2 Utilization of dihydrogen (H_2)

1.2.1 Properties of H_2

Dihydrogen can be considered as the simplest molecule, due to the fact that it consists of only two hydrogen atoms connected by a single covalent bond. The molecular orbital diagram of dihydrogen includes a bonding orbital (σ_{1s}) with 2 electron, and an empty anti-

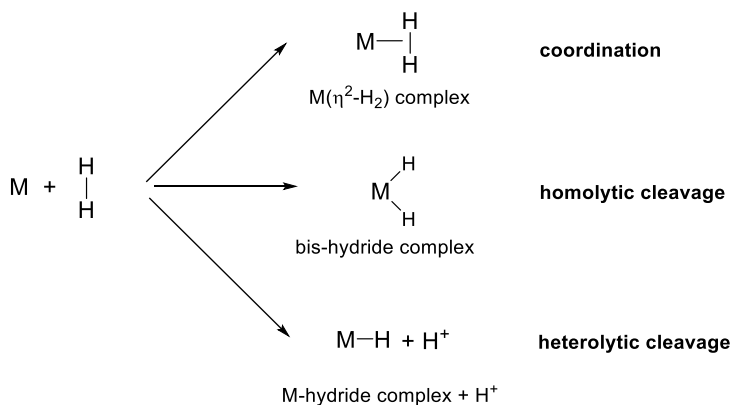
bonding orbital (σ_{1s}^*) (**Figure 1.2.1**).¹⁵ The bond dissociation energy (BDE) for the H–H single bond is relatively high at 104 kcal/mol,^{16, 17} and the p*K*_a for H₂ is estimated to be 35 in THF.^{18, 19} Therefore, homolytic cleavage and heterolytic cleavage of H₂ are both difficult without catalysts.

Figure 1.2.1 Molecular orbital diagram for H₂.



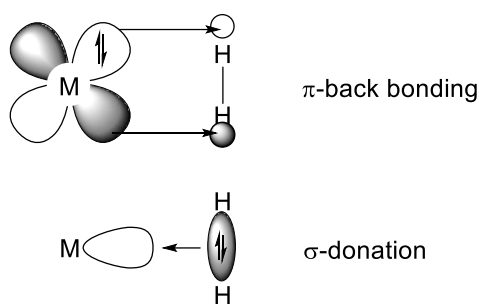
The activation of dihydrogen can be achieved by transition metal complexes. As Figure 1.2.2 summarizes, possible pathways for transition metal assisted H₂ activation include: (1) forming a stable M(η^2 -H₂) complex; (2) undergoing homolytic cleavage to form a bis-hydride complex; and (3) undergoing heterolytic cleavage to form a metal hydride complex by releasing a proton.²⁰ For the heterolytic cleavage, an external base is generally required, although proton transfer to a coordinated base also has precedent.

Figure 1.2.2 Possible pathways for H₂ activation.



As **Figure 1.2.3** shows upon coordination to a transition metal, the electrons in dihydrogen's σ_{1s} orbital can donate to an empty orbital (σ -symmetric), and the electrons in a π -symmetric metal d orbital can back-donate to the H₂ σ^*_{1s} orbital (π -symmetric). It is also revealed that the H–H distance of an η^2 -H₂ (usually 1.0 Å to 1.5 Å) is elongated compared to free H₂ (0.74 Å).²¹⁻²⁵ This increased H–H distance could suggest that the bond strength of H₂ is weakened.²⁶ For example, Morris and coworkers have reported that the BDE for the H–H in complexes $[\text{Os}(\eta^2\text{-H}_2)(\text{L}^z)(\text{dppe})_2]^{(z+2)+}$ ($\text{L}^z = \text{H}^-, \text{CH}_3\text{CN}, \text{Cl}^-, \text{Br}^-$) are 70-80 kcal/mol, which is significantly lower than free H₂ (104 kcal/mol).^{21, 27} The lowered BDE is clear evidence of dihydrogen activation by transition metal complexes. Although there is no clear defined classification for elongated $\text{M}(\eta^2\text{-H}_2)$ complexes and bis-hydride complexes based on the H–H distance, it can be implied that the longer H–H distance represents more complete homolytic cleavage.²⁰ The heterolytic cleavage of H₂ can also be achieved by polarizing H₂ with the assistance of an acid or a base.^{21, 28-30} Recently, “frustrated Lewis pairs” (FLP), a Lewis acid with a base that do not bond, such as $\text{P}(\text{Mes})_3/\text{B}(\text{C}_6\text{F}_5)_3$ (Mes = mesityl), have been reported for facilitating heterolytic cleavage of H₂ under mild conditions.^{28, 31, 32}

Figure 1.2.3 The σ -donation and π -back bonding of an η^2 -H₂ with transition metals (M)



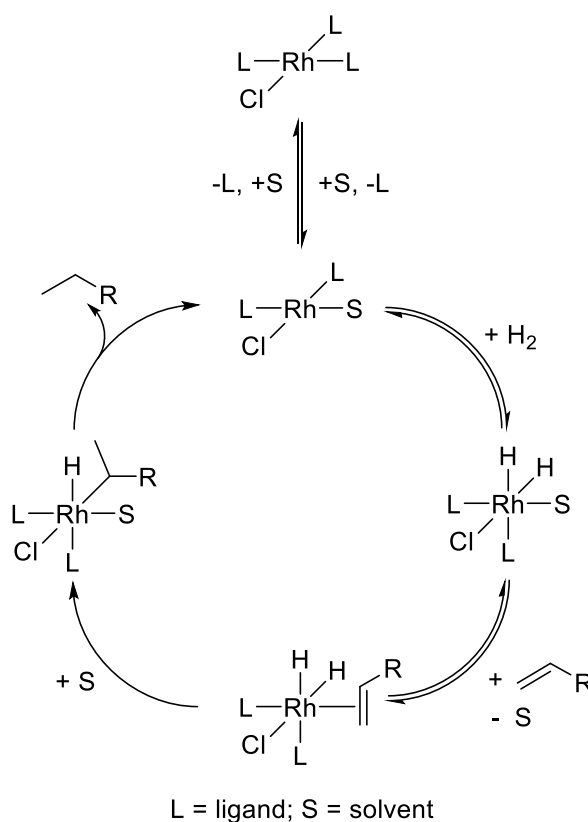
1.2.2 Examples of catalytic H₂ utilization

Many $M(\eta^2\text{-H}_2)$ complexes and metal-hydride complexes have been synthesized in the past century.³³⁻⁵¹ Researchers have discovered that $M(\eta^2\text{-H}_2)$ complexes and metal-hydride complexes can serve as potent catalysts for the hydrogenation of alkenes, alkynes, aldehydes, ketones and imines.⁵² The following paragraphs in this section will introduce a few examples of H₂ utilization with transition metal complexes.

In 1960s, Wilkinson and coworkers developed a catalytic olefin hydrogenation using $[\text{Rh}(\text{PPh}_3)_3\text{Cl}]$ as the catalyst, which is also called “Wilkinson’s catalyst.”⁵³⁻⁵⁷ Wilkinson’s catalyst is capable of catalyzing the hydrogenation of a wide range of mono- and di-substituted olefins, while the reaction rates can vary based on the conformational and steric properties of the olefin substrate.⁵² As a result of the varied rates, Wilkinson’s catalyst is used for selective hydrogenation of substrates with multiple C=C bonds.^{58, 59} The mechanism for the olefin hydrogenation catalyzed by Wilkinson’s catalyst has been studied and illustrated by Halpern and coworkers (**Figure 1.2.4**).⁶⁰⁻⁶⁴ Wilkinson’s catalyst is first converted to a new Rh(I) complex $[\text{Rh}(\text{L})_2(\text{S})(\text{Cl})]$ (L = phosphine ligand, S = solvent), followed by the oxidative addition of H₂ to form the Rh(III)-bishydride complex

$[\text{Rh}(\text{L})_2(\text{H})_2(\text{S})(\text{Cl})]$. Then, the olefin substrate is exchanged with coordinated solvent to form $[\text{Rh}(\text{L})_2(\text{H})_2(\text{olefin})(\text{Cl})]$. After that, the migratory insertion of hydride into the olefin leads to the formation of $[\text{Rh}(\text{L})_2(\text{H})(\text{alkyl})(\text{Cl})]$. Finally, the hydrogenated product is released from the catalyst by reductive elimination, and the active catalyst $[\text{Rh}(\text{L})_2(\text{S})(\text{Cl})]$ is regenerated. This mechanism is also called the “hydrogen first” mechanism because H_2 joins the catalytic cycle prior to the olefin.

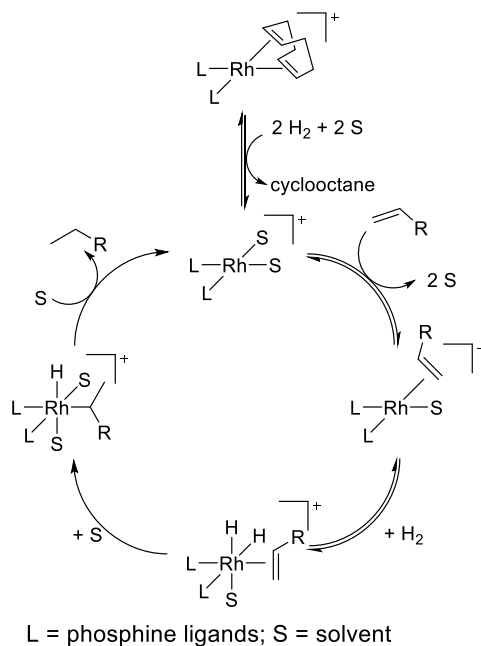
Figure 1.2.4 Proposed catalytic cycle for olefin hydrogenation catalyzed by Wilkinson’s catalyst.



In the 1970s, Osborn and Schrock reported cationic Rh catalyst precursors with the general formula $[\text{Rh}(\text{L})_2(\text{diene})]^+$ (L = phosphine ligand) for catalytic olefin hydrogenation, known as the Schrock-Osborn catalyst.⁶⁵⁻⁶⁷ Crabtree and coworkers also developed a cationic Ir catalyst, $[\text{Ir}(\text{COD})(\text{py})(\text{PR}_3)]^+$ (py = pyridine; R = cyclohexyl or isopropyl), for

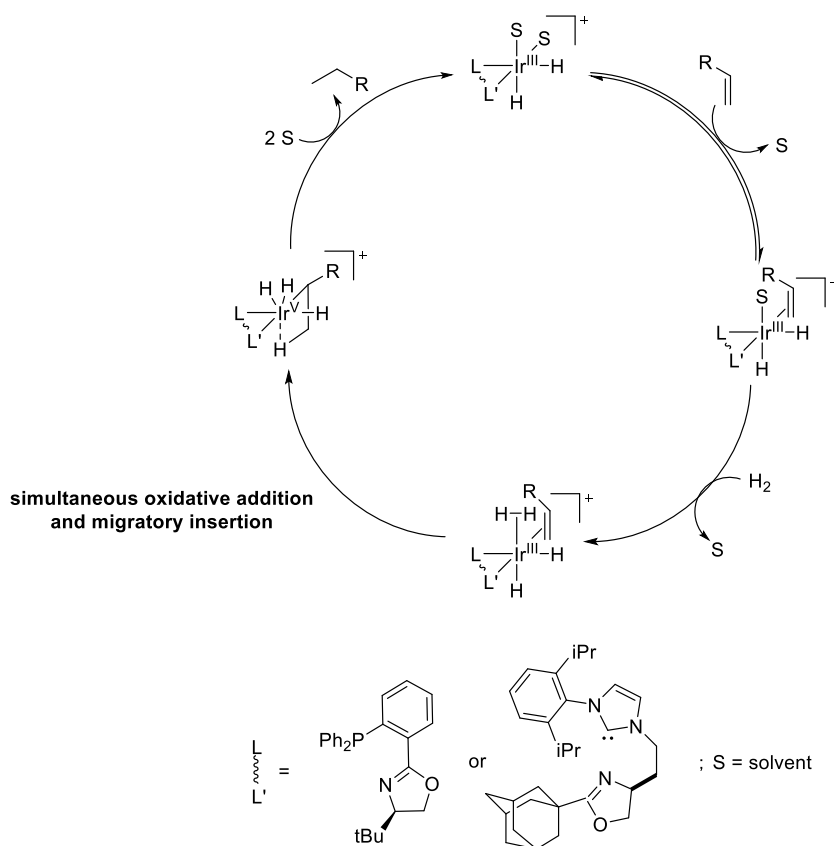
olefin hydrogenation (Crabtree's catalyst).⁶⁸⁻⁷⁰ Both the Schrock-Osborn catalyst and Crabtree's catalyst exhibit significantly faster rates compared to Wilkinson's catalyst for olefin hydrogenation. The mechanism for olefin hydrogenation catalyzed by the Schrock-Osborn catalyst (**Figure 1.2.5**) is found to be different from the hydrogen first mechanism.⁷¹⁻⁷⁵ In this case, the proposed active catalyst $[\text{Rh}(\text{L})_2(\text{S})_2]^+$ (L = phosphine ligand, S = solvent) is formed by ligand exchange. The olefin substrate can replace coordinated solvent to form $[\text{Rh}(\text{L})_2(\text{olefin})(\text{S})]^+$. Oxidative addition of H_2 then takes place, and the complex is transformed to $[\text{Rh}(\text{L})_2(\text{H})_2(\text{olefin})(\text{S})]^+$. After that, the coordinated olefin substrate insert into the Rh-H bond via migratory insertion and converted to $[\text{Rh}(\text{L})_2(\text{H})(\text{alkyl})(\text{S})_2]^+$. Finally, reductive elimination of the hydrogenated product and coordination of the solvent regenerates the active catalyst $[\text{Rh}(\text{L})_2(\text{S})_2]^+$. The major difference between the mechanism for Schrock-Osborn catalyst and Wilkinson's catalyst is that coordination of the olefin substrate is proposed to occur before oxidative addition of H_2 for the olefin hydrogenation catalyzed by Wilkinson's catalyst. This mechanism is referred to as the "alkene first" mechanism.

Figure 1.2.5 Proposed catalytic cycle for olefin hydrogenation catalyzed by the Schrock-Osborn catalyst.



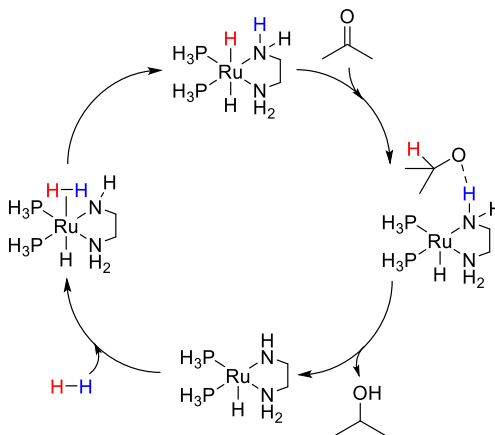
It remains unclear if olefin hydrogenation catalyzed by Crabtree's catalyst undergoes the hydrogen first mechanism or the alkene first mechanism, as the reaction rate is fast and mass transport of hydrogen becomes rate-limiting, which makes kinetic studies challenging.^{52, 76} There are DFT computational data supporting a mechanism in which the complex follows an Ir(III)/Ir(V) catalytic cycle (**Figure 1.2.6**).^{77, 78}

Figure 1.2.6 Proposed Ir(III)/Ir(V) catalytic cycle for Ir catalyzed olefin hydrogenation.



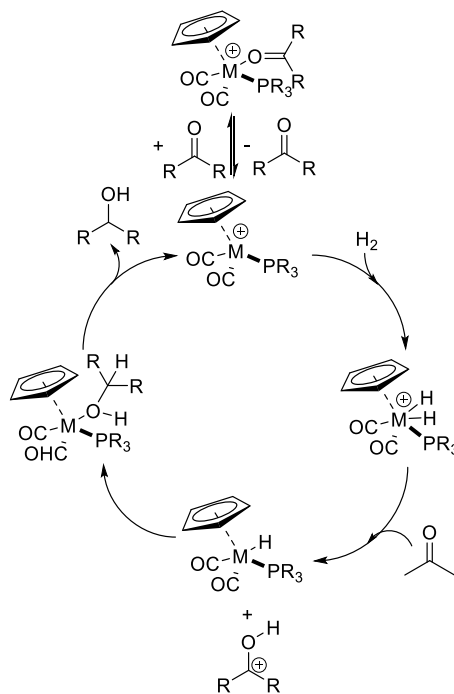
Aldehyde and ketone hydrogenation can also be catalyzed by Rh and Ru complexes.^{47,}
⁷⁹⁻⁸⁶ **Figure 1.2.7** shows the calculated mechanism for acetone hydrogenation catalyzed by $\text{Ru}(\text{H})_2(\text{NH}_2\text{CH}_2\text{CH}_2\text{NH}_2)(\text{PH}_3)_2$.⁸⁷ The dihydrido(diamine) Ru(II) complex can transfer one of the hydride ligands to the carbonyl carbon to form the intermediate $\text{Rh}(\text{H})[\text{OCH}(\text{CH}_3)_2](\text{NH}_2\text{CH}_2\text{CH}_2\text{NH}_2)(\text{PH}_3)_2$. Then, the isopropoxy group abstracts a proton from the diamine nitrogen to release isopropanol, and the Ru complex is converted into $\text{Ru}(\text{H})(\text{NHCH}_2\text{CH}_2\text{NH}_2)(\text{PH}_3)_2$. After that, dihydrogen is coordinated. Unlike the homolytic cleavage in the olefin first mechanism and the hydrogen first mechanism described in **Figure 1.2.4** and **Figure 1.2.5**, the dihydrogen can undergo a heterolytic cleavage to form the dihydrido(diamine) Ru(II) complex.

Figure 1.2.7 Calculated mechanism for $\text{Rh}(\text{H})_2(\text{NH}_2\text{CH}_2\text{CH}_2\text{NH}_2)(\text{PH}_3)_2$ catalyzed acetone hydrogenation.



Catalytic ketone hydrogenation can also occur by an ionic pathway. For example, in **Figure 1.2.8**,⁸⁸ the molybdenum or tungsten complex $[\text{M}(\text{Cp})(\text{CO})_2(\text{PR}_3)(\text{OCR}_2)]^+$ ($\text{M} = \text{Mo}$ or W) can first dissociate the ketone to form $[\text{M}(\text{Cp})(\text{CO})_2(\text{PR}_3)]^+$, followed by oxidative addition of dihydrogen to form $[\text{M}(\text{H})_2(\text{Cp})(\text{CO})_2(\text{PR}_3)]^+$. Then, proton transfer leads to the formation of $\text{M}(\text{H})(\text{Cp})(\text{CO})_2(\text{PR}_3)$ and $(\text{HOCHR}_2)^+$ carbocation. Next, a metal-alcohol complex $[\text{M}(\text{Cp})(\text{CO})_2(\text{PR}_3)(\text{HOCHR}_2)]^+$ is generated via hydride transfer. Finally, the hydrogenation product is released, and the active catalyst $[\text{M}(\text{Cp})(\text{CO})_2(\text{PR}_3)]^+$ is regenerated.

Figure 1.2.8 Proposed mechanism for ketone hydrogenation catalyzed by $[\text{M}(\text{Cp})(\text{CO})_2(\text{PR}_3)(\text{OCR}_2)]^+$ ($\text{M} = \text{Mo}$ or W).



$\text{M} = \text{Mo}$ or W ; $\text{R} = \text{Cy}$, Ph or Me

1.3 Utilization of carbon monoxide (CO)

1.3.1 Properties of CO

The molecular orbital diagram of CO is more complicated than that of H_2 (**Figure 1.3.1**). In the molecular orbital diagram of CO, all three pairs of electrons are located in the bonding orbitals, so the bond order for CO is 3. The 1π orbitals are lower in energy than the 3σ orbital. Hence, the HOMO of CO is a σ bonding orbital, and the LUMO of CO is a π^* antibonding orbital.⁸⁹ Since the CO 3σ orbital is the combination of two carbon atomic orbitals ($2p_z$ and $2s$) but only one oxygen atomic orbital ($2p_z$), the lobe of the 3σ orbital on the carbon side is slightly larger than the lobe on oxygen side.⁸⁹ The $1\pi^*$ orbitals are closer in energy to the carbon $2p$ orbitals than the oxygen $2p$ orbitals. Thus, the better energy matching leads to a greater contribution from the carbon side to the $1\pi^*$ orbitals.

Carbon monoxide can coordinate to transition metals tightly, because CO can serve as both a σ donor and a π -acceptor (**Figure 1.3.2**). The metal-to-ligand π -back bonding can significantly lower the C \equiv O bond strength by donating electron density into the LUMO of CO, which is a C–O π^* orbital. One example of direct evidence is that the frequencies for the C–O stretch in many metal carbonyl complexes are often lower than that of free CO.⁹⁰

91

Figure 1.3.1 Molecular orbital diagram for CO.

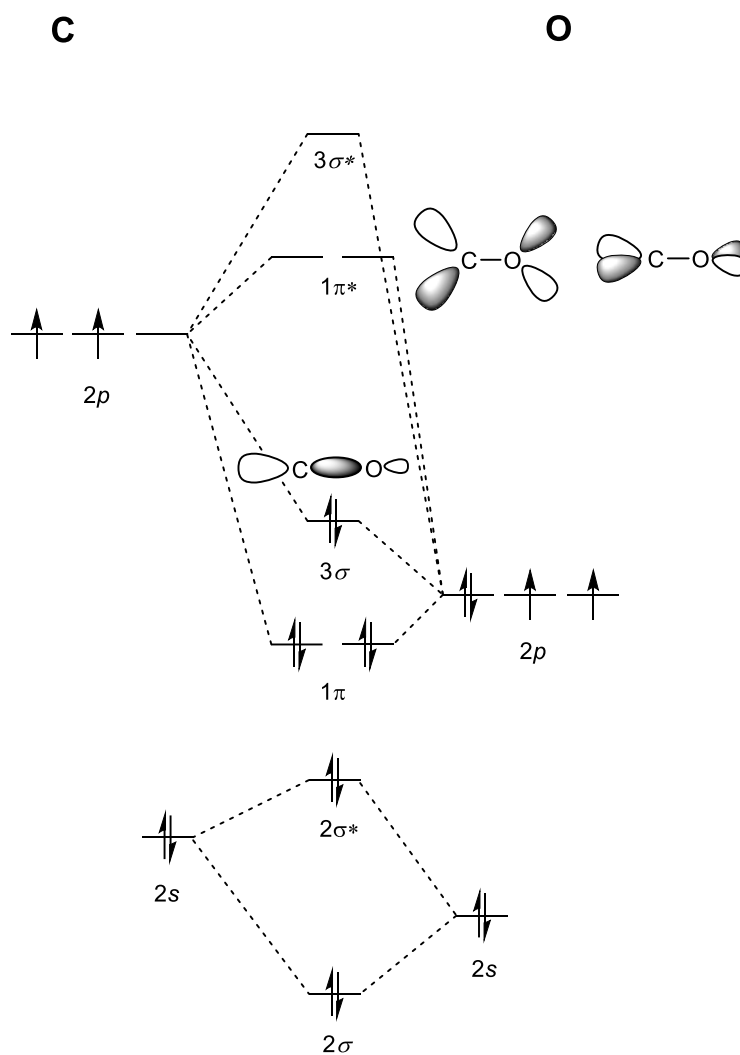
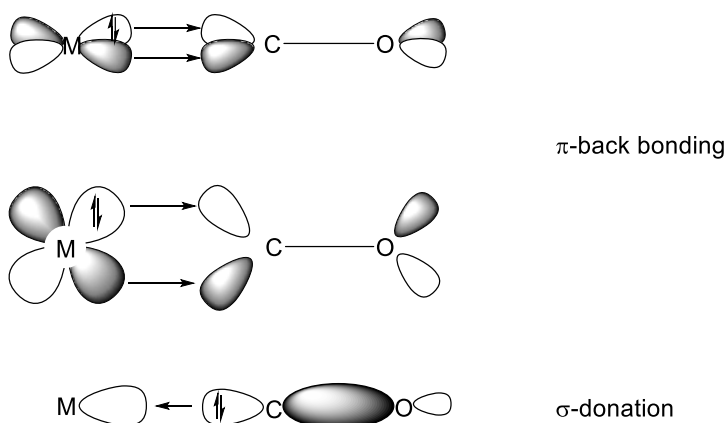


Figure 1.3.2 σ -donation and π -back bonding of a κ^1 -CO with transition metals (M).



1.3.2 Examples of catalytic CO utilization

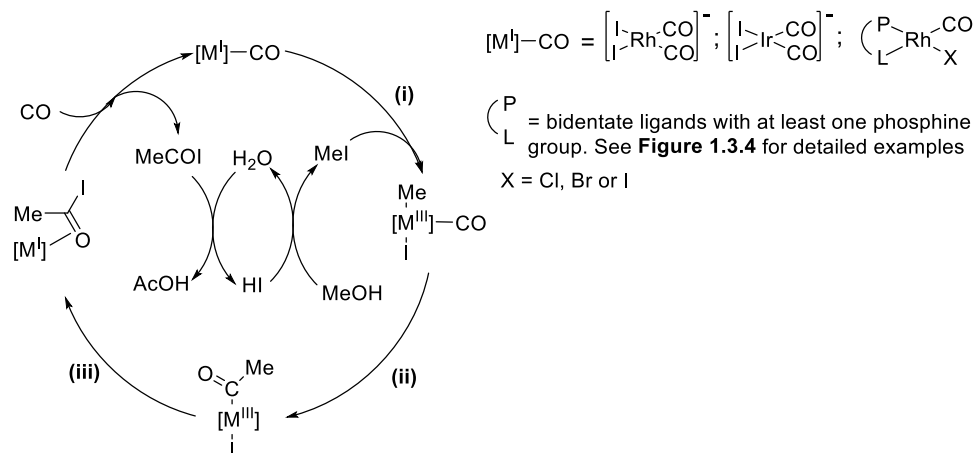
Carbon monoxide is a synthon for the production of aldehydes and carboxylic acids. There are two well-known industrial processes that incorporate CO: methanol carbonylation and hydroformylation. These two processes will be discussed in this section.

Methanol carbonylation is the reaction between methanol and CO to produce acetic acid or methyl acetate. During the last 50 years, industrial methanol carbonylation processes have been developed rapidly. Perhaps the first example of catalytic methanol carbonylation was reported in the 1950s, in which Reppe and coworkers at BASF used cobalt(II) iodide to catalyze the production of acetic acid (AcOH) or its derivatives from methanol (MeOH) and carbon monoxide (CO) under relatively harsh conditions (*c.a.* 250 °C, 600 bar).^{92, 93} In the 1960s, Paulik and Roth at Monsanto developed a rhodium catalyzed methanol carbonylation method (Monsanto process) using methyl iodide and iodide salts as promoters under milder conditions than the previously reported Co catalyzed methanol carbonylation (*c.a.* 175 °C, 30 bar).⁹⁴ The Monsanto acetic acid process was able

to improve the selectivity of the reaction from 90% to > 99% based on methanol, and from 70% to 85% based on CO, compared to the cobalt catalyzed methanol carbonylation described above. In 1996, BP Chemicals announced the Cativa™ process, an iodide promoted iridium catalyzed methanol carbonylation system, which exhibits a greater stability than the Rh-based processes.⁹⁵⁻⁹⁷

The mechanism for the iodide promoted Rh and Ir-catalyzed methanol carbonylation has been studied extensively in the past few decades.⁹⁸⁻¹⁰⁰ In methanol carbonylation chemistry, the oxidative addition of methyl iodide (MeI) to Rh(I) or Ir(I) plays an important role in the catalytic reaction (**Figure 1.3.3**). Through the oxidative addition of MeI to the Rh(I) or Ir(I) catalysts, Rh(III) or Ir(III) intermediates are formed (Step I in **Figure 1.3.3**). Then, the migratory insertion of CO into the M–Me (M = Rh or Ir) bond leads to the formation of a M(III)-acetyl complex (Step ii in **Figure 1.3.3**) and then reductive elimination follows which gives a M(I)- η^2 -acetyl iodide complex (Step iii in **Figure 1.3.3**). Finally, acetyl iodide on the complex exchanges with CO and free acetyl iodide is hydrolyzed to form acetic acid and HI. MeI is regenerated by the reaction of methanol with HI.

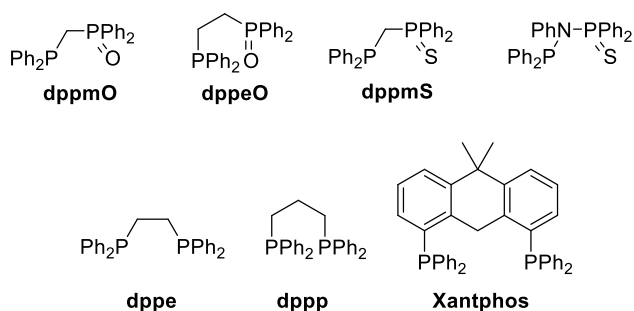
Figure 1.3.3 Proposed mechanism for rhodium and iridium catalyzed methanol carbonylation.



Additionally, various ligands have been reported to facilitate Rh catalyzed methanol carbonylation. **Figure 1.3.4** shows some examples of the ligands that have been studied for Rh catalyzed methanol carbonylation.¹⁰¹⁻¹⁰³ Comparison of catalytic performance of Rh catalyzed methanol carbonylation with dppmO, dppeO, dppmS and Ph₂PN(Ph)PPh₂(S) has been reported by Baker and coworkers.¹⁰¹ The addition of dppmO, dppeO or Ph₂PN(Ph)PPh₂(S) to [Rh(μ-CO)₂Cl]₂ only exhibits minimal improvements (less than 2 fold improvement on turnover frequency compared to using [Rh(μ-CO)₂Cl]₂). However, the addition of dppmS significantly enhances methanol carbonylation by 8.5 times in rate compared to the reaction with the same conditions catalyzed by [Rh(CO)₂Cl]₂.^{101, 102} Further, mechanistic studies suggests that the oxidative addition of MeI to [Rh(CO)(dppmS)I] is approximately 40 times faster than the oxidative addition of MeI to [Rh(μ-CO)₂I]₂.^{104, 105} Although the rate for [(dppe)Rh(I)(CO)]-catalyzed methanol carbonylation is slower than [Rh(μ-CO)₂Cl]₂-catalyzed methanol carbonylation, the diphosphine ligated Rh catalysts exhibits better longevity under harsh conditions (i.e. 150-200 °C, 10-60 bar CO).¹⁰² It was also reported that diphosphine ligands with a larger bite

angle to Rh metal center can enhance the rate of methanol carbonylation.¹⁰⁶ For example, the turnover of methanol carbonylation using [(Xantphos)Rh(Cl)(CO)] is approximately 1.5 times greater than methanol carbonylation using [Rh(μ -CO)₂Cl]₂.¹⁰³

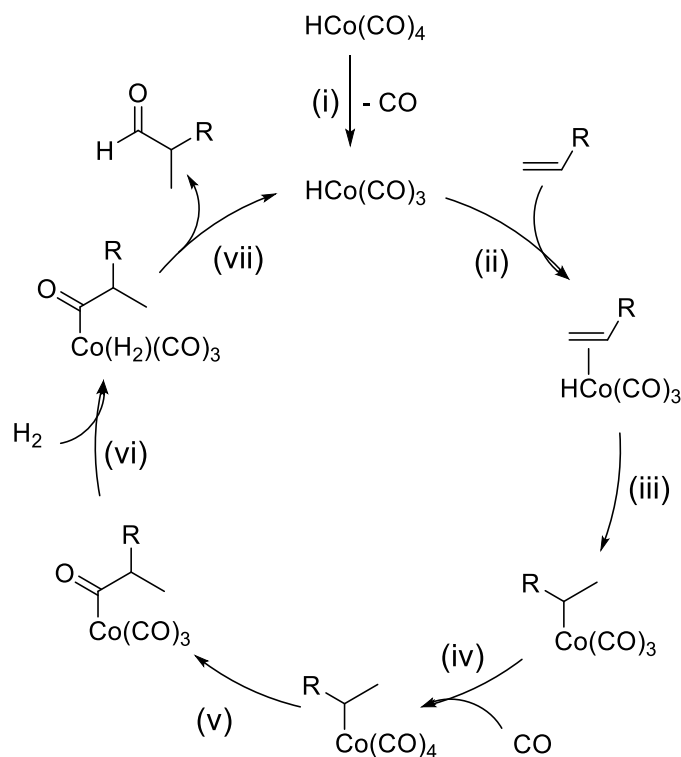
Figure 1.3.4 Examples of ligands studied for Rh catalyzed methanol carbonylation.



Hydroformylation is the reaction of an alkene, CO and H₂ to produce aldehydes.¹⁰⁷ A series of metal-carbonyl complexes with the general formula [HM(CO)_xL_y] (M = Rh, Co, Ir, Ru, Os, Pt, Pd, Fe or Ni; L = organic ligands or CO) have been reported for catalyzing the hydroformylation reaction, and Rh and Co-based complexes generally show the best performances.¹⁰⁸⁻¹¹¹ The mechanism of hydroformylation catalyzed by Co or Rh has been studied by many groups.¹¹²⁻¹²¹ The proposed mechanism of HCo(CO)₄ catalyzed hydroformylation is illustrated in **Figure 1.3.5**. The HCo(CO)₄ catalyzed hydroformylation starts with the dissociation of CO (Step i in **Figure 1.3.5**). The olefin then coordinates to the vacant site to form the η^2 -olefin complex Co(olefin)(H)(CO)₃ (Step ii in **Figure 1.3.5**). The η^2 -olefin complex becomes the Co-alkyl complex, Co(alkyl)(CO)₃, via migratory insertion of hydride into the olefin (Step iii in **Figure 1.3.5**). The coordination of CO (Step iv in **Figure 1.3.5**) followed by migration insertion of CO into the alkyl group (Step v in **Figure 1.3.5**) forms the intermediate Co(COCHRCH₃)(CO)₃. Then, the coordination of H₂

takes place (Step vi in **Figure 1.3.5**), and the reductive elimination of the aldehyde product regenerates the $\text{HCo}(\text{CO})_3$ (Step vii in **Figure 1.3.5**).

Figure 1.3.5 Proposed mechanism for $\text{HCo}(\text{CO})_4$ catalyzed hydroformylation.



The mechanism for Rh catalyzed hydroformylation follows a similar pathway to the Co-catalyzed hydroformylation (**Figure 1.3.6**).^{75, 115} In contrast, Rh catalyzed hydroformylation exhibits higher reactivity and better regioselectivity for the linear product compared to the Co catalyzed hydroformylation.^{122, 123} Although the unmodified (i.e. with $\text{Rh}_4(\text{CO})_{12}$) catalyzed hydroformylation yields almost 1:1 ratio for the linear and branch products,¹²⁴ the presence of a ligand can tune the regioselectivity to prefer the linear products. For example, Hjortkjaer and coworkers reported that $\text{HRh}(\text{CO})(\text{PPh}_3)_3$ catalyzed hydroformylation of propene can reach a linear:branch ratio at 9.8:1.¹²⁵ The regioselectivity of Rh catalyzed hydroformylation of 1-alkenes with bidentate phosphine

ligands also have been studied. The researchers found that the bite angle of the biphosphine ligand was an important factor for the regioselectivity.¹²⁶ **Figure 1.3.7** shows some examples of the bite angles of the ligands on Rh complexes, and the linear: branch ratios for the catalytic hydroformylation of 1-hexene.¹²⁶⁻¹³⁰ It has been proposed that the wider bite angle for the diphosphine ligands can increase the steric effect for the coordinated olefin in the square pyramidal transition states for the olefin insertion step, so the less hindered conformation will be favored (**Figure 1.3.8**).^{126, 130} It is worth noting that the electronic properties of the ligand can also affect the regioselectivity. It was suggested that electron-withdrawing ligands can both lead to better selectivity towards the linear hydroformylation products and enhance the reaction rate.^{123, 131-133}

Figure 1.3.6 Proposed mechanism for Rh catalyzed hydroformylation.

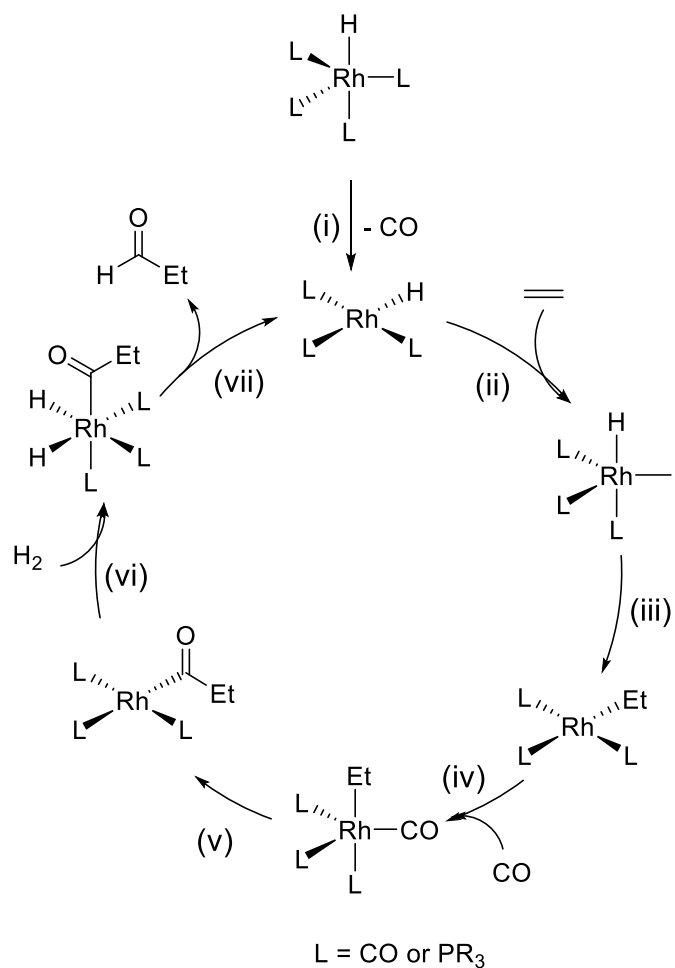
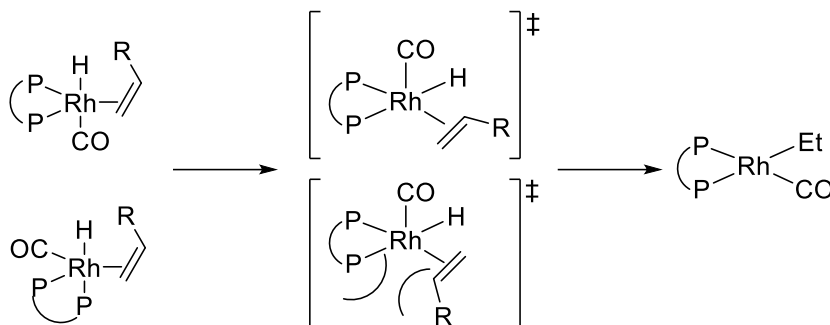


Figure 1.3.7 The bite angles for biphosphine ligands on Rh and the linear:branch (l:b) ratios for catalytic hydroformylation of 1-hexene.

bite angle (deg)	85	97	113
l:b ratio	2.1	5.4	66

Figure 1.3.8 Steric hindrance of biphosphine ligands in square pyramidal transition states of the olefin insertion step.



1.4 Utilization of carbon dioxide (CO₂)

1.4.1 Properties of CO₂

As **Figure 1.4.1** shows, the HOMO of CO₂ is a non-bonding orbital, and the LUMO is the π -anti-bonding orbital. Since the HOMO orbital is localized on the oxygen atoms, the oxygens can be considered Lewis basic. For similar reasons, the carbon can be described Lewis acidic since the LUMO is localized on the center carbon.¹³⁴

It has been summarized that there are four general binding modes for CO₂ coordinated to transition metals (**Figure 1.4.2**):^{134, 135} (1) $\eta^1(\text{C})$: a metal d_z orbital donates electrons to the π^* orbital of CO₂, which is usually favored by electron-rich metals;¹³⁶⁻¹³⁹ (2) $\eta^2(\text{C,O})$: bent CO₂ coordinates with the metal via a side-on fashion. The HOMO of CO₂ donates electrons to the metal d_z orbital, and the metal orbital can also form a back-bonding with the LUMO of CO₂;¹⁴⁰⁻¹⁴² (3) $\eta^1(\text{O})$: linear (or weakly bent) CO₂ coordinates to the metal in an end-on fashion. The $\eta^1(\text{O})$ coordination of CO₂ to U(IV) and V(III) has been observed.^{143, 144} (4) $\eta^2(\text{O,O})$: bent CO₂ coordinates to the metal with both oxygen atoms. It is proposed that the $\eta^2(\text{O,O})$ -CO₂ can be described as metal carboxylate M^+CO_2^- .¹³⁴ This coordination mode can be often observed with alkali and alkaline-earth metals.^{145, 146}

Figure 1.4.1 MO diagram for CO₂.

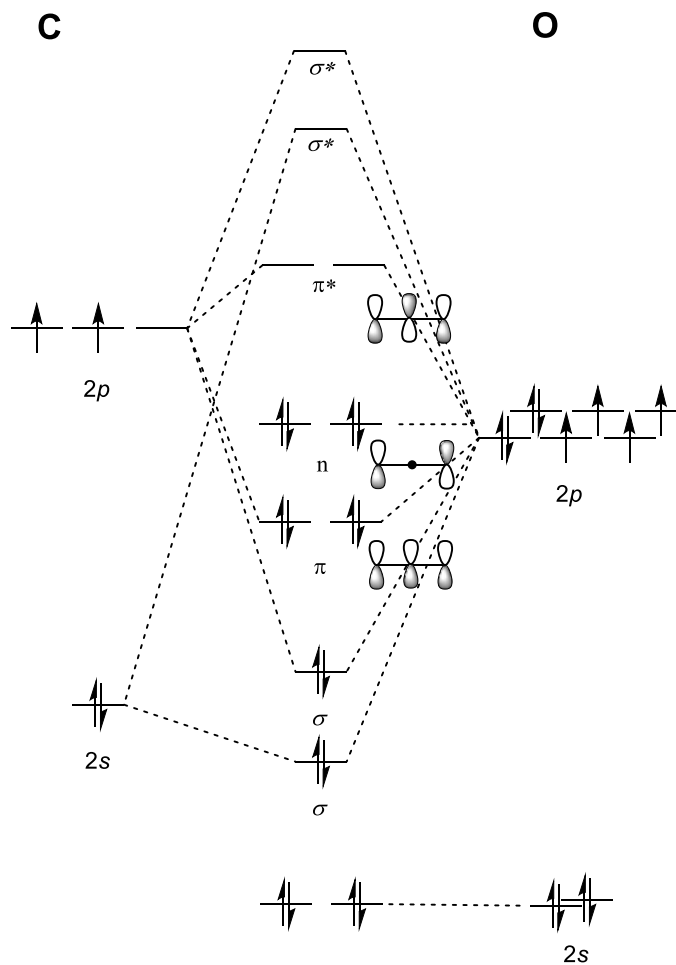
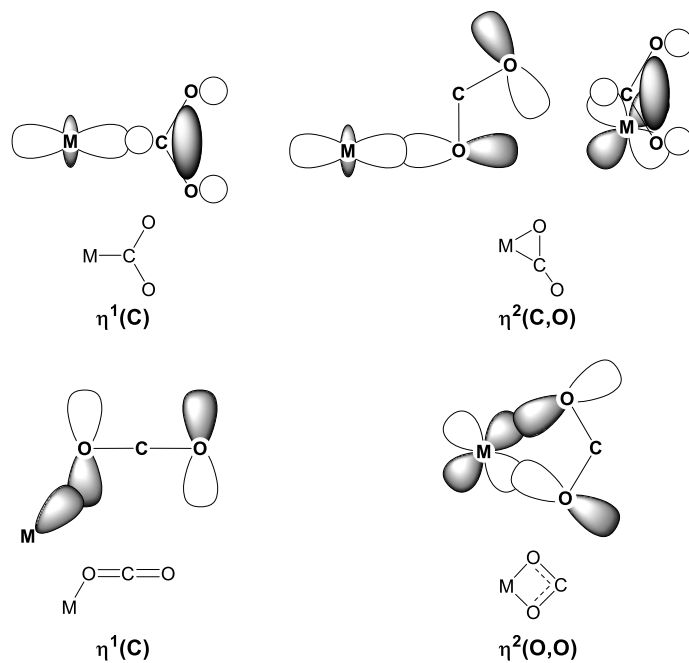


Figure 1.4.2 Possible binding modes for CO₂ coordinated to transition metals.



1.4.2 Examples of catalytic CO₂ utilization

As a result of increasing CO₂ concentration in the atmosphere (420 ppm in 2022),¹⁴⁷ the demand for CO₂ fixation techniques has increased in the past few decades.¹⁴⁸ It has been proposed that CO₂ can be harnessed and used as a C₁ synthon.

One example of utilizing CO₂ in synthetic chemistry would be producing carboxylic acids. **Table 1.4.1** provides a brief summary of the examples of the catalytic carboxylation reaction with various substrates.¹⁴⁸ As **Table 1.4.1** shows, catalytic carboxylation reactions using organotin reagents,¹⁴⁹⁻¹⁵³ organoboron reagents,¹⁵⁴⁻¹⁶¹ organozinc reagents^{162, 163} and organic (pseudo)halides¹⁶⁴⁻¹⁷⁴ are reported. Although the substrates for the carboxylation reactions involving C–C bond formation shows a large diversity, the mechanism for the carboxylation reactions usually involves the formation of a metal-alkyl/aryl/vinyl intermediate, followed by the direct carboxylation to form the corresponding metal carboxylate.¹⁴⁸ The direct carboxylation of hydrocarbon is more remarkable due to the

challenging C–H activation step. A few examples of direct carboxylation of hydrocarbon will be introduced in **Chapter 3**.

Table 1.4.1 Examples of catalytic carboxylation reaction with various substrates

$$\text{R-X} \xrightarrow{\text{CO}_2, \text{cat.}} \text{R-COOH}$$

R	X	Catalyst
Allyl	SnBu ₃ or SnPh ₃	Pd cat. ¹⁴⁹⁻¹⁵³
aryl, vinyl	Bnep	Rh(II), ¹⁵⁴ Cu(I), ¹⁵⁵ Ag(I) ¹⁵⁷ or Ni(II) cat. ¹⁵⁸
Allyl	Bpin	Cu(I) cat. ¹⁵⁹
alkyl, vinyl	9-BBN	Cu(I) cat. ^{160, 161}
alkyl, aryl	ZnX (X = Cl, Br, I)	Pd(II) or Ni(II) cat. ^{162, 163}
aryl, alkyl, vinyl	X (X = Cl, Br, I, OTs)	Cu(I), ^{166, 167} Pd(II) ^{164, 168, 169} or Ni(II) cat. ^{165, 170-174}

Bnep = 5,5-dimethyl-1,3,2-dioxaborinyl; Bpin = 4,4,5,5-tetramethyl-1,3,2-dioxaborolyl;
9-BBN = 9-Borabicyclo[3.3.1]nonane

It is also worthy to note that CO₂ can also be reduced to formic acid or methanol chemically or electrochemically.¹⁷⁵⁻¹⁷⁷ Moreover, processes for cyclic carbonate production involving CO₂ have been also reported.¹⁷⁸ In conclusion, although utilizing CO₂ is challenging, CO₂ can still serve as a C₁ source in synthetic chemistry with the right catalysts and conditions.

1.5 Summary and Conclusions

The SMR and WGS reactions are the major industrial processes for H₂ production, which are both energy intensive and broadly used. Thus, utilizing the SMR and WGS products (CO, H₂ and CO₂) efficiently can be beneficial to the economy by making production of these chemicals more cost-effective.

In the following chapters, studies on the utilization of CO, H₂ and CO₂ are described. In Chapter 2, olefin hydrogenation reactions were used as a model to study the redox chemistry during the catalytic cycle for capping arene ligated Rh complexes. In Chapter 3, direct carboxylation of benzene catalyzed by palladium catalysts was studied. In Chapter 4, methanol carbonylation chemistry catalyzed by capping arene Rh or Ir complexes was studied. In Chapter 5, a new capping arene Co complex was synthesized, and styrene hydrogenation catalyzed by the capping arene Co complex was studied. In Chapter 6, some possible future directions for my studies are proposed.

1.6 References

- (1) Velazquez Abad, A.; Dodds, P. E. Production of Hydrogen. In *Encyclopedia of Sustainable Technologies*, Abraham, M. A. Ed.; Elsevier, 2017; pp 293-304.
- (2) Fajín, J. L. C.; Gomes, J. R. B. Water Gas Shift Reaction Promoted by Bimetallic Catalysts: An Experimental and Theoretical Overview. In *Encyclopedia of Interfacial Chemistry*, Wandelt, K. Ed.; Elsevier, 2018; pp 314-318.
- (3) *Hydrogen Production: Natural Gas Reforming*. Office of Energy Efficiency & Renewable Energy, <https://www.energy.gov/eere/fuelcells/hydrogen-production-natural-gas-reforming> (accessed 2022).

- (4) *Hydrogen Production*. Office of Energy Efficiency & Renewable Energy, <https://www.energy.gov/eere/fuelcells/hydrogen-production#:~:text=With%20approximately%2010%20million%20metric,petroleum%20refining%20and%20ammonia%20production>. (accessed 2022).
- (5) DOE. *Hydrogen Strategy: Enabling a Low-Carbon Economy* Office of Fossil Energy, United States Department of Energy, Washington, DC, 2020.
- (6) IEA. *Global Hydrogen Review 2021*; IEA, Paris, <https://www.iea.org/reports/global-hydrogen-review-2021>.
- (7) Wei, L.; Pordesimo, L. O.; To, F.; Herndon, C.; Batchelor, W. Evaluation of Micro-Scale Syngas Production Costs through Modeling. *Transactions of the ASABE* **2009**, *52*, 1649-1659.
- (8) IEA. *Putting CO₂ to Use*; IEA, Paris, 2019. <https://www.iea.org/reports/putting-co2-to-use>.
- (9) Hock, H.; Lang, S. Autoxydation von Kohlenwasserstoffen, IX. Mitteil.: Über Peroxyde von Benzol-Derivaten. *Ber. Dtsch. Chem. Ges.* **1944**, *77*, 257-264.
- (10) Kraft, S.; Ryan, K.; Kargbo, R. B. Recent Advances in Asymmetric Hydrogenation of Tetrasubstituted Olefins. *J. Am. Chem. Soc.* **2017**, *139*, 11630-11641.
- (11) Arpe, H.-J. r. *Industrielle organische Chemie bedeutende Vor- und Zwischenprodukte*; 2007.
- (12) Vanoye, L.; Aloui, A.; Pablos, M.; Philippe, R.; Percheron, A.; Favre-Réguillon, A.; de Bellefon, C. A Safe and Efficient Flow Oxidation of Aldehydes with O₂. *Org. Lett.* **2013**, *15*, 5978-5981.

- (13) Chauvy, R.; De Weireld, G. CO₂ Utilization Technologies in Europe: A Short Review. *Energy Technology* **2020**, *8*, 2000627.
- (14) Vansant, J.; Koziel, P.-W. Technical and Industrial Applications of CO₂. In *An Economy Based on Carbon Dioxide and Water: Potential of Large Scale Carbon Dioxide Utilization*, Aresta, M., Karimi, I., Kawi, S. Eds.; Springer International Publishing, 2019; pp 73-103.
- (15) Gilbert, T. R.; Kirss, R. V.; Foster, N.; Davies, G. *Chemistry: The Science in Context, Fourth International Student Edition*; W.W. Norton, 2013.
- (16) Blanksby, S. J.; Ellison, G. B. Bond Dissociation Energies of Organic Molecules. *Acc. Chem. Res.* **2003**, *36*, 255-263.
- (17) Ruscic, B.; Feller, D.; Dixon, D. A.; Peterson, K. A.; Harding, L. B.; Asher, R. L.; Wagner, A. F. Evidence for a Lower Enthalpy of Formation of Hydroxyl Radical and a Lower Gas-Phase Bond Dissociation Energy of Water. *The Journal of Physical Chemistry A* **2001**, *105*, 1-4.
- (18) Buncl, E.; Menon, B. Carbanion mechanisms. 6. Metalation of Arylmetanes by Potassium Hydride/18-crown-6 Ether in Tetrahydrofuran and the Acidity of Hydrogen. *J. Am. Chem. Soc.* **1977**, *99*, 4457-4461.
- (19) Abdur-Rashid, K.; Fong, T. P.; Greaves, B.; Gusev, D. G.; Hinman, J. G.; Landau, S. E.; Lough, A. J.; Morris, R. H. An Acidity Scale for Phosphorus-Containing Compounds Including Metal Hydrides and Dihydrogen Complexes in THF: Toward the Unification of Acidity Scales. *J. Am. Chem. Soc.* **2000**, *122*, 9155-9171.
- (20) Jesse W. Tye, M. Y. D., Michael B. Hall. *Activation of Small Molecules*; Wiley Online Books, 2006.

- (21) Morris, R. H. 1995 Alcan Award Lecture New Intermediates in the Homolytic and Heterolytic Splitting of Dihydrogen. *Can. J. Chem.* **1996**, *74*, 1907-1915.
- (22) K. P. Huber, G. H. *Molecular Spectra and Molecular Structure*; Springer New York, NY, 1979.
- (23) Michos, D.; Luo, X.-L.; Howard, J. A. K.; Crabtree, R. H. Stretched H₂ Complexes: Structural Control in ReH₇{P(C₆H₄-*p*-X)₃}₂ (X = CH₃, H, F, CF₃, OMe) Complexes by Electronic Ligand Effects. *Inorg. Chem.* **1992**, *31*, 3914-3916.
- (24) Lin, Z.; Hall, M. B. Transition Metal Polyhydride Complexes: A Theoretical View. *Coord. Chem. Rev.* **1994**, *135-136*, 845-879.
- (25) Lin, Z.; Hall, M. B. Transition-Metal Polyhydride Complexes. 3. Relative Stabilities of Classical and Nonclassical Isomers. *J. Am. Chem. Soc* **1992**, *114*, 6102-6108.
- (26) Gibbs, G.; Hill, F.; Boisen, M.; Downs, R. Power Law Relationships between Bond Length, Bond Strength and Electron Density Distributions. *Phys. Chem. Miner.* **1998**, *25*, 585-590.
- (27) Schlaf, M.; Lough, A. J.; Maltby, P. A.; Morris, R. H. Synthesis, Structure, and Properties of the Stable and Highly Acidic Dihydrogen Complex trans-[Os(η^2 -H₂)(CH₃CN)(dppe)₂](BF₄)₂. Perspectives on the Influence of the trans Ligand on the Chemistry of the Dihydrogen Ligand. *Organometallics* **1996**, *15*, 2270-2278.
- (28) Skara, G.; De Vleeschouwer, F.; Geerlings, P.; De Proft, F.; Pinter, B. Heterolytic Splitting of Molecular Hydrogen by Frustrated and Classical Lewis Pairs: A Unified Reactivity Concept. *Scientific Reports* **2017**, *7*.

- (29) James, B. R. Hydrogenation Reactions Catalyzed by Transition Metal Complexes. In *Advances in Organometallic Chemistry*, Stone, F. G. A., West, R. Eds.; Vol. 17; Academic Press, 1979; pp 319-405.
- (30) Clapham, S. E.; Hadzovic, A.; Morris, R. H. Mechanisms of the H₂-Hydrogenation and Transfer Hydrogenation of Polar Bonds Catalyzed by Ruthenium Hydride Complexes. *Coord. Chem. Rev.* **2004**, *248*, 2201-2237.
- (31) Bullock, R. M.; Chambers, G. M. Frustration Across the Periodic Table: Heterolytic Cleavage of Dihydrogen by Metal Complexes. *Philosophical Transactions of the Royal Society A: Mathematical, Physical and Engineering Sciences* **2017**, *375*, 20170002.
- (32) Welch Gregory, C.; Juan Ronan, R. S.; Masuda Jason, D.; Stephan Douglas, W. Reversible, Metal-Free Hydrogen Activation. *Science* **2006**, *314*, 1124-1126.
- (33) Esteruelas, M. A.; Oro, L. A. Dihydrogen Complexes as Homogeneous Reduction Catalysts. *Chem. Rev.* **1998**, *98*, 577-588.
- (34) Esteruelas, M. A.; Herrero, J.; Lopez, A. M.; Oro, L. A.; Schulz, M.; Werner, H. Hydrogenation of Benzylideneacetone Catalyzed by Chlorodihydridobis(Diisopropylphosphine)Iridium: Kinetic Evidence for the Participation of an Iridium- η^2 -Dihydrogen Complex in the Activation of Molecular Hydrogen. *Inorg. Chem.* **1992**, *31*, 4013-4014.
- (35) Lundquist, E. G.; Folting, K.; Streib, W. E.; Huffman, J. C.; Eisenstein, O.; Caulton, K. G. Reactivity of the Molecular Hydrogen Complex [IrH₄(PMe₂Ph)₃]BF₄ Towards Olefins. The Origin of Stereochemical Rigidity of M(PR₃)₃(olefin)₂ Species. *J. Am. Chem. Soc.* **1990**, *112*, 855-863.

- (36) Marinelli, G.; Rachidi, I. E. I.; Streib, W. E.; Eisenstein, O.; Caulton, K. G. Alkyne Hydrogenation by a Dihydrogen Complex: Synthesis and Structure of an Unusual Iridium-Butyne Complex. *J. Am. Chem. Soc.* **1989**, *111*, 2346-2347.
- (37) Bianchini, C.; Meli, A.; Peruzzini, M.; Vizza, F.; Zanobini, F.; Frediani, P. A Homogeneous Iron(II) System Capable of Selectivity Catalyzing the Reduction of Terminal Alkynes to Alkenes and Buta-1,3-dienes. *Organometallics* **1989**, *8*, 2080-2082.
- (38) Graziani, M.; Rao, C. N. R. *Advances In Catalyst Design, Vol 2: Proceedings Of The 2nd Workshop On Catalyst Design*; World Scientific, 1993.
- (39) Bianchini, C.; Meli, A.; Peruzzini, M.; Frediani, P.; Bohanna, C.; Esteruelas, M. A.; Oro, L. A. Selective Hydrogenation of 1-alkynes to Alkenes Catalyzed by an Iron(II) *cis*-Hydride η^2 -dihydrogen Complex. A Case of Intramolecular Reaction between η^2 -H₂ and σ -vinyl Ligands. *Organometallics* **1992**, *11*, 138-145.
- (40) Bianchini, C.; Farnetti, E.; Graziani, M.; Peruzzini, M.; Polo, A. Chemoselective Hydrogen-Transfer Reduction of α , β -unsaturated Ketones Catalyzed by Isostructural Iron(II), Ruthenium(II), and Osmium(II) *Cis*-hydride (η^2 -dihydrogen) Complexes. *Organometallics* **1993**, *12*, 3753-3761.
- (41) Andriollo, A.; Esteruelas, M. A.; Meyer, U.; Oro, L. A.; Sanchez-Delgado, R. A.; Sola, E.; Valero, C.; Werner, H. Kinetic and Mechanistic Investigation of the Sequential Hydrogenation of Phenylacetylene Catalyzed by OsHCl(CO)(PR₃)₂ [PR₃ = PMe-*tert*-Bu₂ and P-*i*-Pr₃]. *J. Am. Chem. Soc.* **1989**, *111*, 7431-7437.
- (42) Esteruelas, M. A.; Oro, L. A.; Valero, C. Hydrogenation of Benzylideneacetone Catalyzed by OsHCl(CO)(PR₃)₂ (PR₃ = P-*iso*-Pr₃, PMe-*tert*-Bu₂): New Roles of

Dihydrogen Complexes in Homogeneous Catalytic Hydrogenation. *Organometallics* **1992**, *11*, 3362-3369.

(43) Esteruelas, M. A.; Oro, L. A.; Valero, C. Hydrosilylation of Phenylacetylene via an $\text{Os}(\text{SiEt}_3)(\eta^2\text{-H}_2)$ Intermediate Catalyzed by $\text{OsHCl}(\text{CO})(\text{P}^i\text{Pr}_3)_2$. *Organometallics* **1991**, *10*, 462-466.

(44) Esteruelas, M. A.; Valero, C.; Oro, L. A.; Meyer, U.; Werner, H. Insertion Reaction of Acetone- d_6 into the Osmium-Hydrogen Bond of $[\text{OsHCl}(\text{CO})(\text{P}^i\text{Pr}_3)_2]$: Experimental Evidence for the Hydrogen-Transfer Mechanism from Alcohols to Ketones. *Inorg. Chem.* **1991**, *30*, 1159-1160.

(45) Espuelas, J.; Esteruelas, M. A.; Lahoz, F. J.; Oro, L. A.; Valero, C. Reactivity of $\text{OsH}_4(\text{CO})(\text{P}^i\text{Pr}_3)_2$ Toward Terminal Alkynes: Synthesis and Reactions of the Alkynyl-Dihydrogen Complexes $\text{OsH}(\text{C}_2\text{R})(\eta^2\text{-H}_2)(\text{CO})(\text{P}^i\text{Pr}_3)_2$ ($\text{R} = \text{Ph}, \text{SiMe}_3$). *Organometallics* **1993**, *12*, 663-670.

(46) Borowski, A. F.; Sabo-Etienne, S.; Christ, M. L.; Donnadiou, B.; Chaudret, B. Versatile Reactivity of the Bis(dihydrogen) Complex $\text{RuH}_2(\text{H}_2)_2(\text{PCy}_3)_2$ toward Functionalized Olefins: Olefin Coordination versus Hydrogen Transfer via the Stepwise Dehydrogenation of the Phosphine Ligand. *Organometallics* **1996**, *15*, 1427-1434.

(47) Linn, D. E.; Halpern, J. Roles of Neutral and Anionic Ruthenium Polyhydrides in the Catalytic Hydrogenation of Ketones and Arenes. *J. Am. Chem. Soc.* **1987**, *109*, 2969-2974.

(48) Albertin, G.; Amendola, P.; Antoniutti, S.; Ianelli, S.; Pelizzi, G.; Bordignon, E. Reactions of Molecular Hydrogen Ruthenium Complexes $[\text{RuH}(\eta^2\text{-H}_2)\text{P}_4]\text{BF}_4$ with Alkynes: Preparation and Crystal Structure of the $[\text{Ru}\{\eta^3\text{-}(p\text{-tolyl})\text{C}_3\text{CH}(p\text{-tolyl})\}\{\text{PhP}(\text{OEt})_2\}_4]\text{BPh}_4$ Derivative. *Organometallics* **1991**, *10*, 2876-2883.

- (49) Chan, W.-C.; Lau, C.-P.; Chen, Y.-Z.; Fang, Y.-Q.; Ng, S.-M.; Jia, G. Syntheses and Characterization of Hydrotris(1-pyrazolyl)borate Dihydrogen Complexes of Ruthenium and Their Roles in Catalytic Hydrogenation Reactions. *Organometallics* **1997**, *16*, 34-44.
- (50) Joshi, A. M.; MacFarlane, K. S.; James, B. R. Kinetics and Mechanism of H₂-Hydrogenation of Styrene Catalyzed by [RuCl(dppb)(μ-Cl)]₂ (dppb = 1,4-bis(diphenylphosphino)butane). Evidence for Hydrogen Transfer from a Dinuclear Molecular Hydrogen Species. *J. Organomet. Chem.* **1995**, *488*, 161-167.
- (51) Chau, D. E. K. Y.; James, B. R. The Kinetics and Energetics of Formation of a Molecular Hydrogen Complex Involving a Dinuclear Ruthenium(II) Centre. *Inorg. Chim. Acta* **1995**, *240*, 419-425.
- (52) Hartwig, J. F. *Organotransition Metal Chemistry: From Bonding to Catalysis*; University Science book, 2009.
- (53) Young, J. F.; Osborn, J. A.; Jardine, F. H.; Wilkinson, G. Hydride Intermediates in Homogeneous Hydrogenation Reactions of Olefins and Acetylenes Using Rhodium Catalysts. *Chem. Commun.* **1965**, 131-132.
- (54) Evans, D.; Osborn, J. A.; Jardine, F. H.; Wilkinson, G. Homogeneous Hydrogenation and Hydroformylation Using Ruthenium Complexes. *Nature* **1965**, *208*, 1203-1204.
- (55) Osborn, J. A.; Jardine, F. H.; Young, J. F.; Wilkinson, G. The Preparation and Properties of Tris(triphenylphosphine)halogenorhodium(I) and Some Reactions Thereof Including Catalytic Homogeneous Hydrogenation of Olefins and Acetylenes and Their Derivatives. *J. Chem. Soc. A* **1966**, 1711-1732.

- (56) Baird, M. C.; Mague, J. T.; Osborn, J. A.; Wilkinson, G. Addition Reactions of Tris(triphenylphosphine)chlororhodium(I); Hydrido-, Alkyl, and Acyl Complexes; Carbon Monoxide Insertion and Decarbonylation Reactions. *J. Chem. Soc. A* **1967**, 1347.
- (57) Hallman, P. S.; Evans, D.; Osborn, J. A.; Wilkinson, G. Selective Catalytic Homogeneous Hydrogenation of Terminal Olefins Using Tris(triphenylphosphine)hydridochlororuthenium(II); Hydrogen Transfer in Exchange and Isomerisation Reactions of Olefins. *Chem. Commun.* **1967**, 305.
- (58) Koch, G. K.; Dalenberg, J. W. Preparation of [3H]-labelled Prostaglandin E1 by Hydrogenation of Prostaglandin E2 over RhCl(PPh₃)₃. An Example of Selectivity in Homogeneous Hydrogenation. *Journal of Labelled Compounds* **1970**, 6, 395-398.
- (59) Birch, A. J.; Williamson, D. H. Homogeneous Hydrogenation Catalysts in Organic Synthesis. *Organic Reactions* **2011**, 1-186.
- (60) Dawans, F.; Morel, D. The Synthesis of Polymer-Anchored η^3 -Allylic Transition Metal Complexes and Their Use as Catalysts. *J. Mol. Catal.* **1978**, 3, 403-415.
- (61) Halpern, J.; Okamoto, T.; Zakhariev, A. Mechanism of the Chlorotris(triphenylphosphine) Rhodium(I)-Catalyzed Hydrogenation of Alkenes. The Reaction of Chlorodihydridotris(triphenyl-phosphine)rhodium(III) with Cyclohexene. *J. Mol. Catal.* **1977**, 2, 65-68.
- (62) Halpern, J. Mechanism and Stereoselectivity of Asymmetric Hydrogenation. *Science* **1982**, 217, 401-407.
- (63) Chan, A. S. C.; Halpern, J. Interception and Characterization of a Hydridoalkylrhodium Intermediate in a Homogeneous Catalytic Hydrogenation Reaction. *J. Am. Chem. Soc.* **1980**, 102, 838-840.

- (64) Halpern, J.; Wong, C. S. Hydrogenation of Tris(triphenylphosphine)chlororhodium(I). *J. Chem. Soc., Chem. Commun.* **1973**, 629.
- (65) Schrock, R. R.; Osborn, J. A. Catalytic Hydrogenation Using Cationic Rhodium Complexes. I. Evolution of the Catalytic System and the Hydrogenation of Olefins. *J. Am. Chem. Soc.* **1976**, *98*, 2134-2143.
- (66) Schrock, R. R.; Osborn, J. A. Catalytic Hydrogenation Using Cationic Rhodium Complexes. II. The Selective Hydrogenation of Alkynes to *Cis* Olefins. *J. Am. Chem. Soc.* **1976**, *98*, 2143-2147.
- (67) Schrock, R. R.; Osborn, J. A. Catalytic Hydrogenation Using Cationic Rhodium Complexes. 3. The Selective Hydrogenation of Dienes to Monoenes. *J. Am. Chem. Soc.* **1976**, *98*, 4450-4455.
- (68) Crabtree, R. Iridium Compounds in Catalysis. *Acc. Chem. Res.* **1979**, *12*, 331-337.
- (69) Crabtree, R. H.; Hlatky, G. G.; Parnell, C. A.; Segmueller, B. E.; Uriarte, R. J. Solvento Complexes of Tungsten, Rhenium, Osmium, and Iridium and the X-Ray Crystal Structure of $[\text{IrH}_2(\text{Me}_2\text{CO})_2(\text{PPh}_3)_2]\text{BF}_4$. *Inorg. Chem.* **1984**, *23*, 354-358.
- (70) Suggs, J. W.; Cox, S. D.; Crabtree, R. H.; Quirk, J. M. Facile Homogeneous Hydrogenations of Hindered Olefins with $[\text{Ir}(\text{cod})\text{py}(\text{PCy}_3)]\text{PF}_6$. *Tetrahedron Lett.* **1981**, *22*, 303-306.
- (71) Gridnev, I. D.; Higashi, N.; Asakura, K.; Imamoto, T. Mechanism of Asymmetric Hydrogenation Catalyzed by a Rhodium Complex of (*S,S*)-1,2-Bis(*tert*-butylmethylphosphino)ethane. Dihydride Mechanism of Asymmetric Hydrogenation. *J. Am. Chem. Soc.* **2000**, *122*, 7183-7194.

- (72) Gridnev, I. D.; Imamoto, T.; Hoge, G.; Kouchi, M.; Takahashi, H. Asymmetric Hydrogenation Catalyzed by a Rhodium Complex of (*R*)-(tert-Butylmethylphosphino)(di-tert-butylphosphino)methane: Scope of Enantioselectivity and Mechanistic Study. *J. Am. Chem. Soc.* **2008**, *130*, 2560-2572.
- (73) Gridnev, I. D.; Imamoto, T. On the Mechanism of Stereoselection in Rh-Catalyzed Asymmetric Hydrogenation: A General Approach for Predicting the Sense of Enantioselectivity. *Acc. Chem. Res.* **2004**, *37*, 633-644.
- (74) Gridnev, I. D.; Imamoto, T. Mechanism of Enantioselection in Rh-catalyzed Asymmetric Hydrogenation. The Origin of Utmost Catalytic Performance. *Chem. Commun.* **2009**, 7447.
- (75) Gridnev, I. D.; Yamanoi, Y.; Higashi, N.; Tsuruta, H.; Yasutake, M.; Imamoto, T. Asymmetric Hydrogenation Catalyzed by (*S,S*)-R-BisPast;-Rh and (*R,R*)-R-MiniPHOS Complexes: Scope, Limitations, and Mechanism Unknown article. *Adv. Synth. Catal.* **2001**, *343*, 118-136.
- (76) Crabtree, R. H.; Felkin, H.; Fillebeen-Khan, T.; Morris, G. E. Dihydrido-iridium Diolefin Complexes as Intermediates in Homogeneous Hydrogenation. *J. Organomet. Chem.* **1979**, *168*, 183-195.
- (77) Cui, X.; Fan, Y.; Hall, M. B.; Burgess, K. Mechanistic Insights into Iridium-Catalyzed Asymmetric Hydrogenation of Dienes. *Chemistry - A European Journal* **2005**, *11*, 6859-6868.
- (78) Brandt, P.; Hedberg, C.; Andersson, P. G. New Mechanistic Insights into the Iridium-Phosphanooxazoline-Catalyzed Hydrogenation of Unfunctionalized Olefins: A DFT and Kinetic Study. *Chemistry - A European Journal* **2003**, *9*, 339-347.

- (79) Schrock, R. R.; Osborn, J. A. *Journal of the Chemical Society D: Chemical Communications* **1970**, *9*, 567-568.
- (80) Sánchez-Delgado, R. A.; De Ochoa, O. L. Homogeneous Hydrogenation of Ketones to Alcohols with Ruthenium Complex Catalysts. *J. Organomet. Chem.* **1980**, *202*, 427-434.
- (81) Lin, Y.; Zhou, Y. Molecular Hydrogen Complexes in Catalytic Reactions: Reactivity of Neutral Transition Metal Polyhydrides in the Catalytic Transfer Hydrogenation of Ketones. *J. Organomet. Chem.* **1990**, *381*, 135-138.
- (82) Evans, D. A.; Nelson, S. G.; Gagne, M. R.; Muci, A. R. A Chiral Samarium-Based Catalyst for the Asymmetric Meerwein-Ponndorf-Verley Reduction. *J. Am. Chem. Soc.* **1993**, *115*, 9800-9801.
- (83) Vicente, C.; Shul'pin, G. B.; Moreno, B.; Sabo-Etienne, S.; Chaudret, B. Reduction of Ketones by Dihydrogen or Hydrogen Transfer Catalysed by a Ruthenium Complex of the Hydridotris(3,5-dimethyl)pyrazolyl Borate Ligand. *J. Mol. Catal. A: Chem.* **1995**, *98*, L5-L8.
- (84) Fujii, A.; Hashiguchi, S.; Uematsu, N.; Ikariya, T.; Noyori, R. Ruthenium(II)-Catalyzed Asymmetric Transfer Hydrogenation of Ketones Using a Formic Acid-Triethylamine Mixture. *J. Am. Chem. Soc.* **1996**, *118*, 2521-2522.
- (85) Noyori, R.; Hashiguchi, S. Asymmetric Transfer Hydrogenation Catalyzed by Chiral Ruthenium Complexes. *Acc. Chem. Res.* **1997**, *30*, 97-102.
- (86) Noyori, R.; Ohkuma, T. Asymmetric Catalysis by Architectural and Functional Molecular Engineering: Practical Chemo- and Stereoselective Hydrogenation of Ketones. *Angew. Chem. Int. Ed.* **2001**, *40*, 40-73.

- (87) Abdur-Rashid, K.; Clapham, S. E.; Hadzovic, A.; Harvey, J. N.; Lough, A. J.; Morris, R. H. Mechanism of the Hydrogenation of Ketones Catalyzed by *trans*-Dihydrido(diamine)ruthenium(II) Complexes. *J. Am. Chem. Soc.* **2002**, *124*, 15104-15118.
- (88) Bullock, R. M. Catalytic Ionic Hydrogenations. *Chemistry - A European Journal* **2004**, *10*, 2366-2374.
- (89) Miessler, G. L.; Fischer, P. J.; Tarr, D. A. *Inorganic Chemistry*; Pearson, 2014.
- (90) Vaska, L.; DiLuzio, J. W. Carbonyl and Hydrido-Carbonyl Complexes of Iridium by Reaction with Alcohols. Hydrido Complexes by Reaction with Acid. *J. Am. Chem. Soc.* **1961**, *83*, 2784-2785.
- (91) Goldman, A. S.; Krogh-Jespersen, K. Why Do Cationic Carbon Monoxide Complexes Have High C–O Stretching Force Constants and Short C–O Bonds? Electrostatic Effects, Not σ -Bonding. *J. Am. Chem. Soc.* **1996**, *118*, 12159-12166.
- (92) Walter, R. H., F.; Walter, M. Process for the Production of Aliphatic Oxygen Compounds by Carbonylation of Alcohols, Ethers, and Esters. US2729651A, 1956.
- (93) Walter, R. H., F. Acetic Acid Anhydride. US2789137A, 1957.
- (94) Paulik, F. E.; Roth, J. F. Novel Catalysts for the Low-Pressure Carbonylation of Methanol to Acetic Acid. *Chem. Commun.* **1968**, 1578a-1578a.
- (95) Haynes, A.; Maitlis, P. M.; Morris, G. E.; Sunley, G. J.; Adams, H.; Badger, P. W.; Bowers, C. M.; Cook, D. B.; Elliott, P. I. P.; Ghaffar, T.; et al. Promotion of Iridium-Catalyzed Methanol Carbonylation: Mechanistic Studies of the CativaTM Process. *J. Am. Chem. Soc.* **2004**, *126*, 2847-2861.
- (96) Howard, M. J. S., G.J.; Poole, A.D.; Watt, R.J.; Sharma, B.K. New Acetyls Technologies from BP Chemicals. *Stud. Surf. Sci. Catal.* **1999**, *121*, 61-68.

- (97) Sunley, G. J.; Watson, D. J. High Productivity Methanol Carbonylation Catalysis Using Iridium: The Cativa™ Process for the Manufacture of Acetic Acid. *Catal. Today* **2000**, *58*, 293-307.
- (98) Haynes, A. Chapter 1 - Catalytic Methanol Carbonylation. In *Advances in Catalysis*, Gates, B. C., Knözinger, H. Eds.; Vol. 53; Academic Press, 2010; pp 1-45.
- (99) Forster, D. Mechanistic Pathways in the Catalytic Carbonylation of Methanol by Rhodium and Iridium Complexes. In *Advances in Organometallic Chemistry*, Stone, F. G. A., West, R. Eds.; Vol. 17; Academic Press, 1979; pp 255-267.
- (100) Yoneda, N.; Kusano, S.; Yasui, M.; Pujado, P.; Wilcher, S. Recent Advances in Processes and Catalysts for the Production of Acetic Acid. *Applied Catalysis A: General* **2001**, *221*, 253-265.
- (101) Baker, M. J.; Giles, M. F.; Orpen, A. G.; Taylor, M. J.; Watt, R. J. Cis-[RhI(CO)(Ph₂PCH₂P(S)Ph₂)]: a New Catalyst for Methanol Carbonylation. *J. Chem. Soc., Chem. Commun.* **1995**, 197.
- (102) Carraz, C.-A.; Orpen, A. G.; Ellis, D. D.; Pringle, P. G.; Ditzel, E. J.; Sunley, G. J. Rhodium(I) Complexes of Unsymmetrical Diphosphines: Efficient and Stable Methanol Carbonylation Catalysts. *Chem. Commun.* **2000**, 1277-1278.
- (103) Deb, B.; Dutta, D. K. Influence of Phosphorus and Oxygen Donor Diphosphine Ligands on the Reactivity of Rhodium(I) Carbonyl Complexes. *J. Mol. Catal. A: Chem.* **2010**, *326*, 21-28.
- (104) Gonsalvi, L.; Adams, H.; Sunley, G. J.; Ditzel, E.; Haynes, A. A Dramatic Steric Effect on the Rate of Migratory CO Insertion on Rhodium. *J. Am. Chem. Soc.* **1999**, *121*, 11233-11234.

- (105) Gonsalvi, L.; Adams, H.; Sunley, G. J.; Ditzel, E.; Haynes, A. Steric and Electronic Effects on the Reactivity of Rh and Ir Complexes Containing P–S, P–P, and P–O Ligands. Implications for the Effects of Chelate Ligands in Catalysis. *J. Am. Chem. Soc.* **2002**, *124*, 13597-13612.
- (106) Williams, G. L.; Parks, C. M.; Smith, C. R.; Adams, H.; Haynes, A.; Meijer, A. J. H. M.; Sunley, G. J.; Gaemers, S. Mechanistic Study of Rhodium/Xantphos-Catalyzed Methanol Carbonylation. *Organometallics* **2011**, *30*, 6166-6179.
- (107) Franke, R.; Selent, D.; Börner, A. Applied Hydroformylation. *Chem. Rev.* **2012**, *112*, 5675-5732.
- (108) Pruchnik, F. P. *Organometallic chemistry of the transition elements*; Springer Science & Business Media, 2013.
- (109) Beller, M.; Cornils, B.; Frohning, C. D.; Kohlpaintner, C. W. Progress in Hydroformylation and Carbonylation. *J. Mol. Catal. A: Chem.* **1995**, *104*, 17-85.
- (110) Piras, I.; Jennerjahn, R.; Jackstell, R.; Spannenberg, A.; Franke, R.; Beller, M. A General and Efficient Iridium-Catalyzed Hydroformylation of Olefins. *Angew. Chem. Int. Ed.* **2011**, *50*, 280-284.
- (111) Evans, D.; Osborn, J. A.; Wilkinson, G. Hydroformylation of Alkenes by use of Rhodium Complex Catalysts. *J. Chem. Soc. A* **1968**, 3133.
- (112) Heck, R. F.; Breslow, D. S. The Reaction of Cobalt Hydrotetracarbonyl with Olefins. *J. Am. Chem. Soc.* **1961**, *83*, 4023-4027.
- (113) Wender, I.; Metlin, S.; Ergun, S.; Sternberg, H. W.; Greenfield, H. Kinetics and Mechanism of the Hydroformylation Reaction. The Effect of Olefin Structure on Rate. *J. Am. Chem. Soc.* **1956**, *78*, 5401-5405.

- (114) Torrent, M.; Solà, M.; Frenking, G. Theoretical Studies of Some Transition-Metal-Mediated Reactions of Industrial and Synthetic Importance. *Chem. Rev.* **2000**, *100*, 439-494.
- (115) Gleich, D.; Hutter, J. Computational Approaches to Activity in Rhodium-Catalysed Hydroformylation. *Chemistry - A European Journal* **2004**, *10*, 2435-2444.
- (116) Gleich, D.; Schmid, R.; Herrmann, W. A. A Combined QM/MM Method for the Determination of Regioselectivities in Rhodium-Catalyzed Hydroformylation. *Organometallics* **1998**, *17*, 4828-4834.
- (117) Carbó, J. J.; Maseras, F.; Bo, C.; Van Leeuwen, P. W. N. M. Unraveling the Origin of Regioselectivity in Rhodium Diphosphine Catalyzed Hydroformylation. A DFT QM/MM Study. *J. Am. Chem. Soc.* **2001**, *123*, 7630-7637.
- (118) Decker, S. A.; Cundari, T. R. Hybrid QM/MM Study of Propene Insertion into the Rh-H bond of $\text{HRh}(\text{PPh}_3)_2(\text{CO})(\eta^2\text{-CH}_2\text{-CHCH}_3)$: the Role of the Olefin Adduct in Determining Product Selectivity. *J. Organomet. Chem.* **2001**, *635*, 132-141.
- (119) Alagona, G.; Ghio, C.; Lazzaroni, R.; Settambolo, R. Olefin Insertion into the Rhodium-Hydrogen Bond as the Step Determining the Regioselectivity of Rhodium-Catalyzed Hydroformylation of Vinyl Substrates: Comparison between Theoretical and Experimental Results. *Organometallics* **2001**, *20*, 5394-5404.
- (120) Gleich, D.; Schmid, R.; Herrmann, W. A. A Molecular Model To Explain and Predict the Stereoselectivity in Rhodium-Catalyzed Hydroformylation. *Organometallics* **1998**, *17*, 2141-2143.

- (121) Gleich, D.; Herrmann, W. A. Why Do Many C_2 -Symmetric Bisphosphine Ligands Fail in Asymmetric Hydroformylation? Theory in Front of Experiment. *Organometallics* **1999**, *18*, 4354-4361.
- (122) Li, C.; Widjaja, E.; Chew, W.; Garland, M. Rhodium Tetracarbonyl Hydride: The Elusive Metal Carbonyl Hydride. *Angew. Chem. Int. Ed.* **2002**, *41*, 3785 - 3789.
- (123) Kumar, M.; Chaudhari, R. V.; Subramaniam, B.; Jackson, T. A. Ligand Effects on the Regioselectivity of Rhodium-Catalyzed Hydroformylation: Density Functional Calculations Illuminate the Role of Long-Range Noncovalent Interactions. *Organometallics* **2014**, *33*, 4183-4191.
- (124) Pruett, R. L.; Smith, J. A. Low-Pressure System for Producing Normal Aldehydes by Hydroformylation of α -olefins. *J. Org. Chem.* **1969**, *34*, 327-330.
- (125) Lazzaroni, R.; Pertici, P.; Bertozzi, S.; Fabrizi, G. 1-Hexene Rhodium-Catalyzed Hydroformylation at Partial Substrate Conversion: Influence of Reaction Parameters on the Chemoselectivity and Regioselectivity. *J. Mol. Catal.* **1990**, *58*, 75-85.
- (126) Hjortkjaer, J.; Scurrall, M. S.; Simonsen, P. Supported Liquid-Phase Hydroformylation Catalysts Containing Rhodium and Triphenylphosphine. *J. Mol. Catal.* **1979**, *6*, 405-420.
- (127) Leeuwen, P. W. N. M.; Claver, C. *Rhodium Catalyzed Hydroformylation*; Springer Dordrecht, 2002.
- (128) Unruh, J. D.; Christenson, J. R. A Study of the Mechanism of Rhodium/Phosphine-Catalyzed Hydroformylation: Use of 1,1'-bis(diarylphosphino)ferrocene Ligands. *J. Mol. Catal.* **1982**, *14*, 19-34.

- (129) Devon, T. J.; Phillips, G. W.; Puckette, T. A.; Stavinoha, J. L.; Vanderbilt, J. J. Chelate Ligands for Low Pressure Hydroformylation Catalyst and Process Employing Same. US4694109A, 1986.
- (130) Dierkes, P.; Van Leeuwen, P. W. N. M. The Bite Angle Makes the Difference: a Practical Ligand Parameter for Diphosphine Ligands. *J. Chem. Soc., Dalton Trans.* **1999**, 1519-1530.
- (131) Casey, C. P.; Petrovich, L. M. (Chelating Diphosphine)Rhodium-Catalyzed Deuterioformylation of 1-Hexene: Control of Regiochemistry by the Kinetic Ratio of Alkylrhodium Species Formed by Hydride Addition to Complexed Alkene. *J. Am. Chem. Soc.* **1995**, *117*, 6007-6014.
- (132) van Leeuwen, P. W. N. M.; Roobeek, C. F. Hydroformylation of Less Reactive Olefins with Modified Rhodium Catalysts. *J. Organomet. Chem.* **1983**, *258*, 343-350.
- (133) Palo, D. R.; Erkey, C. Effect of Ligand Modification on Rhodium-Catalyzed Homogeneous Hydroformylation in Supercritical Carbon Dioxide. *Organometallics* **2000**, *19*, 81-86.
- (134) Casey, C. P.; Paulsen, E. L.; Beuttenmueller, E. W.; Proft, B. R.; Petrovich, L. M.; Matter, B. A.; Powell, D. R. Electron Withdrawing Substituents on Equatorial and Apical Phosphines Have Opposite Effects on the Regioselectivity of Rhodium Catalyzed Hydroformylation. *J. Am. Chem. Soc.* **1997**, *119*, 11817-11825.
- (135) Mascetti, J. Carbon Dioxide Coordination Chemistry and Reactivity of Coordinated CO₂. In *Carbon Dioxide as Chemical Feedstock*, 2010; pp 55-88.
- (136) Aresta, M.; Dibenedetto, A.; Quaranta, E. *Reaction Mechanisms in Carbon Dioxide Conversion*; Springer Berlin, Heidelberg, 2016.

- (137) Calabrese, J. C.; Herskovitz, T.; Kinney, J. B. Carbon dioxide coordination chemistry. 5. The Preparation and Structure of the Rhodium Complex $\text{Rh}(\eta^1\text{-CO}_2)(\text{Cl})(\text{diars})_2$. *J. Am. Chem. Soc.* **1983**, *105*, 5914-5915.
- (138) Fachinetti, G.; Floriani, C.; Zanazzi, P. F. Bifunctional Activation of Carbon Dioxide. Synthesis and Structure of a Reversible Carbon Dioxide Carrier. *J. Am. Chem. Soc.* **1978**, *100*, 7405-7407.
- (139) Jegat, C.; Fouassier, M.; Tranquille, M.; Mascetti, J. Carbon Dioxide Coordination Chemistry. 2. Synthesis and FTIR Study of (Carbon Dioxide)Bis(Cyclopentadienyl)(Trimethylphosphine) Titanium. *Inorg. Chem.* **1991**, *30*, 1529-1536.
- (140) Herskovitz, T. Carbon Dioxide Coordination Chemistry. 3. Adducts of Carbon Dioxide with Iridium (I) Complexes. *J. Am. Chem. Soc.* **1977**, *99*, 2391-2392.
- (141) Aresta, M.; Nobile, C. F.; Albano, V. G.; Forni, E.; Manassero, M. New Nickel–Carbon Dioxide Complex: Synthesis, Properties, and Crystallographic Characterization of (Carbon Dioxide)-Bis(Tricyclohexylphosphine)Nickel. *Chem. Commun.* **1975**, *0*, 636-637.
- (142) Karsch, H. H. Funktionelle Trimethylphosphinderivate, III. Ambivalentes Verhalten von Tetrakis(trimethylphosphin)eisen : Reaktion mit CO_2 . *Chem. Ber.* **1977**, *110*, 2213-2221.
- (143) Alvarez, R.; Carmona, E.; Marin, J. M.; Poveda, M. L.; Gutierrez-Puebla, E.; Monge, A. Carbon Dioxide Chemistry. Synthesis, Properties, and Structural Characterization of Stable Bis(Carbon Dioxide) Adducts of Molybdenum. *J. Am. Chem. Soc.* **1986**, *108*, 2286-2294.

- (144) Castro-Rodriguez, I.; Nakai, H.; Zakharov Lev, N.; Rheingold Arnold, L.; Meyer, K. A Linear, O-Coordinated η^1 -CO₂ Bound to Uranium. *Science* **2004**, *305*, 1757-1759.
- (145) Viasus, C. J.; Gabidullin, B.; Gambarotta, S. Linear End-On Coordination Modes of CO₂. *Angew. Chem.* **2019**, *131*, 15029-15032.
- (146) Kafafi, Z. H.; Hauge, R. H.; Billups, W. E.; Margrave, J. L. Carbon Dioxide Activation by Alkali Metals. 2. Infrared Spectra of M⁺CO₂⁻ and M₂²⁺CO₂²⁻ in Argon and Nitrogen Matrixes. *Inorg. Chem.* **1984**, *23*, 177-183.
- (147) Freeman, L. A.; Obi, A. D.; Machost, H. R.; Molino, A.; Nichols, A. W.; Dickie, D. A.; Wilson, D. J. D.; Machan, C. W.; Gilliard, R. J. Soluble, Crystalline, and Thermally Stable Alkali CO₂⁻ and Carbonite (CO₂²⁻) Clusters Supported by Cyclic(alkyl)(amino) Carbenes. *Chem. Sci.* **2021**, *12*, 3544-3550.
- (148) Earth., -. T. *co2.earth*. <https://www.co2.earth/> (accessed 07/19/2022).
- (149) Tortajada, A.; Juliá-Hernández, F.; Börjesson, M.; Moragas, T.; Martin, R. Transition-Metal-Catalyzed Carboxylation Reactions with Carbon Dioxide. *Angew. Chem. Int. Ed.* **2018**, *57*, 15948-15982.
- (150) Shi, M.; Nicholas, K. M. Palladium-Catalyzed Carboxylation of Allyl Stannanes. *J. Am. Chem. Soc.* **1997**, *119*, 5057-5058.
- (151) Johansson, R.; Wendt, O. F. Insertion of CO₂ into a Palladiumallyl Bond and a Pd(II) Catalysed Carboxylation of Allyl Stannanes. *Dalton Trans.* **2007**, 488-492.
- (152) Franks, R. J.; Nicholas, K. M. Palladium-Catalyzed Carboxylative Coupling of Allylstannanes and Allyl Halides. *Organometallics* **2000**, *19*, 1458-1460.

- (153) Feng, X.; Sun, A.; Zhang, S.; Yu, X.; Bao, M. Palladium-Catalyzed Carboxylative Coupling of Benzyl Chlorides with Allyltributylstannane: Remarkable Effect of Palladium Nanoparticles. *Org. Lett.* **2013**, *15*, 108-111.
- (154) Wu, J.; Hazari, N. Palladium Catalyzed Carboxylation of Allylstannanes and Boranes using CO₂. *Chem. Commun.* **2011**, *47*, 1069-1071.
- (155) Ukai, K.; Aoki, M.; Takaya, J.; Iwasawa, N. Rhodium(I)-Catalyzed Carboxylation of Aryl- and Alkenylboronic Esters with CO₂. *J. Am. Chem. Soc.* **2006**, *128*, 8706-8707.
- (156) Takaya, J.; Tadami, S.; Ukai, K.; Iwasawa, N. Copper(I)-Catalyzed Carboxylation of Aryl- and Alkenylboronic Esters. *Org. Lett.* **2008**, *10*, 2697-2700.
- (157) Ohishi, T.; Nishiura, M.; Hou, Z. Carboxylation of Organoboronic Esters Catalyzed by N-Heterocyclic Carbene Copper(I) Complexes. *Angew. Chem. Int. Ed.* **2008**, *47*, 5792-5795.
- (158) Zhang, X.; Zhang, W.-Z.; Shi, L.-L.; Guo, C.-X.; Zhang, L.-L.; Lu, X.-B. Silver(i)-Catalyzed Carboxylation of Arylboronic Esters with CO₂. *Chem. Commun.* **2012**, *48*, 6292.
- (159) Makida, Y.; Marelli, E.; Slawin, A. M. Z.; Nolan, S. P. Nickel-Catalysed Carboxylation of Organoboronates. *Chem. Commun.* **2014**, *50*, 8010.
- (160) Duong, H. A.; Huleatt, P. B.; Tan, Q.-W.; Shuying, E. L. Regioselective Copper-Catalyzed Carboxylation of Allylboronates with Carbon Dioxide. *Org. Lett.* **2013**, *15*, 4034-4037.
- (161) Ohmiya, H.; Tanabe, M.; Sawamura, M. Copper-Catalyzed Carboxylation of Alkylboranes with Carbon Dioxide: Formal Reductive Carboxylation of Terminal Alkenes. *Org. Lett.* **2011**, *13*, 1086-1088.

- (162) Ohishi, T.; Zhang, L.; Nishiura, M.; Hou, Z. Carboxylation of Alkylboranes by N-Heterocyclic Carbene Copper Catalysts: Synthesis of Carboxylic Acids from Terminal Alkenes and Carbon Dioxide. *Angew. Chem. Int. Ed.* **2011**, *50*, 8114-8117.
- (163) Yeung, C. S.; Dong, V. M. Beyond Aresta's Complex: Ni- and Pd-Catalyzed Organozinc Coupling with CO₂. *J. Am. Chem. Soc.* **2008**, *130*, 7826-7827.
- (164) Ochiai, H.; Jang, M.; Hirano, K.; Yorimitsu, H.; Oshima, K. Nickel-Catalyzed Carboxylation of Organozinc Reagents with CO₂. *Org. Lett.* **2008**, *10*, 2681-2683.
- (165) Correa, A.; Martín, R. Palladium-Catalyzed Direct Carboxylation of Aryl Bromides with Carbon Dioxide. *J. Am. Chem. Soc.* **2009**, *131*, 15974-15975.
- (166) Fujihara, T.; Nogi, K.; Xu, T.; Terao, J.; Tsuji, Y. Nickel-Catalyzed Carboxylation of Aryl and Vinyl Chlorides Employing Carbon Dioxide. *J. Am. Chem. Soc.* **2012**, *134*, 9106-9109.
- (167) Tran-Vu, H.; Daugulis, O. Copper-Catalyzed Carboxylation of Aryl Iodides with Carbon Dioxide. *ACS Catal.* **2013**, *3*, 2417-2420.
- (168) Ebert, G. W.; Juda, W. L.; Kosakowski, R. H.; Ma, B.; Dong, L.; Cummings, K. E.; Phelps, M. V. B.; Mostafa, A. E.; Luo, J. Carboxylation and Esterification of Functionalized Arylcopper Reagents. *J. Org. Chem.* **2005**, *70*, 4314-4317.
- (169) Zhang, S.; Chen, W.-Q.; Yu, A.; He, L.-N. Palladium-Catalyzed Carboxylation of Benzyl Chlorides with Atmospheric Carbon Dioxide in Combination with Manganese/Magnesium Chloride. *ChemCatChem* **2015**, *7*, 3972-3977.
- (170) Shimomaki, K.; Murata, K.; Martin, R.; Iwasawa, N. Visible-Light-Driven Carboxylation of Aryl Halides by the Combined Use of Palladium and Photoredox Catalysts. *J. Am. Chem. Soc.* **2017**, *139*, 9467-9470.

- (171) Liu, Y.; Cornella, J.; Martin, R. Ni-Catalyzed Carboxylation of Unactivated Primary Alkyl Bromides and Sulfonates with CO₂. *J. Am. Chem. Soc.* **2014**, *136*, 11212-11215.
- (172) Börjesson, M.; Moragas, T.; Martin, R. Ni-Catalyzed Carboxylation of Unactivated Alkyl Chlorides with CO₂. *J. Am. Chem. Soc.* **2016**, *138*, 7504-7507.
- (173) Wang, X.; Liu, Y.; Martin, R. Ni-Catalyzed Divergent Cyclization/Carboxylation of Unactivated Primary and Secondary Alkyl Halides with CO₂. *J. Am. Chem. Soc.* **2015**, *137*, 6476-6479.
- (174) Juliá-Hernández, F.; Moragas, T.; Cornella, J.; Martin, R. Remote carboxylation of halogenated aliphatic hydrocarbons with carbon dioxide. *Nature* **2017**, *545*, 84-88.
- (175) Rebih, F.; Andreini, M.; Moncomble, A.; Harrison-Marchand, A.; Maddaluno, J.; Durandetti, M. Direct Carboxylation of Aryl Tosylates by CO₂ Catalyzed by In situ-Generated Ni⁰. *Chemistry - A European Journal* **2016**, *22*, 3758-3763.
- (176) Jessop, P. G.; Ikariya, T.; Noyori, R. Homogeneous Hydrogenation of Carbon Dioxide. *Chem. Rev.* **1995**, *95*, 259-272.
- (177) Jiang, X.; Nie, X.; Guo, X.; Song, C.; Chen, J. G. Recent Advances in Carbon Dioxide Hydrogenation to Methanol via Heterogeneous Catalysis. *Chem. Rev.* **2020**, *120*, 7984-8034.
- (178) Francke, R.; Schille, B.; Roemelt, M. Homogeneously Catalyzed Electroreduction of Carbon Dioxide—Methods, Mechanisms, and Catalysts. *Chem. Rev.* **2018**, *118*, 4631-4701.
- (179) Pescarmona, P. P. Cyclic carbonates synthesised from CO₂: Applications, Challenges and Recent Research Trends. *Current Opinion in Green and Sustainable Chemistry* **2021**, *29*, 100457.

2 Capping Arene Ligated Rhodium Catalyzed Olefin Hydrogenation

This chapter is adapted with permission from “Zhang, K.; Musgrave, C. B.; Dickie, D. A.; Goddard, W. A.; Gunnoe, T. B. Capping Arene Ligated Rhodium Catalyzed Olefin Hydrogenation: A Model Study of the Ligand Influence on a Catalytic Process that Incorporates Oxidative Addition and Reductive Elimination. Organometallics. ASAP” Copyright 2022 American Chemical Society.

Ke Zhang and Charles B. Musgrave III contributed equally to this work.

All DFT calculations in this chapter were accomplished by Charles B. Musgrave III and William A. Goddard III.

2.1 Introduction

Many homogeneous catalytic processes based on transition metal catalysts occur through catalytic cycles that form transition metal intermediates in different formal oxidation states. For example, for transition metal-based catalytic processes, oxidative addition and reductive elimination reactions are often key steps in catalytic processes, and these fundamental reactions increase formal metal oxidation state and coordination number (oxidative addition) or decrease formal metal oxidation state and coordination number (reductive elimination).¹⁻¹⁰

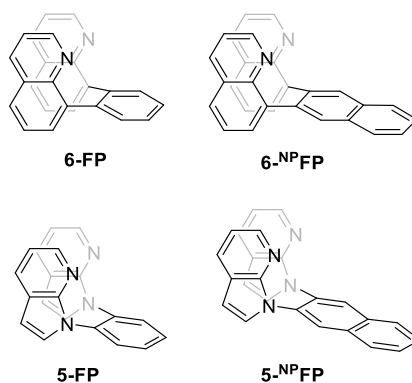
A common motif for processes based on group 9 metals is for a catalytic cycle to involve d^8 (+1 oxidation state) and d^6 (+3 oxidation state) intermediates.^{7, 11-19} For example, methanol carbonylation catalyzed by RhI_3 is proposed to undergo a catalytic cycle that involves a Rh(I) d^8 specie $[\text{Rh}(\text{CO})_2\text{I}_2]^-$ and a Rh(III) d^6 specie $[\text{Rh}(\text{CH}_3)(\text{CO})_2\text{I}_3]^-$.¹² To

improve catalytic activity, studies have been directed toward understanding trends for oxidative addition and reductive elimination by tuning a variety of features (e.g., electronic properties of the metal and ligand, steric properties of the ligand).²⁰⁻³¹

For catalytic processes that proceed through different transition metal redox states, the different oxidation states present variable d-electron counts and idealized geometries. For example, a d^8 configuration is often stable with a square planar geometry, and a d^6 configuration is often stable with an octahedral geometry.³² Ligand design that selectively stabilizes, or destabilizes, a specific formal metal redox state, based on d-electron count and/or a preferred geometry/coordination number, can be potentially used to optimize rates of catalysis.^{23-25, 33-36}

Recently, our group has reported on the use of “capping arene” ligands (FP) with Co, Rh, and Ir metals.^{27, 36-41} Capping arene ligands are a group of nitrogen-based bidentate ligands linked by arene groups, for example, 6-FP (8,8'-(1,2-phenylene)diquinoline), 6-^{NP}FP (8,8'-(2,3-naphthalene)diquinoline), 5-FP (1,2-bis(*N*-7-azaindoly)benzene) and 5-^{NP}FP (2,3-bis(*N*-7-azaindoly)naphthalene) (**Scheme 2.1.1**). When capping arene ligands coordinate to a metal, the arene moiety can block one of the coordination sites for an octahedral complex. Furthermore, the arene to metal bonding interaction can be adjusted by controlling arene-metal distances for 6-FP and 5-FP.

Scheme 2.1.1. Examples of capping arene ligands.

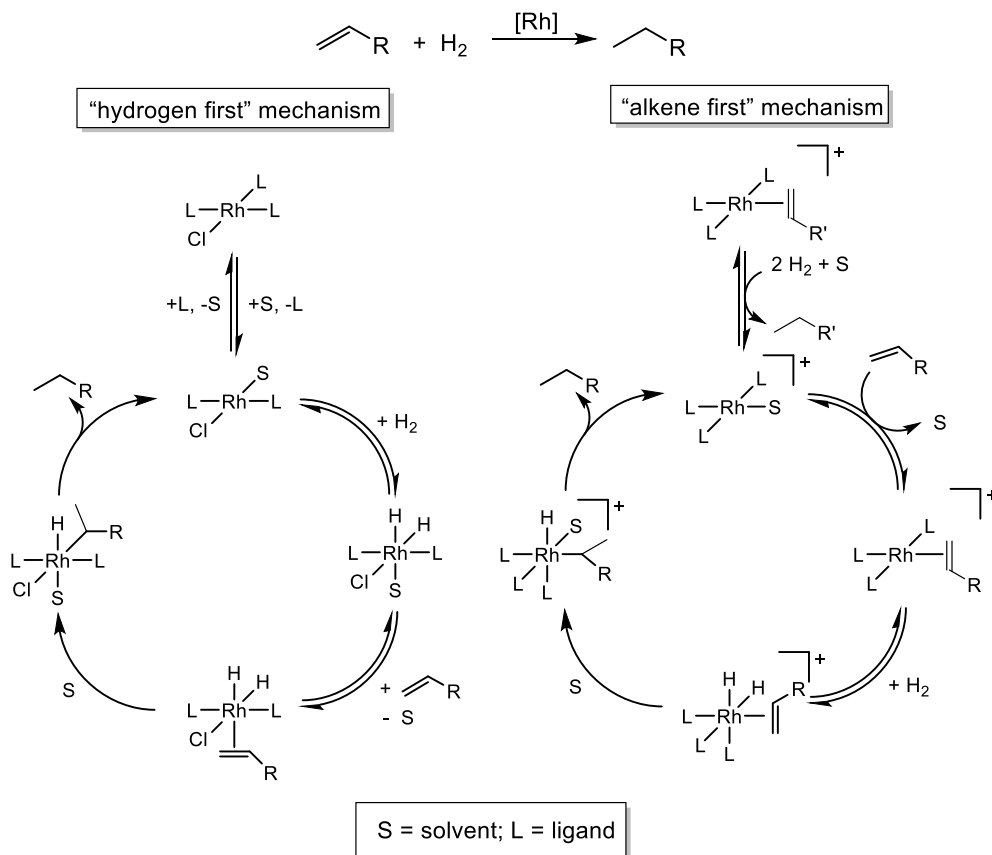


For capping arene-Rh complexes, we have studied the ability of the capping arene structure to modulate the reductive elimination of MeX (X = halides, pseudohalides) from (FP)Rh^{III}(Me)(X)₂.³⁶ In the study, ligand effects were observed on reductive elimination of MeTFA from (FP)Rh^{III}(Me)(TFA)₂, for which the (5-FP)Rh^{III}(Me)(TFA)₂ and (5-NPFP)Rh^{III}(Me)(TFA)₂ exhibit faster MeTFA formation than (6-FP)Rh^{III}(Me)(TFA)₂ or (6-NPFP)Rh^{III}(Me)(TFA)₂.

In this work, we sought to extend our studies of the impact of capping arene ligands using a model catalytic reaction. To do so, we sought a catalytic reaction with a well-defined set of possible mechanistic pathways and clear involvement of Mⁿ and Mⁿ⁺² formal oxidation states that are formed via oxidative addition and reductive elimination reactions. Rh-catalyzed olefin hydrogenation was selected for the model study. Previously, two mechanisms have been proposed for Rh-catalyzed olefin hydrogenation (**Scheme 2.1.2**).^{6, 17, 42-51} In the “hydrogen-first mechanism,” the active species Rh(L)₂(S)(Cl) (L = ligand, S = solvent) first mediates oxidative addition of H₂ to form Rh(H)₂(L)₂(S)(Cl), followed by the coordination of olefin substrate and olefin migratory insertion to form Rh(H)(alkyl)(L)₂(S)(Cl). Finally, the hydrogenated product and the active catalyst are

generated by reductive elimination of alkane. In a “olefin-first mechanism,” the active species $[\text{Rh}(\text{L})_3(\text{S})]^+$ first undergoes a ligand exchange with the olefin substrate to form $[\text{Rh}(\text{L})_3(\text{olefin})]^+$. Oxidative addition of H_2 to $[\text{Rh}(\text{L})_3(\text{olefin})]^+$ then takes place which forms $[\text{Rh}(\text{H})_2(\text{L})_3(\text{olefin})]^+$. After that, the $[\text{Rh}(\text{H})_2(\text{L})_3(\text{olefin})]^+$ is transformed to $[\text{Rh}(\text{H})(\text{alkyl})(\text{L})_3]^+$ via migratory insertion. Subsequently, the hydrogenated product is released by the reductive elimination of alkane, and $[\text{Rh}(\text{L})_3(\text{S})]^+$ is regenerated. Although specific mechanisms may vary based on ligand(s), olefin substrate, and conditions, the key steps of Rh-catalyzed olefin hydrogenation are usually proposed to be oxidative addition of H_2 to form Rh(III)-dihydride complex, olefin coordination, migratory insertion of coordinated olefin into a Rh-hydride bond, and reductive elimination from a $\text{Rh}^{\text{III}}(\text{H})(\text{alkyl})$ intermediate to release the hydrogenated product and form a Rh(I) product (**Scheme 2.1.2**).^{6, 17, 42-51} Previous studies have shown that oxidative addition of H_2 is often the rate-determining step for Rh(I)-catalyzed olefin hydrogenation.^{6, 43-47} Thus, we anticipated that the capping arene ligated Rh(I)-catalyzed olefin hydrogenation would follow one of the general mechanisms shown in **Scheme 2.1.2**, for which the oxidative addition of H_2 on the Rh(I) metal center would likely play an important role in the catalytic cycle.

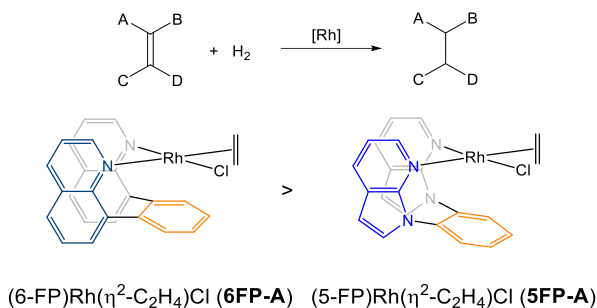
Scheme 2.1.2 General mechanisms for homogenous Rh-catalyzed olefin hydrogenation reactions.



Herein, we report on studies of capping arene ligated Rh(I)-catalyzed olefin hydrogenation including combined experimental and computational studies to understand the mechanism and quantify catalytic performance. Our studies reveal that the reaction rate of olefin hydrogenation is dependent on the capping arene ligands on Rh, for which the trend is identified to be $(6\text{-FP})\text{Rh}(\eta^2\text{-C}_2\text{H}_4)\text{Cl} > (5\text{-FP})\text{Rh}(\eta^2\text{-C}_2\text{H}_4)\text{Cl}$ (**Scheme 2.1.3**). Combined experimental and computational modeling studies allow us to understand and explain the relative rates of reaction based on the identity of the Rh catalyst precursor. Catalytic olefin hydrogenation using $(5\text{-}^{\text{NP}}\text{FP})\text{Rh}(\eta^2\text{-C}_2\text{H}_4)\text{Cl}$ and $(6\text{-}^{\text{NP}}\text{FP})\text{Rh}(\eta^2\text{-C}_2\text{H}_4)\text{Cl}$ was also studied; however, under conditions of catalysis, the complex $(5\text{-}^{\text{NP}}\text{FP})\text{Rh}(\eta^2\text{-C}_2\text{H}_4)\text{Cl}$ likely forms an active catalyst that is not ligated by the 5-^{NP}FP ligand, and thus

comparison of catalysis using $(5\text{-}^{\text{NP}}\text{FP})\text{Rh}(\eta^2\text{-C}_2\text{H}_4)\text{Cl}$ versus $(6\text{-}^{\text{NP}}\text{FP})\text{Rh}(\eta^2\text{-C}_2\text{H}_4)\text{Cl}$ was not possible.

Scheme 2.1.3 Trend of ligand impact on rate of catalytic olefin hydrogenation using capping arene ligated Rh complexes as catalyst precursors.

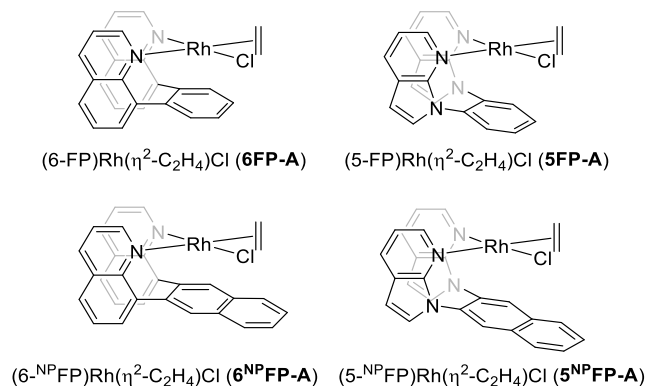


2.2 Comparison of olefin hydrogenation rate with various olefins catalyzed by capping arene rhodium complexes

We studied four capping arene Rh(I) complexes as catalyst precursors for olefin hydrogenation of the general formula (capping arene)Rh($\eta^2\text{-C}_2\text{H}_4$)Cl. The capping arene ligands that we studied include (6-FP)Rh($\eta^2\text{-C}_2\text{H}_4$)Cl (**6FP-A**), (6-^{NP}FP)Rh($\eta^2\text{-C}_2\text{H}_4$)Cl (**6^{NP}FP-A**), (5-FP)Rh($\eta^2\text{-C}_2\text{H}_4$)Cl (**5FP-A**) and (5-^{NP}FP)Rh($\eta^2\text{-C}_2\text{H}_4$)Cl (**5^{NP}FP-A**) (**Scheme 2.2.1**). Our previous studies indicated that the arene groups (benzene for FP, and naphthalene for ^{NP}FP) can coordinate to the Rh center in a dihapto fashion, and the quinolinyl or *N*-7-azaindolyl backbones can be used to tune the coordination of the arene based on the structure and position of the arene moiety.^{36, 39} Structures based on single-crystal X-ray diffraction data show that the distances from Rh center to the closest carbon(s) on the arene moiety are shorter in **6FP-A** than that in **5FP-A** (~2.6 Å vs. ~3.1 Å).³⁶ This structural difference could influence the relative stabilities of Rh(I) complexes, which often favors a square planar structure, versus Rh(III), which often favors an octahedral structure.

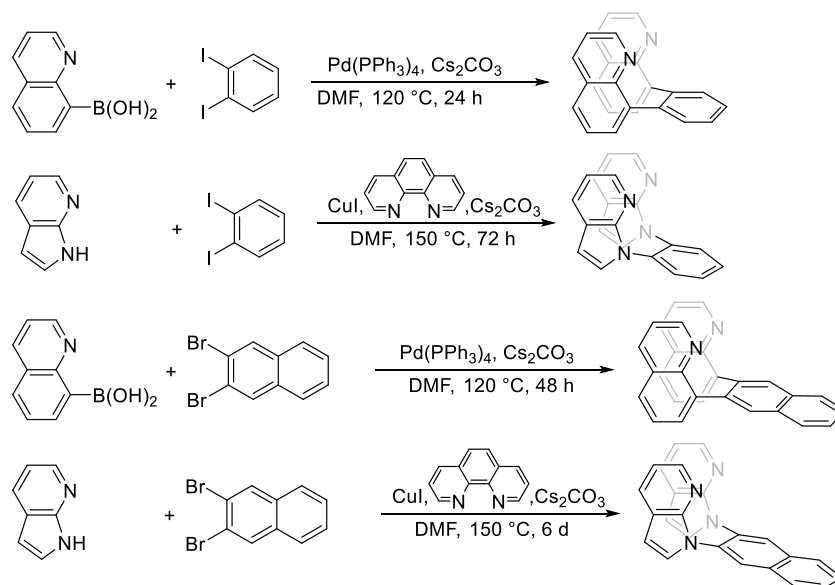
Thus, we anticipated that the relative rates of catalytic olefin hydrogenation would depend on the identity of the capping arene ligand.

Scheme 2.2.1 Examples of (capping arene)Rh(η^2 -C₂H₄)Cl complexes used in this study.

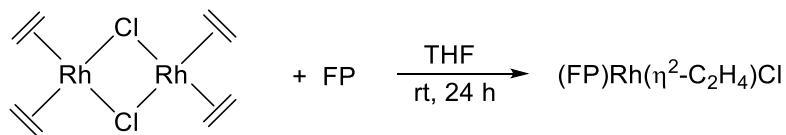


The preparation of capping arene ligands and the Rh complexes in this study followed previously reported methods.³⁶ The 6-FP and 6-NPFP ligands are synthesized by Suzuki coupling reactions, and the 5-FP and 5-NPFP ligands are synthesized by an Ullmann Reaction (**Scheme 2.2.2**). The capping arene-Rh complexes are prepared by mixing the corresponding ligands with [Rh(η^2 -C₂H₄)Cl]₂ (**Scheme 2.2.3**).

Scheme 2.2.2 Synthetic routes for capping arene ligands used in this study.



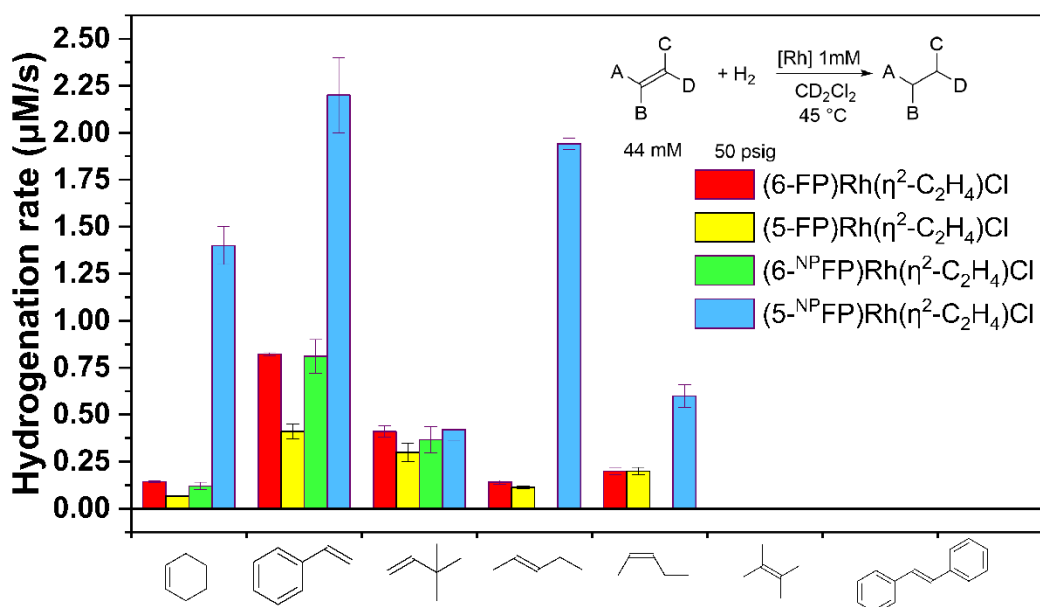
Scheme 2.2.3 General synthetic routes for capping arene ligated Rh complexes used in this study.



We compared Rh-catalyzed hydrogenation of various olefins (**Figure 2.2.1**) by monitoring catalysis *in situ* using ^1H NMR spectroscopy. In a representative experiment, a J. Young tube was charged with 0.4 mL of a 1 mM solution of Rh complex, 4 mM of hexamethylbenzene (HMB, internal standard), and 44 mM of olefin in CD_2Cl_2 followed by pressurizing with 50 psig of H_2 . The reaction tube was heated to 45 °C, and ^1H NMR spectra were collected at 0, 1, 2 and 4 hours. The ^1H NMR spectra for the **6^{NP}FP-A** catalyzed olefin hydrogenation reactions were recorded at 0, 20, 40 and 60 minutes of the reaction, considered to be initial rates, due to the decomposition of catalyst (see below for more details). The concentration of the hydrogenated product was determined by the integration ratio of the product versus HMB. The reaction rate was determined by monitoring the change in concentration of the hydrogenated product versus time. A sample stacked ^1H NMR spectra for the catalytic hydrogenation of cyclohexene with **6FP-A** is provided to demonstrate more details (**Figure 2.2.2**). The concentration of olefin, dihydrogen and the hydrogenated product were determined by the integration with respect to the internal standard HMB. For the hydrogenation of cyclohexene, styrene, *trans*-2-pentene and *cis*-2-pentene (**Figure 2.2.1**), the reaction rate data show that the rate of hydrogenation using both **6FP-A** and **6^{NP}FP-A** are faster than **5FP-A**. The catalyst precursor **5^{NP}FP-A** gives the most rapid catalysis, but we have evidence that **5^{NP}FP-A** converts to a catalyst that is not ligated by the 5-^{NP}FP ligand (see below for more details).

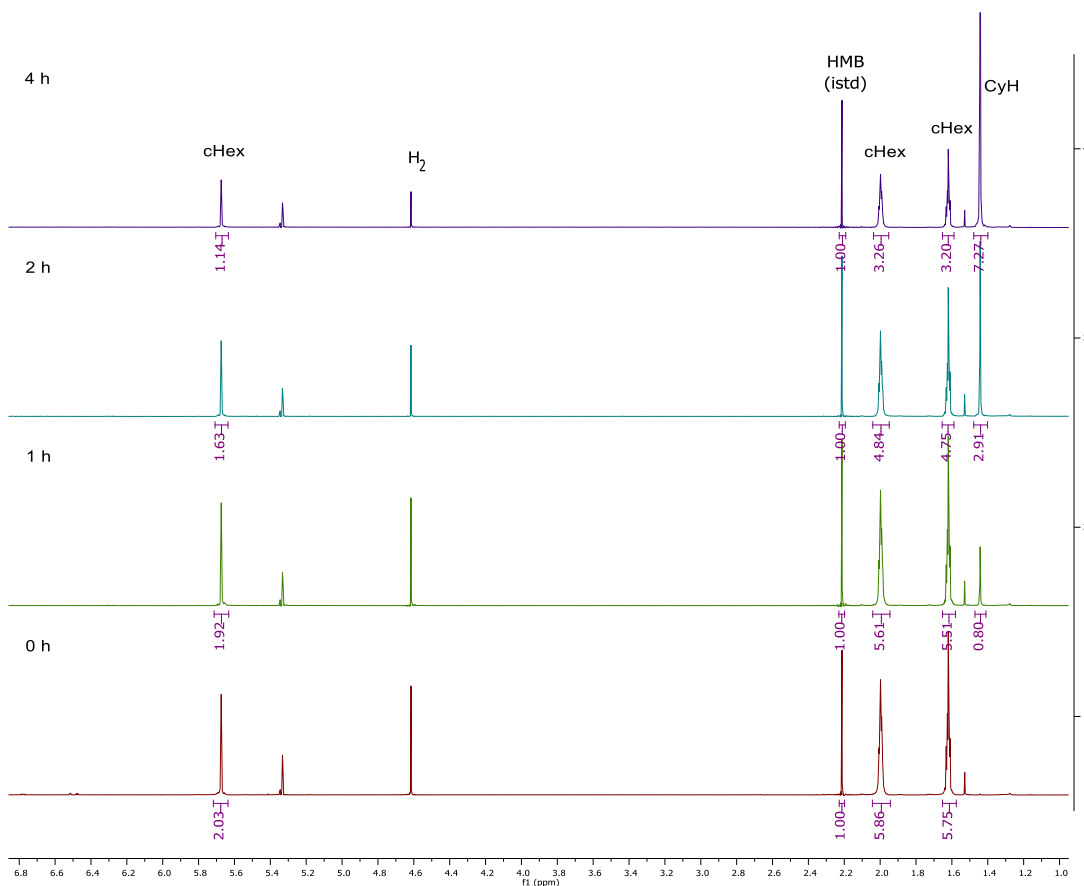
In comparison, the rates for hydrogenation of 3,3-dimethyl-1-butene with the three catalysts do not show a statistically significant difference. The hydrogenation of tri-substituted and tetra-substituted olefins 2-methyl-2-butene and 2,3-dimethyl-butene does not occur with any of the Rh catalysts. Also, the hydrogenation of *trans*-stilbene was not observed.

Figure 2.2.1 Comparison of olefin hydrogenation catalyzed by four capping arene Rh complexes.



The bars show rate data from at least three independent experiments with standard deviations shown as error bars. Standard deviations were determined by the standard error of the slope for the linear regression (**Figure 2.2.5 – Figure 2.2.22**). * The complex **6^{NPFP}A** is not stable during the reaction. Thus, the rate was determined using data collected at 0, 20, 40 and 60 minutes. ** The isomerization of *cis*-2-pentene to *trans*-2-pentene and 1-pentene competes with the hydrogenation of *cis*-2-pentene. Thus, the rate of catalytic hydrogenation of *cis*-2-pentene could not be accurately quantified.

Figure 2.2.2 A sample of catalytic hydrogenation of cyclohexene with "capping arene" ligated Rh catalyst.

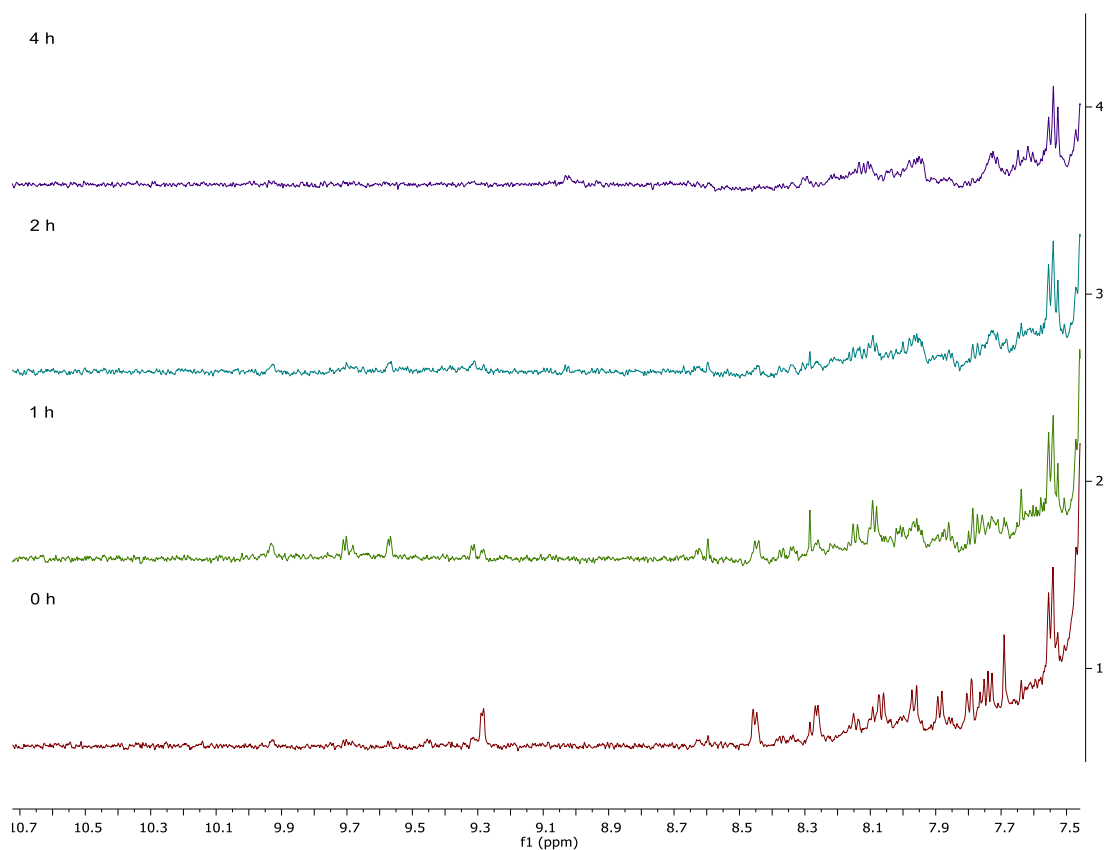


The assignments of the important peaks are labeled on the top of each peak with abbreviations (cHex = cyclohexene, HMB = hexamethylbenzene, CyH = cyclohexane, H₂ = dihydrogen). The reaction is performed with 1mM (5-^{NP}FP)Rh(η²-C₂H₄)Cl (**5^{NP}FP-A**), 44 mM cyclohexene, 50 psig H₂ at 45 °C in CD₂Cl₂. The peaks are integrated against the hexamethylbenzene (internal standard). The reaction time for each spectrum is noted on top left of the corresponding spectrum.

The decomposition of **6^{NP}FP-A** was observed by ¹H NMR spectroscopy during catalytic styrene hydrogenation. As the reaction progressed, the coordinated ligand peaks for **6^{NP}FP-A** decreased and new peaks appeared (**Figure 2.2.3**). The rate of the olefin hydrogenation exhibits a significant decrease as the catalyst is deactivated (**Figure 2.2.15** – **Figure 2.2.17**). In comparison, the decomposition of **6^{NP}FP-A** during the first hour of the catalytic reaction (**Figure 2.2.4**) was not as significant as the decomposition for more prolonged reaction times shown in **Figure 2.2.3**. As a result, the ¹H NMR spectra for

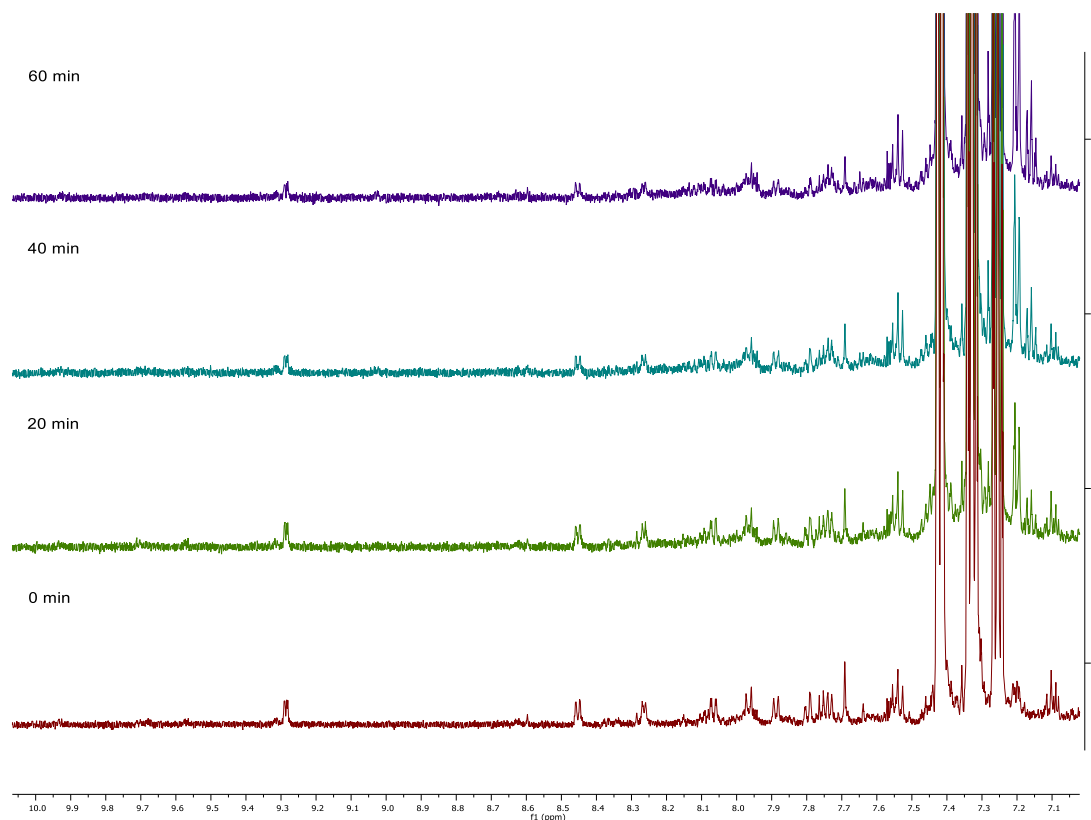
6^{NP}FP-A catalyzed olefin hydrogenations were acquired at 0, 20, 40 and 60 minutes of each reaction.

Figure 2.2.3 Sample ¹H NMR spectra showing the observed decomposition of (6-^{NP}FP)Rh(η²-C₂H₄)Cl (**6^{NP}FP-A**) during catalytic of styrene hydrogenation.



The reaction was conducted with 1 mM of **6^{NP}FP-A**, 44 mM styrene, 50 psig H₂ at 45 °C in CD₂Cl₂. The reaction time is indicated on the top left of each spectrum.

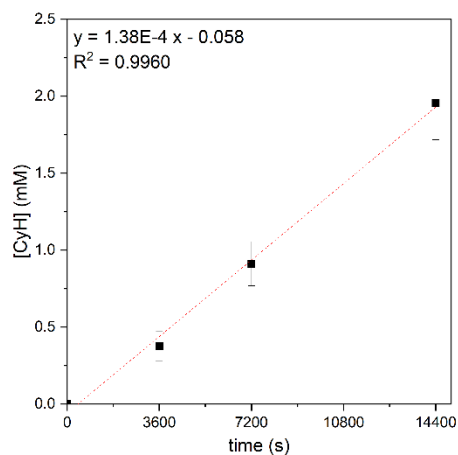
Figure 2.2.4 Sample ^1H NMR spectra for the observation of $(6\text{-}^{15}\text{NFP})\text{Rh}(\eta^2\text{-C}_2\text{H}_4)\text{Cl}$ ($6\text{-}^{15}\text{NFP-A}$) with minimal decomposition at shorter time points during the catalysis of styrene hydrogenation for comparison with **Figure 2.2.3**.



The reaction was conducted with 1mM $6\text{-}^{15}\text{NFP-A}$, 44 mM styrene, 50 psig H_2 at 45 °C in CD_2Cl_2 . The reaction time is indicated on the top left of each spectrum.

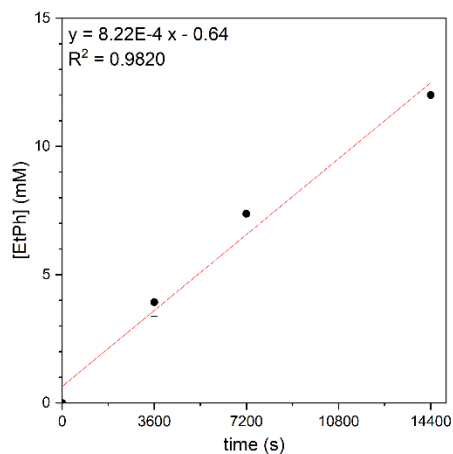
The results for catalytic olefin hydrogenation using $(6\text{-FP})\text{Rh}(\eta^2\text{-C}_2\text{H}_4)\text{Cl}$ (6FP-A) (**Figure 2.2.5 – Figure 2.2.9**), $(5\text{-FP})\text{Rh}(\eta^2\text{-C}_2\text{H}_4)\text{Cl}$ (5FP-A) (**Figure 2.2.10 – Figure 2.2.14**), $(6\text{-}^{15}\text{NFP})\text{Rh}(\eta^2\text{-C}_2\text{H}_4)\text{Cl}$ ($6\text{-}^{15}\text{NFP-A}$) (**Figure 2.2.15 – Figure 2.2.17**) and $(5\text{-}^{15}\text{NFP})\text{Rh}(\eta^2\text{-C}_2\text{H}_4)\text{Cl}$ ($5\text{-}^{15}\text{NFP-A}$) (**Figure 2.2.18 – Figure 2.2.22**) are plotted by the concentration of hydrogenation product (mM) versus time (s). In some of the plots below, the concentration of product at 0 second of the reaction is not zero. The reason for the non-zero initial concentration is because our $t = 0$ includes time to acquire the first ^1H NMR spectrum.

Figure 2.2.5 Plot of [cyclohexane] (mM) vs. time (s) for (6-FP)Rh(η^2 -C₂H₄)Cl (**6FP-A**) catalyzed cyclohexene hydrogenation.



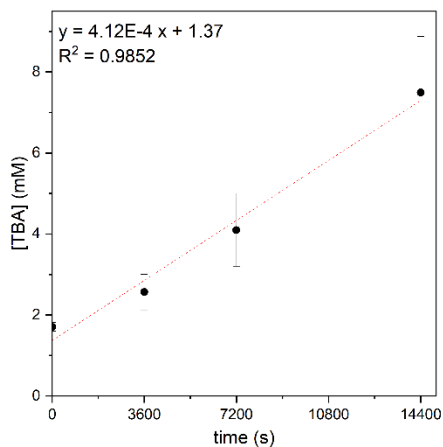
The reaction was performed in triplicate with 1 mM **6FP-A**, 44 mM cyclohexene, 50 psig H₂, 45 °C. CyH = cyclohexane in CD₂Cl₂. The error bars represent the standard deviations of the concentration of CyH among the three trials.

Figure 2.2.6 Plot of [ethylbenzene] (mM) vs. time (s) for (6-FP)Rh(η^2 -C₂H₄)Cl (**6FP-A**) catalyzed styrene hydrogenation.



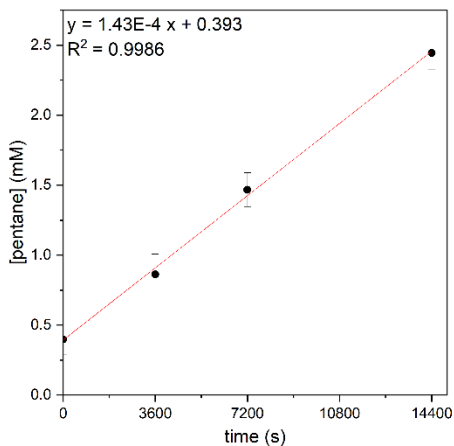
The reaction was performed in triplicate with 1 mM **6FP-A**, 44 mM styrene, 50 psig H₂, 45 °C. EtPh = ethylbenzene. in CD₂Cl₂. The error bars represent the standard deviations of the concentration of EtPh among the three trials.

Figure 2.2.7 Plot of [2,2-dimethylbutane] (mM) vs. time (s) for (6-FP)Rh(η^2 -C₂H₄)Cl (**6FP-A**) catalyzed 3,3-dimethylbutene hydrogenation.



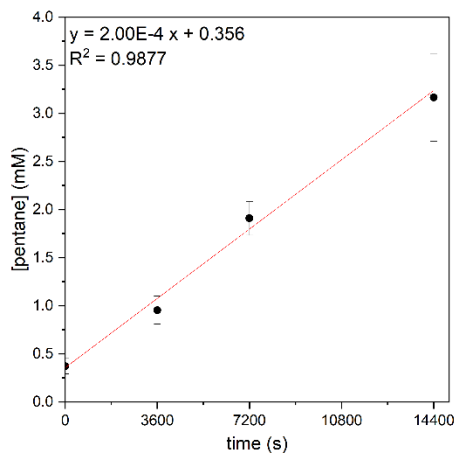
The reaction was performed in triplicate with 1 mM **6FP-A**, 44 mM 3,3-dimethylbutene, 50 psig H₂, 45 °C. TBA = *tert*-butyl ethane = 2,2-dimethylbutane in CD₂Cl₂. The error bars represent the standard deviations of the concentration of TBA among the three trials.

Figure 2.2.8 Plot of [pentane] (mM) vs. time (s) for (6-FP)Rh(η^2 -C₂H₄)Cl (**6FP-A**) catalyzed *trans*-2-pentene hydrogenation.



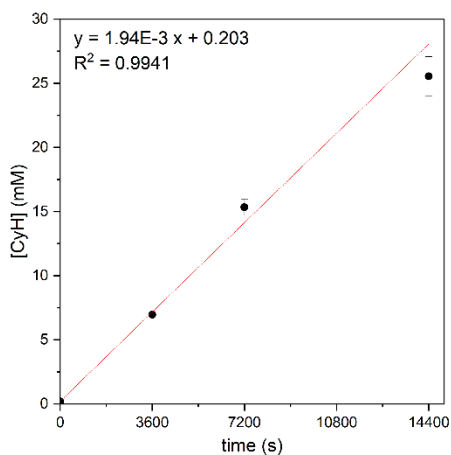
The reaction was performed in triplicate with 1 mM **6FP-A**, 44 mM *trans*-2-pentene, 50 psig H₂, 45 °C in CD₂Cl₂. The error bars represent the standard deviations of the concentration of pentane among the three trials.

Figure 2.2.9 Plot of [pentane] (mM) vs. time (s) for (6-FP)Rh(η^2 -C₂H₄)Cl (**6FP-A**) catalyzed *cis*-2-pentene hydrogenation.



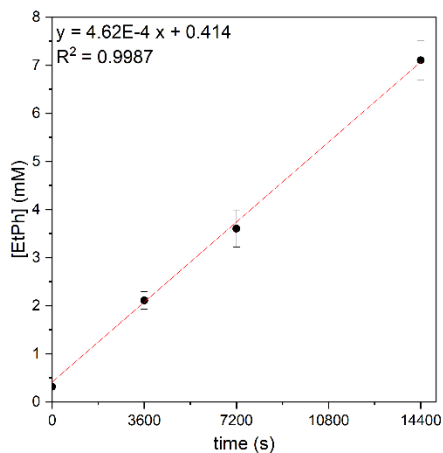
The reaction was performed in triplicate with 1 mM **6FP-A**, 44 mM *cis*-2-pentene, 50 psig H₂, 45 °C in CD₂Cl₂. The error bars represent the standard deviations of the concentration of pentane among the three trials.

Figure 2.2.10 Plot of [cyclohexane] (mM) vs. time (s) for (5-FP)Rh(η^2 -C₂H₄)Cl (**5FP-A**) catalyzed cyclohexene hydrogenation.



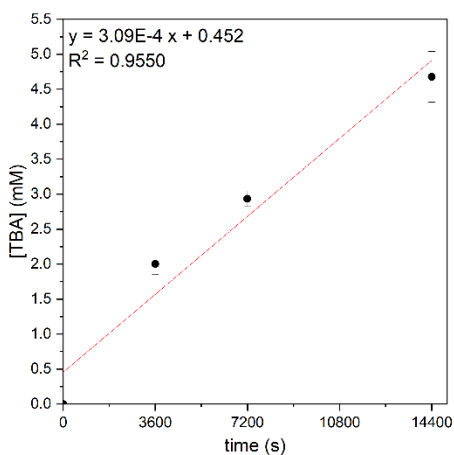
The reaction was performed in triplicate with 1 mM **5FP-A**, 44 mM cyclohexene, 50 psig H₂, 45 °C. CyH = cyclohexane in CD₂Cl₂. The error bars represent the standard deviations of the concentration of CyH among the three trials.

Figure 2.2.11 Plot of [ethylbenzene] (mM) vs. time (s) for (5-FP)Rh(η^2 -C₂H₄)Cl (**5FP-A**) catalyzed styrene hydrogenation.



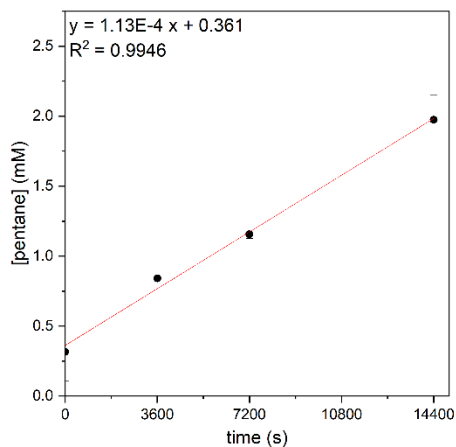
The reaction was performed in triplicate with 1 mM **5FP-A**, 44 mM styrene, 50 psig H₂, 45 °C. EtPh = ethylbenzene in CD₂Cl₂. The error bars represent the standard deviations of the concentration of EtPh among the three trials.

Figure 2.2.12 Plot of [2,2-dimethylbutane] (mM) vs. time (s) for (5-FP)Rh(η^2 -C₂H₄)Cl (**5FP-A**) catalyzed 3,3-dimethylbutene hydrogenation.



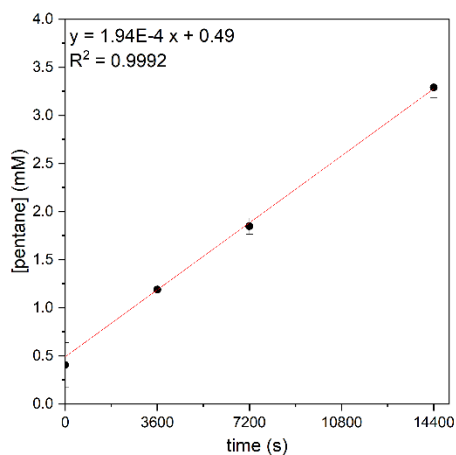
The reaction was performed in triplicate with 1 mM **5FP-A**, 44 mM 3,3-dimethylbutene, 50 psig H₂, 45 °C. TBA = *tert*-butylethane = 2,2-dimethylbutane in CD₂Cl₂. The error bars represent the standard deviations of the concentration of TBA among the three trials.

Figure 2.2.13 Plot of [pentane] (mM) vs. time (s) for (5-FP)Rh(η^2 -C₂H₄)Cl (**5FP-A**) catalyzed *trans*-2-pentene hydrogenation.



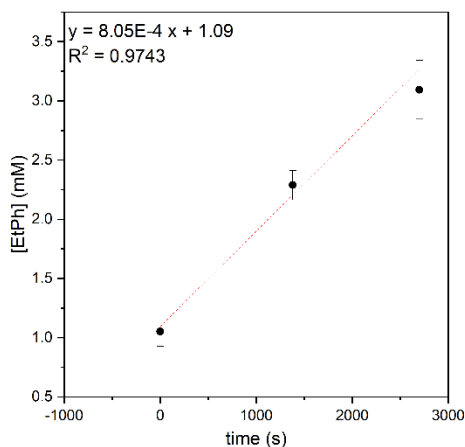
The reaction was performed in triplicate with 1 mM **5FP-A**, 44 mM *trans*-2-pentene, 50 psig H₂, 45 °C in CD₂Cl₂. The error bars represent the standard deviations of the concentration of pentane among the three trials.

Figure 2.2.14 Plot of [pentane] (mM) vs. time (s) for (5-FP)Rh(η^2 -C₂H₄)Cl (**5FP-A**) catalyzed *cis*-2-pentene hydrogenation.



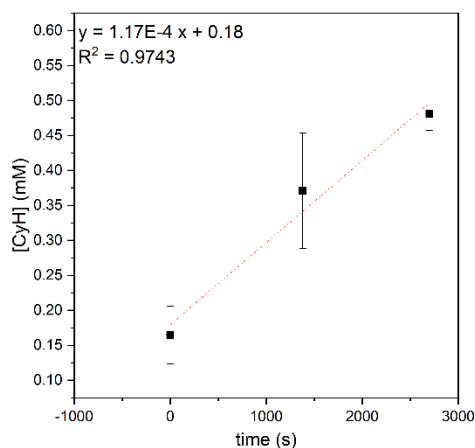
The reaction was performed in triplicate with 1 mM **5FP-A**, 44 mM *cis*-2-pentene, 50 psig H₂, 45 °C in CD₂Cl₂. The error bars represent the standard deviations of the concentration of pentane among the three trials.

Figure 2.2.15 Plot of [cyclohexane] (mM) vs. time (s) for (6-^{NP}FP)Rh(η^2 -C₂H₄)Cl (6^{NP}FP-A) catalyzed cyclohexene hydrogenation.



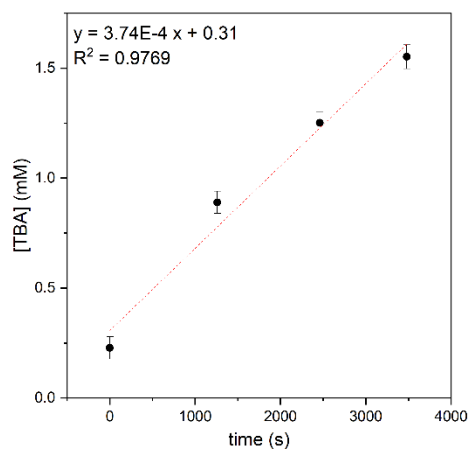
The reaction was performed in triplicate with 1 mM 6^{NP}FP-A, 44 mM cyclohexene, 50 psig H₂, 45 °C. CyH = cyclohexane in CD₂Cl₂. The error bars represent the standard deviations of the concentration of CyH among the three trials.

Figure 2.2.16 Plot of [ethylbenzene] (mM) vs. time (s) for (6-^{NP}FP)Rh(η^2 -C₂H₄)Cl (6^{NP}FP-A) catalyzed styrene hydrogenation.



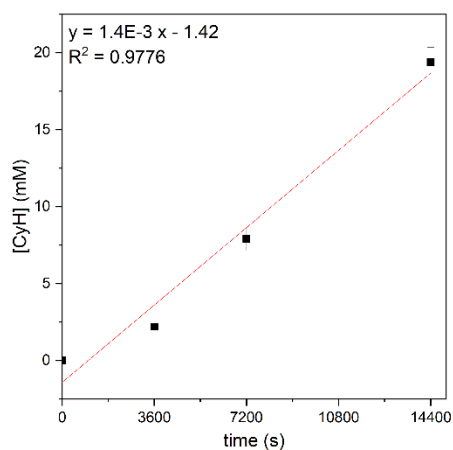
The reaction was performed in triplicate with 1 mM 6^{NP}FP-A, 44 mM styrene, 50 psig H₂, 45 °C. EtPh = ethylbenzene in CD₂Cl₂. The error bars represent the standard deviations of the concentration of EtPh among the three trials.

Figure 2.2.17 Plot of [2,2-dimethylbutane] (mM) vs. time (s) for (6-^{NP}FP)Rh(η^2 -C₂H₄)Cl (6^{NP}FP-A) catalyzed 3,3-dimethylbutene hydrogenation.



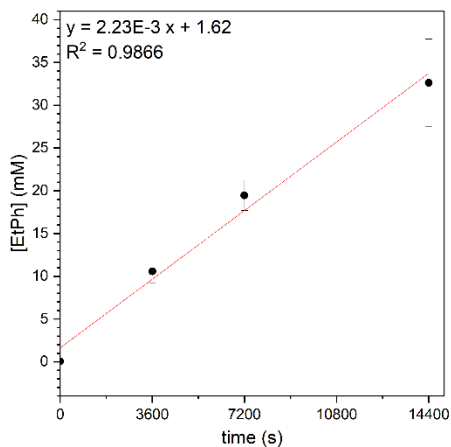
The reaction was performed in triplicate with 1 mM 6^{NP}FP-A, 44 mM 3,3-dimethylbutene, 50 psig H₂, 45 °C. TBA = *tert*-butylethane = 2,2-dimethylbutane in CD₂Cl₂. The error bars represent the standard deviations of the concentration of TBA among the three trials.

Figure 2.2.18 Plot of [cyclohexane] (mM) vs. time (s) for (5-^{NP}FP)Rh(η^2 -C₂H₄)Cl (5^{NP}FP-A) catalyzed cyclohexene hydrogenation.



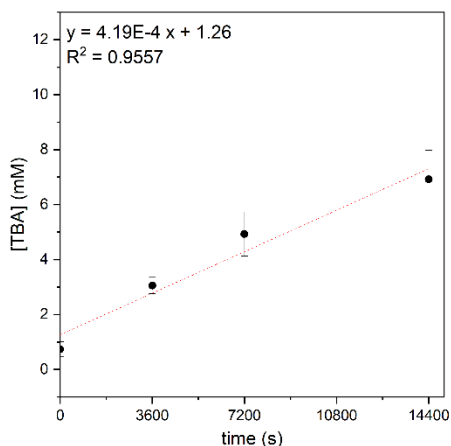
The reaction was performed in triplicate with 1 mM 5^{NP}FP-A, 44 mM cyclohexene, 50 psig H₂, 45 °C. CyH = cyclohexane in CD₂Cl₂. The error bars represent the standard deviations of the concentration of CyH among the three trials.

Figure 2.2.19 Plot of [ethylbenzene] (mM) vs. time (s) for $(5\text{-}^{\text{NP}}\text{FP})\text{Rh}(\eta^2\text{-C}_2\text{H}_4)\text{Cl}$ (5^{NP}FP-A) catalyzed styrene hydrogenation.



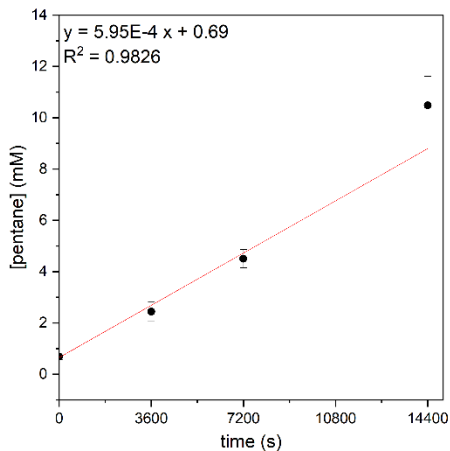
The reaction was performed in triplicate with 1 mM 5^{NP}FP-A , 44 mM styrene, 50 psig H_2 , 45 °C. EtPh = ethylbenzene in CD_2Cl_2 . The error bars represent the standard deviations of the concentration of pentane among the three trials.

Figure 2.2.20 Plot of [2,2-dimethylbutane] (mM) vs. time (s) for $(5\text{-}^{\text{NP}}\text{FP})\text{Rh}(\eta^2\text{-C}_2\text{H}_4)\text{Cl}$ (5^{NP}FP-A) catalyzed 3,3-dimethylbutene hydrogenation.



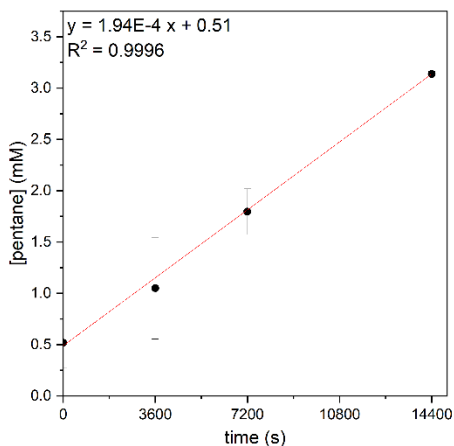
The reaction was performed in triplicate with 1 mM 5^{NP}FP-A , 44 mM 3,3-dimethylbutene, 50 psig H_2 , 45 °C. TBA = *tert*-butylethane = 2,2-dimethylbutane in CD_2Cl_2 . The error bars represent the standard deviations of the concentration of TBA among the three trials.

Figure 2.2.21 Plot of [pentane] (mM) vs. time (s) for $(5\text{-}^{\text{NP}}\text{FP})\text{Rh}(\eta^2\text{-C}_2\text{H}_4)\text{Cl}$ (5^{NP}FP-A) catalyzed *trans*-2-pentene hydrogenation.



The reaction was performed in triplicate with 1 mM 5^{NP}FP-A , 44 mM *trans*-2-pentene, 50 psig H_2 , 45 °C in CD_2Cl_2 . The error bars represent the standard deviations of the concentration of pentane among the three trials.

Figure 2.2.22 Plot of [pentane] (mM) vs. time (s) for $(5\text{-}^{\text{NP}}\text{FP})\text{Rh}(\eta^2\text{-C}_2\text{H}_4)\text{Cl}$ (5^{NP}FP-A) catalyzed *cis*-2-pentene hydrogenation.

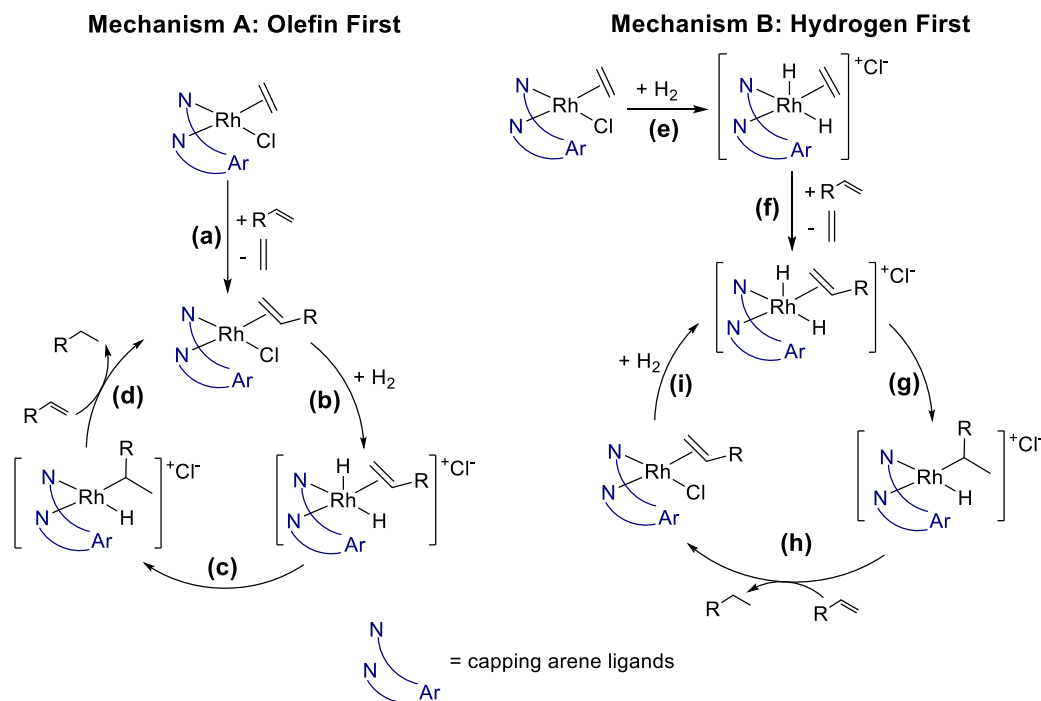


The reaction was performed in triplicate with 1 mM 5^{NP}FP-A , 44 mM *cis*-2-pentene, 50 psig H_2 , 45 °C in CD_2Cl_2 . The error bars represent the standard deviations of the concentration of pentane among the three trials.

2.3 Mechanistic studies

2.3.1 Overview of possible catalytic mechanism

To understand the trend of the ligand effect shown in **Figure 2.2.1**, a series of mechanistic studies was performed. **Scheme 2.3.1** shows two mechanisms for catalytic olefin hydrogenation using $(FP)Rh(\eta^2-C_2H_4)Cl$ based on the general mechanisms of Rh catalyzed olefin hydrogenation shown in **Scheme 2.1.2**.^{6, 17, 43, 51} The proposed mechanism on the left (**Scheme 2.3.1A**) is the “olefin first” mechanism. In this mechanism, the precursor $(FP)Rh^I(\eta^2-C_2H_4)Cl$ first undergoes olefin exchange to form $(FP)Rh^I(\eta^2-olefin)Cl$ (Step **a**). Then, oxidative addition of H_2 takes place to generate the cationic Rh(III) complex $[(FP)Rh^{III}(H)_2(\eta^2-olefin)]^+$ with an outer sphere chloride anion (Step **b**). After that, olefin migratory insertion leads to the formation of $[(FP)Rh^{III}(H)(\kappa^1-hydrocarbyl)]Cl$ (Step **c**). Finally, the hydrogenated product is released by reductive elimination, and the Rh complex coordinates another equivalent of olefin to form $(FP)Rh^I(\eta^2-olefin)Cl$ (Step **d**). The proposed mechanism on the right (**Scheme 2.3.1B**) is the “hydrogen first” mechanism. In this mechanism, $(FP)Rh^I(\eta^2-C_2H_4)Cl$ reacts with H_2 first to give the oxidative addition product (Step **e**), followed by olefin exchange to form $[(FP)Rh^{III}(H)_2(\eta^2-olefin)]Cl$ (Step **f**). The catalytic cycle starting with $[(FP)Rh^{III}(H)_2(\eta^2-olefin)]Cl$ is similar to the cycle in **Scheme 2.3.1A**, which undergoes an olefin migratory insertion (Step **g**), reductive elimination and olefin coordination (Step **h**), and H_2 oxidative addition (Step **i**).

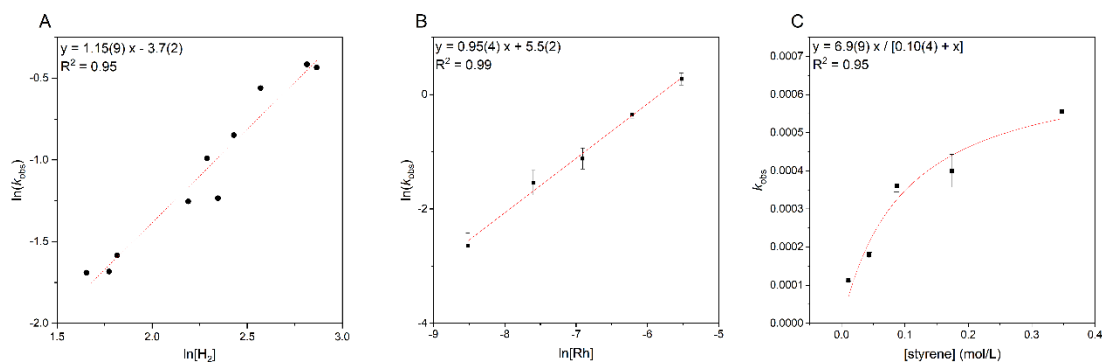
Scheme 2.3.1 Two proposed mechanisms for FP-Rh catalyzed olefin hydrogenation.

2.3.2 Kinetic studies of **6FP-A** catalyzed styrene hydrogenation

To further understand the mechanism of the FP-Rh catalyzed olefin hydrogenation, we studied the dependence of reaction rate on dihydrogen pressure using **6FP-A** and styrene using the method of initial rates. The initial concentration of dihydrogen in solution phase was determined by the integration of the resonance due to dissolved H_2 compared to the internal standard HMB. A plot of $\ln(k_{\text{obs}})$ versus $\ln[\text{H}_2]$ (**Figure 2.3.1A**) shows a slope close to 1, indicating the reaction likely has a first order dependence on dihydrogen concentration. Next, we studied dependence of reaction rate on **6FP-A** concentration. The plot of $\ln(k_{\text{obs}})$ versus $\ln[\text{6FP-A}]$ (**Figure 2.3.1B**) shows a slope of 0.95(5), indicating a likely first order dependence on the concentration of **6FP-A**. Then, the dependence of reaction rate on styrene concentration was studied. A plot of $1/k_{\text{obs}}$ versus $1/[\text{styrene}]$ shows a linear

relationship, indicating a Michaelis–Menten relationship (**Figure 2.3.1C**). One possible explanation for the Michaelis–Menten relationship based on concentration of styrene is a reversible exchange of ethylene between **6FP-A** and styrene prior to the H₂ oxidative addition.⁵² When the styrene hydrogenation is performed with a substantial excess of styrene, which is calculated to be 0.33(9) mol/L for the experimental condition (see below for more details), the styrene exchange becomes the fast step, which would lead to a zero-order rate law in styrene.⁵² Based on these studies, a rate equation for the **6FP-A** catalyzed styrene hydrogenation is shown in **Eq. 2-1**. When styrene concentration is significant ($\geq 1.0(4)$ M for the studied reaction conditions), the rate equation can be expressed by **Eq. 2-2**.

Figure 2.3.1 Studies of reaction order for hydrogenation of styrene using (6-FP)Rh(Cl)(η^2 -C₂H₄) (**6FP-A**).



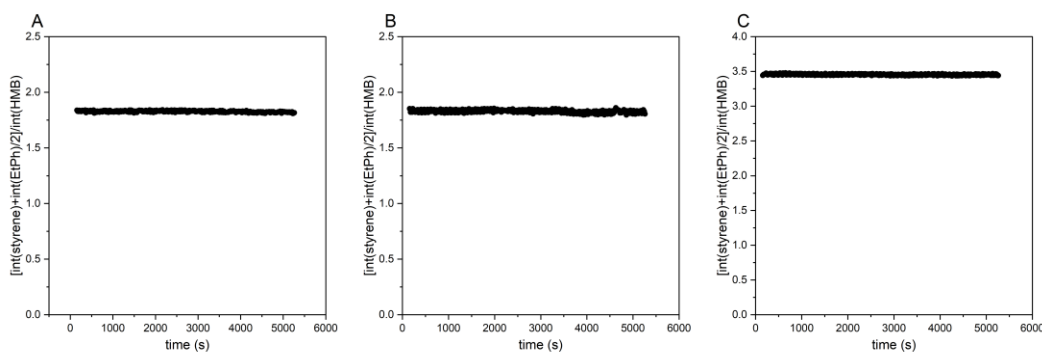
The reaction conditions are: For the determination of order in H₂ (A): 1 mM **6FP-A**, 44 mM styrene, variable psig of H₂ (20, 30, 40 or 50 psig) in CD₂Cl₂, 45 °C. For the determination of order in **6FP-A** (B): variable mM **6FP-A** (0.2, 0.5, 1, 2 or 4 mM), 44 mM styrene, 50 psig H₂ in CD₂Cl₂, 45 °C. For the determination of order in styrene (C): 0.5 mM **6FP-A**, variable mM styrene (11, 44, 87, 174 or 348 mM), 50 psig H₂ in CD₂Cl₂, 45 °C. The standard deviations for (B) and (C) were determined from the standard deviation of three trials with the same condition (see **Figure 2.3.8** – **Figure 2.3.17**).

$$\text{rate} = k[\mathbf{6FP-A}][\text{H}_2][\text{styrene}] \quad \text{Eq. 2-1}$$

$$\text{rate} = k'[\mathbf{6FP-A}][\text{H}_2] \quad \text{Eq. 2-2}$$

The initial rate method was used to determine the dependence on concentration of H_2 , $\mathbf{6FP-A}$ and styrene for $\mathbf{6FP-A}$ catalyzed styrene hydrogenation. Due to the low concentration, the peaks for ethylbenzene (EtPh) would have a relatively lower S/N ratio. Thus, an alternative quantification method was used. Instead of determining the concentration of ethylbenzene from the integration of ethylbenzene relative to hexamethylbenzene (HMB, internal standard), the decrease in concentration of styrene was quantified. In the absence of by-product formation, based on the principle of mass conservation, the sum of [styrene] and [EtPh] at any points of the reaction should be constant which equals [styrene]₀ (Eq. 2-1). During this catalytic styrene hydrogenation reaction, the sum of integration for styrene and EtPh is constant (Figure 2.3.2). Hence, the rate of styrene consumption is determined, which should equal to the rate of EtPh formation (Eq. 2-2).

Figure 2.3.2 Scatter plots for $[\text{styrene}] + [\text{EtPh}]/2 / [\text{HMB}]$ vs. time (s) for (6-FP)Rh($\eta^2\text{-C}_2\text{H}_4$)Cl ($\mathbf{6FP-A}$) catalyzed styrene hydrogenation.

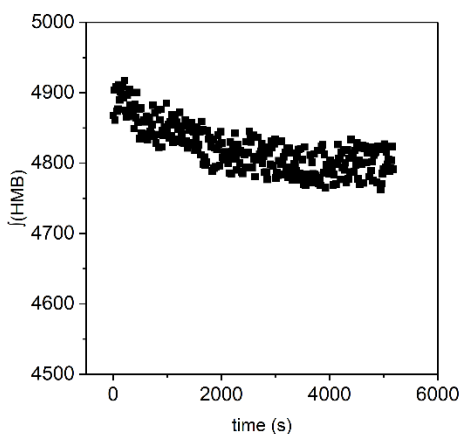


The data are selected from (A): kinetic studies for the order on [Rh], the reaction condition were 1 mM $\mathbf{6FP-A}$, 44 mM styrene, 50 psig H_2 in CD_2Cl_2 , 45 °C; (B): kinetic studies for the order on $[\text{H}_2]$,

the reaction conditions were 1 mM **6FP-A**, 44 mM styrene, 50 psig H₂ in CD₂Cl₂, 45 °C; (C): kinetic studies for the order on [styrene], the reaction conditions were 0.5 mM **6FP-A**, 44 mM styrene, 50 psig H₂ in CD₂Cl₂, 45 °C.

In some of the kinetic plots below (**Figure 2.3.4 – Figure 2.3.17**), the slopes shows a decrease during the starting *c.a.* 500–1000 seconds. The changed slopes potentially can be attributed to the instrumental error caused by a disturbed shimming during the prolonged experiment, which causes a slight decrease in the integration of the HMB peak (**Figure 2.3.3**). Although such decrements on the HMB peak integration are trivial (*c.a.* 5%), it is enough to cause changes in slope. The detailed plots for kinetics studies in **Figure 2.3.1** are illustrated (**Figure 2.3.4 – Figure 2.3.17**):

Figure 2.3.3 ∫HMB vs. time (s) plot for (6-FP)Rh(η²-C₂H₄)Cl (**6FP-A**) catalyzed styrene hydrogenation.



The reaction was performed in triplicate with 4 mM **6FP-A**, 44 mM styrene, 50 psig H₂ in CD₂Cl₂, 45 °C.

Figure 2.3.4 Plots of [styrene] (mM) vs. time (s) for (6-FP)Rh(η^2 -C₂H₄)Cl (**6FP-A**) catalyzed styrene hydrogenation with 1 mM **6FP-A**, 44 mM styrene, 20 psig H₂ in CD₂Cl₂, 45 °C in triplicate.

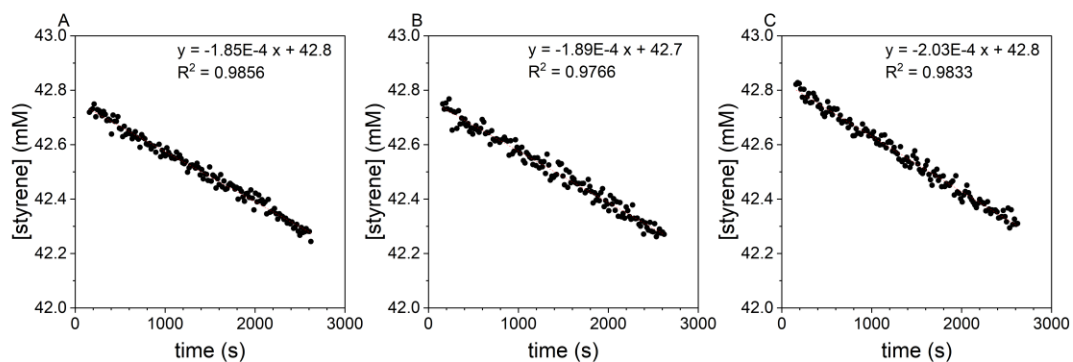


Figure 2.3.5 Plots of [styrene] (mM) vs. time (s) for (6-FP)Rh(η^2 -C₂H₄)Cl (**6FP-A**) catalyzed styrene hydrogenation with 1 mM **6FP-A**, 44 mM styrene, 30 psig H₂ in CD₂Cl₂, 45 °C in triplicate.

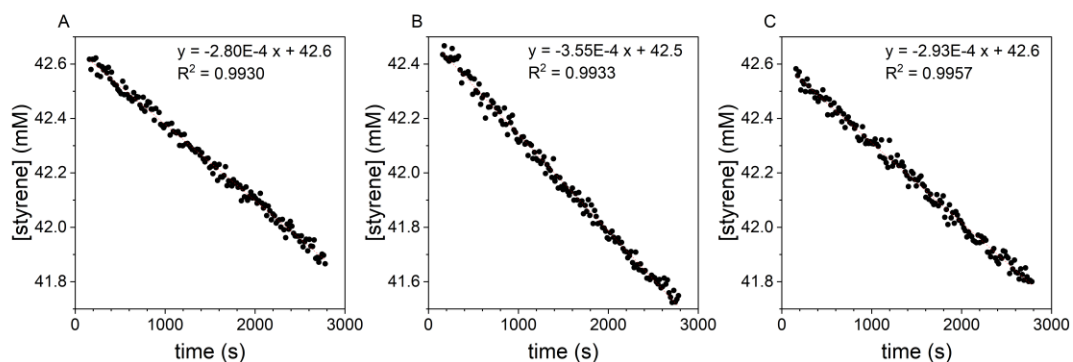


Figure 2.3.6 Plots of [styrene] (mM) vs. time (s) for (6-FP)Rh(η^2 -C₂H₄)Cl (**6FP-A**) catalyzed styrene hydrogenation 1 mM **6FP-A**, 44 mM styrene, 40 psig H₂ in CD₂Cl₂, 45 °C in triplicate.

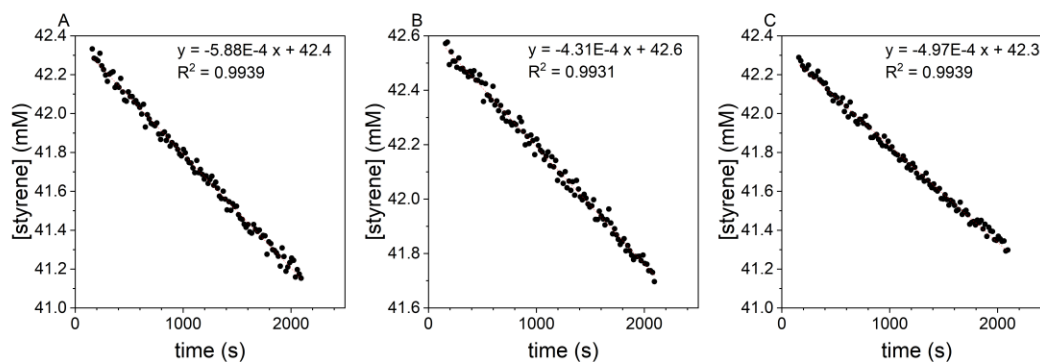


Figure 2.3.7 Plots of [styrene] (mM) vs. time (s) for (6-FP)Rh(η^2 -C₂H₄)Cl (**6FP-A**) catalyzed styrene hydrogenation 1 mM **6FP-A**, 44 mM styrene, 50 psig H₂ in CD₂Cl₂, 45 °C in triplicate.

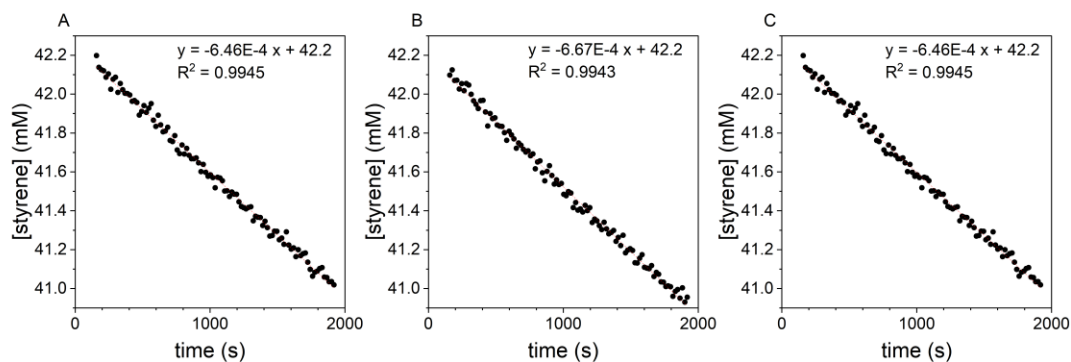


Figure 2.3.8 Plots of [styrene] (mM) vs. time (s) for (6-FP)Rh(η^2 -C₂H₄)Cl (**6FP-A**) catalyzed styrene hydrogenation with 4 mM **6FP-A**, 44 mM styrene, 50 psig H₂ in CD₂Cl₂, 45 °C in triplicate.

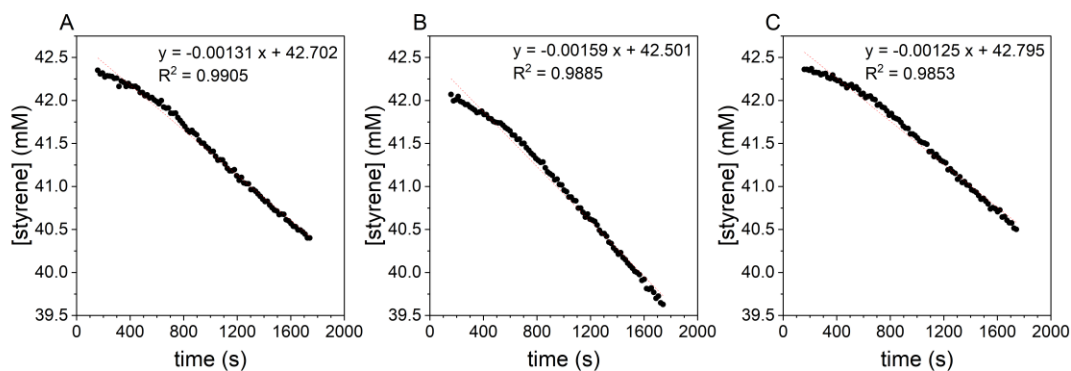


Figure 2.3.9 Plots of [styrene] (mM) vs. time (s) for (6-FP)Rh(η^2 -C₂H₄)Cl (**6FP-A**) catalyzed styrene hydrogenation with 2 mM **6FP-A**, 44 mM styrene, 50 psig H₂ in CD₂Cl₂, 45 °C in triplicate.

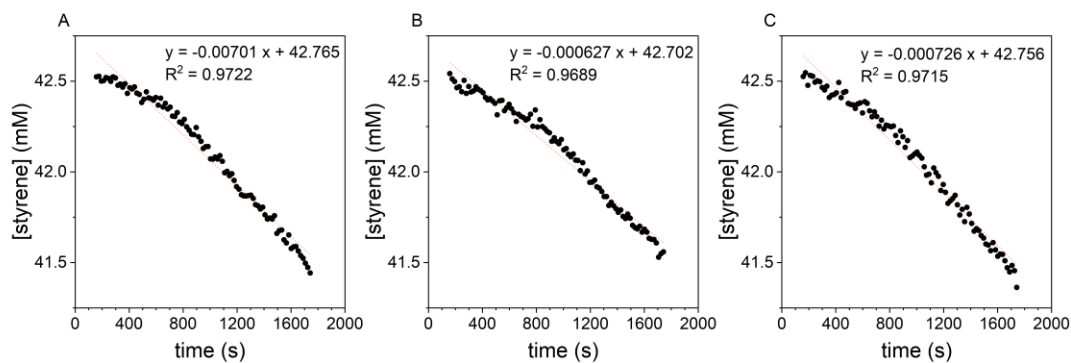


Figure 2.3.10 Plots of [styrene] (mM) vs. time (s) for (6-FP)Rh(η^2 -C₂H₄)Cl (**6FP-A**) catalyzed styrene hydrogenation with 1 mM **6FP-A**, 44 mM styrene, 50 psig H₂ in CD₂Cl₂, 45 °C in triplicate.

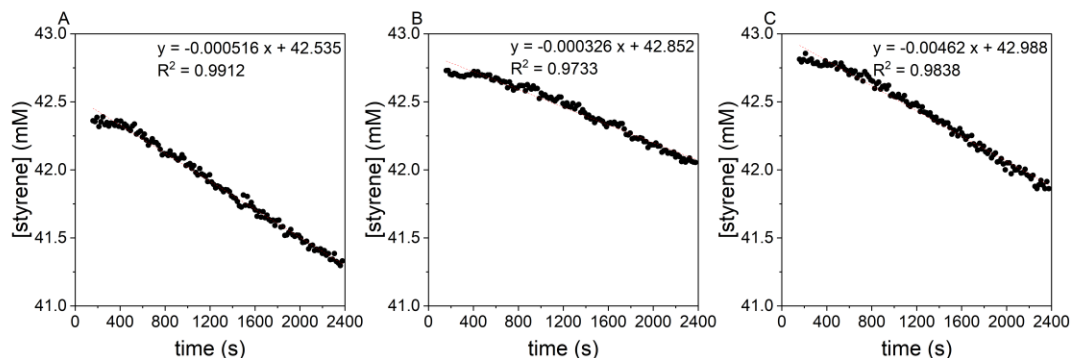


Figure 2.3.11 Plots of [styrene] (mM) vs. time (s) for (6-FP)Rh(η^2 -C₂H₄)Cl (**6FP-A**) catalyzed styrene hydrogenation with 0.5 mM **6FP-A**, 44 mM styrene, 50 psig H₂ in CD₂Cl₂, 45 °C in triplicate.

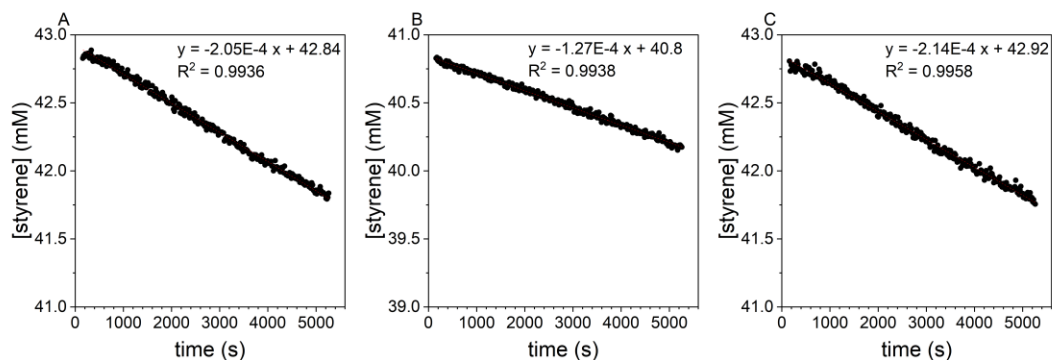


Figure 2.3.12 Plots of [styrene] (mM) vs. time (s) for (6-FP)Rh(η^2 -C₂H₄)Cl (**6FP-A**) catalyzed styrene hydrogenation with 0.25 mM **6FP-A**, 44 mM styrene, 50 psig H₂ in CD₂Cl₂, 45 °C in triplicate.

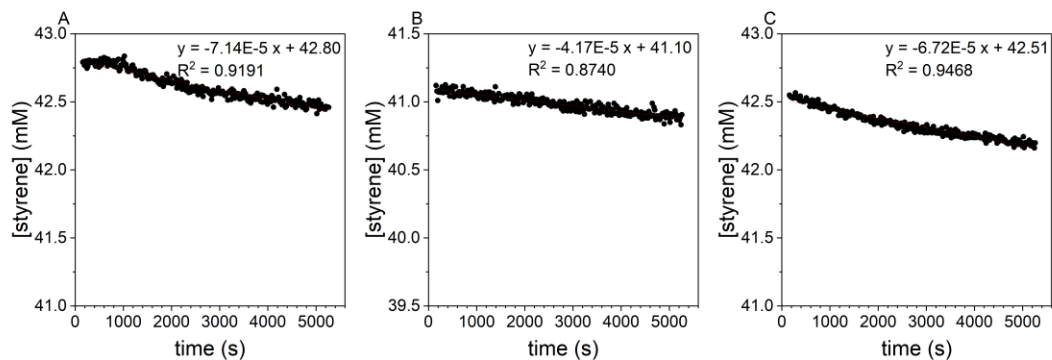


Figure 2.3.13 Plots of [styrene] (mM) vs. time (s) for (6-FP)Rh(η^2 -C₂H₄)Cl (**6FP-A**) catalyzed styrene hydrogenation with 0.5 mM **6FP-A**, 11 mM styrene, 50 psig H₂ in CD₂Cl₂, 45 °C in triplicate.

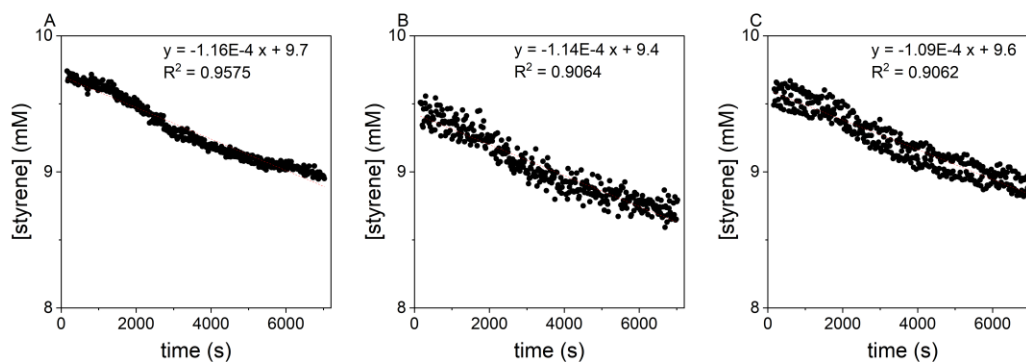


Figure 2.3.14 Plots of [styrene] (mM) vs. time (s) for (6-FP)Rh(η^2 -C₂H₄)Cl (**6FP-A**) catalyzed styrene hydrogenation with 0.5 mM **6FP-A**, 44 mM styrene, 50 psig H₂ in CD₂Cl₂, 45 °C in triplicate.

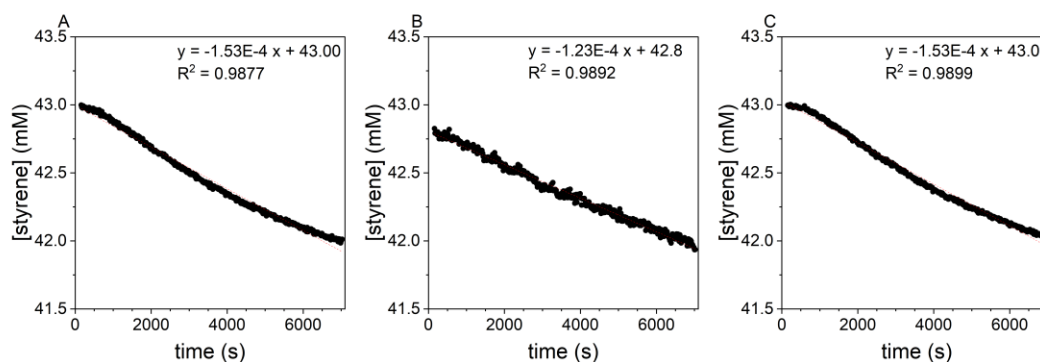


Figure 2.3.15 Plots of [styrene] (mM) vs. time (s) for (6-FP)Rh(η^2 -C₂H₄)Cl (**6FP-A**) catalyzed styrene hydrogenation with 0.5 mM **6FP-A**, 87 mM styrene, 50 psig H₂ in CD₂Cl₂, 45 °C in triplicate.

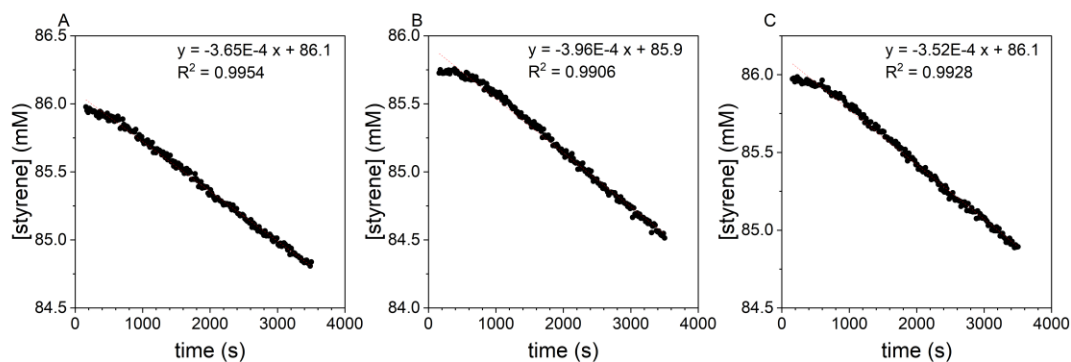


Figure 2.3.16 Plots of [styrene] (mM) vs. time (s) for (6-FP)Rh(η^2 -C₂H₄)Cl (**6FP-A**) catalyzed styrene hydrogenation with 0.5 mM **6FP-A**, 174 mM styrene, 50 psig H₂ in CD₂Cl₂, 45 °C in triplicate.

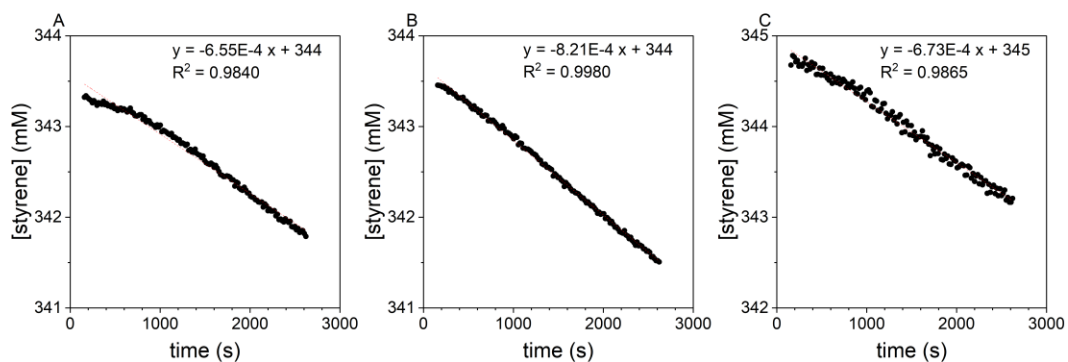
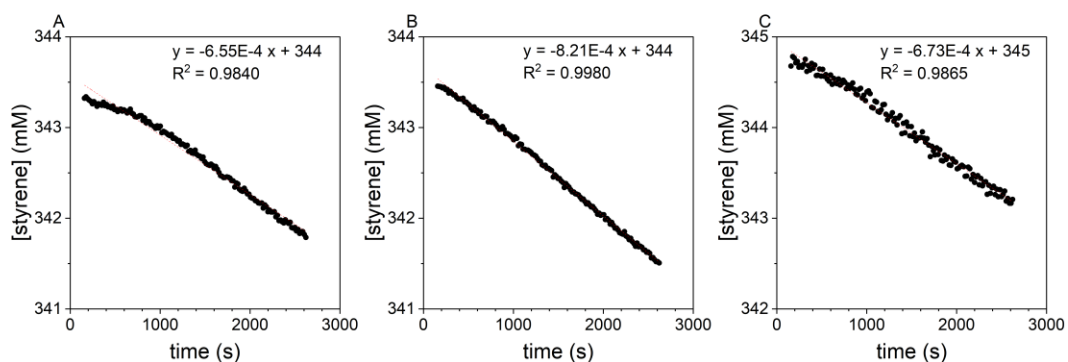


Figure 2.3.17 Plots of [styrene] (mM) vs. time (s) for (6-FP)Rh(η^2 -C₂H₄)Cl (**6FP-A**) catalyzed styrene hydrogenation with 0.5 mM **6FP-A**, 348 mM styrene, 50 psig H₂ in CD₂Cl₂, 45 °C in triplicate.



The Michaelis-Menten equation (Eq. 2-3 and Eq. 2-4) was used to demonstrate the dependence of [styrene] on **6FP-A** catalyzed styrene hydrogenation, in which v = rate of reaction; V_{\max} = maximum rate that could be achieved by the system; $[S]$ = concentration of substrate; K_M = Michaelis constant.⁵² Using the rate data collected in **Figure 2.3.13** – **Figure 2.3.17**, a k_{obs} vs. [styrene] plot with a curve fit using the function $y = ax / (b + x)$ ($a = V_{\max}$, $b = K_M$) is shown in **Figure 2.3.1C**. The estimated Michaelis constant K_M , which is the value of the b from **Figure 2.3.1C**, is 0.10(4) M. Thus, to achieve a nearly zero-order rate law in styrene, $[S]$ needs to be at least greater than $10K_M$ so that the dependence of v

on K_M would be negligible in **Eq. 2-3** (shown in **Eq. 2-5**). In this case, the dependence on styrene for **6FP-A** catalyzed styrene hydrogenation would be close to zero-order on styrene when $[\text{styrene}] > 1.0(4) \text{ M}$ with the given condition in **Figure 2.3.1C**.

$$v = V_{\max}[\text{S}]/(K_M + [\text{S}]) \quad \text{Eq. 2-3}$$

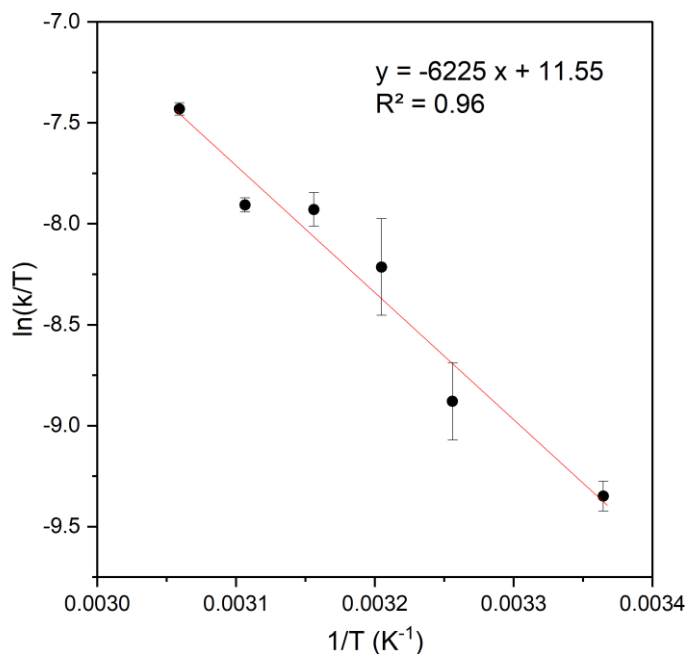
$$1/v = (K_M + [\text{S}])/V_{\max}[\text{S}] = (K_M/V_{\max}) \times (1/[\text{S}]) + 1/V_{\max} \quad \text{Eq. 2-4}$$

$$\text{When } [\text{S}] \gg K_M, \text{ then } v \approx V_{\max} \times ([\text{S}]/[\text{S}]) = V_{\max} \quad \text{Eq. 2-5}$$

2.3.3 Eyring equation determination on catalytic hydrogenation of styrene with **6FP-A**

To estimate the activation energy for our Rh-catalyzed styrene hydrogenation, an Eyring analysis was performed by measuring the reaction rate at temperatures from 25 °C to 55 °C. The resulting Eyring plot shows a linear fit with $R^2 > 0.95$. The ΔH^\ddagger and ΔS^\ddagger values were calculated to be 12.5(6) kcal/mol and $-23(2) \text{ cal/K}\cdot\text{mol}$, respectively (**Figure 2.3.18**). The negative value of activation entropy (ΔS^\ddagger) is similar to the ΔS^\ddagger for styrene hydrogenation catalyzed by Wilkinson's catalyst ($-21.5 \text{ cal/K}\cdot\text{mol}$).⁵³

Figure 2.3.18 Eyring plot for the hydrogenation of styrene catalyzed by (6-FP)Rh(η^2 -C₂H₄)Cl (**6FP-A**).



All data points and standard deviations are based on at least three independent experiments. Reaction conditions: 1 mM **6FP-A**, 44 mM styrene, 50 psig H₂ in CD₂Cl₂, variable temperature (24, 34, 39, 43, 49 or 54 °C).

The temperatures for all variable temperature NMR experiments were calibrated based on the chemical shift difference between the two solvent resonances of a MeOH-*d*₄ standard using **Eq. 2-6**, in which T = calculated temperature, $\Delta\delta$ = difference between the two solvent resonances of a MeOH-*d*₄ standard (resonance for OH, δ = 4.85 ppm at 25 °C; resonance for CHD₂, δ = 3.31 ppm at 25 °C).⁵⁴ The set temperature, observed chemical shifts for the MeOH-*d*₄ standard, and the calibrated temperature used for this study are shown in **Table 2.3.1**. The detailed [styrene] (mM) vs. time (s) plots are illustrated in **Figure 2.3.19 – Figure 2.3.24**

$$T(\text{K}) = -14.68 \times (\Delta\delta)^2 - 65.06 \times \Delta\delta + 159.48 + 3.8 \times 10^{-15} e^{-13.2\Delta\delta} \quad \text{Eq. 2-6}$$

Table 2.3.1 The set temperature, observed chemical shifts for the MeOH- d_4 standard and the calibrated temperature used for the Eyring equation determination.

Set temperature (°C)	$\delta(\text{OD})$ (ppm)	$\delta(\text{CD}_3)$ (ppm)	$\Delta\delta$ (ppm)	Calculated temperature (K)	Calculated temperature (°C)
25	4.85	3.31	1.54	297	24
35	4.76	3.31	1.45	307	34
40	4.72	3.31	1.41	312	39
45	4.68	3.31	1.37	316	43
50	4.62	3.31	1.31	322	49
55	4.58	3.31	1.27	327	54

Figure 2.3.19 Plots of [styrene] (mM) vs. time (s) for (6-FP)Rh(η^2 -C₂H₄)Cl (**6FP-A**) catalyzed styrene hydrogenation. The reaction is performed in triplicate with 1 mM **6FP-A**, 44 mM styrene, 50 psig H₂ in CD₂Cl₂, 24 °C.

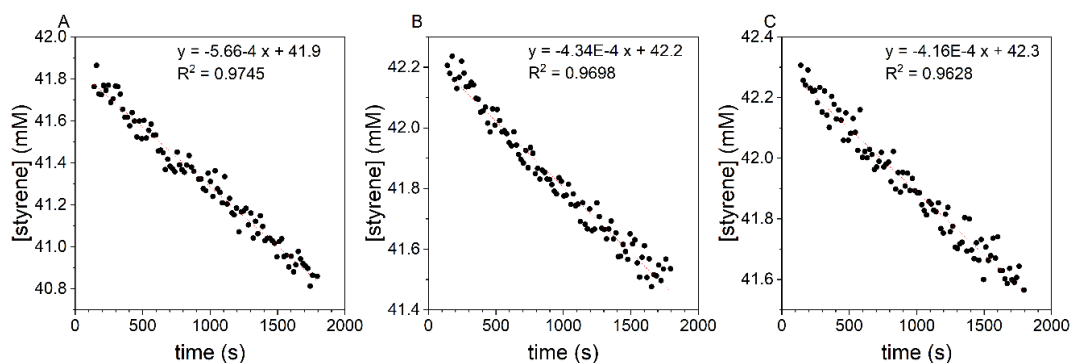


Figure 2.3.20 Plots of [styrene] (mM) vs. time (s) for (6-FP)Rh(η^2 -C₂H₄)Cl (**6FP-A**) catalyzed styrene hydrogenation. The reaction is performed in triplicate with 1 mM **6FP-A**, 44 mM styrene, 50 psig H₂ in CD₂Cl₂, 34 °C.

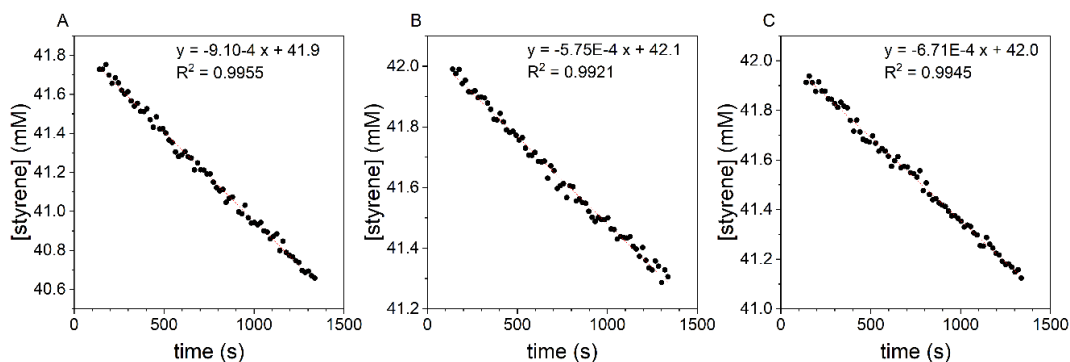


Figure 2.3.21 Plots of [styrene] (mM) vs. time (s) for (6-FP)Rh(η^2 -C₂H₄)Cl (**6FP-A**) catalyzed styrene hydrogenation. The reaction is performed in triplicate with 1 mM **6FP-A**, 44 mM styrene, 50 psig H₂ in CD₂Cl₂, 39 °C.

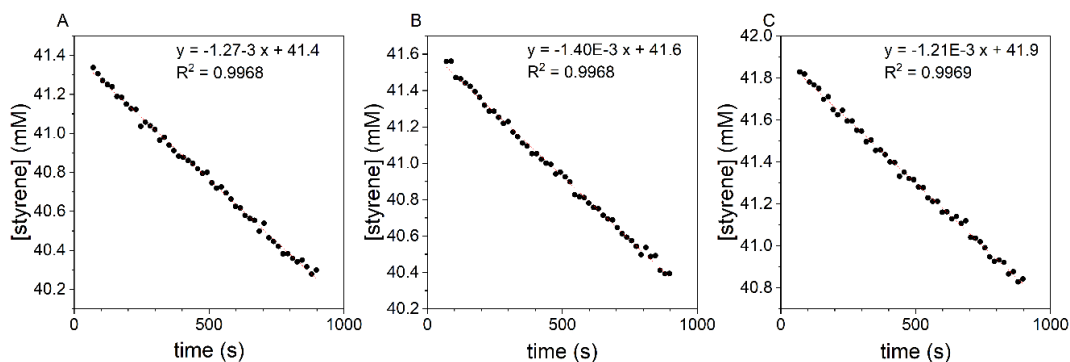


Figure 2.3.22 Plots of [styrene] (mM) vs. time (s) for (6-FP)Rh(η^2 -C₂H₄)Cl (**6FP-A**) catalyzed styrene hydrogenation. The reaction is performed in triplicate with 1 mM **6FP-A**, 44 mM styrene, 50 psig H₂ in CD₂Cl₂, 43 °C.

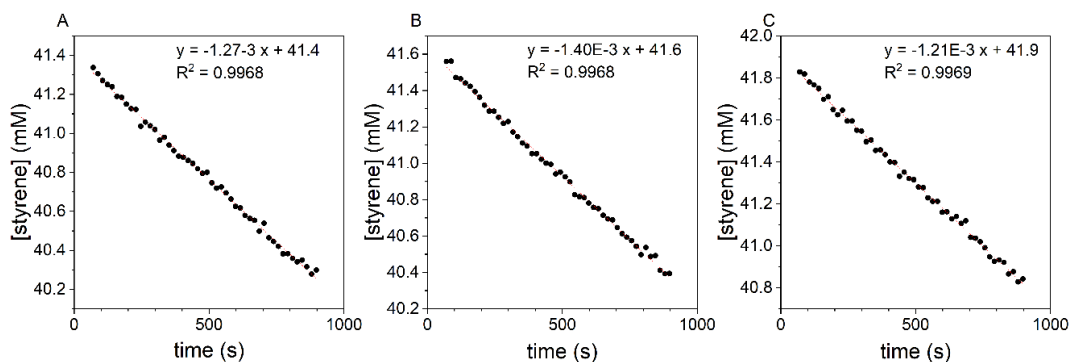


Figure 2.3.23 Plots of [styrene] (mM) vs. time (s) for (6-FP)Rh(η^2 -C₂H₄)Cl (**6FP-A**) catalyzed styrene hydrogenation. The reaction is performed in triplicate with 1 mM **6FP-A**, 44 mM styrene, 50 psig H₂ in CD₂Cl₂, 49 °C.

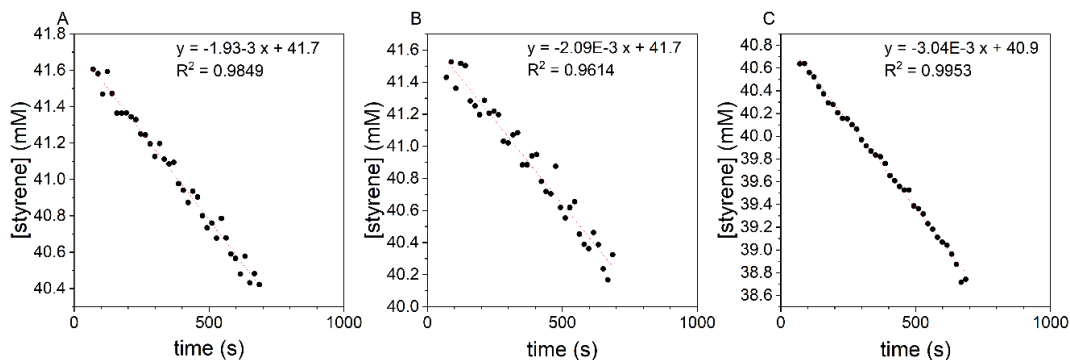
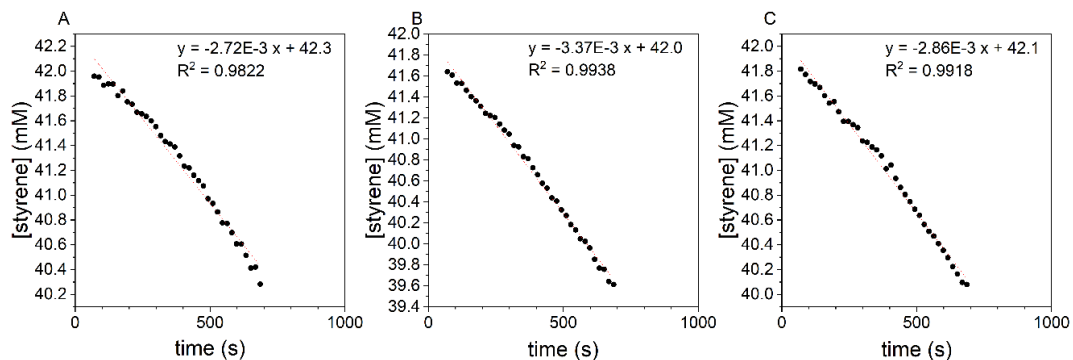


Figure 2.3.24 Plots of [styrene] (mM) vs. time (s) for (6-FP)Rh(η^2 -C₂H₄)Cl (**6FP-A**) catalyzed styrene hydrogenation. The reaction is performed in triplicate with 1 mM **6FP-A**, 44 mM styrene, 50 psig H₂ in CD₂Cl₂, 54 °C.



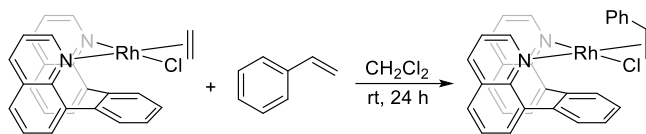
2.3.4 Observation and characterization of (6-FP)Rh(Cl)(η^2 -styrene)

While monitoring styrene hydrogenation using **6FP-A** as catalyst precursor by ¹H NMR spectroscopy, new resonances in the aromatic region were observed, which could be due to an intermediate for the Rh-catalyzed styrene hydrogenation or a catalyst precursor. To study the identity of this new Rh complex, styrene and **6FP-A** were mixed in CD₂Cl₂, which leads to the formation of (6-FP)Rh(Cl)(η^2 -styrene) (**6FP-B**). Since the new aromatic resonances in the ¹H NMR spectrum of styrene hydrogenation catalyzed by **6FP-A** are consistent with the chemical shifts of the isolated **6FP-B** formed by olefin exchange, we

propose that the first step of this styrene hydrogenation reaction is likely to be the formation of **6FP-B**.

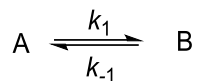
The ^1H NMR spectrum of isolated **6FP-B** shows two sets of resonances with an integration ratio of $\sim 1:1.5$. This ratio does not show a detectable change at different concentrations of **6FP-B**. Exchange peaks between the two species observed by ^1H NMR spectroscopy were observed by a 2D-Exchange Spectroscopy (2D-EXSY) experiment, which indicates that the two species likely undergo exchange (**Figure 2.3.25**). The rate constant for the exchange between the two species was determined to be 0.076 s^{-1} (see below for more details). Coalescence or line broadening of the two species is not observed by raising the temperature of the NMR probe up to $70\text{ }^\circ\text{C}$. Instead, decomposition of **6FP-B** is observed at $70\text{ }^\circ\text{C}$.

Scheme 2.3.2 Synthesis of $(6\text{-FP})\text{Rh}(\text{Cl})(\eta^2\text{-styrene})$ (**6FP-B**).



The calculations on the exchange rate for the two species observed in CD_2Cl_2 solution of **6FP-B** is based on **Eq. 2-7**, in which k is the exchange rate constant, t_m is the mixing time for 2D-EXSY experiment (0.600 s for this experiment), X_A and X_B are the mole fractions of A and B. I_{AA} , I_{BB} , I_{AB} and I_{BA} are the peak intensity of the cross peaks or dihedral peaks between A and B. In this case, X_A and X_B are determined to be 0.41 and 0.59 , and I_{AA} , I_{BB} , I_{AB} and I_{BA} are 9.27 , 12.5 , 0.24 and 0.24 respectively. Therefore, the calculated rate constant k is 0.076 s^{-1} .

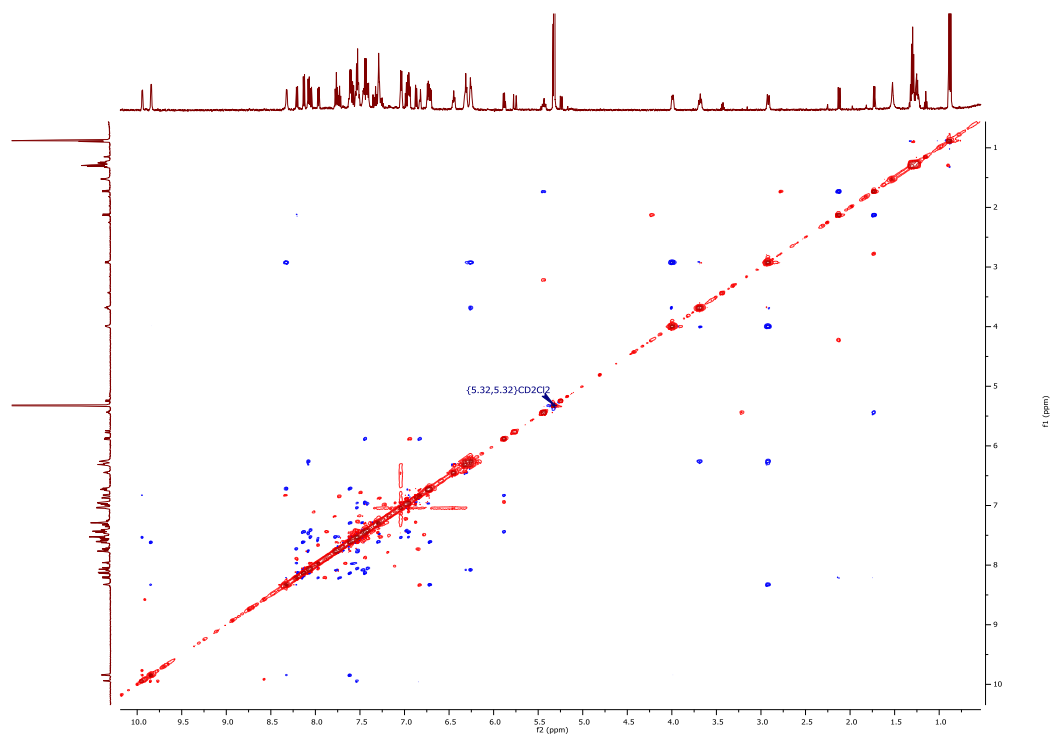
For an exchange reaction:



$$k = k_1 + k_{-1} = (1/t_m) \cdot \ln[(r+1)/(r-1)] \quad \text{Eq. 2-7}$$

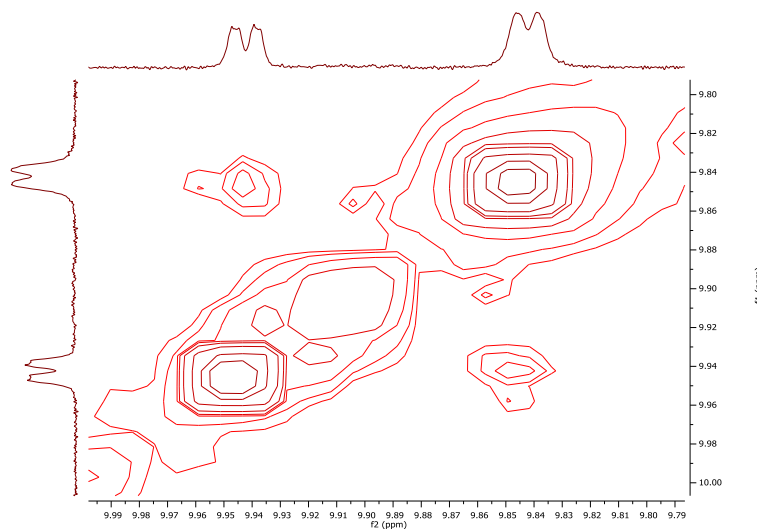
$$r = 4X_A X_B (I_{AA} + I_{BB}) / (I_{AB} + I_{BA}) - (X_A - X_B)^2 \quad \text{Eq. 2-8}$$

Figure 2.3.25 The 2D-Exchange Spectroscopy (2D-EXSY) plot for (6-FP)Rh(Cl)(η^2 -styrene) (**6FP-B**).



The resonances in phase with the dihedral resonances (red) indicate the exchange between the two sets of peaks described above. The resonances in blue represent COSY-like signals.

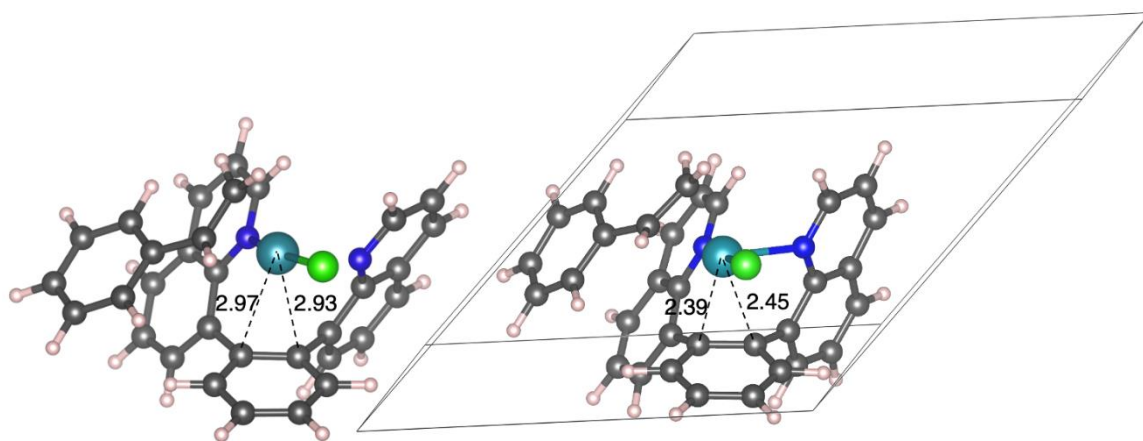
Figure 2.3.26 2D-EXSY peaks used for the exchange rate for the two species observed in CD₂Cl₂ solution of (6-FP)Rh(η^2 -styrene)Cl (**6FP-B**) based on 2D-EXSY.



It is established that the generally preferred olefin orientation in square planar and d⁸ complexes is with the C=C bond perpendicular to the square plane;^{41, 55, 56} however, the capping arene ligand of **6FP-B** can potentially be considered a tridentate ligand, which complicates consideration of the coordination environment around Rh including olefin orientation and rotational dynamics (**Figure 2.3.27**).³⁹ A single crystal X-ray diffraction study of **6FP-B** indicates that the 6-FP capping arene ligand serves as a tridentate ligand, coordinating to the Rh center with two quinoline nitrogen atoms (N1, N2) and the benzene ring in η^2 fashion (C10 and C11) (**Figure 2.3.28**). The geometry of **6FP-B** is approximately trigonal bipyramidal, in which the triangular plane consists of one of the quinoline nitrogen (N1), arene moiety on the ligand (C10 and C11) and the styrene (C25 and C26), and the axial positions are coordinated to the second quinoline nitrogen (N2) and the chloride (Cl1). The bond angles are slightly distorted from the ideal trigonal bipyramidal geometry. The bond angle between N1 and the centroid of C10 and C11 is 88.1°. The angles between the centroid of the styrene C=C bond and N1 or centroid of C10 and C11 are 137.2° and 133.7°,

respectively. The styrene C=C bond is oriented in the trigonal plane with a slight distortion (the dihedral angle between the plane of N1–Rh1–C10–C11 and the plane of N1–Rh1–C25–C26 is 6.01°). The bond lengths between Rh center and ligated atoms do not exhibit a significant difference from the corresponding bond lengths in **6FP-A** (≥ 0.04 Å).²³ Interestingly, although the DFT calculations on the structure of **6FP-B** in the solid-state are consistent with the crystal structure, DFT calculations (performed by Charles Musgrave III and William Goddard III from Caltech) suggest a square planer conformation with the arene moiety at the axial position of the plane when **6FP-B** is dissolved in dichloromethane. One explanation for the preference of trigonal bipyramidal conformation for **6FP-B** in the solid phase is that the π - π stacking between the phenyl ring of coordinated styrene and the quinoline ring with N2 (the distance between the centroids of these two rings is 3.484 Å) could stabilize the trigonal bipyramidal conformation (**Figure 2.3.28**).

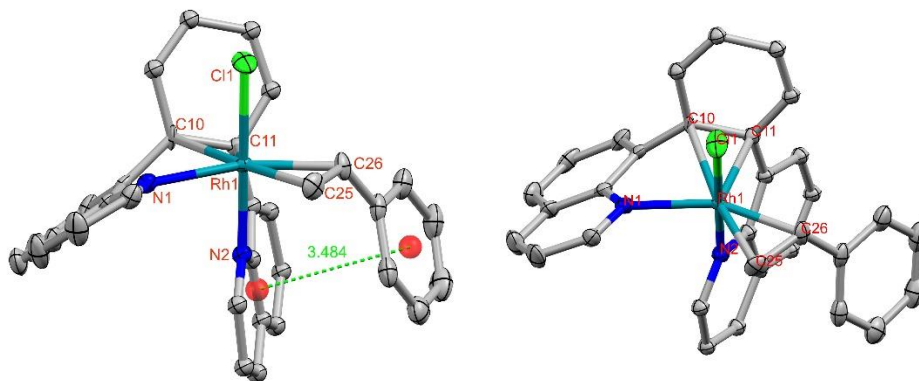
Figure 2.3.27 DFT calculated structure of (6-FP)Rh(Cl)(η^2 -styrene) (**6FP-B**).



The left structure is calculated using solvent parameters with dielectric constant = 8.93 and probe radius = 2.33 Å to match dichloromethane. The right structure is calculated using crystal optimization.

Figure 2.3.28 ORTEP of (6-FP)Rh(Cl)(η^2 -styrene) (**6FP-B**). Ellipsoids are drawn at 50% probability level. Hydrogen atoms and noncoordinating solvents are omitted for clarity. Selected bond lengths for **6FP-B** (Å): Rh1–N1 2.188(4), Rh1–N2 2.093(10), Rh1–Cl1 2.3448(12), Rh1–C10

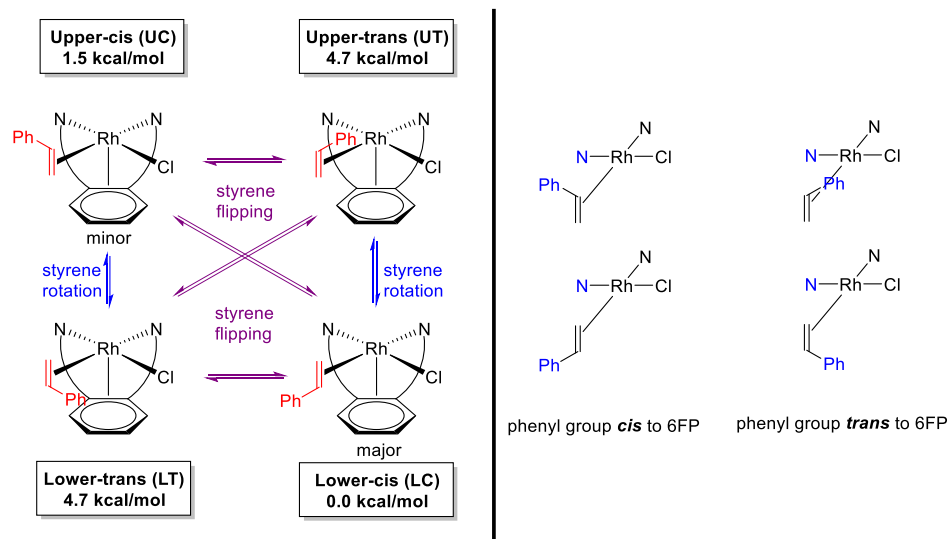
2.541(5), Rh1-C11 2.522(16), Rh1-C25 2.060(5), Rh1-C26 2.122(5), C25-C26 1.420(8). Selected bond angles for **6FP-B** (deg): Cl1-Rh1-N1 94.08(10), Cl1-Rh1-N2 178.4(3), Cl1-Rh1-C10 95.98(12), Cl1-Rh1-C11 104.0(3), Cl1-Rh1-C25 87.08(16), Cl1-Rh1-C26 88.88(15), N1-Rh1-N2 86.2(3), N1-Rh1-C10 71.86(16), N1-Rh1-C11 104.6(3), N1-Rh1-C25 117.2(2), N1-Rh1-C26 156.53(19), N2-Rh1-C10 83.6(3), N2-Rh1-C11 74.4(4), N2-Rh1-C25 94.2(3), N2-Rh1-C26 91.5(4), C10-Rh1-C11 34.7(3), C10-Rh1-C25 170.6(2), C10-Rh1-C26 131.12(18), C11-Rh1-C25 136.0(4), C25-Rh1-C26 39.6(2). The distance between the centroid of the phenyl ring of coordinated styrene and the centroid of the quinoline ring containing N2 is 3.484 Å.



The observation of exchange peaks in the ^1H NMR spectrum of **6FP-B** are attributed to dynamics of the C=C bond of coordinated styrene. Assuming a preferred C=C orientation in the square plane of the approximately square planar structure (see above and **Figure 2.3.27**), four styrene isomers are possible (**Scheme 2.3.3**). The four isomers can undergo exchange by either rotation of the styrene C=C bond or face flipping (either with or without styrene dissociation).⁵⁷⁻⁶¹ The observation of two isomers by ^1H NMR spectroscopy indicates that the conformational changes are likely slow on the NMR timescale and that two isomers are likely thermodynamically favored. The thermodynamics of these conformers were probed with DFT by Musgrave and Goddard (**Scheme 2.3.3**). DFT predicts the LC (lower-cis, *cis* relative to the 6-FP backbone) conformation to be the lowest in Gibbs free energy due to favorable Van der Waals (VdW) interactions between the aryl ring of styrene and the capping arene. At 318 K, the UC (upper-cis) conformation lies 1.5

kcal/mol above the LC conformer according to DFT. UC also benefits from favorable VdW interactions with the 6-FP moiety, although here the π - π stacking is poorly aligned such that UC is not stabilized as much as LC. The UT (upper-trans) and the LT (lower-trans) structures reside 4.71 and 4.74 kcal/mol above the LC configuration. Neither of these conformers exhibit VdW stabilizing interactions between styrene and the capping arene. Thus, the DFT calculations predict that the two experimentally observed species are LC (major) and UC (minor), and the calculated $\Delta\Delta G$ ($\Delta\Delta G = \Delta G_{UC} - \Delta G_{LC}$) for LC and UC is 1.5 kcal/mol. This $\Delta\Delta G$ value agrees with the 1.5 for K_{eq} ($\Delta\Delta G \approx 0.2$ kcal/mol) observed experimentally (see above).

Scheme 2.3.3 Possible conformational isomers of (6-FP)Rh(Cl)(η^2 -styrene) (**6FP-B**) and proposed exchange pathways



The conformers' short-hand names and DFT free energies at 318 K are boxed; U (upper) indicates the phenyl group of styrene points to the opposite position of the arene moiety of the 6-FP ligand, L (lower) indicates the phenyl group of styrene points towards the arene moiety of the 6-FP ligand, C indicates *cis* to the 6-FP ligand backbone, T indicates *trans* to the 6-FP ligand backbone, which is illustrated on the right of **Scheme 2.3.3**

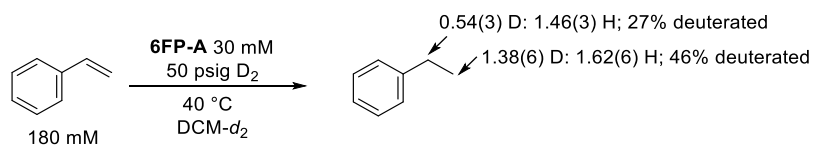
2.3.5 Isotopic studies on styrene hydrogenation catalyzed by (6-FP)Rh(Cl)(η^2 -C₂H₄)

A study using D₂ and styrene was performed to further explore the catalytic styrene hydrogenation. In a J. Young tube, a CD₂Cl₂ solution with 180 mM of **styrene**, 30 mM of **6FP-A** was charged with 50 psig D₂ and heated to 40 °C. The reaction reached completion after 48 hours. The NMR spectra of the reaction solution were recorded.

The result of this isotopic study showed that deuterium from D₂ is incorporated into ethylbenzene most selectively in the terminal methyl position of the ethyl group (**Scheme 2.3.4**). For a catalytic process that involves irreversible oxidative addition of H₂ (or D₂), it is expected that D might be nearly equally incorporated into the benzylic and methyl positions of ethylbenzene.⁶² Monitoring the conversion of styrene and D₂ to ethylbenzene using **6FP-A** as catalyst precursor reveals that the benzylic position of ethylbenzene contains 0.54(3) ²D and 1.46(3) ¹H (or 27% deuterated), and the methyl position of ethylbenzene contains 1.38(6) ²D and 1.62 (6) ¹H (or 46% deuterated). Hence, the styrene hydrogenation process likely involves reversible activation of H₂ and irreversible ethylbenzene formation because the distribution of D on ethylbenzene would be equivalent at both the benzylic and methyl positions if an irreversible H₂ oxidative addition pathway is followed. Further, isotopic scrambling between styrene and D₂ was observed. After 48 hours of reaction with the conditions indicated in **Scheme 2.3.4**, the product of H/D exchange was observed by ¹H NMR spectroscopy (**Figure 2.3.29**). The major H/D exchange products for styrene are the terminal substituted products, *trans*-1-deutero-styrene (6.74 ppm, ³J_{HH} = 11 Hz; 5.25 ppm, *d*, ³J_{HH} = 11 Hz) and *cis*-1-deutero-styrene (6.75 ppm, *d*, ³J_{HH} = 18 Hz; 5.77 ppm, *d*, ³J_{HH} = 18 Hz). Additionally, resonances for free

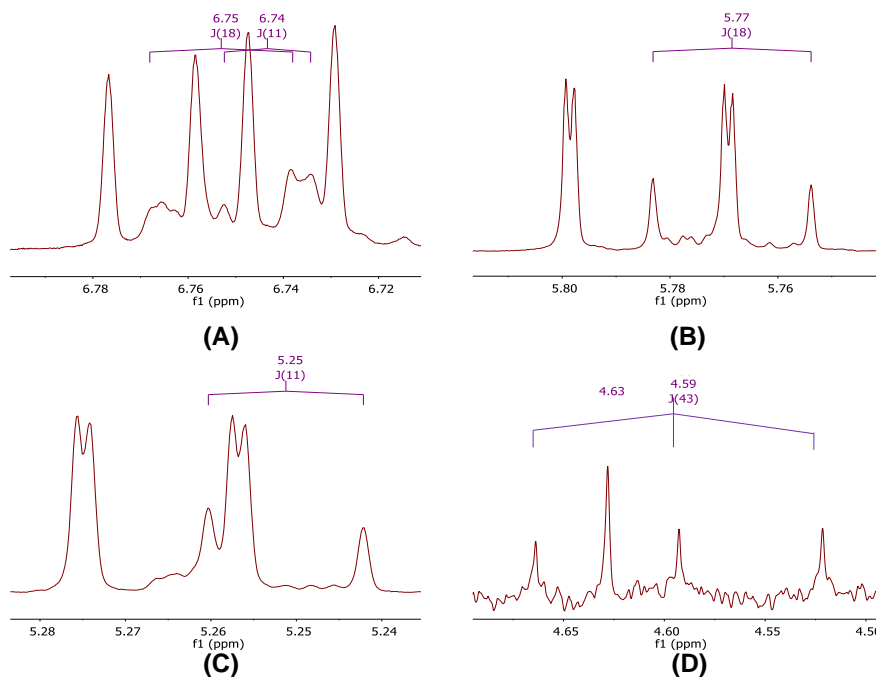
HD (4.59 ppm, *t*, $^1J_{\text{HD}} = 43$ Hz) and H₂ (4.59 ppm, *s*) are observed, which can be attributed to the H/D exchange between styrene and D₂. Thus, the observation of isotopic scrambling between styrene and D₂ provides evidence that the activation of styrene and dihydrogen are likely both reversible.

Scheme 2.3.4 Isotopic study for (6-FP)Rh(Cl)(η^2 -C₂H₄) (**6FP-A**) catalyzed styrene hydrogenation.



The reaction is performed in triplicate with the following conditions: 0.5 mL CD₂Cl₂, 180 mM styrene, 30 mM **6FP-A**, 50 psig D₂, 40 °C. The reaction is monitored by ¹H NMR spectroscopy every 24 hours. The data for deuterium incorporation are after 48 hours of reaction.

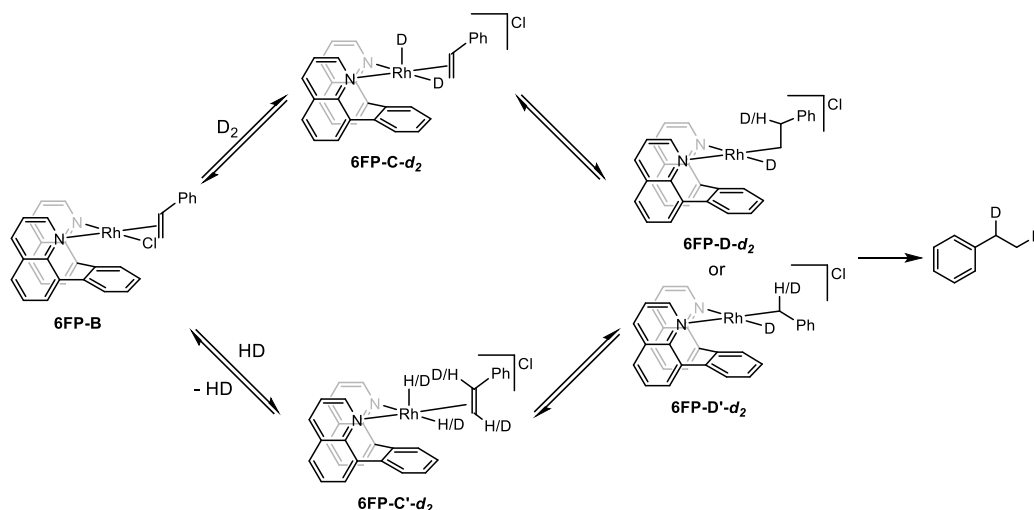
Figure 2.3.29 ¹H NMR spectroscopy evidence for H/D exchange between styrene and D₂.



(A), (B), (C): the three vinyl peaks for styrene. (D): the HD and H₂ peaks. The reaction was performed in triplicate with the following conditions: 0.5 mM CD₂Cl₂, 180 mM styrene, 30 mM (6-FP)Rh(Cl)(η^2 -C₂H₄) (**6FP-A**), 50 psig D₂, 40 °C. The reaction was monitored by ¹H NMR spectroscopy every 24 hours. The data for deuterium incorporation correspond to 48 hours of reaction.

Based on our experimental studies, a mechanism for the styrene hydrogenation process using **6FP-B** as catalyst is proposed (**Scheme 2.3.5**). The oxidative addition of D_2 (or H_2) to **6FP-B** forms $[(6\text{-FP})\text{Rh}(\text{D})_2(\eta^2\text{-styrene})]\text{Cl}$ (**6FP-C-d₂**), and **6FP-C-d₂** can mediate migratory insertion of styrene into a Rh–D bond to form $[(6\text{-FP})\text{Rh}(\text{D})(1\text{-phenyl-2-D-ethyl})]\text{Cl}$ or $[(6\text{-FP})\text{Rh}(\text{D})(1\text{-D-2-phenylethyl})]\text{Cl}$ (**6FP-D-d₂** or **6FP-D'-d₂**). The reverse reaction, β -hydride elimination, can form $[(6\text{-FP})\text{Rh}(\text{H})(\text{D})(\eta^2\text{-styrene-d}_1)]\text{Cl}$ (**6FP-C'-d₂**), which can undergo ligand exchange with free styrene to generate free styrene-d₁ and $[(6\text{-FP})\text{Rh}(\text{H})(\text{D})(\eta^2\text{-styrene})]\text{Cl}$ (**6FP-C-d₁**). Net H–D reductive elimination of $[(6\text{-FP})\text{Rh}(\text{H})(\text{D})(\eta^2\text{-styrene})]\text{Cl}$ can occur to form the observed formation of free HD. The formation of dihydrogen (H_2) is likely generated from H/D exchange between HD and styrene via the same pathway. Moreover, the observation of the terminal exchange product ($C_6H_5\text{-CH=CHD}$) can be explained by the favored formation of the branched olefin insertion product $[(6\text{-FP})\text{Rh}(\text{D})(1\text{-phenyl-2-D-ethyl})]\text{Cl}$ (**6FP-D'-d₂**) rather than the olefin insertion product $[(6\text{-FP})\text{Rh}(\text{D})(1\text{-D-2-phenylethyl})]\text{Cl}$ (**6FP-D-d₂**).

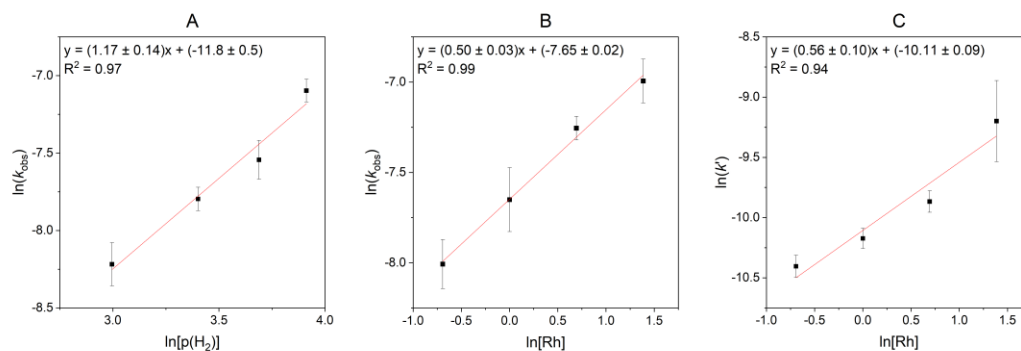
Scheme 2.3.5 Proposed mechanism that explains deuterium incorporation into ethylbenzene during styrene hydrogenation using $(6\text{-FP})\text{Rh}(\text{Cl})(\eta^2\text{-C}_2\text{H}_4)$ (**6FP-A**) as catalyst precursor and D_2 .



2.3.6 Kinetic studies on 5^{NP}FP-A catalyzed styrene hydrogenation

In all cases, catalysis with 5^{NP}FP-A is substantially faster than the other capping arene Rh complexes. The rate dependences on $[\text{H}_2]$ and $[\text{Rh}]$ for the 5^{NP}FP-A catalyzed styrene hydrogenation were determined. Similar to 6FP-A catalyzed styrene hydrogenation, a first-order dependence on $[\text{H}_2]$ was observed (**Figure 2.3.30A**). However, the results in **Figure 2.3.30B** suggest a half-order dependence on the concentration of 5^{NP}FP-A , which is different from the first-order relationship with the catalyst for 6FP-A catalyzed styrene hydrogenation. This half-order dependence on $[5^{\text{NP}}\text{FP-A}]$ suggests the possible formation of a dimeric Rh complex from 5^{NP}FP-A .^{63, 64} For example, dissociation of the 5^{NP}FP ligand could form a chloride-bridged Rh dimer, which could serve as the catalyst precursor. Consistent with this hypothesis, the rate dependence on $[\text{Rh}]$ using $[\text{Rh}(\eta^2\text{-C}_2\text{H}_4)_2(\mu\text{-Cl})_2]$ as the catalyst precursor for styrene hydrogenation revealed a half-order dependence (**Figure 2.3.30C**), and the observed rate is at least 10 times faster than the 5^{NP}FP-A catalyzed styrene hydrogenation under the same conditions. Although the active species in 5^{NP}FP-A catalyzed styrene hydrogenation could be different from the active species for $[\text{Rh}(\eta^2\text{-C}_2\text{H}_4)_2(\mu\text{-Cl})_2]$, the difference in rate law on $[5^{\text{NP}}\text{FP-A}]$ and $[6\text{FP-A}]$ for their catalytic styrene hydrogenation is evidence that the catalytic styrene hydrogenation for 5^{NP}FP-A and 6FP-A undergoes different mechanisms, in which 5^{NP}FP-A is likely to form a dimeric species without the 5^{NP}FP ligand during the catalysis, while the active catalyst for 6FP-A maintains the monomeric form during catalysis.

Figure 2.3.30 Studies of reaction order for hydrogenation of styrene using (5-^{NP}FP)Rh(Cl)(η^2 -C₂H₄) (**5^{NP}FP-A**) or [Rh(η^2 -C₂H₄)(μ -Cl)]₂.



Reaction conditions: For the determination of order in H₂ (A): 1 mM **5^{NP}FP-A**, 87 mM styrene, variable psig of H₂ (20, 30, 40 or 50 psig) in CD₂Cl₂, 45 °C. For the determination of order in **5^{NP}FP-A** (B): variable mM **5^{NP}FP-A** (0.5, 1, 1.5, 2 or 4 mM), 87 mM styrene, 50 psig H₂ in CD₂Cl₂, 45 °C. For the determination of order in [Rh(η^2 -C₂H₄)(μ -Cl)]₂ (C): variable mM **5^{NP}FP-A** (0.25, 0.5, 0.75, 1 or 2 mM), 44 mM styrene, 50 psig H₂ in CD₂Cl₂, 45 °C. The standard deviations for (B) and (C) were determined from the standard deviation of three trials under the same conditions (see **Figure 2.3.31 – Figure 2.3.43**).

The rate order dependences on the concentration of H₂ and **5^{NP}FP-A** for **5^{NP}FP-A** catalyzed styrene hydrogenation were determined by measuring the observed rate (k_{obs}) under different concentrations of H₂ or **5^{NP}FP-A**, respectively. Similar to the method described in the kinetic studies for the **6FP-A** catalyzed styrene hydrogenation, the rate for styrene consumption was used instead of the rate for ethylbenzene (EtPh) formation to avoid the interference of low S/N ratio when the EtPh concentration is low. The [styrene] vs. time plots used for k_{obs} determination are shown in **Figure 2.3.31 – Figure 2.3.38**.

Figure 2.3.31 Plots of [styrene] (mM) vs. time (s) for $(5\text{-}^{\text{NP}}\text{FP})\text{Rh}(\eta^2\text{-C}_2\text{H}_4)\text{Cl}$ (**5^{NP}FP-A**) catalyzed styrene hydrogenation. The reaction was performed in triplicate with 1 mM **5^{NP}FP-A**, 87 mM styrene, 50 psig H_2 in CD_2Cl_2 , 45 °C.

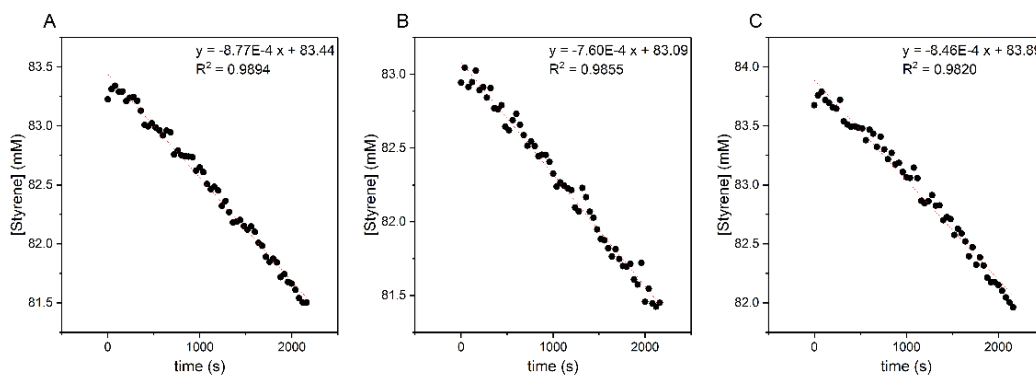


Figure 2.3.32 Plots of [styrene] (mM) vs. time (s) for $(5\text{-}^{\text{NP}}\text{FP})\text{Rh}(\eta^2\text{-C}_2\text{H}_4)\text{Cl}$ (**5^{NP}FP-A**) catalyzed styrene hydrogenation. The reaction was performed in triplicate with 1 mM **5^{NP}FP-A**, 87 mM styrene, 40 psig H_2 in CD_2Cl_2 , 45 °C.

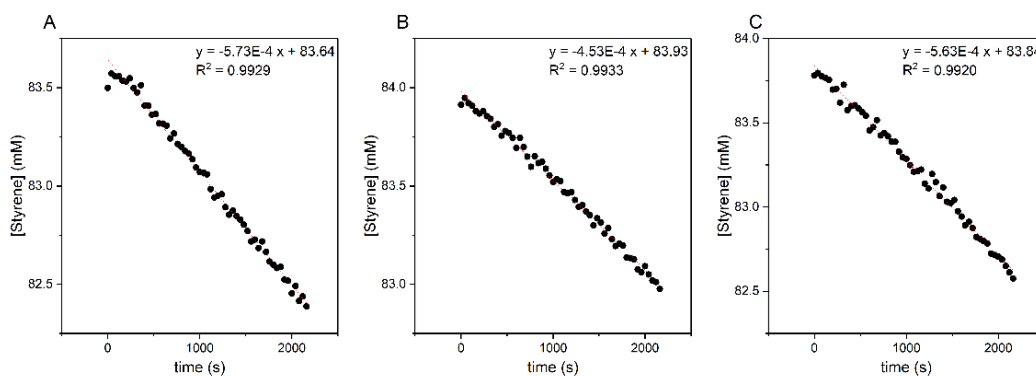


Figure 2.3.33 Plots of [styrene] (mM) vs. time (s) for $(5\text{-}^{\text{NP}}\text{FP})\text{Rh}(\eta^2\text{-C}_2\text{H}_4)\text{Cl}$ (**5^{NP}FP-A**) catalyzed styrene hydrogenation. The reaction was performed in triplicate with 1 mM **5^{NP}FP-A**, 87 mM styrene, 30 psig H_2 in CD_2Cl_2 , 45 °C.

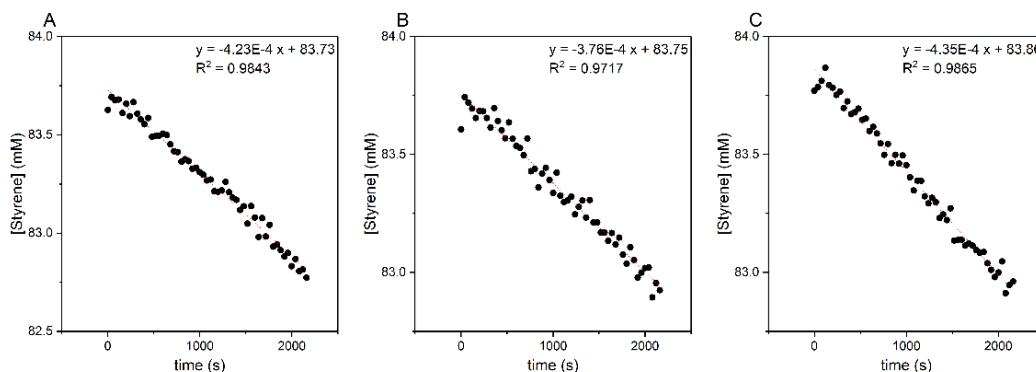


Figure 2.3.34 Plots of [styrene] (mM) vs. time (s) for $(5\text{-}^{\text{NP}}\text{FP})\text{Rh}(\eta^2\text{-C}_2\text{H}_4)\text{Cl}$ (5^{NP}FP-A) catalyzed styrene hydrogenation. The reaction was performed in triplicate with 1 mM 5^{NP}FP-A , 87 mM styrene, 20 psig H_2 in CD_2Cl_2 , 45 °C.

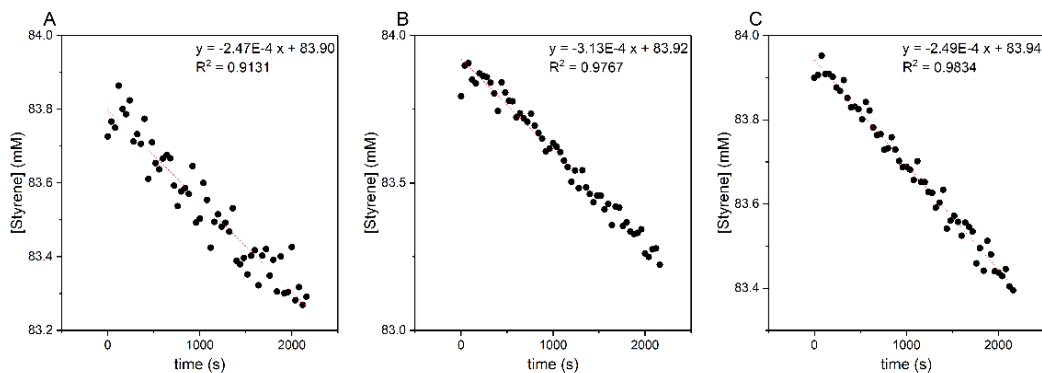


Figure 2.3.35 Plots of [styrene] (mM) vs. time (s) for $(5\text{-}^{\text{NP}}\text{FP})\text{Rh}(\eta^2\text{-C}_2\text{H}_4)\text{Cl}$ (5^{NP}FP-A) catalyzed styrene hydrogenation. The reaction was performed in triplicate with 4 mM 5^{NP}FP-A , 87 mM styrene, 50 psig H_2 in CD_2Cl_2 , 45 °C.

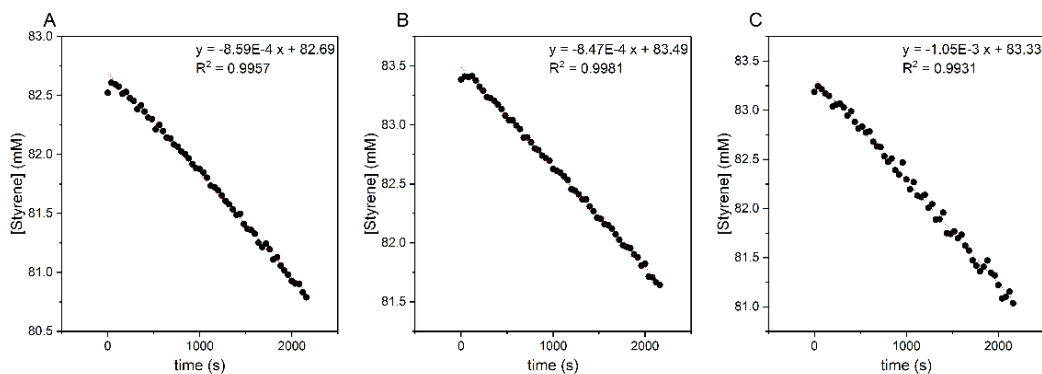


Figure 2.3.36 Plots of [styrene] (mM) vs. time (s) for $(5\text{-}^{\text{NP}}\text{FP})\text{Rh}(\eta^2\text{-C}_2\text{H}_4)\text{Cl}$ (5^{NP}FP-A) catalyzed styrene hydrogenation. The reaction was performed in triplicate with 2 mM 5^{NP}FP-A , 87 mM styrene, 50 psig H_2 in CD_2Cl_2 , 45 °C.

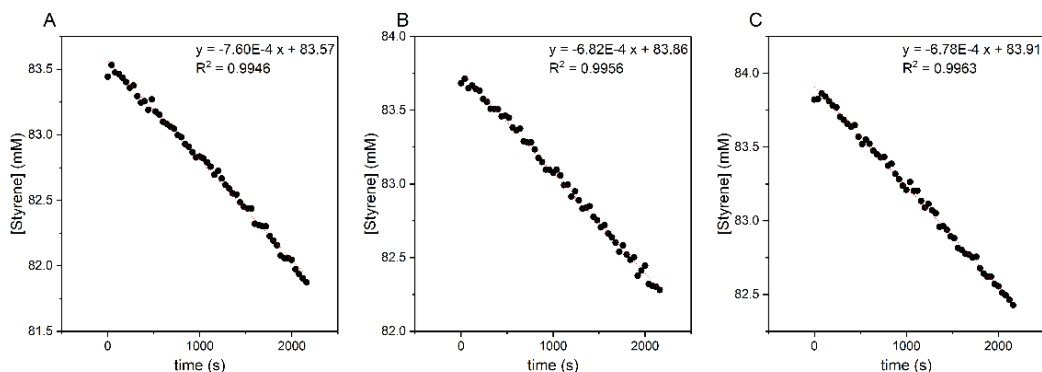


Figure 2.3.37 Plots of [styrene] (mM) vs. time (s) for $(5\text{-}^{\text{NP}}\text{FP})\text{Rh}(\eta^2\text{-C}_2\text{H}_4)\text{Cl}$ (**5^{NP}FP-A**) catalyzed styrene hydrogenation. The reaction was performed in triplicate with 1 mM **5^{NP}FP-A**, 87 mM styrene, 50 psig H_2 in CD_2Cl_2 , 45 °C.

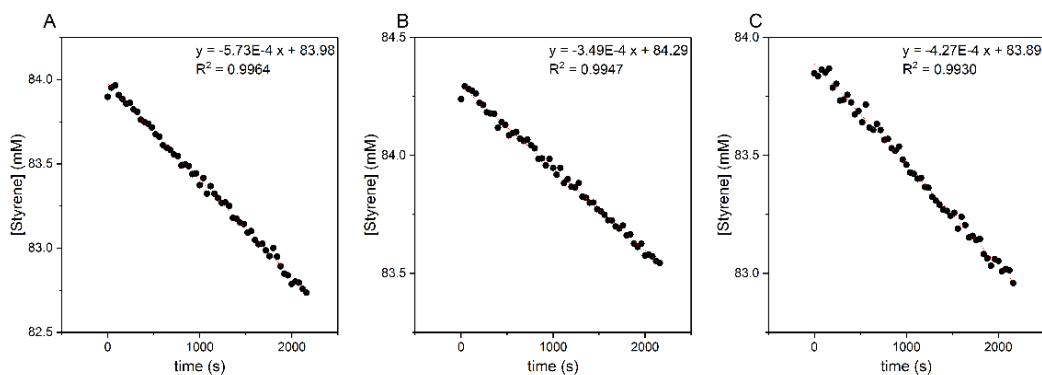
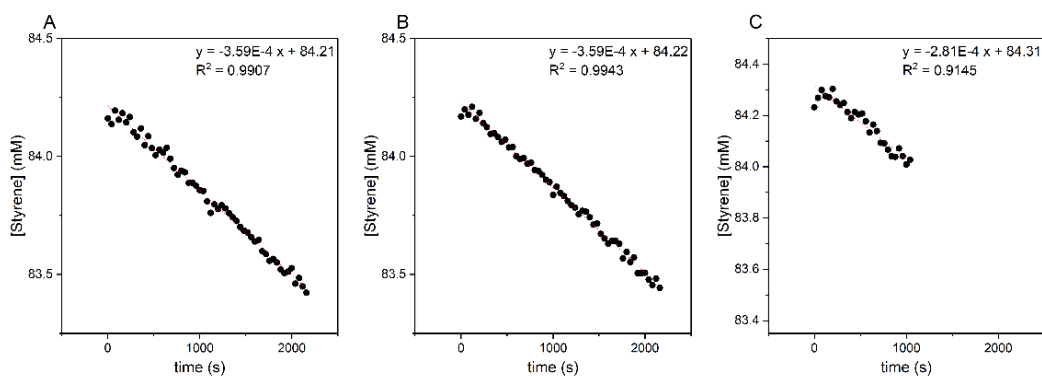


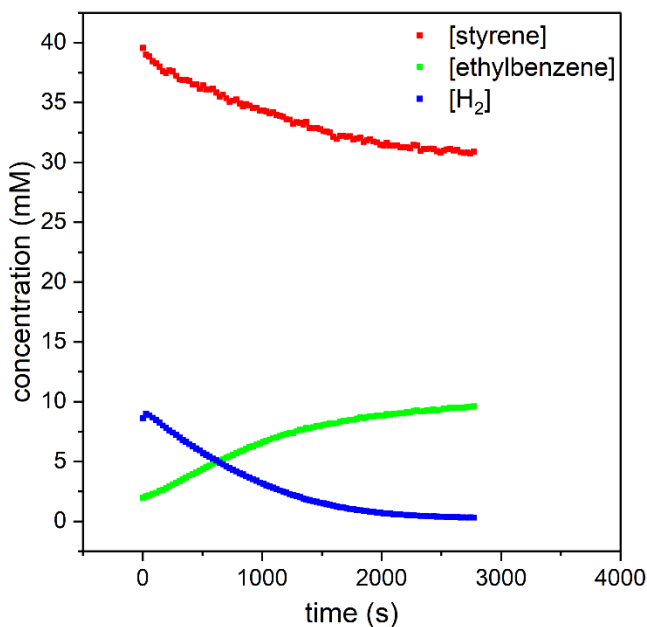
Figure 2.3.38 Plots of [styrene] (mM) vs. time (s) for $(5\text{-}^{\text{NP}}\text{FP})\text{Rh}(\eta^2\text{-C}_2\text{H}_4)\text{Cl}$ (**5^{NP}FP-A**) catalyzed styrene hydrogenation. The reaction was performed in triplicate with 0.5 mM **5^{NP}FP-A**, 87 mM styrene, 50 psig H_2 in CD_2Cl_2 , 45 °C.



The $[\text{Rh}(\eta^2\text{-C}_2\text{H}_4)_2(\mu\text{-Cl})_2]$ catalyzed styrene hydrogenation exhibits a much higher reactivity than $(6\text{-FP})\text{Rh}(\eta^2\text{-C}_2\text{H}_4)\text{Cl}$ (**6FP-A**) and $(5\text{-}^{\text{NP}}\text{FP})\text{Rh}(\eta^2\text{-C}_2\text{H}_4)\text{Cl}$ (**5^{NP}FP-A**). As a result, it is difficult to apply the initial rate method in this case because (1) the $[\text{Rh}(\eta^2\text{-C}_2\text{H}_4)_2(\mu\text{-Cl})_2]$ catalyzed styrene hydrogenation is too rapid for the determination of initial data at high concentration of the Rh catalyst; and (2) due to the reaction before the data acquisition, the consumption of H_2 has already started. Thus, the initial concentration of

H₂ is inconsistent for different experiments. To avoid the complications in the initial rate method, an alternative method was applied for rate determination. Based on the concentration vs. time plots (**Figure 2.3.39**), we elucidated that the reaction is first-order on the concentration of H₂ and styrene. The rate equation is shown in **Eq. 2-9**, in which [Rh] represents the concentration of [Rh(η^2 -C₂H₄)₂(μ -Cl)]₂, and the variable x is the order on [Rh(η^2 -C₂H₄)₂(μ -Cl)]₂ that needs to be determined. Since [Rh(η^2 -C₂H₄)₂(μ -Cl)]₂ is the catalyst, the [Rh] should be a constant during the reaction. Thus, for each entry with a known initial [Rh], the rate equation could be expressed as a second-order reaction with first-order kinetics on both styrene and H₂ (**Eq. 2-10**).

Figure 2.3.39 Plots of [styrene], [ethylbenzene] and [H₂] (mM) vs. time (s) for [Rh(η^2 -C₂H₄)₂(μ -Cl)]₂ catalyzed styrene hydrogenation.



The reaction was performed in triplicate with 0.25 mM [Rh(η^2 -C₂H₄)₂(μ -Cl)]₂; 44 mM styrene, 50 psig H₂ in CD₂Cl₂, 45 °C.

$$\text{rate} = d[\text{EtPh}]/dt = k[\text{Rh}]^x[\text{H}_2][\text{styrene}]$$

Eq. 2-9

$$\text{rate} = k'[\text{H}_2][\text{styrene}] \quad (k' = k[\text{Rh}]^x) \quad \text{Eq. 2-10}$$

For a second-order reaction that is first-order in both reactants, **Eq. 2-11** can be used to estimate k , in which $\{[\text{B}]_o - [\text{A}]_o\}t$ is proportional to $\ln\{[\text{B}][\text{A}]_o/[\text{A}][\text{B}]_o\}$.^{36, 65} In this study, it is proposed that k' can be estimated by solving for the slope of plot for $\{[\text{styrene}]_o - [\text{H}_2]_o\}t$ vs. $\ln\{[\text{styrene}][\text{H}_2]_o/[\text{H}_2][\text{styrene}]_o\}$, which is shown in **Figure 2.3.40** – **Figure 2.3.43** with the reaction conditions and estimated slopes indicated.

For a reaction $\text{A} + \text{B} \rightleftharpoons \text{P}$ and rate = $k[\text{A}][\text{B}]$

$$\ln\{[\text{B}][\text{A}]_o/[\text{A}][\text{B}]_o\} = \{[\text{B}]_o - [\text{A}]_o\}kt \quad \text{Eq. 2-11}$$

$[\text{A}]$, $[\text{B}]$ = detected concentration at time t ; $[\text{A}]_o$, $[\text{B}]_o$ = original concentration of A and B

Figure 2.3.40 Plots of $\ln\{[\text{styrene}][\text{H}_2]_o/[\text{H}_2][\text{styrene}]_o\}$ vs. $\{[\text{styrene}]_o - [\text{H}_2]_o\}t$ ($\text{mM}\cdot\text{s}$) for $[\text{Rh}(\eta^2\text{-C}_2\text{H}_4)_2(\mu\text{-Cl})_2]$ catalyzed styrene hydrogenation. The reaction was performed in triplicate with 2 mM $[\text{Rh}(\eta^2\text{-C}_2\text{H}_4)_2(\mu\text{-Cl})_2]$, 44 mM styrene, 50 psig H_2 in CD_2Cl_2 , 45 °C.

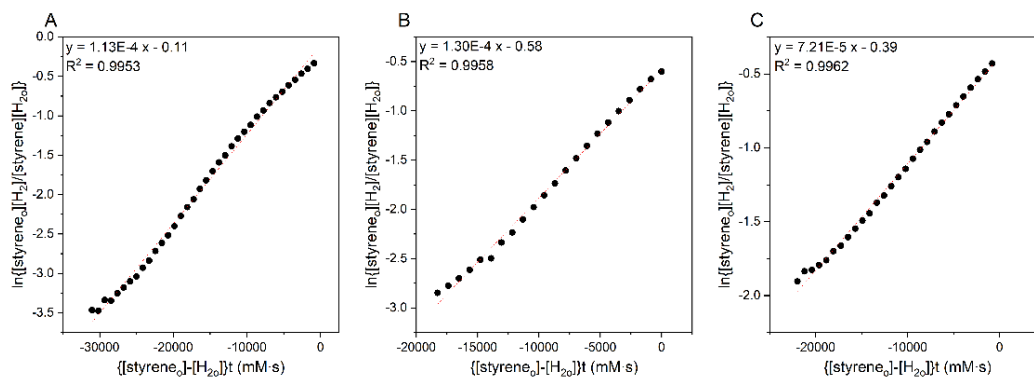


Figure 2.3.41 Plots of $\ln\{[\text{styrene}][\text{H}_2]_o/[\text{H}_2][\text{styrene}]_o\}$ vs. $\{[\text{styrene}]_o - [\text{H}_2]_o\}t$ (mM·s) for $[\text{Rh}(\eta^2\text{-C}_2\text{H}_4)_2(\mu\text{-Cl})_2]$ catalyzed styrene hydrogenation. The reaction was performed in triplicate with 1 mM $[\text{Rh}(\eta^2\text{-C}_2\text{H}_4)_2(\mu\text{-Cl})_2]$, 44 mM styrene, 50 psig H_2 in CD_2Cl_2 , 45 °C.

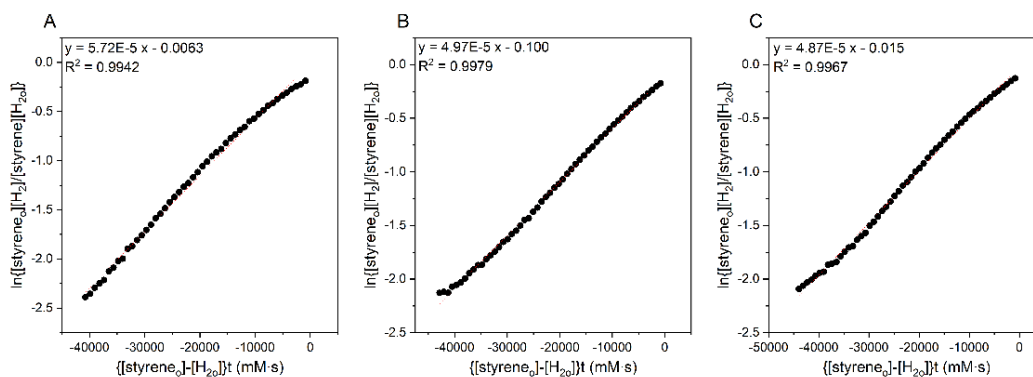


Figure 2.3.42 Plots of $\ln\{[\text{styrene}][\text{H}_2]_o/[\text{H}_2][\text{styrene}]_o\}$ vs. $\{[\text{styrene}]_o - [\text{H}_2]_o\}t$ (mM·s) for $[\text{Rh}(\eta^2\text{-C}_2\text{H}_4)_2(\mu\text{-Cl})_2]$ catalyzed styrene hydrogenation. The reaction was performed in triplicate with 0.5 mM $[\text{Rh}(\eta^2\text{-C}_2\text{H}_4)_2(\mu\text{-Cl})_2]$, 44 mM styrene, 50 psig H_2 in CD_2Cl_2 , 45 °C.

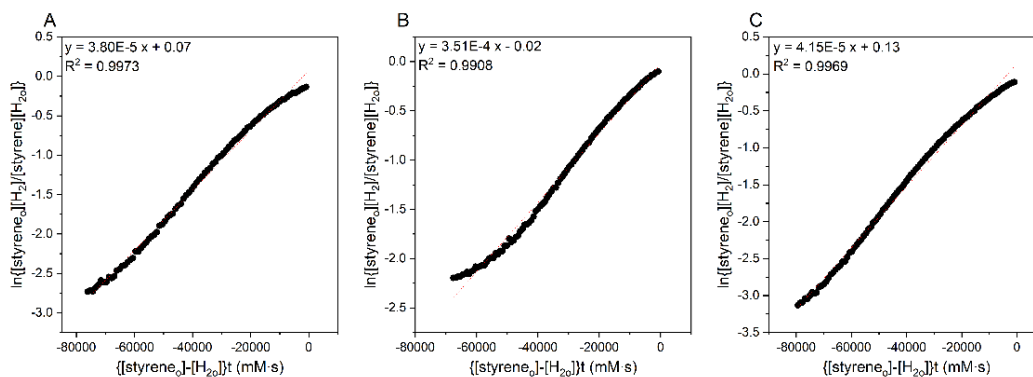
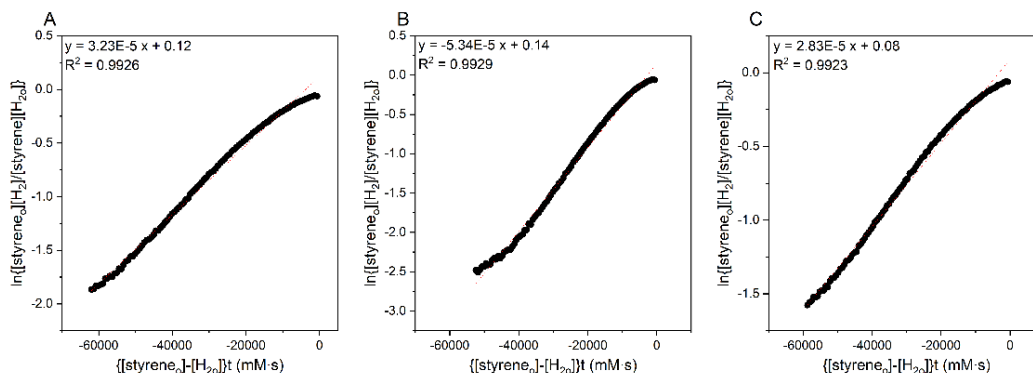


Figure 2.3.43 Plots of $\ln\{[\text{styrene}][\text{H}_2]_0/[\text{H}_2][\text{styrene}]_0\}$ vs. $\{[\text{styrene}]_0-[\text{H}_2]_0\}t$ (mM·s) for $[\text{Rh}(\eta^2\text{-C}_2\text{H}_4)_2(\mu\text{-Cl})_2]$ catalyzed styrene hydrogenation. The reaction was performed in triplicate with 0.25 mM $[\text{Rh}(\eta^2\text{-C}_2\text{H}_4)_2(\mu\text{-Cl})_2]$, 44 mM styrene, 50 psig H_2 in CD_2Cl_2 , 45 °C.



As shown in **Figure 2.3.44**, $(5\text{-}^{\text{NP}}\text{FP})\text{Rh}(\eta^2\text{-C}_2\text{H}_4)\text{Cl}$ (**5^{NP}FP-A**) is partially transformed to multiple species when mixing with styrene and dihydrogen (**Figure 2.3.44a**). Although **5^{NP}FP-B** has not been successfully isolated, a crystal structure of **5^{NP}FP-B** was obtained by reacting **5^{NP}FP-A** with excess of styrene, followed by vapor diffusion of pentane into the concentrated benzene solution. The ^1H NMR spectrum of the crude product from the reaction between styrene and **5^{NP}FP-A** is consistent with the new peaks shown in **Figure 2.3.44a** compared to **Figure 2.3.44c**. After 1 hour of the catalytic hydrogenation, although the peaks for the proposed **5^{NP}FP-B** remain, the resonances for **5^{NP}FP-A** have disappeared (**Figure 2.3.44b**), which likely undergo a ligand dissociation process. We were unable to isolate the Rh products from dissociation of the capping arene, but it seems reasonable that a dimeric complex(es) with bridging chloride ligands could form, and this speculation is consistent with our kinetic studies.

Figure 2.3.44 ^1H NMR evidence for the decomposition of $(5\text{-}^{\text{NP}}\text{FP})\text{Rh}(\eta^2\text{-C}_2\text{H}_4)\text{Cl}$ (**5^{NP}FP-A**) during the catalytic styrene hydrogenation. Conditions: (a) 4 mM **5^{NP}FP-A**, 87 mM styrene, 50

psig H₂, 25 °C, 0 hour in CD₂Cl₂; (b) 4 mM 4, 87 mM styrene, 50 psig H₂, 45 °C, 1 hour in CD₂Cl₂; (c) 4 in CD₂Cl₂.

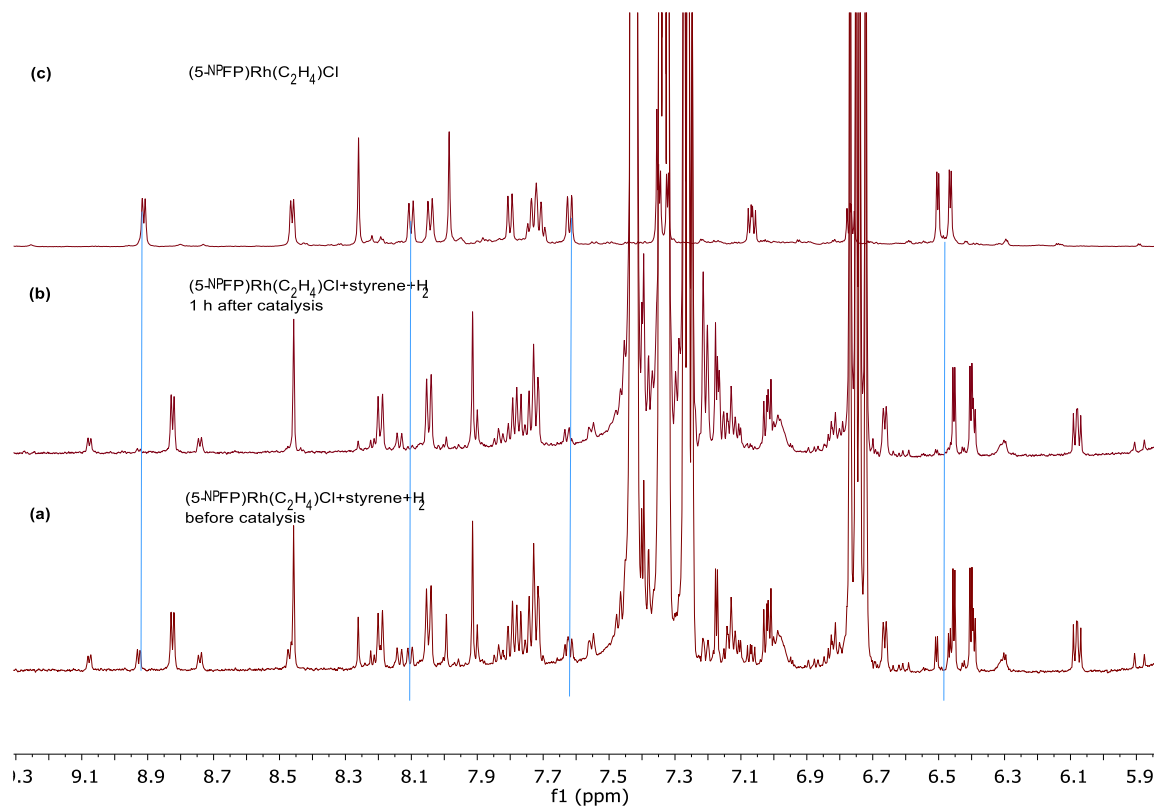
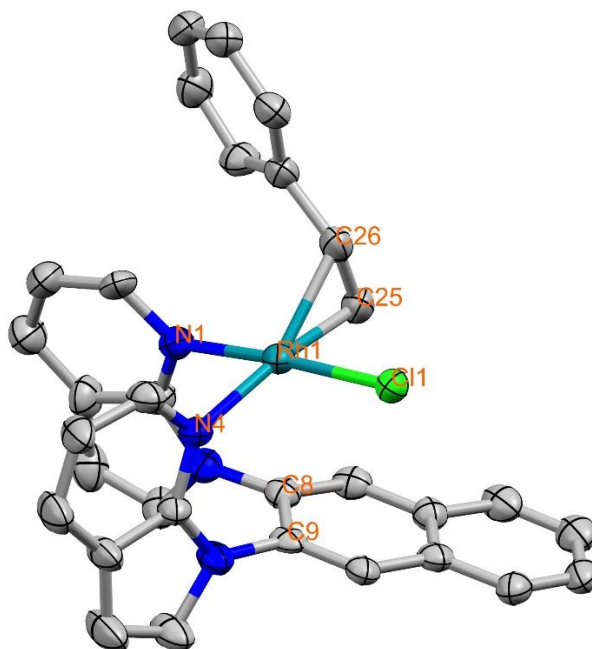
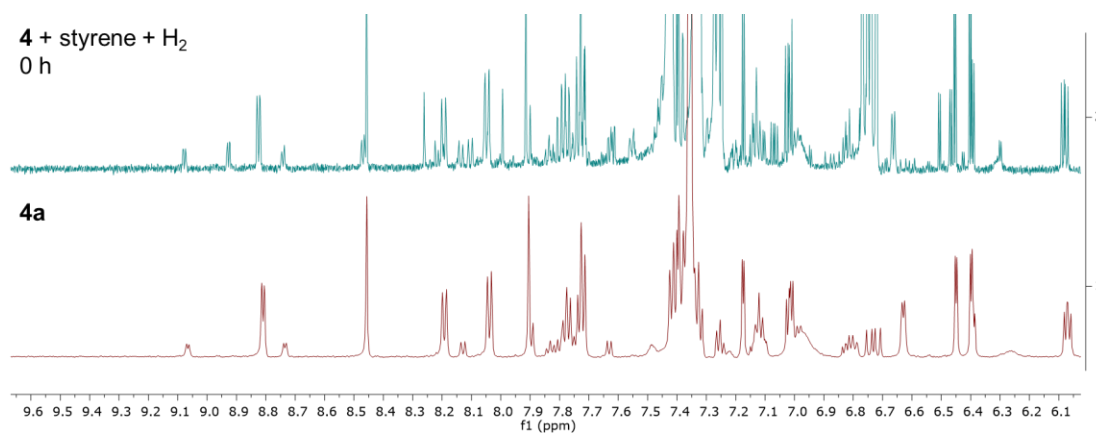


Figure 2.3.45 ORTEP of (5-^{NP}FP)Rh(Cl)(η^2 -styrene) (**5^{NP}FP-B**). Ellipsoids are drawn at 50% probability level. Hydrogen atoms and noncoordinating solvents are omitted for clarity.



Selected bond lengths for **5^{NP}FP-B** (Å): Rh1-N1 2.043(6), Rh1-N4 2.141(5), Rh1-Cl1 2.347(2), Rh1-C25 2.107(8), Rh1-C26 2.137(6), C25-C26 1.38(1). Selected bond angles for **5^{NP}FP-B** (deg): N1-Rh1-N4 83.2(2), N1-Rh1-C25 92.7(3), N1-Rh1-Cl1 176.0(2), N4-Rh1-Cl1 93.4(2), Cl1-Rh1-C25 90.3(2).

Figure 2.3.46 Comparison of the ¹H NMR spectra for (1) 4 mM **5^{NP}FP-A**, 87 mM styrene, 50 psig H₂, 25 °C, 0 hour in CD₂Cl₂ (above); (2) crystal of **5^{NP}FP-B** in CD₂Cl₂ (below).



2.3.7 Mechanistic Studies based on Density Functional Theory

In this part, all the computational results are from our collaborator Charles B. Musgrave III and William A. Goddard III from the California Institute of Technology.

To understand how the capping arene ligand identity influences the Rh-catalyzed hydrogenation of olefins, we performed Density Functional Theory (DFT) calculations. These calculations utilized the B3LYP functional with the D3 correction for London dispersion (van der Waals attraction) forces.

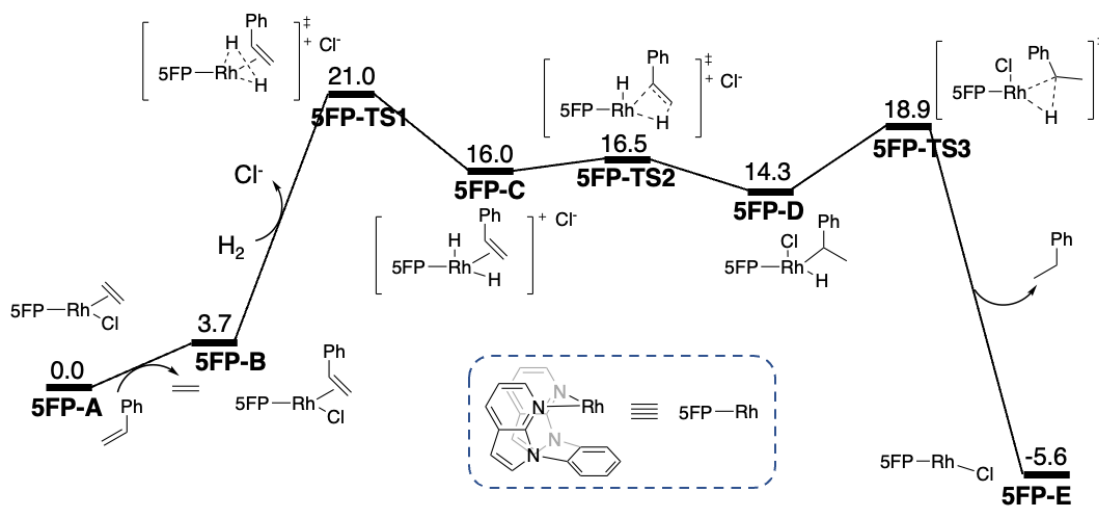
The mechanism we studied, based on experimental results (see above), begins with displacement of a coordinated ligand with the olefin to be hydrogenated. The metal catalyst then undergoes oxidative addition by H₂ to generate two hydride ligands. With two hydrides and the olefin present, the olefin then undergoes insertion into an [M]–H bond (M = metal) to form an alkyl ligand. Finally, the catalyst reductively eliminates the second hydride to form the alkane.

Starting with (5-FP)Rh(C₂H₄)Cl (**5FP-A**), displacement of ethylene with styrene is uphill by 3.7 kcal/mol. As expected, styrene prefers to bind the Rh via the alkenyl chain as opposed to the phenyl ring. The DFT calculations predict little geometric change between Rh and the capping arene when ethylene and styrene are exchanged. The Rh–C_{cap} distances for **5FP-A** are calculated to be 3.14 Å and 3.16 Å; whereas when styrene is coordinated these distances are both calculated to be 3.12 Å. With the formation of (5-FP)Rh(η²-styrene)Cl (**5FP-B**), the complex can now dissociate chloride and undergo subsequent H₂ oxidative addition towards [(5-FP)Rh(H)₂(η²-styrene)]Cl (**5FP-C**). The oxidative addition transition state (**5FP-TS1**) lies 21.0 kcal/mol above the starting state. In **5FP-TS1**, one of the H atoms from H₂ maintains a non-covalent interaction with the nearby chloride, leading

to unequal Rh–H distances: one Rh–H distance is 1.53 Å while the other is 1.67 Å (the former H being in-plane with the N–Rh–N and the latter being the axial H directed towards Cl). Additionally, in **5FP-TS1**, the C=C bond of styrene orients parallel to the N–Rh–N plane (**Figure 2.3.48**), despite the preferred orthogonal orientation in **5FP-B**. Following oxidative addition of dihydrogen, the free energy of **5FP-C** lies 16.0 kcal/mol above the starting state; this high free energy confirms the bias towards Rh(I) when bound to the capping arene ligand. The complex **5FP-C** can undergo styrene migratory insertion into a Rh–H bond to form **5FP-D**. This migratory insertion transition state (**5FP-TS2**) has 4 possible styrene conformations. The aryl ring of styrene can reside in the UC, LC, UT, or LT conformations, where U and L are upper and lower (relative to the N–Rh–N plane), C and T are cis and trans (relative to the 5FP backbone). DFT predicts the **5FP-TS2-LC** conformation to be the most favorable, resulting in a free energy barrier of 16.5 kcal/mol relative to **5FP-A**. The LC conformation enables favorable interaction between styrene and the 5-FP ligand, similar to **6FP-B**. In ascending free energy and relative to **5FP-A**, the other **5FP-TS2** barriers for UC, LT, and UT are 17.6, 20.8, and 22.9 kcal/mol, respectively. Again, we see the C conformations to be lower in free energy due to the favorable VdW interactions between styrene and the 5-FP ligand. In **5FP-D**, the H axial to the N–Rh–N plane reorients to reside in the plane; the chloride subsequently binds to Rh via the axial coordination site so that Rh remains 5-coordinate. Finally, the complex overcomes the last barrier (**5FP-TS3**) in which the second H atom is transferred leading to reductive elimination of ethylbenzene. The transition state **5FP-TS3** lies 18.9 kcal/mol above **5FP-A**, and the reduced intermediate [(5-FP)RhCl]⁺ and free ethylbenzene (**5FP-E**) are –5.6 kcal/mol relative to the starting state. Our calculations are consistent with the oxidative

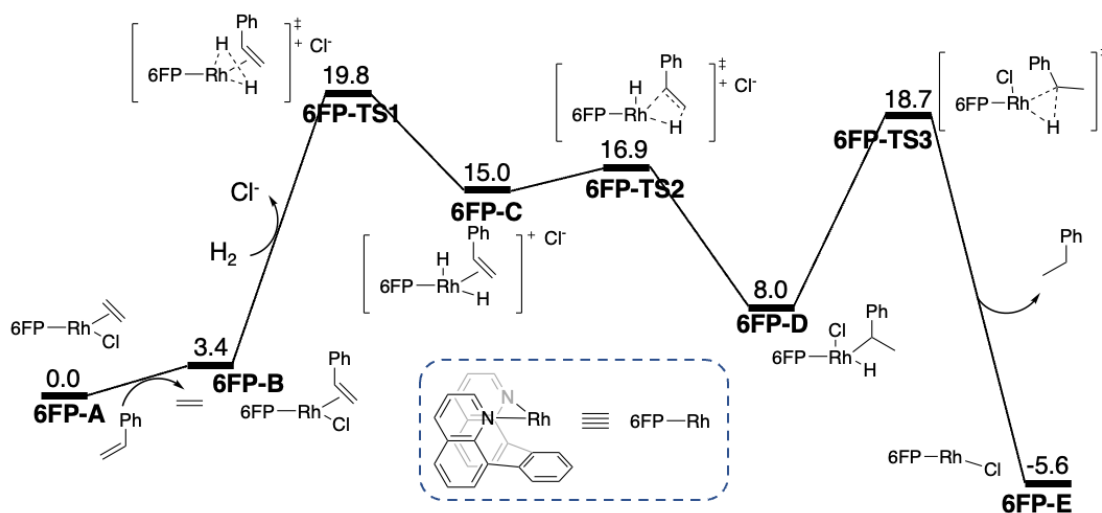
addition of dihydrogen (**5FP-TS1**) being the rate-limiting step; **5FP-TS3** requires 2.1 kcal/mol less than **5FP-TS1**.

Scheme 2.3.6 DFT free energies at 318 K for conversion of styrene to ethylbenzene using (5-FP)Rh(η^2 -C₂H₄)Cl (**5FP-A**) as catalyst precursor. Free energies are in kcal/mol.



For comparison, we also predicted the Gibbs free energy surface for the catalytic hydrogenation of styrene using **6FP-A** as catalyst precursor. Experiments reveal that at 318 K, Rh with the 6-FP ligand produces ethylbenzene nearly twice as fast as Rh with the 5-FP ligand. The complex **5FP-A** generates ethylbenzene at a rate of 0.41(4) $\mu\text{M/s}$ while **6FP-A** gives a catalytic rate of 0.822(8) $\mu\text{M/s}$ (**Figure 2.2.1**). The rate-limiting oxidative addition barrier for the 5-FP ligand is calculated to be 21.0 kcal/mol (**5FP-TS1**). We anticipated that the 6-FP ligand might lower the activation barrier and improve the thermodynamics for oxidative addition of dihydrogen since the arene moiety would be positioned closer to the Rh center and consequently favor the Rh(III) product, hence providing a stabilizing effect. The free energy surface for conversion of styrene to ethylbenzene by **6FP-A** is displayed below (**Scheme 2.3.7**).

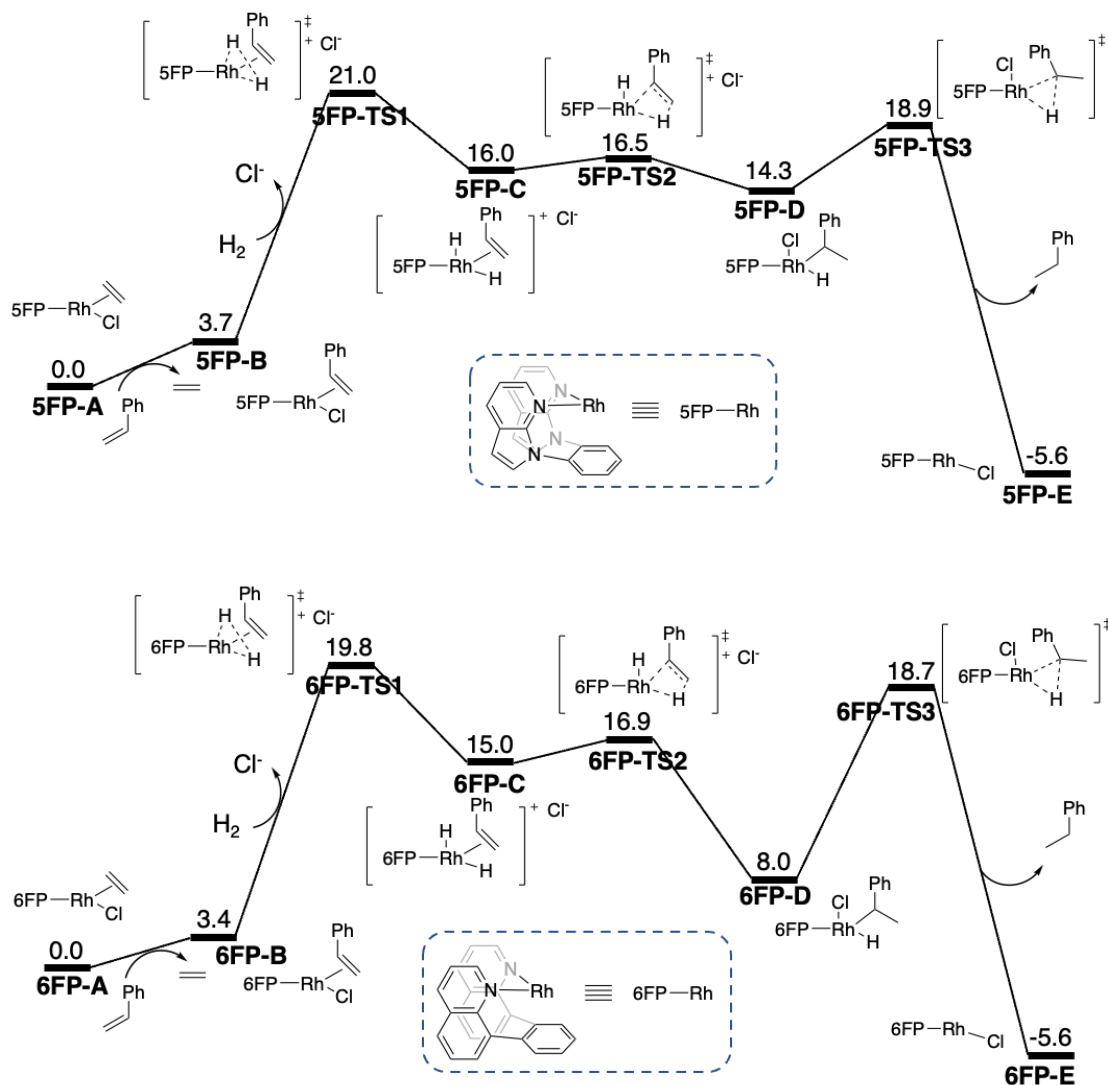
Scheme 2.3.7 DFT free energies at 318 K for conversion of styrene to ethylbenzene via the (6-FP)Rh(η^2 -C₂H₄)Cl (**6FP-A**) catalyst. Free energies are in kcal/mol.



Starting with **6FP-A** at 0.0 kcal/mol, the displacement of ethylene by styrene is endergonic by 3.4 kcal/mol (**6FP-B**). For **6FP-A**, the Rh–C_{cap} distances are calculated to be 2.96 Å and 3.03 Å; for **6FP-B**, these same distances are decreased to 2.91 Å and 3.00 Å. Oxidative addition of H₂ requires a free energy barrier of 19.8 kcal/mol (**6FP-TS1**), leading to **6FP-C** at 15.0 kcal/mol above the starting state. For subsequent styrene insertion into a Rh–H bond, DFT predicts a barrier of 16.9 kcal/mol (**6FP-TS2-UC**). For **6FP-TS2**, the LC, UT, and LT conformers stand 17.3, 19.2, and 20.7 kcal/mol above **6FP-A**, such that the UC yields the lowest barrier. Again, the C conformations are lower in energy than the T analogs; however, **6FP-TS2** prefers structure UC while **5FP-TS2** prefers LC. This is a consequence of the stacking orientation of styrene with the 5-FP and 6-FP ligands. The following intermediate, (6-FP)Rh(C₈H₉)Cl (**6FP-D**) lies significantly lower than the 5-FP analog at 8.0 kcal/mol relative to **6FP-A**. We hypothesize that this lowering in free energy is due to stabilization of the Rh^{III} center by the 6-FP capping arene moiety. Rh^{III} is a saturated 18-electron system that prefers an octahedral coordination environment. The 5-

FP ligand prevents Rh^{III} of this preferred 6-coordinate geometry since the arene is positioned at a distance that challenges arene to Rh electron-donation; however, 6-FP allows the Rh^{III} in **6FP-D** to achieve a pseudo-octahedral coordination with a Rh–C_{cap} distance of 2.49 Å, thus making **6FP-D** a low-energy intermediate. In comparison, the analogous Rh–C_{cap} distance in **5FP-D** is 2.74 Å. The trend that a Rh^{III} complex with 6-FP ligand is more stable than the similar Rh^{III} complex with 5-FP ligand is consistent with our previous studies, in which the reductive elimination of (5-FP)Rh(Me)(TFA)₂ (TFA = trifluoroacetate) is faster than (6-FP)Rh(Me)(TFA)₂.³⁶ Finally, reductive elimination to form free ethylbenzene through **6FP-TS3** is predicted by DFT to be 18.7 kcal/mol above the starting state, leading to (6-FP)RhCl (**6FP-E**) and free ethylbenzene at –5.6 kcal/mol. A comparison of the energy diagram for the styrene hydrogenation catalyzed by **6FP-A** and **5FP-A** is shown in **Figure 2.3.47**.

Figure 2.3.47 Comparison of the energy diagram for the styrene hydrogenation catalyzed by **6FP-A** and **5FP-A**.



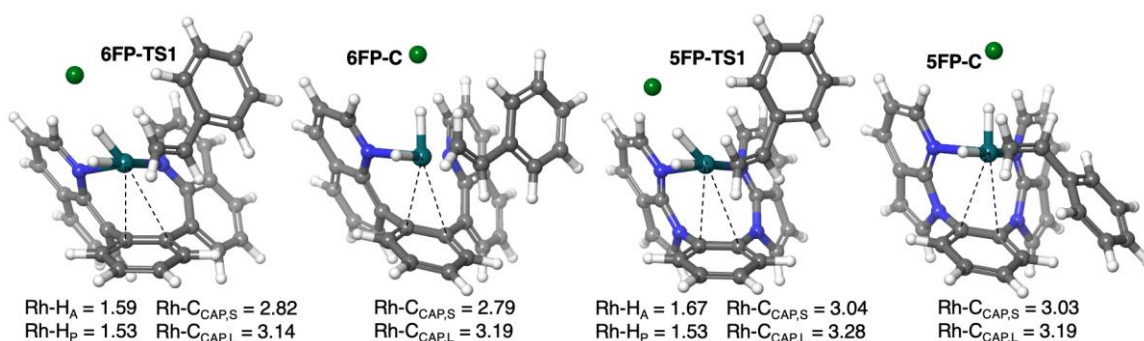
Because TS1 is calculated to be the highest barrier for catalyst precursors with both the 5-FP and 6-FP mechanisms, it is likely the primary contributor to the kinetic rate for styrene hydrogenation. In calculated pathway using the 5-FP ligand, ΔG_{5FP}^\ddagger for the dihydrogen oxidative addition is 21.0 kcal/mol. For the 6-FP ligand, ΔG_{6FP}^\ddagger is reduced to 19.8 kcal/mol.

The calculated ΔG_{6FP}^\ddagger is consistent with the experimental value from the Eyring plot, which is 20.0(8) kcal/mol.

The difference in barriers for dihydrogen oxidative addition ($\Delta\Delta G^\ddagger = \Delta G_{6FP}^\ddagger - \Delta G_{5FP}^\ddagger$) is -1.2 kcal/mol. Using the Eyring equation along with our computed $\Delta\Delta G^\ddagger$, we predict that the 6-FP ligand enables Rh to produce ethylbenzene 6.6 times faster than 5-FP, which, given deviations in both experimental and computational data, agree well with the experimentally observed rate enhancement of approximately 2-fold for 6-FP over 5-FP. These results are consistent with our hypothesis that 6-FP ligands should favor Rh(III) states more than 5-FP ligands. Our rationalization is that the 6-FP structure places the arene group of the capping arene ligand in closer proximity to Rh(III), hence enhancing arene to Rh donation and providing a more stable complex. In contrast, the 5-FP structure, which positions the arene group farther, should relatively destabilize the Rh(III) state. The calculated Rh–C_{cap} distances in both the transition states for dihydrogen oxidative addition and the products are consistent with this explanation. In **5FP-TS1** the Rh–C_{cap} distances are 3.04 and 3.28 Å. The analogous distances for **6FP-TS2** are 2.82 and 3.14 Å (**Figure 2.3.48**). **Table 2.3.2** shows a comparison of the C_{cap}–C_{cap} bond distances of the two closest carbon on the arene moiety for **5FP-A** and **6FP-A** measured from the crystal structures. The Rh–C_{cap} distances are 3.041 Å and 3.110 Å for **5FP-A**, and the Rh–C_{cap} distances are 2.578 Å and 2.553 Å for **6FP-A**. The C_{cap}–C_{cap} bond distance for **6FP-A** is 0.020(4) Å longer than for the 6-FP ligand; whereas the C_{cap}–C_{cap} bond distance for **5FP-A** does not show a statically meaningful difference from the 5-FP ligand {1.397(3) vs. 1.399(1)}. The elongated C_{cap}–C_{cap} bond in **6FP-A** is consistent with the proposed electronic interaction between the capping moiety and the Rh metal center. Additionally, the non-covalent

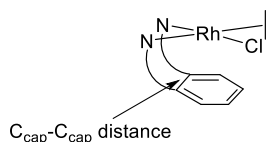
interaction of the outer-shell Cl^- with the reacting H_2 seems to play a role. In **5FP-TS1**, the Cl-H distance is quite short at 1.86 Å (not shown), whereas this distance is increased to 2.05 Å in **6FP-TS1**, indicating a weaker interaction. Because Cl^- induces a partial positive charge on the H, a stronger interaction means a more positive H, which is less likely to bind to Rh. Indeed, the free energy surfaces show this to be the case. The Cl-H distance in **5FP-TS1** is shorter by 0.19 Å, resulting in a stronger dipole and thus more positive charge on H, which in turn requires a higher free energy barrier to oxidize Rh.

Figure 2.3.48 DFT-optimized transition states (**6FP-TS1** and **5FP-TS1**) and products (**6FP-C** and **5FP-C**) for H_2 oxidative addition for: (5-FP)Rh(η^2 -styrene)Cl (left) and (6-FP)Rh(η^2 -styrene)Cl (right).



DFT-optimized transition states (**6FP-TS1** and **5FP-TS1**) and products (**6FP-C** and **5FP-C**) for H_2 oxidative addition for: (5-FP)Rh(η^2 -styrene)Cl (left) and (6-FP)Rh(η^2 -styrene)Cl (right).

Table 2.3.2 Rh–C_{cap} distances and C_{cap}–C_{cap} bond distance for (5-FP)Rh(η^2 -C₂H₄)Cl (**5FP-A**) and (6-FP)Rh(η^2 -C₂H₄)Cl (**6FP-A**).



Molecule	Rh–C _{cap} distances	C _{cap} –C _{cap} bond distance
	(Å)	(Å)
5-FP ligand	N/A	1.399(1)
6-FP ligand	N/A	1.402(2)
5FP-A	3.041, 3.110	1.397(3)
6FP-A	2.578, 2.553	1.422(4)

Although the transition states for the reductive elimination of ethylbenzene from **5FP-D** and **6FP-D** show a very close relative energy (~ 0.2 kcal/mol difference) with respect to the catalyst precursor (**5FP-A** or **6FP-A**, respectively), the difference between the activation energies for the reductive elimination of **5FP-D** and **6FP-D** is significant. The calculated activation energy for the reductive elimination of **5FP-D** is 4.6 kcal/mol, whereas the activation energy for the reductive elimination of **6FP-D** is 10.7 kcal/mol. This activation barrier difference in reductive elimination could be attributed to the difference in stability of **5FP-D** and **6FP-D**, as discussed above.

2.4 Summary and Conclusions

We have investigated the ligand effect of four capping arene-Rh complexes on olefin hydrogenation reactions. The trend on reaction rates indicates an observed dependence on the coordinated capping arene ligand where **5^{NP}FP-A** > **6FP-A** > **5FP-A**, while the **6^{NP}FP-**

A undergoes rapid decomposition process to generate free ligand. Based on the kinetic and computational modeling studies, an “olefin first” hydrogenation mechanism has been proposed. For the comparison of **5FP-A** and **6FP-A**, the DFT calculations are consistent with our hypothesis. Relative to 5-FP, the structure of the 6-FP ligand stabilizes Rh(III) complexes and the dihydrogen oxidative addition transition state that forms the first Rh(III) intermediate. Our computational modeling suggests that the rate-determining step is probably the oxidative addition of dihydrogen, and the calculated activation barrier for **6FP-A** catalyzed styrene hydrogenation is 1.2 kcal/mol lower than that for **5FP-A**, which is consistent with our experimental results. We anticipate that the strategy of using the structural features of capping arene ligands, and specifically metal/arene distance and bonding, to modulate the energetics of intermediates and transition states can be extended to other catalytic reactions, especially those that proceed via formal redox and coordination number/geometry changes.

2.5 Experimental section

General Methods. Unless otherwise noted, all reactions were operated under a dinitrogen atmosphere in a glovebox ($O_2 < 10$ ppm) or using standard Schlenk line techniques. All solvents were dried, degassed and stored in the glovebox with 4Å molecular sieves. All glassware was dried in an oven (150 °C) overnight before use. All NMR spectra were recorded on Varian Inova 600 MHz spectrometer or Bruker Advance III 800 MHz spectrometer. The operating frequency for $^{13}C\{^1H\}$ NMR spectroscopy is 150 MHz (on 600 MHz instrument) or 201 MHz (on 800 MHz instrument). All 1H NMR and $^{13}C\{^1H\}$ NMR spectra are referenced against the residual 1H resonances (1H NMR) or the $^{13}C\{^1H\}$ resonances ($^{13}C\{^1H\}$ NMR) of the deuterated solvents. All spectra were recorded at 25 °C

unless otherwise indicated. The temperature for all variable temperature NMR experiments were calibrated using a MeOH- d_4 standard.⁶⁶ The preparation of $[\text{Rh}(\eta^2\text{-C}_2\text{H}_4)_2(\mu\text{-Cl})_2]$, 5-FP, 6-FP, 5- $^{\text{NP}}$ FP, 6- $^{\text{NP}}$ FP, (5-FP)Rh(Cl)($\eta^2\text{-C}_2\text{H}_4$), (6-FP)Rh(Cl)($\eta^2\text{-C}_2\text{H}_4$), (5- $^{\text{NP}}$ FP)Rh(Cl)($\eta^2\text{-C}_2\text{H}_4$), (6- $^{\text{NP}}$ FP)Rh(Cl)($\eta^2\text{-C}_2\text{H}_4$) followed reported procedures.^{36, 67}

Synthesis and Characterization of (6-FP)Rh(Cl)(η^2 -styrene). To a THF solution (25 mL) of (6-FP)Rh(Cl)($\eta^2\text{-C}_2\text{H}_4$) (20 mg, 40 μmol), styrene (0.20 mL, 182 mg, 1.75 mmol) was added and stirred at room temperature for 24 hours. The reaction solution was filtered through a Buchner funnel with fine fritted disc. The amount of solvent was reduced by vacuum to obtain a concentrated solution. 30 mL of pentanes was added to the solution, and the products precipitated as an orange powder. X-ray quality crystals of (6-FP)Rh(Cl)(η^2 -styrene) were obtained by slow vapor diffusion of *n*-pentane into a benzene solution. Two isomers were obtained with a molecular ratio of approximately 1 (species **A**) to 1.5 (species **B**). ^1H NMR (600 MHz, CD_2Cl_2) δ 9.95 (d, $J = 4$ Hz, 1H, Ar-*H*, **A**), 9.85 (d, $J = 4$ Hz, 1H, Ar-*H*, **B**), 8.33 (d, $J = 4$ Hz, 1H, Ar-*H*, **B**), 8.21 (d, $J = 8$ Hz, 1H, Ar-*H*, **A**), 8.13 (d, $J = 8$, 1H, Ar-*H*, **B**), 8.08 (d, $J = 8$ Hz, 1H, Ar-*H*, **B**), 8.05 (d, $J = 8$ Hz, 1H, Ar-*H*, **A**), 7.97 (d, $J = 7$ Hz, 1H, Ar-*H*, **A**), 7.77 (t, $J = 8$ Hz, 1H, Ar-*H*, **B**), 7.73 (t, $J = 8$ Hz, 1H, Ar-*H*, **A**), 7.63 – 7.59 (m, 2H, Ar-*H*, **B**), 7.58 (d, $J = 7$ Hz, 1H, Ar-*H*, **A**), 7.56 – 7.50 (m, 5H), 7.47 – 7.45 (m, 1H, Ar-*H*, **B**), 7.44 (d, $J = 8$ Hz, 2H, Ar-*H*, **B**), 7.43 – 7.39 (m, 2H, Ar-*H*, **A**), 7.32 (t, $J = 8$ Hz, 1H, Ar-*H*, **A**), 7.30 – 7.27 (m, 1H, Ar-*H*, **A**; 1H, Ar-*H*, **B**), 6.98 (t, $J = 8$ Hz, 1H, Ar-*H*, **A**), 6.96 – 6.93 (m, 1H, Ar-*H*, **A**; 1H, Ar-*H*, **B**), 6.87 (dd, $J = 7$ Hz, 1H, Ar-*H*, **A**), 6.82 (d, $J = 5$ Hz, 1H, Ar-*H*, **A**), 6.76 – 6.69 (m, 4H), 6.45 (t, $J = 7$ Hz, 1H, Ar-*H*, **B**), 6.31 (t, $J = 7$ Hz, 2H, Ar-*H*, **B**), 6.25 (d, $J = 7$ Hz, 2H, Ar-*H*, **B**), 5.88 (dd, $J = 8, 5$ Hz, 1H, **A**), 5.46 – 5.40 (m, 1H, PhCH=C, **A**), 3.99 (d, $^3J_{\text{HH}} = 8$ Hz, 1H,

PhC=C–H, **B**), 3.68 (t, $^3J_{\text{HH}} = 10$ Hz, 1H, PhCH=C, **B**), 2.92 (d, $^3J_{\text{HH}} = 11$ Hz, 1H, PhC=C–H, **B**), 2.12 (d, $^3J_{\text{HH}} = 12$ Hz, 1H, PhC=C–H, **A**), 1.73 (d, $^3J_{\text{HH}} = 8$ Hz, 1H, PhC=C–H, **A**). ^{13}C NMR (201 MHz, CD_2Cl_2) δ 156.6, 154.3, 154.1, 153.9, 151.1, 150.2, 150.2, 147.0, 146.8, 141.3, 141.2, 140.7, 140.6, 138.1, 137.4, 136.9, 136.8, 135.5, 135.1, 134.9, 134.6, 133.9, 133.4, 132.8, 132.5, 131.5, 131.4, 131.2, 130.2, 127.8, 127.6, 127.5, 127.4, 127.2, 127.1, 126.9, 126.8, 126.7, 126.4, 126.3, 124.4, 124.1, 122.4, 122.2, 121.8, 121.5, 120.5, 114.1, 57.8 (d, $^1J_{\text{Rh-C}} = 18$ Hz, Ph–C for coordinated styrene on **A**), 48.2 (d, $^1J_{\text{Rh-C}} = 13$ Hz, Ph–C for coordinated styrene on **B**), 41.6 (d, $^1J_{\text{Rh-C}} = 21$ Hz, PhC=C for coordinated styrene on **B**), 33.5 (d, $^1J_{\text{Rh-C}} = 13$ Hz, PhC=C for coordinated styrene on **A**). We were unable to obtain satisfactory elemental analysis since the complex decomposes under vacuum.

Eyring plots for (6-FP)Rh(Cl)(η^2 -C₂H₄) catalyzed styrene hydrogenation. The sample preparation is similar to the kinetic studies described above. A J. Young tube was loaded with 0.40 mL of stock solution in CD_2Cl_2 containing 1 mM (6-FP)Rh(Cl)(η^2 -C₂H₄), 44 mM styrene and 0.6 mM HMB (internal standard) under N₂ atmosphere, and then pressurized with 50 psig H₂. The J. Young tube was heated to the designated temperature noted in **Figure 2.3.18** in the NMR instrument. Arrayed ^1H NMR spectra were obtained to measure the initial rates of the styrene hydrogenation.

Isotopic study for (6-FP)Rh(Cl)(η^2 -C₂H₄) catalyzed styrene hydrogenation. In a J. Young tube, 8 mg (0.02 mmol) (6-FP)Rh(Cl)(η^2 -C₂H₄) and 10 μL (9.1 mg, 0.087 mmol) styrene were added and dissolved in 0.5 mL CD_2Cl_2 under N₂ atmosphere. The tube was charged with 50 psig of D₂, and heated to 40 °C in an oil bath. The reaction was monitored by ^1H NMR every 24 hours.

Computational Methods. All Density Functional Theory calculations were performed using the Jaguar v10.9 software package by Schrödinger Inc.⁶⁸ All calculations utilized the B3LYP hybrid functional^{69, 70} but including the Grimme-Becke-Jonson D3 correction for London dispersion forces.⁷¹ Rh atoms were described using the Los Alamos large-core pseudopotential (9 explicit electrons)^{72, 73} augmented with diffuse and polarization functions. All other atoms were described by the 6-311G**++ basis set, including polarization and diffuse functions (designated LAV3P**++ in Jaguar). All calculations also included implicit solvent as described by the PBF Poisson Boltzmann continuum model.^{74, 75} We use solvent parameters of: dielectric constant = 8.93 and probe radius = 2.33 Å to match dichloromethane.

Following geometry optimizations, we performed frequency calculations. These calculations served to confirm the intermediate states (no negative eigenmodes in the Hessian) and transition states (single negative eigenmodes in the Hessian). Frequency calculations also served to predict the thermochemical properties (enthalpies, entropies, and free energies) at 318 K.

We also performed periodic calculations using the VASP Software.⁷⁶ These calculations utilized the PBE GGA functional⁷⁷ with the Grimme-Becke-Johnson D3 correction for London dispersion. PAW pseudopotentials were used for all atoms. The plane-wave basis set cutoff was set to 500 eV. Implicit solvent via the VASPsol^{78, 79} module was used with a dielectric constant = 8.93.

Crystallographic Details. A crystal of **6FP-B** or **5^{NP}FP-B** was coated with Paratone oil and mounted on a MiTeGen MicroLoop. The X-ray intensity data were measured on a Bruker D8 Venture Photon III Kappa four-circle diffractometer system equipped with an

Incoatec I μ S 3.0 micro-focus sealed X-ray tube (Mo K α , $\lambda = 0.71073$ Å; Cu K α , $\lambda = 1.54178$ Å) and a HELIOS double bounce multilayer mirror monochromator. The frames were integrated with the Bruker SAINT software package⁸⁰ using a narrow-frame algorithm. Data were corrected for absorption effects using the Multi-Scan method (SADABS).⁸⁰ The structure was solved and refined using the Bruker SHELXTL Software Package⁸¹ within APEX3/4⁸⁰ and OLEX2⁸². Non-hydrogen atoms were refined anisotropically. Each solvent site and part of the main molecule were disordered over two positions. The vinylic hydrogen atoms on C25 and C26 in **5^{NP}FP-B** were located in the electron density map and refined isotropically. All other hydrogen atoms in both structures were placed in geometrically calculated positions with $U_{iso} = 1.2U_{equiv}$ of the parent atom. In **6FP-B**, each solvent site and part of the main molecule were disordered over two positions. The relative occupancy at each site was freely refined. Constraints and restraints were used on the anisotropic displacement parameters and bond lengths of most of the disordered atoms. CCDC 2166578 and 2201532 contains the supplementary crystallographic data for this chapter.

Table 2.5.1 Crystal Structure Data for (6-FP)Rh(Cl)(η^2 -styrene) (**6FP-B**) and (5-^{NP}FP)Rh(Cl)(η^2 -styrene) (**5^{NP}FP-B**).

	(6-FP)Rh(Cl)(η^2-styrene) (6FP-B)	(5-^{NP}FP)Rh(Cl)(η^2-styrene) (5^{NP}FP-B)
CDCC	2166578	2201532
Chemical formula	C ₄₄ H ₃₆ ClN ₂ Rh	C ₃₂ H ₂₄ ClN ₄ Rh
FW (g/mol)	731.11	602.91
T (K)	100(2)	100(2)
λ (Å)	0.71073	1.54178
Crystal size (mm)	0.028 x 0.044 x 0.190	0.040 x 0.059 x 0.078
Crystal habit	orange plate	red plate
Crystal system	monoclinic	monoclinic

Space group	P 2 ₁ /n	P 2 ₁ /c
a (Å)	10.6104(5)	12.7659(4)
b (Å)	11.3240(6)	13.8981(4)
c (Å)	28.4021(18)	15.6464(5)
α (°)	90	90
β (°)	93.462(2)	107.682(2)
γ (°)	90	90
V (Å³)	3406.3(3)	2644.86(14)
Z	4	4
ρ_{calc} (g/cm³)	1.426	1.514
μ (mm⁻¹)	0.615	6.371
F(000)	1504	1224
θ range (°)	2.01 to 26.39	3.63 to 68.40
Index ranges	-13 ≤ h ≤ 13 -12 ≤ k ≤ 14 -35 ≤ l ≤ 35	-15 ≤ h ≤ 15 -16 ≤ k ≤ 16 -17 ≤ l ≤ 18
Reflections collected	36901	23031
Independent reflections	6980 [R(int) = 0.1088]	4844 [R(int) = 0.1311]
Data /restraints / parameters	6980 / 186 / 487	4844 / 0 / 355
Goodness-of-fit on F²	1.127	1.045
R₁ [I > 2σ(I)]	0.0680	0.0577
wR₂ [all data]	0.1116	0.1400

2.6 References

- (1) Hartwig, J. F. *Organotransition Metal Chemistry: From Bonding to Catalysis*; University Science book, 2009.
- (2) Crabtree, R. H. *Oxidative Addition and Reductive Elimination*; 2014.
- (3) Biffis, A.; Centomo, P.; Del Zotto, A.; Zecca, M. Pd Metal Catalysts for Cross-Couplings and Related Reactions in the 21st Century: A Critical Review. *Chem. Rev.* **2018**, *118*, 2249-2295.

- (4) Chinchilla, R.; Nájera, C. Recent advances in Sonogashira reactions. *Chem. Soc. Rev.* **2011**, *40*, 5084-5121.
- (5) Schmidt, A. F.; Kurokhtina, A. A. Distinguishing Between The Homogeneous and Heterogeneous Mechanisms of Catalysis in the Mizoroki-Heck and Suzuki-Miyaura Reactions: Problems And Prospects. *Kinet. Catal.* **2012**, *53*, 714-730.
- (6) Esteruelas, M. A.; Oro, L. A. Dihydrogen Complexes as Homogeneous Reduction Catalysts. *Chem. Rev.* **1998**, *98*, 577-588.
- (7) Sunley, G. J.; Watson, D. J. High Productivity Methanol Carbonylation Catalysis Using Iridium: The Cativa™ Process for the Manufacture of Acetic Acid. *Catal. Today* **2000**, *58*, 293-307.
- (8) Hjortkjaer, J.; Jensen, V. W. Rhodium Complex Catalyzed Methanol Carbonylation. *Product R&D* **1976**, *15*, 46-49.
- (9) Paulik, F. E.; Roth, J. F. Novel Catalysts for the Low-Pressure Carbonylation of Methanol to Acetic Acid. *Chem. Commun.* **1968**, 1578a-1578a.
- (10) Miyaura, N.; Suzuki, A. Palladium-Catalyzed Cross-Coupling Reactions of Organoboron Compounds. *Chem. Rev.* **1995**, *95*, 2457-2483.
- (11) Maitlis, P. M.; Haynes, A.; Sunley, G. J.; Howard, M. J. Methanol Carbonylation Revisited: Thirty Years On. *J. Chem. Soc., Dalton Trans.* **1996**, 2187-2196.
- (12) Forster, D. Mechanistic Pathways in the Catalytic Carbonylation of Methanol by Rhodium and Iridium Complexes. In *Advances in Organometallic Chemistry*, Stone, F. G. A., West, R. Eds.; Vol. 17; Academic Press, 1979; pp 255-267.
- (13) Kalck, P.; Le Berre, C.; Serp, P. Recent Advances in the Methanol Carbonylation Reaction into Acetic Acid. *Coord. Chem. Rev.* **2020**, *402*, 213078.

- (14) Heck, R. F.; Breslow, D. S. The Reaction of Cobalt Hydrotetracarbonyl with Olefins. *J. Am. Chem. Soc.* **1961**, *83*, 4023-4027.
- (15) Evans, D.; Osborn, J. A.; Wilkinson, G. Hydroformylation of Alkenes by use of Rhodium Complex Catalysts. *J. Chem. Soc. A* **1968**, 3133-3142.
- (16) Birch, A. J.; Williamson, D. H. Homogeneous Hydrogenation Catalysts in Organic Synthesis. *Organic Reactions* **2011**, 1-186.
- (17) Halpern, J.; Okamoto, T.; Zakhariyev, A. Mechanism of the Chlorotris(triphenylphosphine) Rhodium(I)-Catalyzed Hydrogenation of Alkenes. The Reaction of Chlorodihydrido-tris(triphenyl-phosphine)rhodium(III) with Cyclohexene. *J. Mol. Catal.* **1977**, *2*, 65-68.
- (18) Roseblade, S. J.; Pfaltz, A. Iridium-Catalyzed Asymmetric Hydrogenation of Olefins. *Acc. Chem. Res.* **2007**, *40*, 1402-1411.
- (19) Schrock, R. R.; Osborn, J. A. Catalytic Hydrogenation Using Cationic Rhodium Complexes. II. The Selective Hydrogenation of Alkynes to *Cis* Olefins. *J. Am. Chem. Soc.* **1976**, *98*, 2143-2147.
- (20) Niu, S.; Hall, M. B. Theoretical Studies on Reactions of Transition-Metal Complexes. *Chem. Rev.* **2000**, *100*, 353-406.
- (21) Thompson, W. H.; Sears, C. T. Kinetics of Oxidative Addition to Iridium(I) Complexes. *Inorg. Chem.* **1977**, *16*, 769-774.
- (22) Kubota, M.; Kiefer, G. W.; Ishikawa, R. M.; Bencala, K. E. Kinetics of Reactions of Methyl Iodide with Four-Coordinated Iridium(I) Complexes. *Inorg. Chim. Acta* **1973**, *7*, 195-202.

- (23) Gu, S.; Nielsen, R. J.; Taylor, K. H.; Fortman, G. C.; Chen, J.; Dickie, D. A.; Goddard, W. A.; Gunnoe, T. B. Use of Ligand Steric Properties to Control the Thermodynamics and Kinetics of Oxidative Addition and Reductive Elimination with Pincer-Ligated Rh Complexes. *Organometallics* **2020**, *39*, 1917-1933.
- (24) Feller, M.; Iron, M. A.; Shimon, L. J. W.; Diskin-Posner, Y.; Leitun, G.; Milstein, D. Competitive C–I versus C–CN Reductive Elimination from a Rh^{III} Complex. Selectivity is Controlled by the Solvent. *J. Am. Chem. Soc.* **2008**, *130*, 14374-14375.
- (25) Feller, M.; Diskin-Posner, Y.; Leitun, G.; Shimon, L. J. W.; Milstein, D. Direct Observation of Reductive Elimination of MeX (X = Cl, Br, I) from Rh^{III} Complexes: Mechanistic Insight and the Importance of Sterics. *J. Am. Chem. Soc.* **2013**, *135*, 11040-11047.
- (26) O'Reilly, M. E.; Pahls, D. R.; Webb, J. R.; Boaz, N. C.; Majumdar, S.; Hoff, C. D.; Groves, J. T.; Cundari, T. R.; Gunnoe, T. B. Reductive Functionalization of a Rhodium(III)–methyl Bond by Electronic Modification of the Supporting Ligand. *Dalton Trans.* **2014**, *43*, 8273-8281.
- (27) O'Reilly, M. E.; Fu, R.; Nielsen, R. J.; Sabat, M.; Goddard, W. A.; Gunnoe, T. B. Long-Range C–H Bond Activation by Rh^{III}-Carboxylates. *J. Am. Chem. Soc.* **2014**, *136*, 14690-14693.
- (28) Albrecht, M.; van Koten, G. Platinum Group Organometallics Based on “Pincer” Complexes: Sensors, Switches, and Catalysts. *Angew. Chem. Int. Ed.* **2001**, *40*, 3750-3781.
- (29) Choi, J.; MacArthur, A. H. R.; Brookhart, M.; Goldman, A. S. Dehydrogenation and Related Reactions Catalyzed by Iridium Pincer Complexes. *Chem. Rev.* **2011**, *111*, 1761-1779.

- (30) Goldberg, J. M.; Wong, G. W.; Brastow, K. E.; Kaminsky, W.; Goldberg, K. I.; Heinekey, D. M. The Importance of Steric Factors in Iridium Pincer Complexes. *Organometallics* **2015**, *34*, 753-762.
- (31) Goldberg, J. M.; Cherry, S. D. T.; Guard, L. M.; Kaminsky, W.; Goldberg, K. I.; Heinekey, D. M. Hydrogen Addition to (pincer)Ir^I(CO) Complexes: The Importance of Steric and Electronic Factors. *Organometallics* **2016**, *35*, 3546-3556.
- (32) Miessler, G. L.; Fischer, P. J.; Tarr, D. A. *Inorganic Chemistry*; Pearson, 2014.
- (33) Frech, C. M.; Milstein, D. Direct Observation of Reductive Elimination of Methyl Iodide from a Rhodium(III) Pincer Complex: The Importance of Sterics. *J. Am. Chem. Soc.* **2006**, *128*, 12434-12435.
- (34) Shaffer, D. W.; Ryken, S. A.; Zarkesh, R. A.; Heyduk, A. F. Ligand Effects on the Oxidative Addition of Halogens to (dpp-nacnac^R)Rh(phdi). *Inorg. Chem.* **2012**, *51*, 12122-12131.
- (35) Donoghue, P. J.; Helquist, P.; Wiest, O. Ligand and Substrate Effects on the Mechanism of Rhodium-Catalyzed Hydrogenation of Enamides. *J. Org. Chem.* **2007**, *72*, 839-847.
- (36) Gu, S.; Chen, J.; Musgrave, C. B.; Gehman, Z. M.; Habgood, L. G.; Jia, X.; Dickie, D. A.; Goddard, W. A.; Gunnoe, T. B. Functionalization of Rh^{III}-Me Bonds: Use of "Capping Arene" Ligands to Facilitate Me-X Reductive Elimination. *Organometallics* **2021**, *40*, 1889-1906.
- (37) O'Reilly, M. E.; Johnson, S. I.; Nielsen, R. J.; Goddard, W. A.; Gunnoe, T. B. Transition-Metal-Mediated Nucleophilic Aromatic Substitution with Acids. *Organometallics* **2016**, *35*, 2053-2056.

- (38) Fu, R.; O'Reilly, M. E.; Nielsen, R. J.; Goddard III, W. A.; Gunnoe, T. B. Rhodium Bis(quinolinyl)benzene Complexes for Methane Activation and Functionalization. *Eur. J. Chem.* **2015**, *21*, 1286-1293.
- (39) Gu, S.; Musgrave, C. B.; Gehman, Z. M.; Zhang, K.; Dickie, D. A.; Goddard, W. A.; Gunnoe, T. B. Rhodium and Iridium Complexes Bearing "Capping Arene" Ligands: Synthesis and Characterization. *Organometallics* **2021**, *40*, 2808–2825.
- (40) Liu, C.; Geer, A. M.; Webber, C.; Musgrave, C. B.; Gu, S.; Johnson, G.; Dickie, D. A.; Chhabra, S.; Schnegg, A.; Zhou, H.; et al. Immobilization of "Capping Arene" Cobalt(II) Complexes on Ordered Mesoporous Carbon for Electrocatalytic Water Oxidation. *ACS Catal.* **2021**, *11*, 15068-15082.
- (41) Chen, J.; Nielsen, R. J.; Goddard, W. A.; McKeown, B. A.; Dickie, D. A.; Gunnoe, T. B. Catalytic Synthesis of Superlinear Alkenyl Arenes Using a Rh(I) Catalyst Supported by a "Capping Arene" Ligand: Access to Aerobic Catalysis. *J. Am. Chem. Soc.* **2018**, *140*, 17007-17018.
- (42) Chan, A. S. C.; Halpern, J. Interception and Characterization of a Hydridoalkylrhodium Intermediate in a Homogeneous Catalytic Hydrogenation Reaction. *J. Am. Chem. Soc.* **1980**, *102*, 838-840.
- (43) Halpern, J. Mechanism and Stereoselectivity of Asymmetric Hydrogenation. *Science* **1982**, *217*, 401-407.
- (44) Yuan, X.; Bi, S.; Ding, Y.; Liu, L.; Sun, M. DFT Study of Alkene Hydrogenation Catalyzed by Rh(acac)(CO)₂. *J. Organomet. Chem.* **2010**, *695*, 1576-1582.
- (45) Imamoto, T.; Tamura, K.; Zhang, Z.; Horiuchi, Y.; Sugiya, M.; Yoshida, K.; Yanagisawa, A.; Gridnev, I. D. Rigid P-Chiral Phosphine Ligands with tert-

Butylmethylphosphino Groups for Rhodium-Catalyzed Asymmetric Hydrogenation of Functionalized Alkenes. *J. Am. Chem. Soc.* **2012**, *134*, 1754-1769.

(46) Meakin, P.; Jesson, J. P.; Tolman, C. A. Nature of Chlorotris(triphenylphosphine)rhodium in Solution and Its Reaction with Hydrogen. *J. Am. Chem. Soc.* **1972**, *94*, 3240-3242.

(47) Ke, Z.; Li, Y.; Hou, C.; Liu, Y. Homogeneously Catalyzed Hydrogenation and Dehydrogenation Reactions – From a Mechanistic Point of View. *Phys. Sci. Rev.* **2018**, *3*, 20170038.

(48) Luo, J.; Oliver, A. G.; Scott McIndoe, J. A Detailed Kinetic Analysis of Rhodium-Catalyzed Alkyne Hydrogenation. *Dalton Trans.* **2013**, *42*, 11312-11318.

(49) Guo, X.; Scott, P. J.; Rempel, G. L. Catalytic Hydrogenation of Diene Polymers: Part II. Kinetic Analysis and Mechanistic Studies on the Hydrogenation of Styrene—Butadiene Copolymers in the Presence of $\text{RhCl}(\text{PPh}_3)_3$. *J. Mol. Catal.* **1992**, *72*, 193-208.

(50) Ungváry, F. Transition Metals in Organic Synthesis: Hydroformylation, Reduction, and Oxidation. Annual Survey Covering the Year 1992. *J. Organomet. Chem.* **1994**, *477*, 363-430.

(51) Straub, B. F. Organotransition Metal Chemistry. From Bonding to Catalysis. Edited by John F. Hartwig. *Angew. Chem. Int. Ed.* **2010**, *49*, 7622-7622.

(52) Srinivasan, B. Words of Advice: Teaching Enzyme Kinetics. *The FEBS Journal* **2021**, *288*, 2068-2083.

(53) Jardine, F. H.; Osbron, J. A.; Wilkinson, G. Further Studies on the Homogeneous Hydrogenation of Olefins Using Tris(Triphenylphosphine)Halogenorhodium(I) Catalysts. *J. Chem. Soc. A* **1967**, 1574-1578.

- (54) Hoffman, R. E. Standardization of Chemical Shifts of TMS and Solvent Signals in NMR Solvents. *Magn. Reson. Chem.* **2006**, *44*, 606-616.
- (55) Chatt, J.; Venanzi, L. M. Olefin Complexes of Rhodium. *Nature* **1956**, *177*, 852-853.
- (56) Albright, T. A. H., R.; Thibeault, J.C.; Thorn, D.L. Ethylene Complexes. Bonding, Rotational Barriers, and Conformational Preferences. *J. Am. Chem. Soc.* **1979**, *101*, 3801-3812.
- (57) Cramer, R. Olefin Coordination Compounds of Rhodium: The Barrier to Rotation of Coordinated Ethylene and the Mechanism of Olefin Exchange. *J. Am. Chem. Soc.* **1964**, *86*, 217-222.
- (58) Kaneshima, T.; Yumoto, Y.; Kawakami, K.; Tanaka, T. Rotation of olefins in Dithiocarbamatobis(isocyanide)(olefin)rhodium Complexes. *Inorg. Chim. Acta* **1976**, *18*, 29-34.
- (59) Bodner, G. S. F., J. M.; Arif, A. M.; Gladysz, J. A. Selective Binding of One Enantioface of Monosubstituted Alkenes to the Chiral Transition Metal Lewis Acid $[(\eta^5\text{-C}_5\text{H}_5)\text{Re}(\text{NO})(\text{PPh}_3)]^+$. *J. Am. Chem. Soc.* **1988**, 4082-4084.
- (60) Valahovic, M. T.; Gunnoe, T. B.; Sabat, M.; Harman, W. D. Ligand-Modulated Stereo- and Regioselective Tandem Addition Reactions of Rhenium-Bound Naphthalene. *J. Am. Chem. Soc.* **2002**, *124*, 3309-3315.
- (61) Brooks, B. C.; Meiere, S. H.; Friedman, L. A.; Carrig, E. H.; Gunnoe, T. B.; Harman, W. D. Interfacial and Intrafacial Linkage Isomerizations of Rhenium Complexes with Aromatic Molecules. *J. Am. Chem. Soc.* **2001**, *123*, 3541-3550.

- (62) Larpent, C.; Patin, H. Mechanistic Aspects of Alkenes Hydrogenation and Deuteration Catalyzed by Dispersion of Hydroxyhydridorhodium Colloids in Aqueous Medium. *J. Mol. Catal.* **1990**, *61*, 65-73.
- (63) Jeske, G.; Lauke, H.; Mauermann, H.; Schumann, H.; Marks, T. J. Highly Reactive Organolanthanides. A Mechanistic Study of Catalytic Olefin Hydrogenation by Bis(Pentamethylcyclopentadienyl) and Related 4f Complexes. *J. Am. Chem. Soc.* **1985**, *107*, 8111-8118.
- (64) Vazquez-Serrano, L. D. Catalytic Homogeneous Hydrogenation of Olefins Using N-Heterocyclic Carbene Complexes of Rhodium and Iridium. Ph.D. Dissertation, Purdue University, Ann Arbor, MI., 2004.
- (65) Houston, P. L. *Chemical Kinetics and Reaction Dynamics*; Dover Publication, Inc., 2006.
- (66) Findeisen, M.; Brand, T.; Berger, S. A ¹H-NMR Thermometer Suitable for Cryoprobes. *Magn. Reson. Chem.* **2007**, *45*, 175-178.
- (67) Zhao, S.-B.; Song, D.; Jia, W.-L.; Wang, S. Regioselective C-H Activation of Toluene with a 1,2-Bis(N-7-azaindolyl)benzene Platinum(II) Complex. *Organometallics* **2005**, *24*, 3290-3296.
- (68) Bochevarov, A. D.; Harder, E.; Hughes, T. F.; Greenwood, J. R.; Braden, D. A.; Philipp, D. M.; Rinaldo, D.; Halls, M. D.; Zhang, J.; Friesner, R. A. Jaguar: A High-Performance Quantum Chemistry Software Program with Strengths in Life and Materials Sciences. *Int. J. Quantum Chem* **2013**, *113*, 2110-2142.
- (69) Becke, A. D. Density-Functional Thermochemistry. III. The Role of Exact Exchange. *J. Chem. Phys.* **1993**, *98*, 5648-5652.

- (70) Lee, C.; Yang, W.; Parr, R. G. Development of the Colle-Salvetti Correlation-Energy Formula into a Functional of the Electron Density. *Phys. Rev. B* **1988**, *37*, 785-789.
- (71) Grimme, S.; Antony, J.; Ehrlich, S.; Krieg, H. A Consistent and Accurate *Ab Initio* Parametrization of Density Functional Dispersion Correction (DFT-D) for the 94 Elements H-Pu. *J. Chem. Phys.* **2010**, *132*, 154104.
- (72) Kahn, L. R.; Goddard, W. A. *Ab Initio* Effective Potentials for Use in Molecular Calculations. *J. Chem. Phys.* **1972**, *56*, 2685-2701.
- (73) Roy, L. E.; Hay, P. J.; Martin, R. L. Revised Basis Sets for the LANL Effective Core Potentials. *J. Chem. Theory Comput.* **2008**, *4*, 1029-1031.
- (74) Friedrichs, M.; Zhou, R.; Edinger, S. R.; Friesner, R. A. Poisson-Boltzmann Analytical Gradients for Molecular Modeling Calculations. *J. Phys. Chem. B* **1999**, *103*, 3057-3061.
- (75) Tannor, D. J.; Marten, B.; Murphy, R.; Friesner, R. A.; Sitkoff, D.; Nicholls, A.; Honig, B.; Ringnalda, M.; Goddard, W. A. Accurate First Principles Calculation of Molecular Charge Distributions and Solvation Energies from *Ab Initio* Quantum Mechanics and Continuum Dielectric Theory. *J. Am. Chem. Soc.* **1994**, *116*, 11875-11882.
- (76) Hafner, J. *Ab initio* simulations of materials using VASP: Density-Functional Theory and Beyond. *J. Comput. Chem.* **2008**, *29*, 2044-2078.
- (77) Perdew, J. P.; Burke, K.; Ernzerhof, M. Generalized Gradient Approximation Made Simple. *Phys. Rev. Lett.* **1996**, *77*, 3865-3868.
- (78) Mathew, K.; Sundararaman, R.; Letchworth-Weaver, K.; Arias, T. A.; Hennig, R. G. Implicit Solvation Model for Density-Functional Study of Nanocrystal Surfaces and Reaction Pathways. *J. Chem. Phys.* **2014**, *140*, 084106.

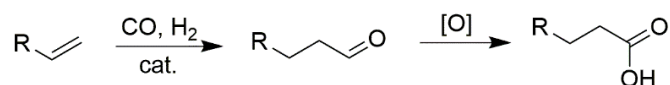
- (79) Mathew, K.; Kolluru, V. S. C.; Mula, S.; Steinmann, S. N.; Hennig, R. G. Implicit Self-Consistent Electrolyte Model in Plane-Wave Density-Functional Theory. *J. Chem. Phys.* **2019**, *151*, 234101.
- (80) *Saint*; *SADABS*; *APEX3*; Bruker AXS Inc.: Madison, Wisconsin, USA., 2012. (accessed 2022).
- (81) Sheldrick, G. SHELXT - Integrated Space-Group and Crystal-Structure Determination. *Acta Crystallogr. A* **2015**, *71*, 3-8.
- (82) Dolomanov, O. V.; Bourhis, L. J.; Gildea, R. J.; Howard, J. A. K.; Puschmann, H. OLEX2: a Complete Structure Solution, Refinement and Analysis Program. *J. Appl. Crystallogr.* **2009**, *42*, 339-341.

3 Direct carboxylation of benzene using PCP-Pd complexes as a catalyst

3.1 Introduction

Carboxylic acids have broad applications in polymers, agrochemicals, material coatings, food additives, cosmetic ingredients and medicines.¹⁻⁸ The major industrial route to synthesize C4-C11 carboxylic acids is by oxidation of aldehydes, which are usually prepared by hydroformylation of alkenes with carbon monoxide and dihydrogen catalyzed by cobalt or rhodium complexes (**Scheme 3.1.1**).^{9, 10} One of the major concerns for this synthetic route is the usage of carbon monoxide. Although carbon monoxide is a traditional C1 building block, it is a hazardous and poisonous gas, requiring extra effort for safety and waste processing.¹¹ Additionally, the production of syngas (CO and H₂) requires a tremendous amount of energy.¹² Thus, CO₂ could be a useful C1 starting material, especially with efficient future carbon capture techniques.¹³

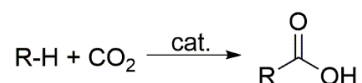
Scheme 3.1.1 The two-step carboxylic acid synthesis by hydroformylation followed by oxidation.



Compared to current methods, the direct carboxylation of hydrocarbons using carbon dioxide provides a more straightforward method for the synthesis of carboxylic acids (**Scheme 3.1.2**). In this case, carbon dioxide is formally inserted into a C–H bond to yield the carboxylic acid. This synthetic route could have an economic advantage over the route in **Scheme 3.1.1** because CO₂ is an abundant C1 source. Also, due to the toxicity of CO, using can be more dangerous than using CO₂.¹¹ More importantly, the oxidant used for the aldehyde oxidation can also oxidize other functional groups, which can limit application

for some types of compounds. As a result, the one-step direct carboxylation of hydrocarbons without an oxidation step would be advantageous. Thus, my research project seeks to develop a catalytic process that directly yields carboxylic acids from hydrocarbons using CO₂ as a C1 source.

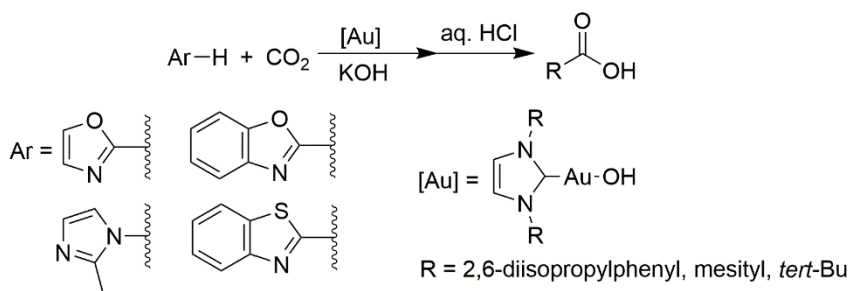
Scheme 3.1.2 Proposed reaction for carboxylic acid synthesis.



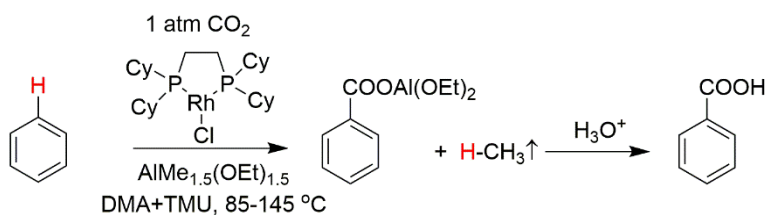
The use of CO₂ for carboxylic acid synthesis has been studied by several groups. Boogaerts and coworkers developed a direct carboxylation method catalyzed by Au(I) N-heterocyclic carbene (NHC) complexes (**Scheme 3.1.3**).^{14, 15} Although this reaction operates efficiently under mild conditions, its application is limited by the requirement of an acidic C_{aryl}-H bond. It is found that the proton *pK_a* (in DMSO) must be lower than 30 in order for the hydroxyl group of the NHC-Au(I)-OH complexes to deprotonate the aromatic C-H bond, which is a key step of the mechanism. Thus, the carboxylation of less acidic C-H bonds, such as benzene (*pK_a* = 47, in DMSO), cannot be achieved by the NHC-Au(I)-OH complexes, which limits the substrate scope for these catalysts. Additionally, the Iwasawa and Takaya groups reported the direct carboxylation of benzene catalyzed by Rh(I) complexes using AlMe_{1.5}(OEt)_{1.5} as a methylating reagent (**Scheme 3.1.4**).¹⁶ The reaction is proposed to be initiated by the methylation of Rh(I)-Cl to form a Rh(I)-Me intermediate. The Rh(I)-Me intermediate activates a C-H bond of benzene via oxidative addition to form Rh(III)(Me)(Ph)(H), which then undergoes reductive elimination to release methane and form a Rh(I)-Ph complex. Thus, the activation of one equivalent of benzene requires one

equivalent of methylating reagent, which is less atom-economically efficient compared to direct carboxylation routes.

Scheme 3.1.3 Direct carboxylation of acidic heteroaromatic C–H bond by NHC-Au(I)-OH catalysts.



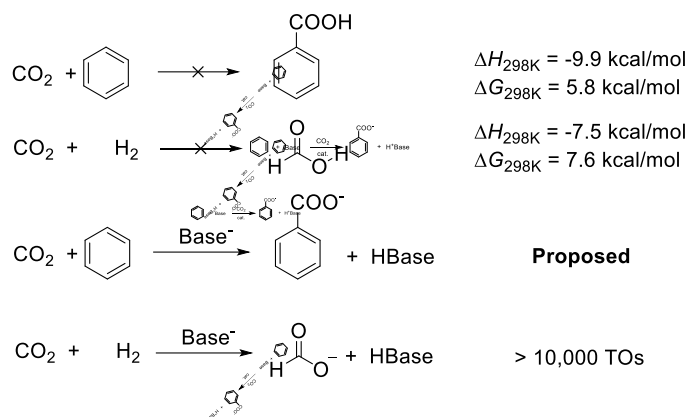
Scheme 3.1.4 Carboxylation of benzene by a Rh catalyst assisted by aluminum based methylating reagents.



Despite these fundamental advancements using CO_2 to directly yield carboxylic acids following the activation of hydrocarbyl C–H bonds, the direct carboxylation of unactivated C–H bonds without using strong reducing reagents is rare. In fact, the conversion of benzene and CO_2 to benzoic acid is thermodynamically disfavored under ambient conditions ($\Delta H = -9.9$ kcal/mol; $\Delta G = 5.8$ kcal/mol at 298 K).^{17, 18} The analogous reaction, hydrogenation of CO_2 , is also exothermic ($\Delta H = -7.5$ kcal/mol) but thermodynamically unfavorable ($\Delta G = 7.6$ kcal/mol at 298 K).^{17, 18} The use of additives, such as a base, could be a possible solution to the thermodynamic difficulty because the negative ΔG of an acid-base reaction can reduce the overall free energy, making the reaction favorable (**Scheme 3.1.5**). The strategy has been successful with the hydrogenation of CO_2 yielding formate

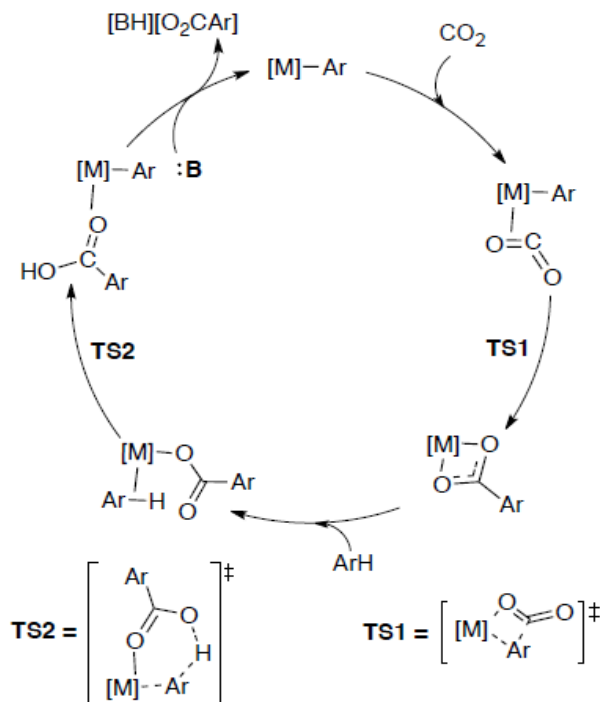
with over 10,000 turnovers (**Scheme 3.1.5**), in which the acid-base reaction shifts the chemical equilibrium towards the product side.¹⁹⁻²³

Scheme 3.1.5 Comparison of direct carboxylation of benzene and CO₂ hydrogenation.



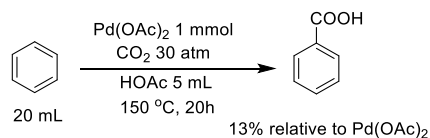
In addition to the thermodynamic challenge, activation of an inert C–H bond and CO₂ is challenging. According to the proposed mechanism (**Scheme 3.1.6**), a carboxylate group coordinated to a metal center may be able to activate the C_{aryl}–H bond by undergoing carboxylate-assisted C–H activation (**Scheme 3.1.6**, TS2), which is also known as concerted metalation deprotonation (CMD).²⁴⁻²⁸ Furthermore, if the CO₂ insertion step is facilitated by π -basic (electron-rich) metal centers, the basicity of the metal center can be enhanced by using strongly electron-donating ancillary ligands.²⁹⁻³¹ Thus, we propose that benzene and its derivatives might undergo late transition metal catalyzed direct carboxylation under basic conditions.

Scheme 3.1.6 Proposed mechanism for direct carboxylation of arenes under basic conditions.

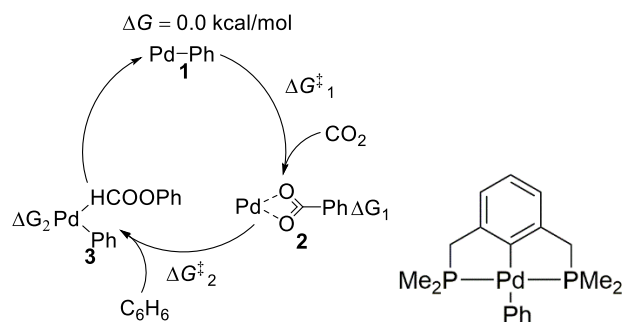


In 1984, the Fujiwara group reported benzene direct carboxylation using CO_2 catalyzed by $Pd(OAc)_2$ under acidic conditions (**Scheme 3.1.7**).³² Although Fujiwara and coworkers only achieved a 13% yield based on amount of $Pd(OAc)_2$, performing the Pd(II)-catalyzed direct carboxylation of benzene under basic conditions may give an opportunity to achieve higher yields than 13% since the equilibrium might be shifted toward the benzoate product.

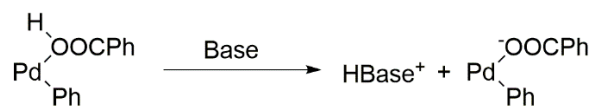
Scheme 3.1.7 Reported direct carboxylation of benzene catalyzed by $Pd(OAc)_2$ under acidic conditions.³²



In collaboration with the Ess group at Brigham Young University, we have computationally probed the viability of our proposed mechanism using a simple Pd salt and a Pd-pincer complex, and examined the free energies of potential intermediates and transition states (**Table 3.1.1**).³³⁻³⁵ As shown in **Table 3.1.1**, the catalytic cycle for phenyl{2,6-*bis*[methyl(dimethylphosphino)]phenyl}palladium [(^{Me}PCP)PdPh] has lower activation energies for transition states and free energies for intermediates than that of the corresponding intermediates for Pd(OAc)₂. The lower calculated ΔG^\ddagger for (^{Me}PCP)PdPh compared to that for Pd(OAc)₂ is consistent with the prediction that electron donating ligands could improve the reactivity of the catalyst, since the σ -donation from phosphine's lone pair electrons of the PCP as well as the phenyl-carbon increases the electron density of the metal center. In particular, the transformation of **1** to **2** is endergonic for Pd(OAc)₂, while exergonic for the Pd(II) pincer complex. The Ess group also calculated the effect of base on the overall free energy for Pd(OAc)₂ facilitated direct carboxylation (**Table 3.1.2**). Each of the three bases lead to a significant decrease in the free energy, indicating that the overall reaction would become more favorable with the addition of base. With the help of preliminary calculations, we considered that PCP ligated palladium complexes might be capable of catalyzing direct carboxylation of benzene under basic conditions.

Table 3.1.1 Proposed mechanism and DFT calculations for Pd(OAc)₂ and (^{Me}PCP)PdPh.

Catalyst	ΔG_1^\ddagger (kcal/mol)	ΔG_2^\ddagger (kcal/mol)	ΔG_1 (kcal/mol)	ΔG_2 (kcal/mol)
Pd(OAc) ₂	30.9	31.9	9.1	15.3
(^{Me} PCP)PdPh	25.2	31.7	-5.8	15.0

Table 3.1.2 DFT calculations for the effect of base on overall free energy.

Base	$\Delta G_{\text{without base, 298K}}$ (kcal/mol)	$\Delta G_{\text{with base, 298K}}$ (kcal/mol)
DBU ^a	15.3	2.3
KO ^t Bu	15.3	-15.6
NEt ₃	15.3	10.9

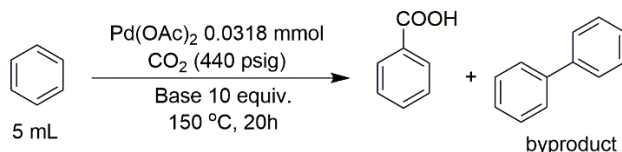
a. DBU = 1,8-Diazabicyclo(5.4.0)undec-7-ene

3.2 Preliminary conditions screening for Pd catalyzed direct carboxylation of benzene under basic conditions.

Guided by the computational results from the Ess group, several bases were screened for Pd catalyzed carboxylation of benzene using Pd(OAc)₂ as the catalyst. A modification of Fujiwara's method was used for the base screenings on Pd(OAc)₂, and the results are summarized in **Table 3.2.1**.³⁶ In all cases, a large amount of black precipitate formed during the reaction, which could not be dissolved by 37% HCl (aq), indicating that Pd(OAc)₂ is likely being reduced to Pd(0). As **Table 3.2.1** shows, only the entries for Pd(OAc)₂ with no base or with NaOAc yields biphenyl, while entries 2-4 yield neither benzoic acid nor biphenyl. The formation of biphenyl is likely from the reductive elimination from a diphenylpalladium(II) complex, which results in the formation of Pd(0). Thus, the formation of biphenyl implies that Pd(OAc)₂ is capable of performing benzene C–H activation.³⁷ One possible reason for the suppression of C–H activation is the ligand substitution in the presence of a stronger base than acetate, in which an acetate group is released from Pd(OAc)₂. This subsequently inhibits C–H activation via a CMD mechanism. Thus, base screening with the addition of 10 equivalents of NaOAc and 10 equivalents of strong base (KOtBu or Cs₂CO₃) were tested (entries 6 and 7). An 11% yield of benzoic acid, relative to Pd, was observed for Cs₂CO₃ (entry 7), while no products were detected using KOtBu (entry 6). This suggests that the substitution of acetate group by Cs₂CO₃ might be mitigated by the addition of an acetate source, while the basicity of KOtBu is too strong for Pd(OAc)₂ catalyzed direct carboxylation. Under some conditions (**Table 3.2.1**, entries 1 and 5), the formation of biphenyl is observed. The formation of biphenyl has also

been reported by Fujiwara and coworkers under similar conditions, which can be explained by the C–H activation of benzene followed by the C–C coupling of phenyl ligands.³²

Table 3.2.1 Yields of benzoic acid and biphenyl for screenings on Pd(OAc)₂ catalyzed benzene direct carboxylation under basic conditions



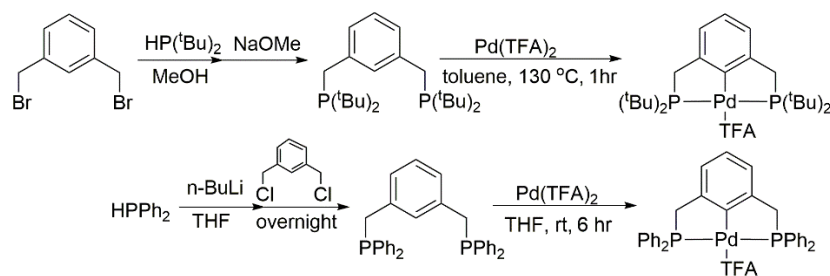
Entry	Base	Yield of benzoic acid	Yield of biphenyl
		(%)	(%)
1	None	0	162
2	KO ^t Bu	0	0
3	Cs ₂ CO ₃	0	0
4	NEt ₃	0	0
5	NaOAc	0	161
6	NaOAc + KO ^t Bu	0	0
7	NaOAc + Cs ₂ CO ₃	11	Trace

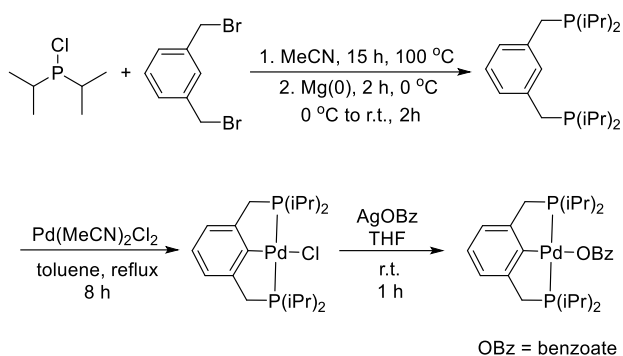
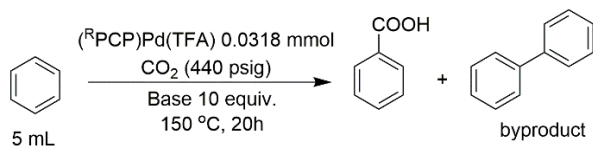
a. Isolated yield relative to Pd(OAc)₂

Based on DFT calculations (**Table 3.1.1**), palladium (II) PCP-pincer complexes are predicted to be viable catalysts for the direct carboxylation of benzene. Moreover, according to Selander and Szabo, the tridentate coordination provides stability against complex decomposition to Pd(0), a suspected decomposition product of Pd(OAc)₂.³⁸ Furthermore, the σ -donation of the PCP-pincer ligand will electronically enrich the Pd metal center, which should promote CO₂ insertion into a Pd(II)–Ph bond.³⁹ Phenyl{2,6-

bis[methyl(*tert*-butylphosphino)]phenyl}palladium trifluoroacetate [(^tBuPCP)Pd(TFA)] and phenyl{2,6-*bis*[methyl(diphenylphosphino)]phenyl}palladium trifluoroacetate [(^{Ph}PCP)Pd(TFA)] were prepared following the procedures shown in **Scheme 3.2.1**.⁴⁰⁻⁴³ Phenyl{2,6-*bis*[methyl(isopropylphosphino)]phenyl}palladium benzoate [(ⁱPrPCP)Pd(OBz)] was synthesized by the method described in **Scheme 3.2.2**.⁴⁴⁻⁴⁷ The detailed synthetic procedure and the NMR spectra of the palladium(II) PCP-pincer complexes mentioned above can be found in the Experimental Section (Section 3.6). The base screening of (^tBuPCP)Pd(TFA) and (^{Ph}PCP)Pd(TFA) mediated carboxylation of benzene was performed under the same conditions used for Pd(OAc)₂, and the results are summarized in **Table 3.2.2**. Although no black precipitate was observed after any of the reactions, no quantifiable amounts of benzoic acid or biphenyl were detected. One possible reason explanation could be that the sterics of the *tert*-butyl and phenyl groups suppress benzene coordination and subsequent C–H activation. Therefore, palladium(II) pincer complexes with less steric bulk on phosphine moieties were deemed as the next synthetic targets.

Scheme 3.2.1 Synthetic routes for (^tBuPCP)Pd(TFA) and (^{Ph}PCP)Pd(TFA).



Scheme 3.2.2 Synthetic routes for (ⁱPrPCP)Pd(OBz).**Table 3.2.2.** Yield of benzoic acid and biphenyl for screenings of (^RPCP)Pd(TFA) catalyzed benzene direct carboxylation under basic conditions.

Entries	R	Base	Yield of	
			benzoic acid (%) ^a	biphenyl (%) ^a
1	tBu	None	0	0
2	tBu	NaOMe	0	0
3	tBu	Cs ₂ CO ₃	Trace	0
4	tBu	Na ₂ CO ₃	0	0
5	tBu	NEt ₃	0	0
6	tBu	NaOAc	0	0
7	tBu	NaOAc + Cs ₂ CO ₃	0	0
8	Ph	None	0	0
9	Ph	NaOMe	0	Trace
10	Ph	NaOAc + Cs ₂ CO ₃	0	0
11 ^b	iPr	None	0	0

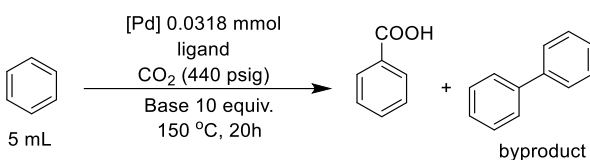
12 ^b	iPr	Cs ₂ CO ₃	0	0
13 ^b	iPr	DBU ^c	0	0

-
- a. Isolated yield of product is relative to Pd catalyst.
 b. (ⁱPrPCP)PdOBz (OBz = benzoate) is used instead of (ⁱPrPCP)PdTFA
 c. DBU = 1,8-diazabicyclo[5.4.0]undec-7-ene

In addition to PCP pincer ligands, some bidentate ligands have been tested for catalytic carboxylation of benzene (**Table 3.2.3**) because these ligands can facilitate the direct carboxylation driven by a methylating reagent.¹⁶ With the addition of ligands, the formation of Pd(0) is not significant in this reaction. The addition of 1 equivalent of diphenylphosphinopropane (dppp) ligand to generate (κ^2 -dppp)Pd(OAc)₂ *in situ* resulted in 12% isolated yield of benzoic acid relative to Pd(OAc)₂. Increasing the loading of dppp to 2 equivalents gives a significant increase in the yield of benzoic acid to 65% compared to 1 equivalent of dppe (entries 1 and 2), whereas increasing the amount to 4 equivalents leads to only 11% yield of benzoic acid (entry 3). One explanation for this observation is that dppp ligand not only forms the (κ^2 -dppp)Pd(OAc)₂ complex *in situ*, but also may facilitate the reaction by serving as a base. However, the addition of a larger excess of dppp to the reaction mixture suppresses the reaction (entry 3). The addition of large excess of dppp might lead to *in situ* formation of [(κ^2 -dppp)₂Pd][OAc]₂, which is likely to be catalytically inactive. The chelation effect of dppp prevents ligand dissociation to provide a site for substrate coordination to the Pd center. Additionally, stronger bases (Cs₂CO₃ and DBU) result in lower yields of benzoic acid (entries 5-7). Although simple bidentate phosphine ligands provided a positive result, extension to simple nitrogen based bidentate ligands, such as bipyridine, provided no observed benzoic acid or biphenyl under identical

conditions (entries 7-11). This could be attributed to differences in nucleophilicities due to the π -acidity of the bipyridine ligands.

Table 3.2.3 Yields of benzoic acid and biphenyl for screenings on bidentate assisted Pd(II) catalyzed benzene direct carboxylation under basic condition.



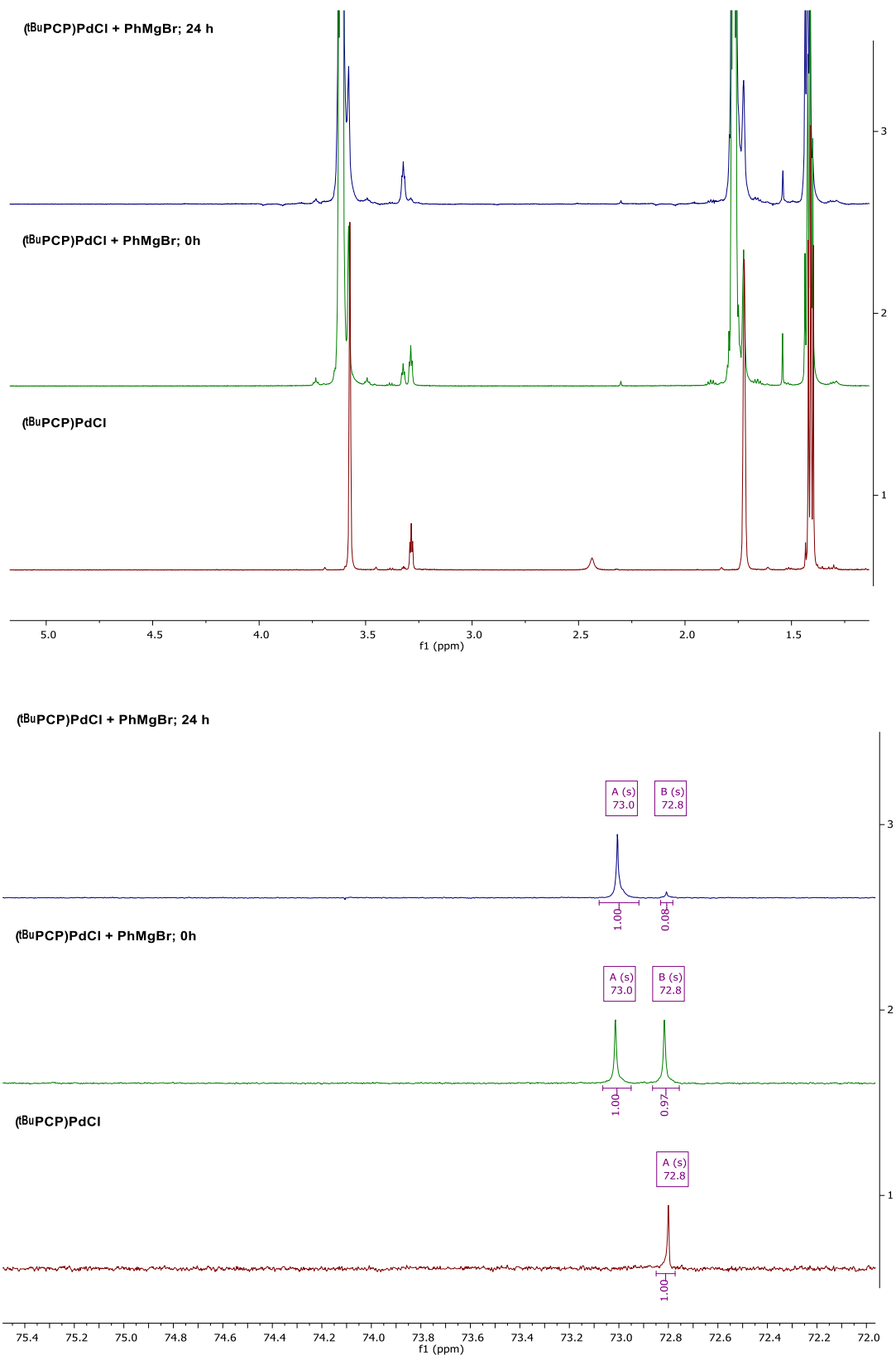
Entries	Catalysts	Base	Yield of benzoic acid (%)	Yield of biphenyl (%) ^b
1	dppp (1 eq.) + Pd(OAc) ₂	NaOAc (10 eq.)	12	1
2	dppp (2 eq.) + Pd(OAc) ₂	NaOAc (10 eq.)	13	1
3	dppp (4 eq.) + Pd(OAc) ₂	NaOAc (10 eq.)	11	1
4	dppp (1 eq.) + Pd(OAc) ₂	NaOAc (40 eq.)	39	2
5	dppp (1 eq.) + Pd(OAc) ₂	NaOAc (10 eq.) + Cs ₂ CO ₃ (10 eq.)	Trace	Trace
6	dppp (1 eq.) + Pd(OAc) ₂	NaOAc (10 eq.) + DBU (10 eq.)	7	Trace
7	(^t Bu ₂ bpy)Pd(OAc) ₂	NaOMe (10 eq.)	0	0
8	(^t Bu ₂ bpy)Pd(OAc) ₂	NEt ₃ (10 eq.) ^c	0	0
9	(^t Bu ₂ bpy)Pd(OAc) ₂	KO ^t Bu (10 eq.)	0	0
10	(^t Bu ₂ bpy)Pd(OAc) ₂	NaOAc (10 eq.)	0	0
11	(^t Bu ₂ bpy)Pd(OAc) ₂	NaOAc (10 eq.) + Cs ₂ CO ₃ (10 eq.)	0	0

3.3 Studies of CO₂ insertion using (^RPCP)PdPh complexes

Although the Pd catalyzed benzene direct carboxylation was not entirely successful, it would be beneficial to understand what caused the unexpected low reactivity. Thus, a series of studies were performed to investigate the proposed mechanism (**Scheme 3.1.6**). Therefore, the CO₂ insertion into the Pd–Ph complex, and the Pd-catalyzed benzene C–H activation were studied.

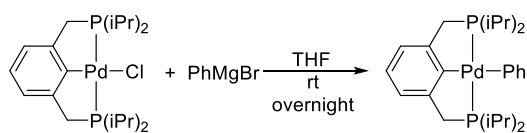
The synthesis of (^tBuPCP)PdPh was attempted by mixing (^tBuPCP)PdCl with various phenylating reagents including PhMgBr, LiPh, Ph₂Mg and Ph₂Zn. The ¹H NMR and ³¹P NMR spectra indicate the (^tBuPCP)PdCl was mostly transformed to a new (PCP)Pd species *in situ* with 1.5 equivalents of PhMgBr (**Figure 3.3.1**). However, isolation of the new (PCP)Pd complex was not successful. Only (^tBuPCP)PdCl was observed from the crude material by removing THF (solvent) *in vacuo* from the reaction solution.

Figure 3.3.1 ^1H NMR (top) and ^{31}P NMR (bottom) evidence for *in situ* formation of new PCP-Pd species through reaction of $(^t\text{BuPCP})\text{PdPh}$ and PhMgBr .



To circumvent the obstacle in the synthesis of (^tBuPCP)PdPh, (ⁱPrPCP)PdPh was successfully synthesized (**Scheme 3.3.1**) following a previously reported procedure. Also, (ⁱPrPCP)PdOBz (OBz = benzoate) was synthesized by the reacting (ⁱPrPCP)PdCl with silver benzoate (**Scheme 3.3.2**). The NMR spectra and single crystal X-ray diffraction data are shown in **Figure 3.3.2** – **Figure 3.3.7**. The crystal structure of (ⁱPrPCP)PdPh (**Figure 3.3.4**) indicates that (ⁱPrPCP)PdPh complex possesses σ -symmetry with a mirror plane along C15–Pd1–C1–C2 plane. The plane of the phenyl group is perpendicular to the C15–Pd1–C1–P1 plane. The benzoate group in (ⁱPrPCP)PdOBz is coordinated to the Pd in κ^1 fashion (**Figure 3.3.7**). The distance between Pd1 and O1 is 2.100(3) Å, and the distance between Pd1 and O2 is 3.240 Å. The (ⁱPrPCP)PdOBz does not show the similar σ -symmetry as (ⁱPrPCP)PdPh. In comparison, the dihedral angle between the plane for the benzoate group and the Pd1–P1–P2–C13–O1 plane is 60.1°. Moreover, the PCP backbone is slightly distorted, as the the dihedral angle between the Pd1–P1–P2–C13–O1 plane and the C8–C12–C13 plane is 10.68°.

Scheme 3.3.1 Synthesis of (ⁱPrPCP)PdPh.



Scheme 3.3.2 Synthesis of (ⁱPrPCP)PdOBz (OBz = benzoate).

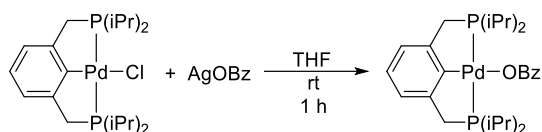


Figure 3.3.2 ^1H NMR spectrum of phenyl {2,5-di[(di-*iso*-propyl phosphino)methyl]phenyl palladium} ($i^{\text{Pr}}\text{PCP}$)PdPh in CD_3CN . Unlabeled peaks are from residual solvent (*n*-pentane) in the NMR solvent due to the atmosphere in the glovebox.

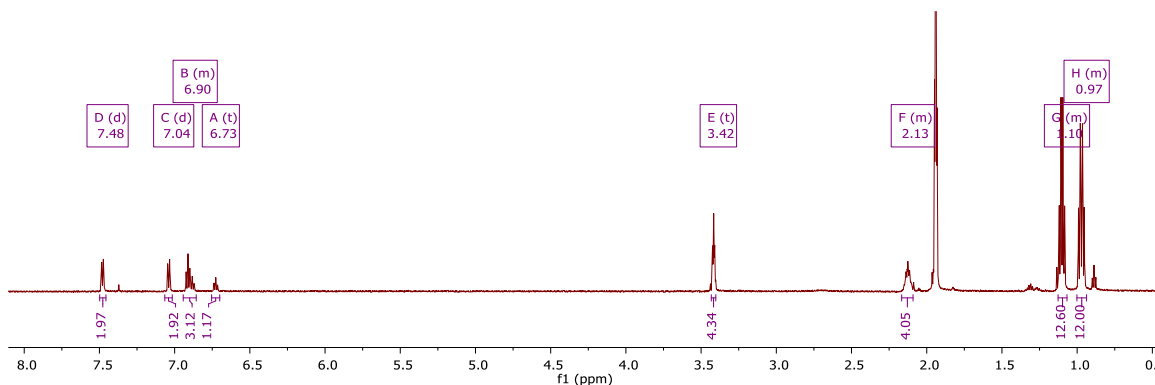


Figure 3.3.3 ^{31}P NMR spectrum for phenyl {2,5-di[(di-*iso*-propyl phosphino)methyl]phenyl palladium} ($i^{\text{Pr}}\text{PCP}$)PdPh in CD_3CN .

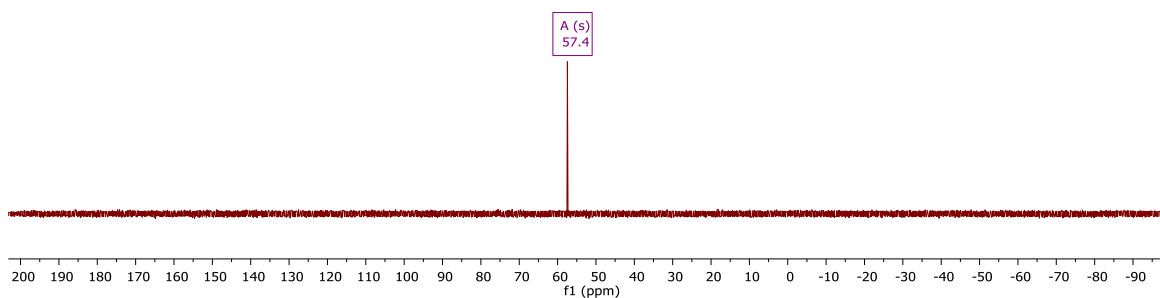
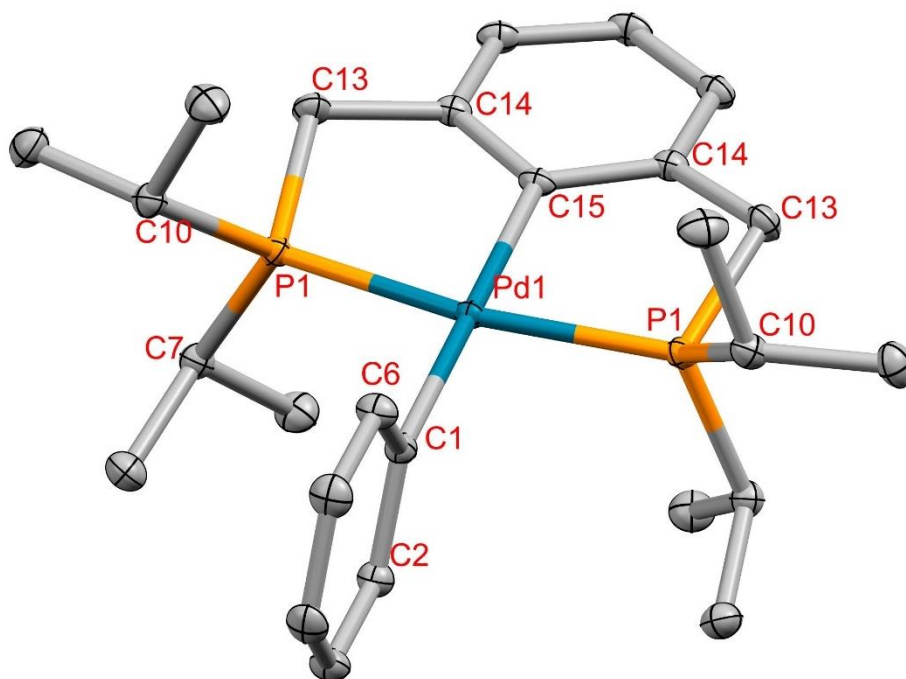


Figure 3.3.4 ORTEP of phenyl{2,5-di[(di-*iso*-propyl phosphino)methyl]phenyl palladium} ($i^{\text{Pr}}\text{PCP}$)PdPh. Ellipsoids are drawn at 50% probability level. Hydrogen atoms are omitted for clarity.



Selected bond lengths for ($i^{\text{Pr}}\text{PCP}$)PdPh (Å): Pd1–P1 2.267, Pd1–C1 2.096, Pd1–C15 2.073, P1–C7 1.846, P1–C10 1.842, C1–C2 1.411, C1–C10 1.402, C13–C14 1.515(2), C14–C15 1.414. Selected bond angles (deg): P1–Pd1–C1 97.03, P1–Pd1–C15 82.98, P1–Pd1–P1 165.39, C1–Pd1–C15 179.92, C1–Pd1–P1 97.03, C15–Pd1–P1 82.98, Pd1–P1–C7 116.37, Pd1–P1–C10 119.86, Pd1–P1–C13 104.53, C7–P1–C10 105.80, C2–C1–C6 115.6.

Figure 3.3.5 ^1H NMR spectrum of 2,5-di[(di-*iso*-propyl phosphino)methyl]phenyl palladium benzoate ($i^{\text{Pr}}\text{PCP}$)PdOBz in CD_3CN . Unlabeled peaks are from residual solvent (Et_2O and THF) in the NMR solvent due to the atmosphere in the glovebox.

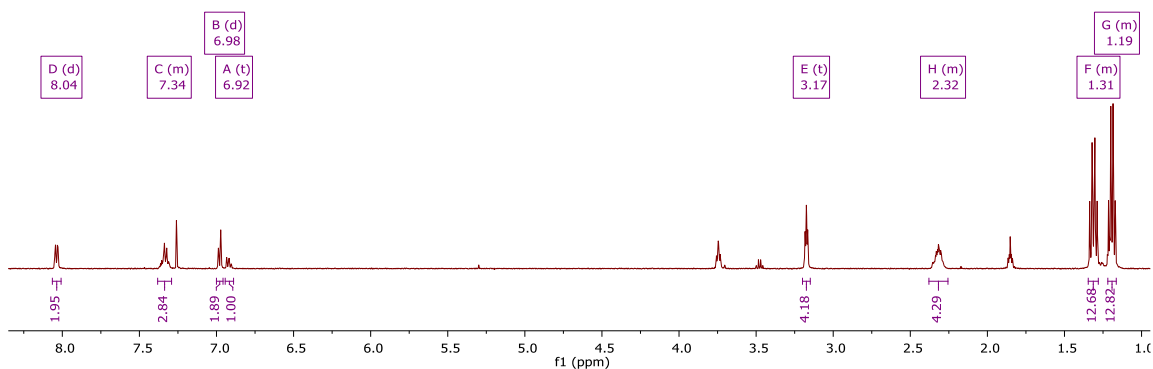


Figure 3.3.6 ^{31}P NMR spectrum for 2,5-di[(di-*iso*-propyl phosphino)methyl]phenyl palladium benzoate ($^{i\text{Pr}}\text{PCP}$)PdOBz in CD_3CN .

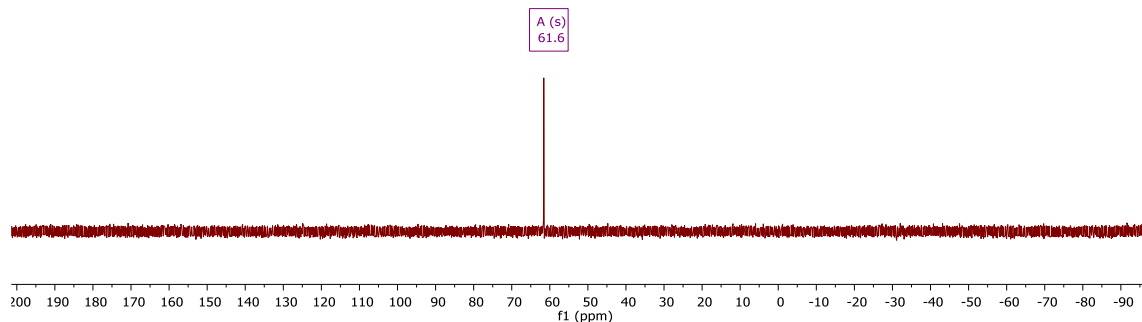
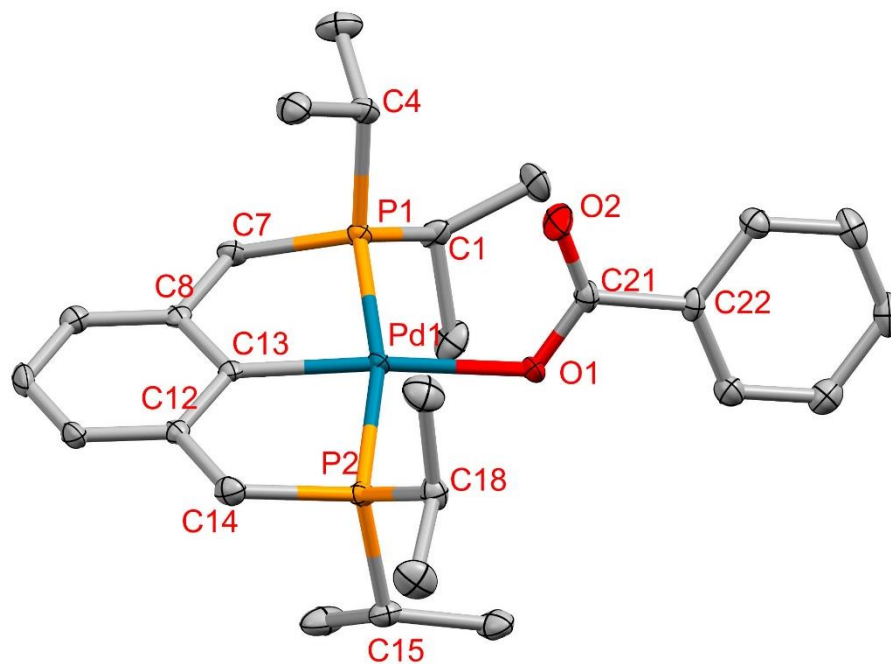


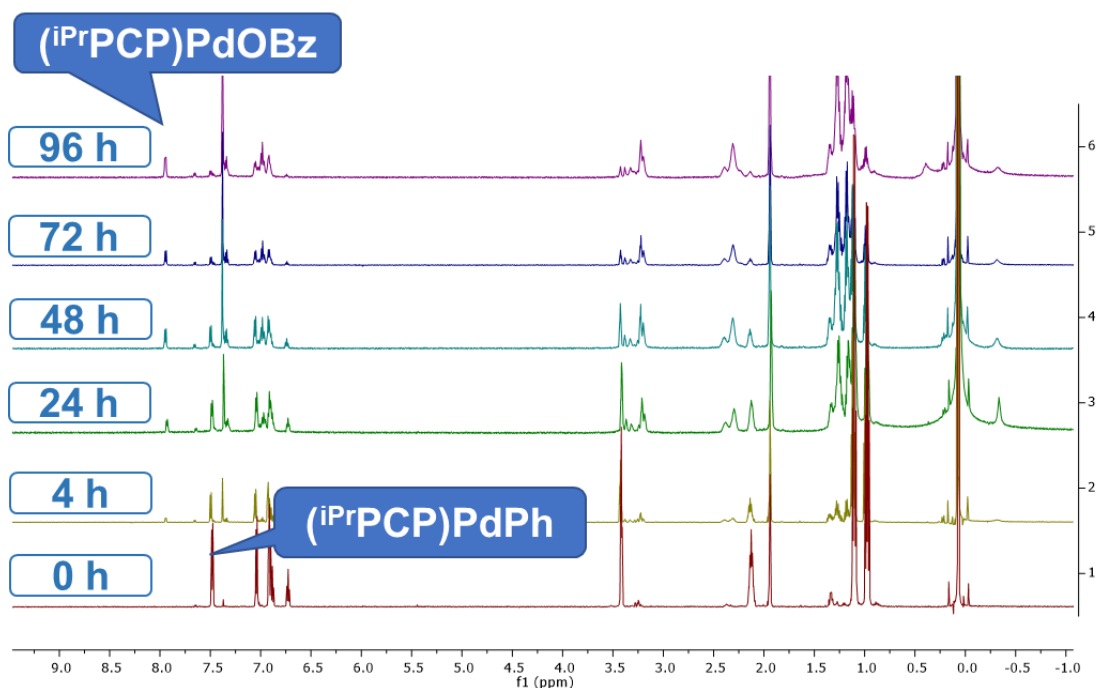
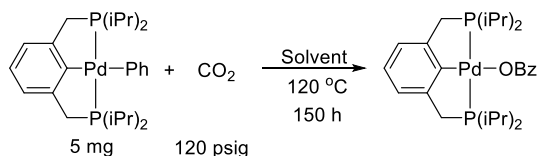
Figure 3.3.7 ORTEP of 2,5-di[(di-*iso*-propyl phosphino)methyl]phenyl palladium benzoate [$^{i\text{Pr}}\text{PCP}$)PdOBz]. Ellipsoids are drawn at 50% probability level. Hydrogen atoms are omitted for clarity.



Selected bond lengths for ($^{i\text{Pr}}\text{PCP}$)PdOBz (Å): Pd1–P1 2.289(1), Pd1–P2 2.268(1), Pd(1) – O1 2.100(3), Pd1–C13 2.010(5), P1–C1 1.842(6), P1–C4 1.837(5), P1–C7 1.838(5), P2–C14 1.837(5), P2–C15 1.837(5), P2–C18 1.827(5), O1–C21 1.281(6), O2–C21 1.232(7), C7–C8 1.507(6), C8–C13 1.410(7), C12–C13 1.416(6), C12–C14 1.509(7), C21–C22 1.516(7). Selected bond angles (deg): P1–Pd1–P2 167.36(5), P1–Pd1–O1 98.32(9), P1–Pd1–C13 83.7(1), P2–Pd1–O1 94.19(9), P2–Pd1–C13 83.6(1), O1–Pd1–C13 174.1(2), Pd1–P1–C1 117.9(2), Pd1–P1–C4 115.8(2), Pd1–P1–C7 102.2(2), C1–P1–C4 107.7(2),

C1–P1–C7 105.0(2), C4–P1–C7 107.0(2), Pd1–P2–C14 103.3(2), Pd1–P2–C15 113.4(2), Pd1–P2–C18 117.0(2), C14–P2–C15 107.4(2), C14–P2–C18 108.6(2), C15–P2–C18 106.7(2), Pd1–O1–C21 122.1(3), C7–C8–C13 119.8(4), C13–C12–C14 120.0(4).

With the characterization data of (ⁱPrPCP)PdPh and (ⁱPrPCP)PdOBz, the CO₂ insertion reaction of (ⁱPrPCP)PdPh to form (ⁱPrPCP)PdOBz was studied using ¹H NMR spectroscopy. **Figure 3.3.8** displays the ¹H NMR resonances for (ⁱPrPCP)PdOBz and (ⁱPrPCP)PdPh in MeCN-*d*₃ during the CO₂ insertion of (ⁱPrPCP)PdPh. A series of NMR scale reactions were performed with 5 mg (ⁱPrPCP)PdPh, 120 psig CO₂ and various NMR solvents. Interestingly, the CO₂ insertion of (ⁱPrPCP)PdPh exhibited a dependence on the solvent (**Table 3.3.1**). Although no/minimal CO₂ insertion into (ⁱPrPCP)PdPh was observed in THF-*d*₈, benzene-*d*₆ or DMSO-*d*₆, the formation of (ⁱPrPCP)PdOBz was detected when the CO₂ insertion was performed in MeCN-*d*₃ and DMF-*d*₇ with 37% and 19% yield respectively.

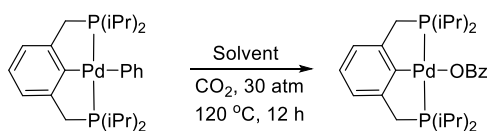
Figure 3.3.8 ^1H NMR spectra for CO_2 insertion into $(i\text{PrPCP})\text{PdPh}$ to form $(i\text{PrPCP})\text{PdOBz}$.**Table 3.3.1** NMR scale studies on CO_2 insertion into $(i\text{PrPCP})\text{PdPh}$.

Solvent	% NMR Yield of $(i\text{PrPCP})\text{PdOBz}$
THF- d_8	trace
benzene- d_6	0
MeCN- d_3	37
DMF- d_7	19
DMSO- d_6	0

To mimic the catalytic conditions used in **Table 3.2.2**, the CO_2 insertion into $(i\text{PrPCP})\text{PdPh}$ under higher CO_2 pressure was examined (**Table 3.3.2**). Similar to the NMR

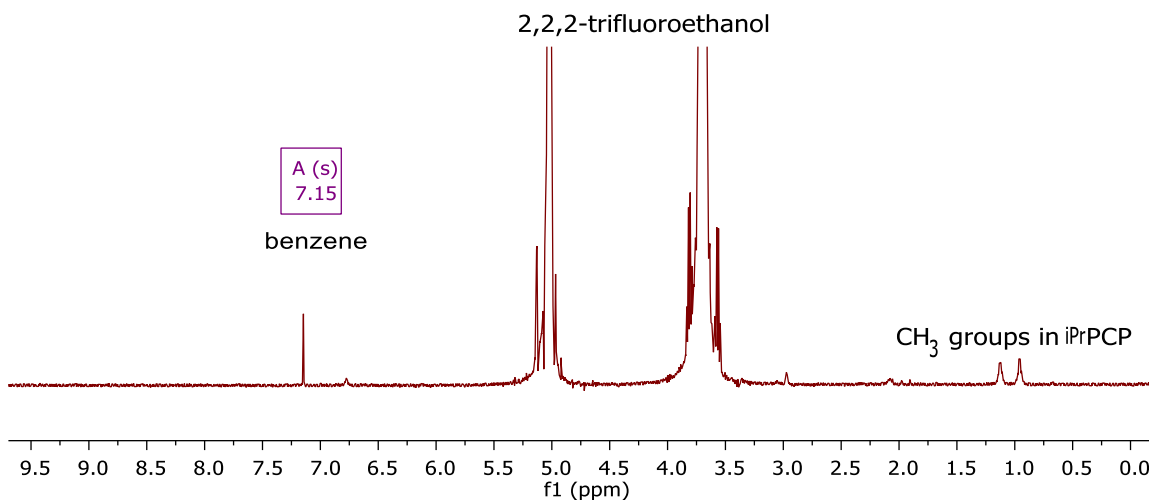
scale conditions with lower pressure (**Table 3.3.1**), (ⁱPrPCP)PdPh also reacted with CO₂ in MeCN, which gave a 72% NMR yield. Dimethylacetamide (DMA) is also capable of facilitating CO₂ insertion, in which 55% of (ⁱPrPCP)PdPh is transformed to (ⁱPrPCP)PdOBz. Benzene, propylene carbonate, and THF were also tested, but no (ⁱPrPCP)PdOBz was observed. When 2,2,2-trifluoroethanol was used as the solvent, 2,2,2-trifluoroethanol immediately reacted with (ⁱPrPCP)PdPh, leading to the formation of benzene (**Figure 3.3.9**).

Table 3.3.2 Studies on CO₂ insertion into (ⁱPrPCP)PdPh with high pressure of CO₂



Solvent	% NMR Yield of (ⁱ PrPCP)PdOBz
MeCN	72
DMA	55
CF ₃ CH ₂ OH	0
benzene	0
propylene carbonate	0
THF	0

Figure 3.3.9 Observed formation of benzene in the ^1H NMR spectra for $(i\text{Pr}^{\text{r}}\text{PCP})\text{PdPh}$ in 2,2,2-trifluoroethanol.



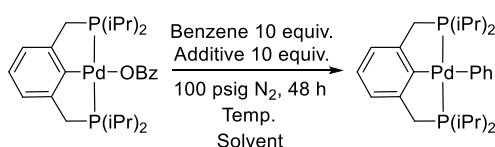
In summary, the CO_2 insertion into $(i\text{Pr}^{\text{r}}\text{PCP})\text{PdPh}$ exhibits a significant dependence on the solvent. It needs to be pointed out that, despite the fact that the CO_2 can react with $(i\text{Pr}^{\text{r}}\text{PCP})\text{PdPh}$ in some solvents such as MeCN, DMF and DMA, no evidence for the CO_2 insertion into $(i\text{Pr}^{\text{r}}\text{PCP})\text{PdPh}$ in benzene can be found. Hence, the result from the studies on CO_2 insertion into $(i\text{Pr}^{\text{r}}\text{PCP})\text{PdPh}$ suggests that with the conditions shown in **Table 3.2.2**, in which benzene serves as both a reactant and a solvent, the CO_2 insertion step could be troublesome.

3.4 Studies of benzene C–H activation by $(i\text{Pr}^{\text{r}}\text{PCP})\text{PdOBz}$

The mechanism in **Scheme 3.1.6** proposes that C–H activation of benzene is mediated by the Pd–carboxylate species after the CO_2 insertion. Thus, the possibility of C–H activation of benzene by $(^{\text{R}}\text{PCP})\text{PdX}$ ($\text{R} = \text{tBu}, \text{Ph}$ or $i\text{Pr}$; $\text{X} = \text{carboxylate}$) was evaluated. It was speculated that if $(^{\text{R}}\text{PCP})\text{PdX}$ could C–H activate benzene, the formation of the corresponding $(^{\text{R}}\text{PCP})\text{Pd-Ph}$ complex should be observed. Hence, $(i\text{Pr}^{\text{r}}\text{PCP})\text{PdOBz}$ was selected as a model for this study because the observation of $(i\text{Pr}^{\text{r}}\text{PCP})\text{PdPh}$ would be easier

to detect than (^tBuPCP)PdPh thanks to the relatively more complete characterization data for the isolated (ⁱPrPCP)PdPh. (ⁱPrPCP)PdOBz and base additive were added to a solution with at least 10 equivalents of benzene (**Table 3.4.1**). The solution was pressurized with 100 psig N₂, and then heated to the temperature listed in **Table 3.4.1**. The consumption of (ⁱPrPCP)PdOBz and the formation of (ⁱPrPCP)PdPh were monitored by ¹H NMR and ³¹P NMR spectroscopy. Although the consumption of (ⁱPrPCP)PdOBz can be observed in some conditions, the detection of (ⁱPrPCP)PdPh in the reaction solution was not achieved in any of the reactions with the conditions shown in **Table 3.4.1**.

Table 3.4.1 Investigation of (ⁱPrPCP)PdOBz mediated benzene C–H activation.



Conditions			(ⁱ PrPCP)PdOBz	(ⁱ PrPCP)PdPh
Solvent	Additive	Temperature (°C)	consumed?	formed?
	None	120	No	No
CD ₃ CN	Cs ₂ CO ₃	100	Yes	No
	DMAP	100	Yes	No
	DMAP	120	Yes	No
	NEt ₃	100	Yes	No
	NEt ₃	120	Yes	No
	None	120	No	No
C ₆ D ₆	Cs ₂ CO ₃	120	No	No
	NaOMe	120	No	No

	None	150	No	No
	Cs ₂ CO ₃	150	No	No
	Cs ₂ CO ₃	120	No	No
C ₆ H ₆	DBU	120	No	No
	NEt ₃	150	Yes	No

Another method to investigate the C–H activation of benzene with (ⁱPrPCP)PdOBz is to study the H/D exchange between benzene and benzene-*d*₆. In this study, 2 mL of 1:1 (v:v) mixture of benzene and benzene-*d*₆ was mixed with 10 mg of (ⁱPrPCP)PdOBz, and then diluted to 5 mL with MeCN, THF or toluene. The solution was heated at 150 °C for 48 hours. The reaction solution was analyzed by GC-MS. If the H/D exchange between benzene and benzene-*d*₆ occurs, an expected observation is the detection of isotopologues of benzene, such as benzene-*d*₁₋₅, which can be distinguished from the peak of protio benzene using GC-MS based on their differing *m/z* of their molecular ion peaks. **Figure 3.4.1–Figure 3.4.3** demonstrate the comparison of the percentage of different benzene isotopologues in the stock solution and the reaction solution. In all three attempted conditions, the distribution of the benzene isotopologues does not show a significant change. This result could suggest that the C–H activation of (ⁱPrPCP)PdOBz does not occur.

Figure 3.4.1 Changes in the percentage of different isotopic labeled benzene. Conditions: 1 mL benzene, 1 mL benzene- d_6 , 3 mL acetonitrile, 10 mg (iPr PCP)PdOBz, 150 °C, 48 hours.

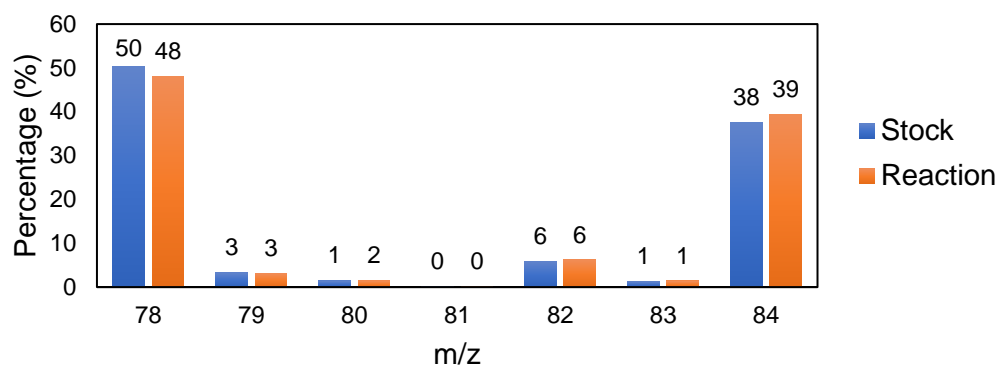


Figure 3.4.2 Changes in the percentage of different isotopic labeled benzene. Conditions: 1 mL benzene, 1 mL benzene- d_6 , 3 mL tetrahydrofuran, 10 mg (iPr PCP)PdOBz, 150 °C, 48 hours.

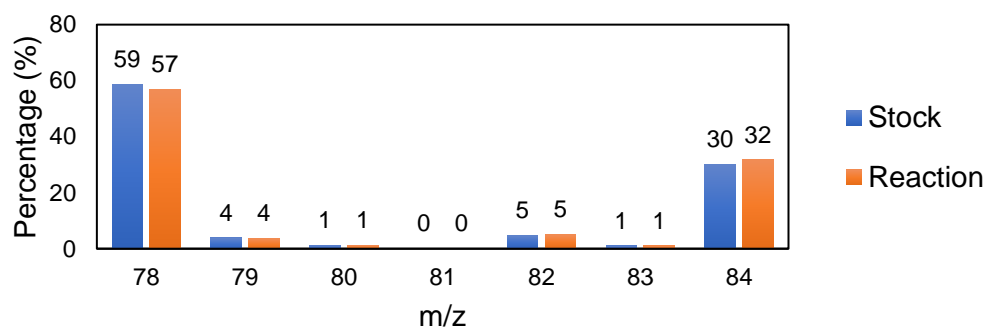
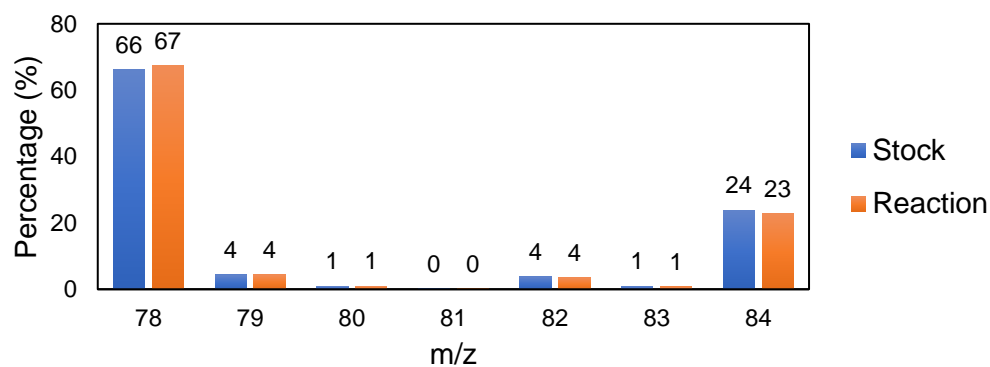


Figure 3.4.3 Changes in the percentage of different isotopic labeled benzene. Conditions: 1 mL benzene, 1 mL benzene- d_6 , 3 mL toluene, 10 mg (iPr PCP)PdOBz, 150 °C, 48 hours.



3.5 Conclusions

Based on previous studies, a synthetic route to benzoic acid through base-mediated direct carboxylation of benzene catalyzed by (PCP)PdX (X = carboxylate) was proposed. DFT calculations predicted that the (^{Me}PCP)PdOAc-catalyzed benzene direct carboxylation has achievable activation barriers for both C–H activation of benzene via concerted metalation deprotonation (CMD) and CO₂ insertion into the Pd–Ph bond of (^{Me}PCP)PdPh. Although a series of the conditions (Pd catalysts and base additives) were screened, the formation of benzoic acid or benzoate salts were not observed for a majority of the attempted conditions.

In order to investigate the kinetic challenges in the proposed catalytic cycle, the CO₂ insertion into the (^{iPr}PCP)PdPh complex and the C–H activation of benzene by (^{iPr}PCP)PdOBz were both studied. The insertion of CO₂ into the Pd–Ph bond of (^{iPr}PCP)PdPh was examined with various solvents, temperatures and pressures of CO₂. Although CO₂ insertion into (^{iPr}PCP)PdPh is observed when the reaction was performed in MeCN, THF, DMA and DMF, no evidence can be found for CO₂ insertion using (^{iPr}PCP)PdPh is active in benzene, which serves as both the solvent and the substrate for the screenings on catalytic direct carboxylation of benzene. Moreover, no evidence could support that (^{iPr}PCP)PdOBz is able to perform C–H activation benzene.

3.6 Experimental section

General Procedures. All experiments with metal complexes and phosphine ligands were performed under an atmosphere of dinitrogen in a glovebox or using Schlenk techniques. All solvents were reagent grade or better. Solvents in the glovebox were distilled from either potassium and benzophenone (for THF and diethyl ether) or CaH₂ (for

MeCN), purged under dinitrogen flow, and then stored with molecular sieves.⁴⁸ Deuterated solvents were kept in the glovebox with molecular sieves (3Å or 4Å, depending on the type of solvent⁴⁸). Molecular sieves were dried in a vacuum oven at 150 °C overnight before transferring into the glovebox. All celite used in this chapter was Celite™ 545 purchased from Fisher Chemical (LOT 225266). Commercially available reagents were used as received.

¹H and ³¹P NMR spectra were collected at 600 MHz and 243 MHz frequencies, respectively, on a Varian NMRS 600 with multiple probes. ¹H NMR spectra were referenced against residual proton signals of the deuterated solvent.⁴⁹ ³¹P NMR spectra were referenced against an external H₃PO₄ standard (0 ppm).

GC-MS data were collected on a Shimadzu GCMS-QP 2010 gas chromatograph mass spectrometer with a DB-FFAP capillary column (60 m × 0.250 mm × 0.25 μm). The temperature of the oven was set to start from 50 °C and hold for 0.5 min, then heat up by a 15 °C/min increment until the temperature reached 230 °C, and finally hold at 230 °C for 10 min. The retention time of hexamethylbenzene (HMB, internal standard), biphenyl, and benzoic acid were 12.59 min, 13.32 min, and 17.44 min, respectively. Calibration curves for biphenyl and benzoic acid were recorded for quantitative measurements (**Figure 3.6.1** and **Figure 3.6.2**).

Figure 3.6.1 Calibration curve for quantification of biphenyl using hexamethylbenzene as a standard.

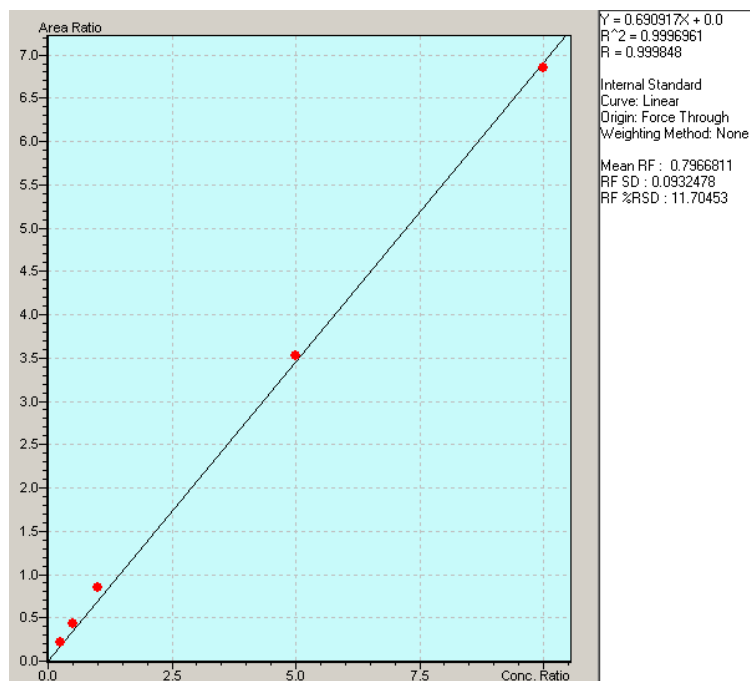
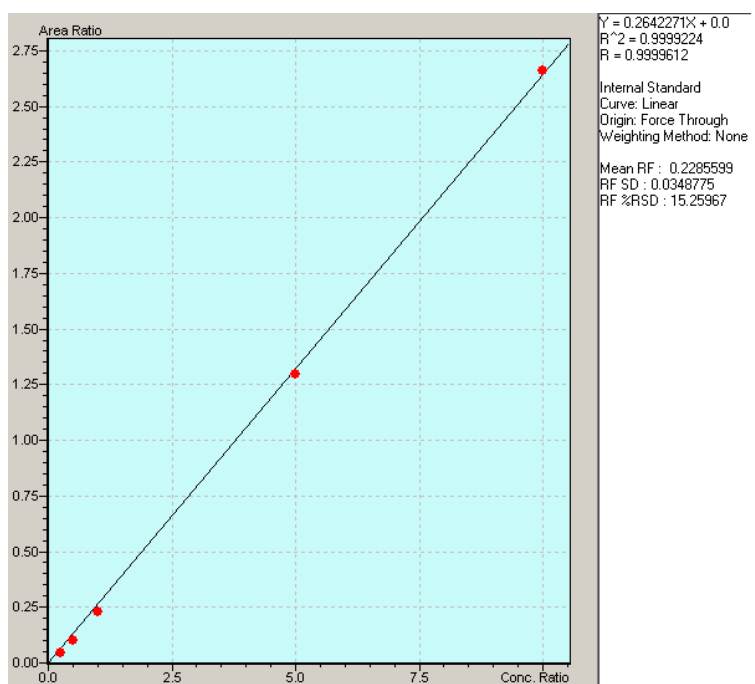


Figure 3.6.2 Calibration curve for quantification of benzoic acid using hexamethylbenzene as a standard.



Synthesis of 1,3-di[(diphenylphosphino)methyl]benzene (^{Ph}PCPH). The procedure is adapted from a reported procedure with minor modifications.⁴⁰ In a Schlenk flask, diphenylphosphine (1.0 mL, 2.9 mmol) was dissolved in 15 mL THF. The solution was cooled to -40 °C under N₂ flow. The base, 1.6 M *n*-butyllithium in hexane solution (1.8 mL, 2.9 mmol), was added dropwise and stirred for 30 minutes. The pale-yellow solution turned orange. The mixture was warmed to room temperature and stirred for 1 hour. The mixture was then cooled to -70 °C. A 5 mL THF solution of α,α' -dichloro-*m*-xylene (0.500 g, 1.45 mmol) was added to the mixture dropwise. The solution was allowed to warm to room temperature and stirred overnight under N₂ flow. In a glove box, the solvent was removed under reduced pressure. The white solid that formed was extracted with diethyl ether. Diethyl ether was removed under reduced pressure and a colorless paste was obtained. Washing the paste with pentane and drying under vacuum yielded a white solid. The white solid was washed with 5 mL pentane and dried three times, and 1.15 g (2.4 mmol, 84% yield) of ^{Ph}PCPH was obtained. ¹H NMR (600 MHz, chloroform-*d*) δ 7.37 – 7.33 (m, Ar-H, 8H), 7.30 (m, Ar-H, 12H), 6.95 (t, ³J_{H-H} = 7 Hz, 1H), 6.87 (s, Ar-H, 1H), 6.78 (d, ³J_{H-H} = 7 Hz, 2H), 3.30 (s, PCH₂, 4H). ³¹P{¹H} NMR (243 MHz, chloroform-*d*) δ -10.2.

Figure 3.6.3 ¹H NMR spectrum for 1,3-di[(diphenylphosphino)methyl]benzene (^{Ph}PCPH). Unlabeled peaks are from residual solvent (including Et₂O, THF, DCM, toluene) in the NMR solvent due to the atmosphere in the glovebox.

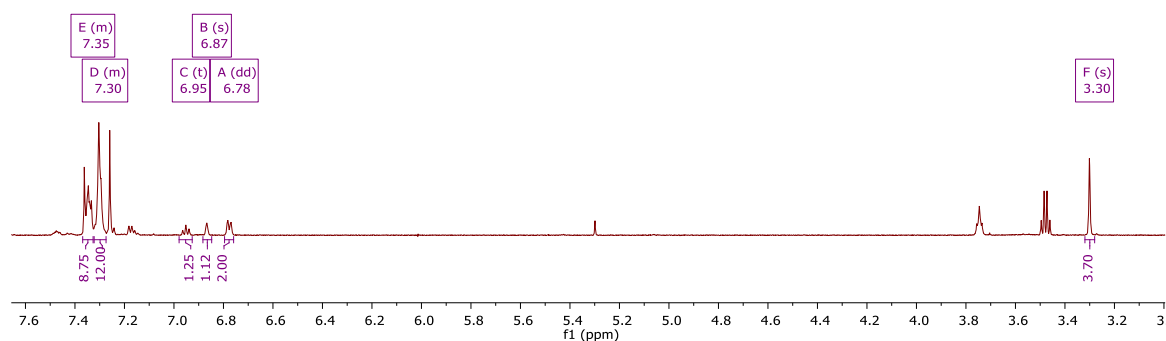
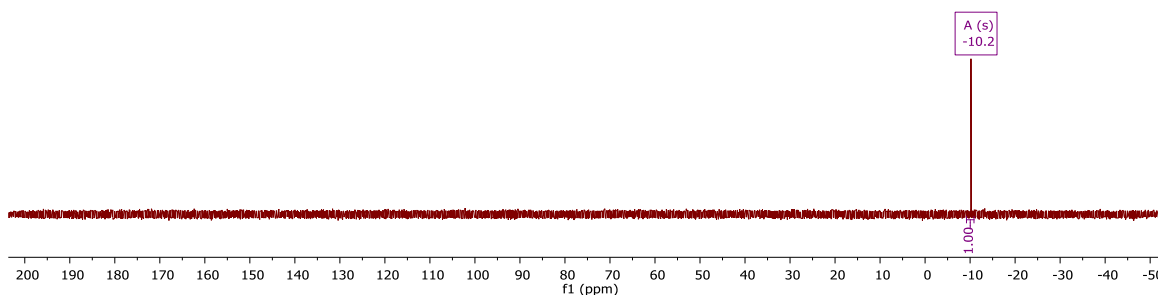


Figure 3.6.4 ^{31}P NMR spectrum for 1,3-di[(diphenylphosphino)methyl]benzene ($^{\text{Ph}}\text{PCPH}$).



Synthesis of 1,3-di[(di-*tert*-butylphosphino)methyl]benzene ($^{\text{tBu}}\text{PCPH}$). The procedure is adapted from a reported procedure with minor modifications.^{41, 42} In a glove box, α,α' -dibromo-*m*-xylene (0.380 g, 1.45 mmol) was dissolved in 10 mL methanol in a round bottom flask. Di-*tert*-butylphosphine (0.55 mL, 2.9 mmol) was added dropwise. The mixture was stirred for 24 hours. Sodium methoxide (0.156 g, 2.90 mmol) was added to the reaction solution and stirred for 4 hours. Methanol was evaporated under reduced pressure. 30 mL of dichloromethane was used to wash the solid. Filtration under reduced pressure through celite was performed to remove sodium bromide. Dichloromethane was removed under reduced pressure to yield $^{\text{tBu}}\text{PCPH}$ as a white solid (0.488 g, 1.24 mmol, 85% yield). ^1H NMR (600 MHz, benzene- d_6) δ 7.63 (s, 1H, Ar-H), 7.30 (d, $^3J_{\text{H-H}} = 7$ Hz, 2H), 7.18 (overlaped with benzene- d_6 , 1H), 2.79 (d, $^2J_{\text{H-P}} = 2$ Hz, 4H), 1.08 (d, $^3J_{\text{H-P}} = 11$ Hz, 36H). $^{31}\text{P}\{^1\text{H}\}$ NMR (243 MHz, benzene- d_6) δ 33.7.

Figure 3.6.5 ^1H NMR spectrum for 1,3-di[(di-*tert*-butylphosphino)methyl]benzene ($^t\text{BuPCPH}$). Unlabeled peaks are from residual solvent (including Et_2O , THF, cyclohexane) in the NMR solvent due to the atmosphere in the glovebox.

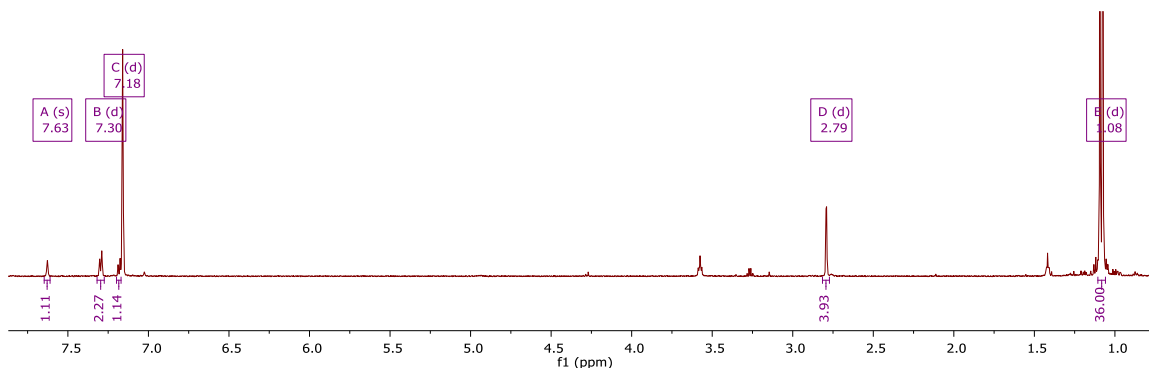
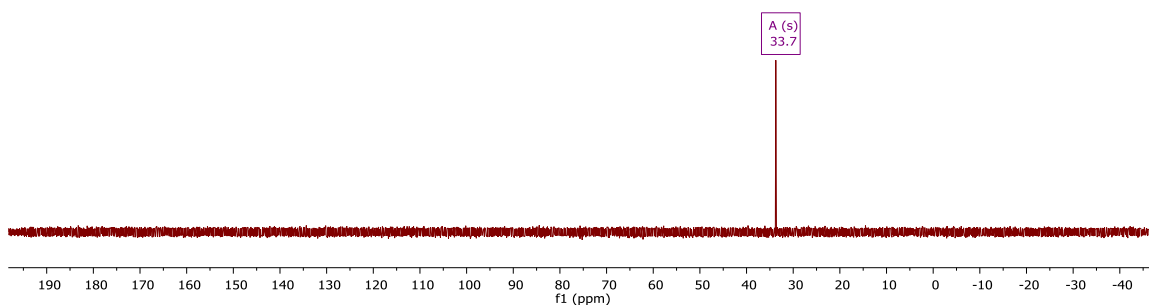


Figure 3.6.6 ^{31}P NMR spectrum for 1,3-di[(di-*tert*-butylphosphino)methyl]benzene ($^t\text{BuPCPH}$).



Synthesis of 1,3-di[(di-*iso*-propylphosphino)methyl]benzene ($^i\text{PrPCPH}$). The procedure is adapted from a reported procedure with minor modifications.⁴⁴ In a glovebox, di-*iso*-propylphosphinochloride (610 mg, 0.64 mL, 4.0 mmol) was dissolved in 5 mL acetonitrile. A solution of α,α' -dibromo-*m*-xylene (528 mg, 2.00 mmol) in 5 mL of acetonitrile was added to the di-*iso*-propylphosphinochloride solution dropwise. The mixture was stirred at 100 °C for 15 hours. The solution was then cooled in an ice bath and then polished magnesium powder (122 mg, 5.00 mmol) was added under nitrogen atmosphere. The reaction mixture was stirred in ice bath for 2 hours, and allowed to stir at room temperature for another 2 hours. The product was extracted with pentane (3×20 mL) in a glovebox. Solvent was removed under reduced pressure, yielding 465 mg (68 % yield)

of ⁱPrPCPH as a yellow oil. ¹H NMR (600 MHz, benzene-*d*₆) δ 7.44 (br s, 1 H), 7.16 (m, 3 H), 2.69 (br s, 4 H), 1.61 (dsp, ²J_{H-P} = 2 Hz, ³J_{H-H} = 7 Hz, 4 H), 1.02 (d, ³J_{H-H} = 7 Hz, 12 H), 1.00 (d, ³J_{H-H} = 7 Hz, 12 H). ³¹P{¹H} NMR (243 MHz, benzene-*d*₆): δ 10.3.

Figure 3.6.7 ¹H NMR spectrum for 1,3-di[(di-*iso*-propylphosphino)methyl]benzene (ⁱPrPCPH).

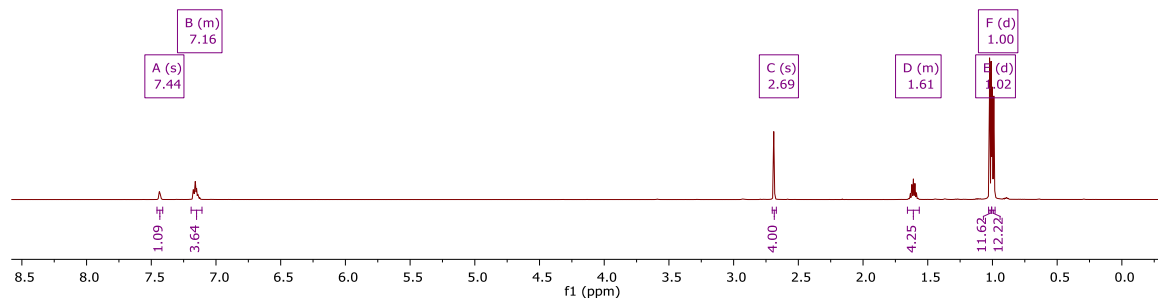
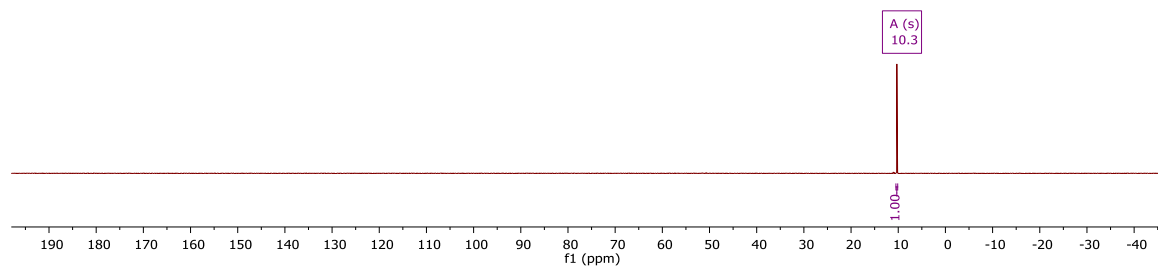


Figure 3.6.8 ³¹P NMR spectrum for 1,3-di[(di-*iso*-propylphosphino)methyl]benzene (ⁱPrPCPH).



Synthesis of 2,5-di[(diphenylphosphino)methyl]phenyl palladium trifluoroacetate (^{Ph}PCP)Pd(TFA). The procedure is adapted from a reported procedure with minor modifications.⁴³ To a 10 mL THF suspension of palladium(II) trifluoroacetate (175 mg, 0.53 mmol), 10 mL of a toluene solution of ^tBuPCPH (250 mg, 0.53 mmol) was added dropwise to a Schlenk flask. The reaction mixture was stirred at room temperature for 6 hours during which the yellow solution turned black. The solution was filtered through celite, and the resulting solid was extracted with methanol. The methanol was removed *in vacuo*, resulting in formation of (^{Ph}PCP)Pd(TFA) (105 mg, 28% yield) as a pale-yellow

solid. ^1H NMR (600 MHz, benzene- d_6) δ 7.77 (m, 8H), 7.01 (t, $^3J_{\text{H-H}} = 7$ Hz, 8H), 6.95 (m, 5H, Ar-H), 6.87 (d, $^3J_{\text{H-H}} = 8$ Hz, 2H), 3.32 (vt, 4H). $^{31}\text{P}\{^1\text{H}\}$ NMR (243 MHz, benzene- d_6) δ 36.4.

Figure 3.6.9 ^1H NMR spectrum for 2,5-di[(diphenylphosphino)methyl]phenyl palladium trifluoroacetate ($^{\text{Ph}}\text{PCP}$)Pd(TFA). Unlabeled peaks are from residual solvent (including Et₂O, THF, DCM) in the NMR solvent due to the atmosphere in the glovebox.

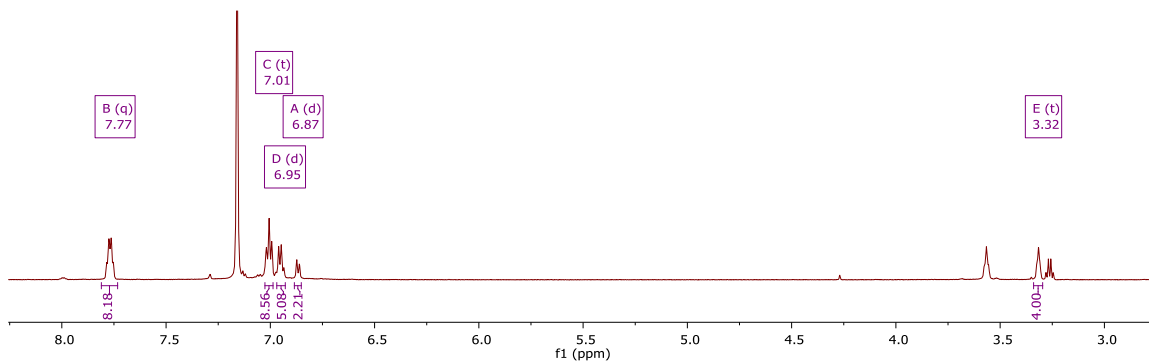
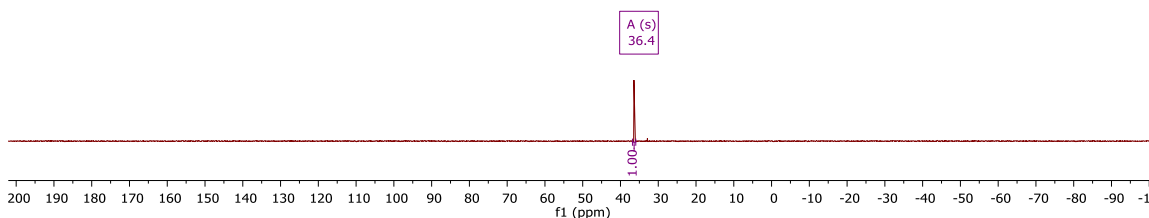


Figure 3.6.10 ^{31}P NMR spectrum for 2,5-di[(diphenylphosphino)methyl]phenyl palladium trifluoroacetate ($^{\text{Ph}}\text{PCP}$)Pd(TFA).



Synthesis of 2,5-di[(di-*tert*-butyl phosphino)methyl]phenyl palladium trifluoroacetate ($^{\text{tBu}}\text{PCP}$)Pd(TFA). The procedure is adapted from a reported procedure with minor modifications.⁴⁰ To a 5 mL toluene suspension of palladium (II) trifluoroacetate (335 mg, 1.27 mmol), 5 mL of a toluene solution of $^{\text{tBu}}\text{PCPH}$ (400 mg, 1.01 mmol) was added dropwise in a pressure tube. The reaction mixture was stirred at 130 °C for 1 hour. The solution was filtered through celite and the resulting solid was dried *in vacuo*. 515 mg (86.2 % yield) of ($^{\text{tBu}}\text{PCP}$)Pd(TFA) was yielded as a pale yellow/white solid. ^1H NMR (600

MHz, benzene- d_6) δ 6.98 (t, $^3J_{\text{H-H}} = 7$ Hz, 1H), 6.84 (d, $^3J_{\text{H-H}} = 7$ Hz, 2H), 2.84 (vt, 4H), 1.19 (vt, 36H). $^{31}\text{P}\{^1\text{H}\}$ NMR (243 MHz, benzene- d_6) δ 73.8.

Figure 3.6.11 ^1H NMR spectrum for 2,5-di[(di-*tert*-butyl phosphino)methyl]phenyl palladium trifluoroacetate [$^{\text{iBu}}\text{PCP}$]Pd(TFA). Unlabeled peaks are from residual solvent (including Et₂O, THF, DCM, n-pentane) in the NMR solvent due to the atmosphere in the glovebox.

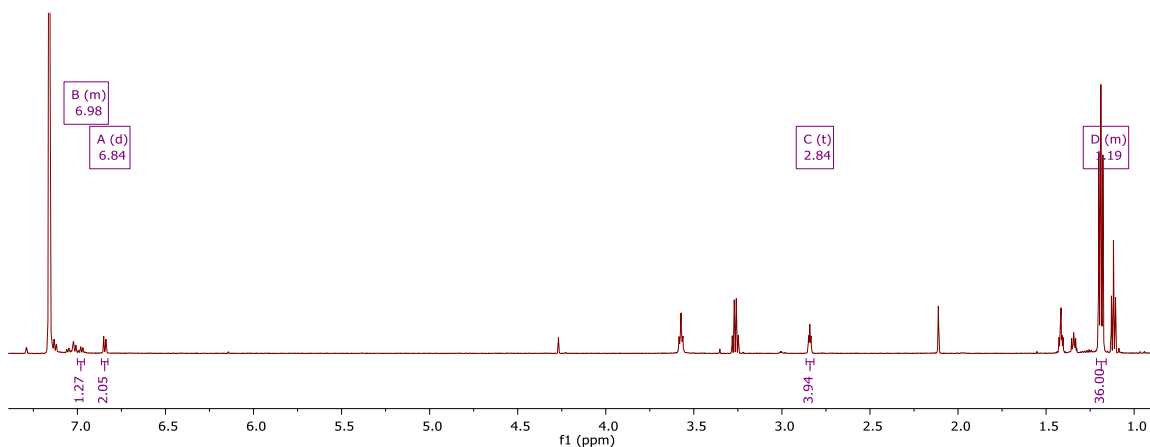


Figure 3.6.12 ^{31}P NMR spectrum for 2,5-di[(di-*tert*-butyl phosphino)methyl]phenyl palladium trifluoroacetate ($^{\text{iBu}}\text{PCP}$)Pd(TFA).

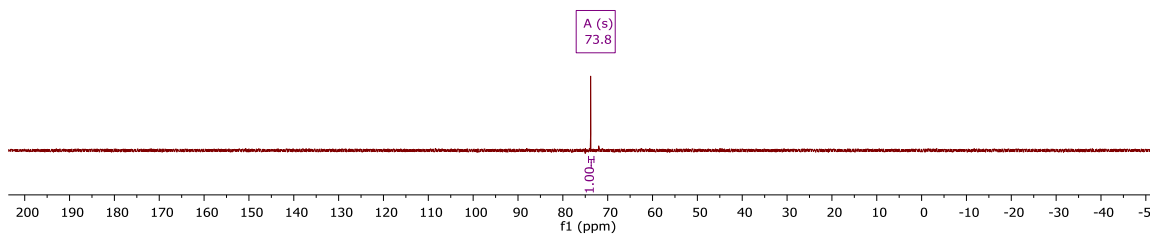
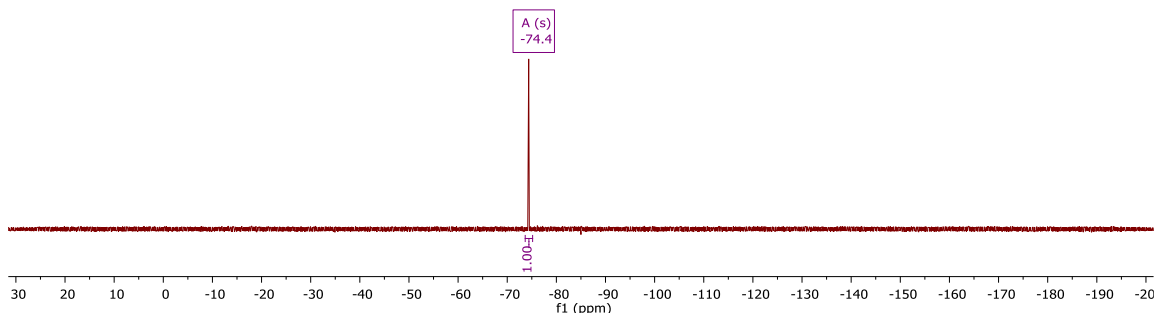


Figure 3.6.13 ^{19}F NMR spectrum for 2,5-di[(di-*tert*-butyl phosphino)methyl]phenyl palladium trifluoroacetate ($^{\text{tBu}}\text{PCP}$)Pd(TFA).



Synthesis of 2,5-di[(di-*tert*-butyl phosphino)methyl]phenyl palladium chloride ($^{\text{tBu}}\text{PCP}$)PdCl. The procedure is adapted from a reported procedure with minor modifications.⁵⁰ 0.14 g (0.49 mmol) ammonium tetrachloropalladate, $(\text{NH}_4)_2\text{PdCl}_4$, was dissolved in 20 mL 2-methoxyethanol under nitrogen atmosphere. 0.20 g (0.51 mmol) $^{\text{tBu}}\text{PCPH}$ (free ligand) was quickly added to the flask under nitrogen flow, followed by degassing to remove residual air. The mixture was heated at 100 °C for 40 minutes. The reaction solution solvent was removed to *ca.* 5 mL *in vacuo*, and 15 mL DI water was added to the mixture to obtain a white precipitate. The precipitate was isolated by filtration through a fine grade frit, and washed with 10 mL 4:1 (v:v) ethanol and water 3 times. The resulting product was dried under vacuum overnight, yielding 145.9 mg (23.6 mmol, 48% yield) product as a white powder. ^1H NMR (600 MHz, chloroform-*d*) δ 6.97 (d, $^3J_{\text{H-H}} = 7$ Hz, 2H), 6.91 (t, $^3J_{\text{H-H}} = 7$ Hz, 1H), 3.23 (vt, 4H), 1.42 (vt, 36H). $^{31}\text{P}\{^1\text{H}\}$ NMR (243 MHz, Chloroform-*d*) δ 72.7.

Figure 3.6.14 ^1H NMR spectrum for 2,5-di[(di-*tert*-butyl phosphino)methyl]phenyl palladium chloride ($^t\text{BuPCP}$)PdCl

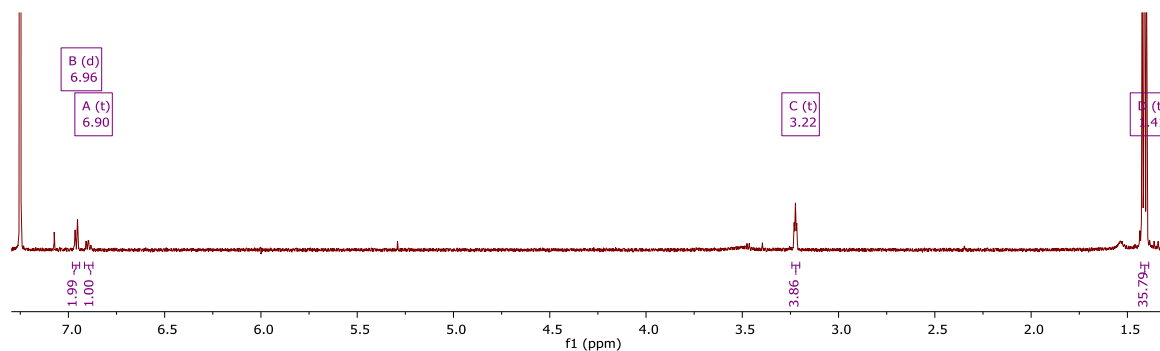
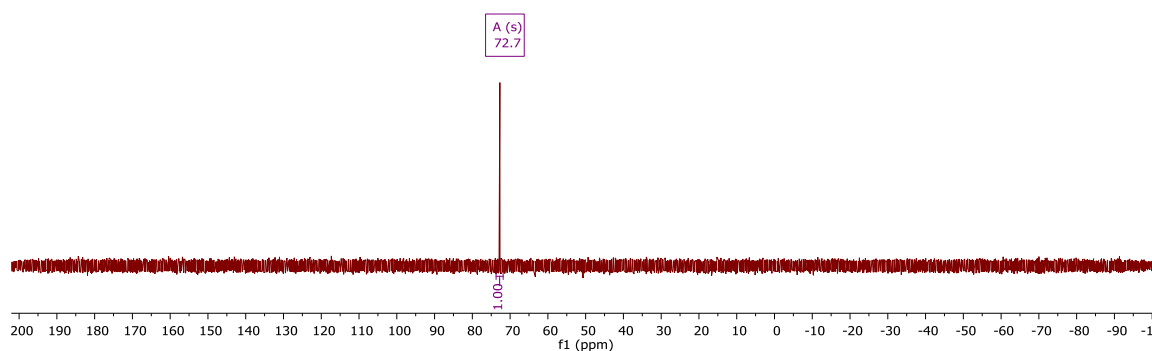


Figure 3.6.15 ^{31}P NMR spectrum for 2,5-di[(di-*tert*-butyl phosphino)methyl]phenyl palladium chloride [$^t\text{BuPCP}$]PdCl



Synthesis of 2,5-di[(di-*iso*-propyl phosphino)methyl]phenyl palladium chloride ($^i\text{PrPCP}$)PdCl. The procedure is adapted from a reported procedure with minor modifications.⁴⁵ In a glovebox, 0.200 g (0.70 mmol) dichloro(1,5 - cyclooctadiene)palladium, Pd(COD)Cl₂, and 0.234 g (0.70 mmol) $^i\text{PrPCPH}$ (free ligand) were dissolved in 50 mL toluene. The solution was heated to reflux under N₂ atmosphere for 8 hours. The solvent was then removed *in vacuo* and the crude product was washed with 10 mL *n*-pentane 3 times. It was then dissolved in Et₂O followed by filtration. The Et₂O solution was concentrated under vacuum, and the product was crystallized from the ethereal solution at -30 °C as a white solid (145 mg, 0.30 mmol, 43% yield). ^1H NMR (600

MHz, benzene- d_6) δ 7.07 – 7.03 (t, $^3J_{\text{H-H}} = 8$ Hz), 6.98 (d, $^3J_{\text{H-H}} = 8$ Hz, 2H), 2.80 (vt, 4H), 2.10 – 2.04 (m, 4H), 1.40 – 1.34 (m, 12H), 0.92 – 0.87 (m, 12H). ^{31}P NMR (243 MHz, benzene- d_6) δ 61.9.

Figure 3.6.16 ^1H NMR spectrum for 2,5-di[(di-*iso*-propyl phosphino)methyl]phenyl palladium chloride ($i\text{PrPCP}$)PdCl.

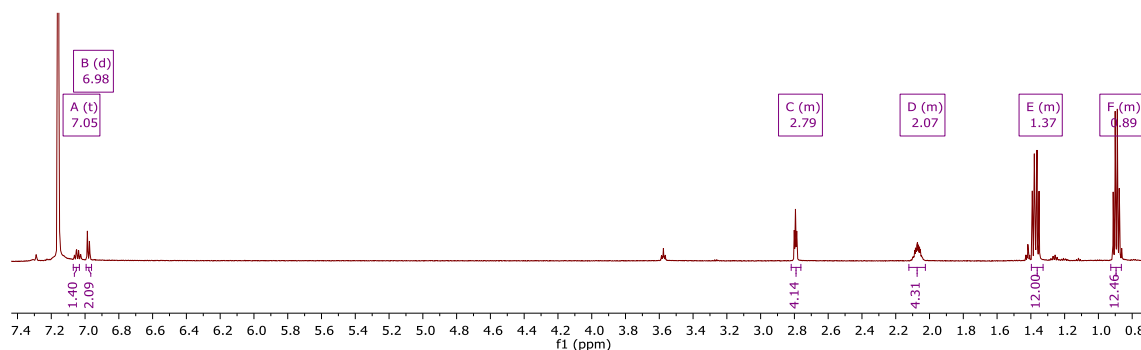
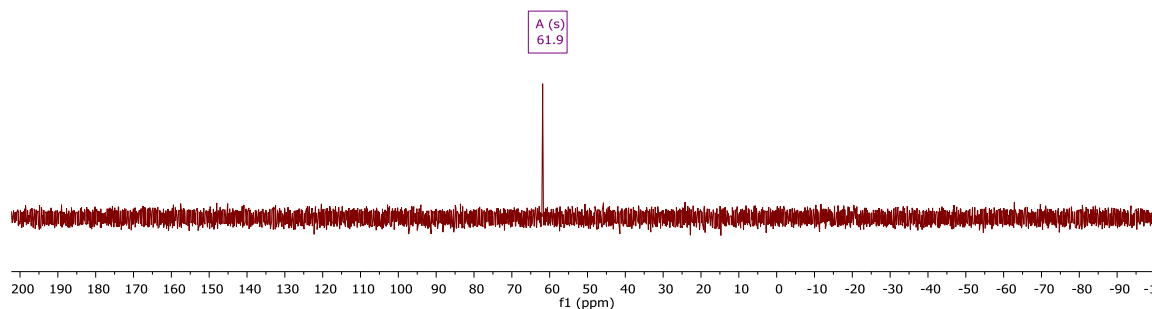


Figure 3.6.17 ^{31}P NMR spectrum 2,5-di[(di-*iso*-propyl phosphino)methyl]phenyl palladium chloride ($i\text{PrPCP}$)PdCl.



Synthesis of phenyl {2,5-di[(di-*iso*-propyl phosphino)methyl]phenyl palladium} ($i\text{PrPCP}$)PdPh. The procedure is adapted from a reported procedure with minor modifications.⁵¹ In a glovebox, 250 mg (0.522 mmol) ($i\text{PrPCP}$)PdCl was dissolved in 15 mL THF. 0.53 mL of 1.5 M (0.79 mmol) THF solution of phenylmagnesium bromide was added to the solution dropwise. The mixture was stirred under a dinitrogen atmosphere at room temperature overnight. The solvent was then removed *in vacuo*, and the resulting white solid was dissolved in 20 mL Et₂O and filtered through a frit. The filtrate was collected, and the solvent was removed *in vacuo*. The solid was washed with 5 mL n-

pentane 3 times and filtered through a frit. The product was dried *in vacuo* and 0.254 g (0.487 mmol, 93.4% yield) product was obtained. ^1H NMR (600 MHz, acetonitrile- d_3) δ 7.48 (d, $^3J_{\text{H-H}} = 7\text{ Hz}$, 2H), 7.04 (d, $^3J_{\text{H-H}} = 7\text{ Hz}$, 2H), 6.94 – 6.86 (m, 3H), 6.73 (t, $^3J_{\text{H-H}} = 7\text{ Hz}$, 1H), 3.42 (vt, 4H), 2.17 – 2.09 (m, 4H), 1.10 (dvt, 12H), 0.97 (dvt, 12H). ^{31}P NMR (243 MHz, acetonitrile- d_3) δ 57.4.

Figure 3.6.18 ^1H NMR spectrum for phenyl {2,5-di[(di-*iso*-propyl phosphino)methyl]phenyl palladium} ($i^{\text{Pr}}\text{PCP}$)PdPh. Unlabeled peaks are from residual solvent (n-pentane) in the NMR solvent due to the atmosphere in the glovebox.

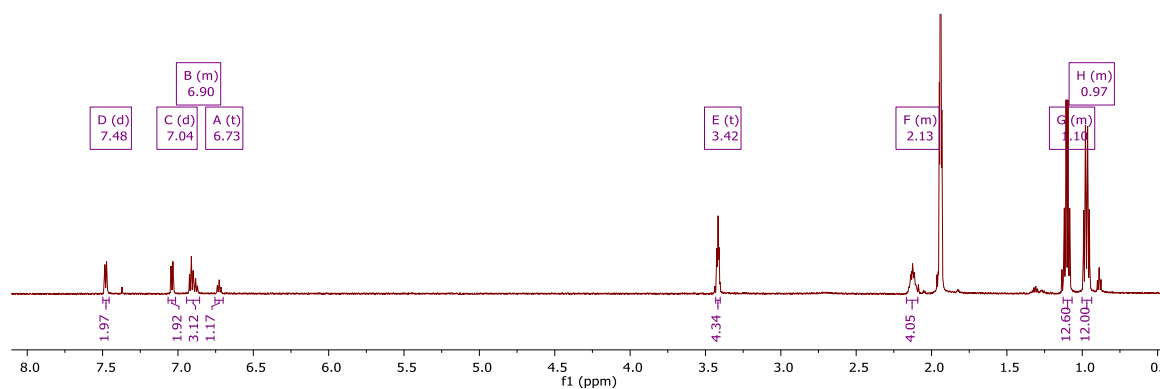


Figure 3.6.19 ^{31}P NMR spectrum for phenyl {2,5-di[(di-*iso*-propyl phosphino)methyl]phenyl palladium} ($i^{\text{Pr}}\text{PCP}$)PdPh.

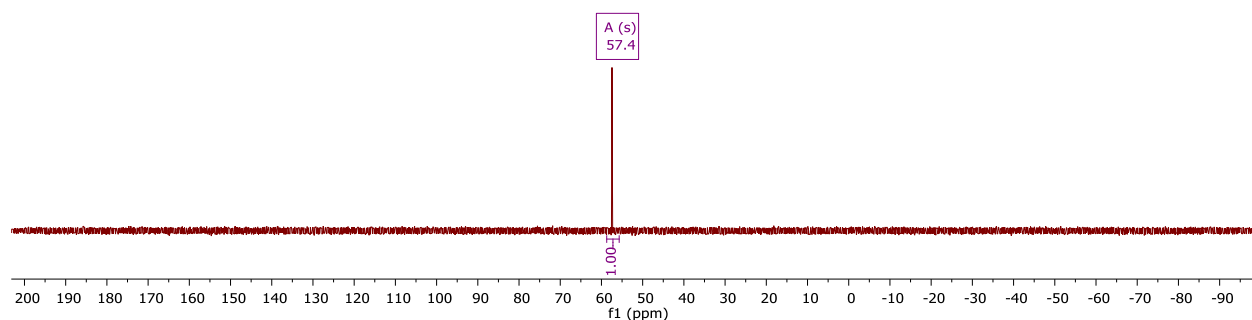
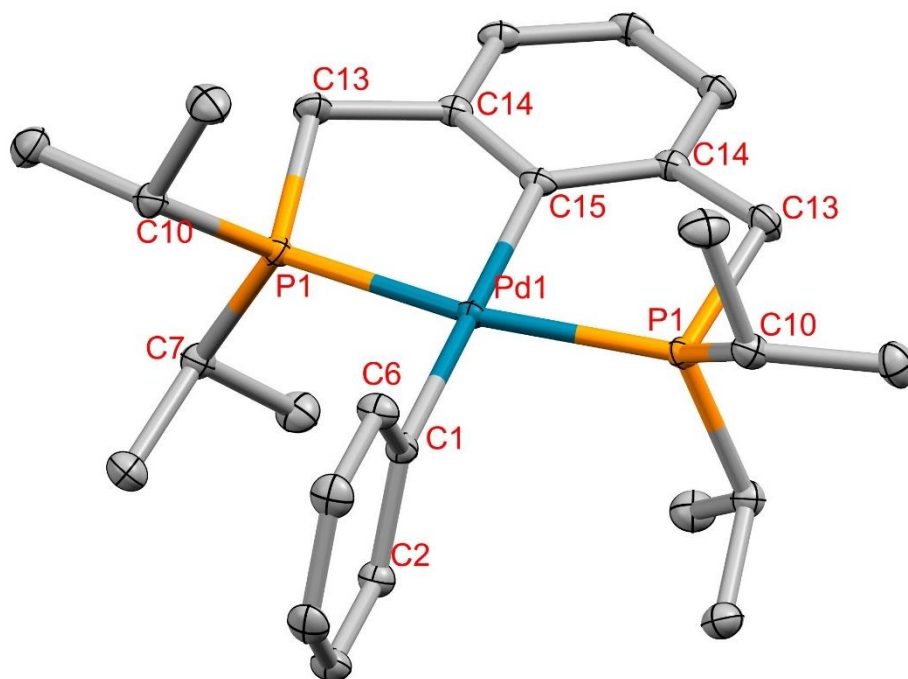


Figure 3.6.20 ORTEP of phenyl{2,5-di[(di-*iso*-propyl phosphino)methyl]phenyl palladium} ($i^{\text{Pr}}\text{PCP}$)PdPh. Ellipsoids are drawn at 50% probability level. Hydrogen atoms are omitted for clarity.



Selected bond lengths for ($i^{\text{Pr}}\text{PCP}$)PdPh (Å): Pd1–P1 2.267, Pd1–C1 2.096, Pd1–C15 2.073, P1–C7 1.846, P1–C10 1.842, C1–C2 1.411, C1–C10 1.402, C13–C14 1.515(2), C14–C15 1.414. Selected bond angles (deg): P1–Pd1–C1 97.03, P1–Pd1–C15 82.98, P1–Pd1–P1 165.39, C1–Pd1–C15 179.92, C1–Pd1–P1 97.03, C15–Pd1–P1 82.98, Pd1–P1–C7 116.37, Pd1–P1–C10 119.86, Pd1–P1–C13 104.53, C7–P1–C10 105.80, C2–C1–C6 115.6.

Synthesis of 2,5-di[(di-*iso*-propyl phosphino)methyl]phenyl palladium benzoate

($i^{\text{Pr}}\text{PCP}$)PdOBz. In a glovebox, 100 mg of ($i^{\text{Pr}}\text{PCP}$)PdCl (0.209 mmol) was dissolved in 20 mL of THF. Silver benzoate (52.2 mg, 0.209 mmol) was then added to the solution. The solution was stirred in the dark at room temperature for 1 hour. The reaction solution was filtered through a plug of celite, and the solvent was removed from the filtrate *in vacuo*. The solid was extracted with Et₂O followed by filtration and the removal of solvent. The crude product was dissolved in *n*-pentane and cooled to -35 °C. The product was obtained as X-ray quality crystals (white, 109 mg, 0.193 mmol, 92.3%). ¹H NMR (497 MHz,

chloroform-*d*) δ 8.04 (d, $^3J_{\text{H-H}} = 7$ Hz, 2H), 7.38 – 7.29 (m, 3H), 6.98 (d, $^3J_{\text{H-H}} = 7$ Hz, 2H), 6.92 (t, $^3J_{\text{H-H}} = 7$ Hz, 1H), 3.17 (vt, 4H), 2.32 (m, 4H), 1.31 (m, 12H), 1.19 (m, 12H). ^{31}P NMR (201 MHz, chloroform-*d*) δ 61.6.

Figure 3.6.21 ^1H NMR spectrum for 2,5-di[(di-*iso*-propyl phosphino)methyl]phenyl palladium benzoate ($^i\text{PrPCP}$)PdOBz. Unlabeled peaks are from residual solvent (Et_2O and THF) in the NMR solvent due to the atmosphere in the glovebox.

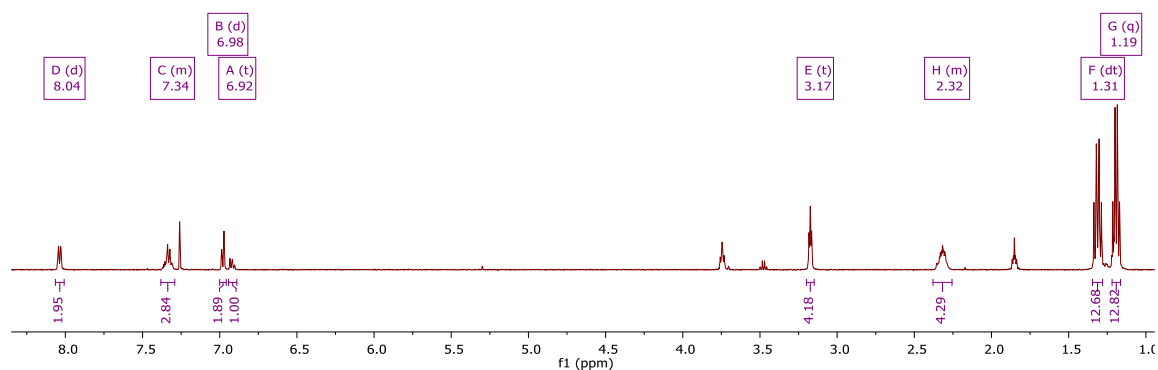


Figure 3.6.22 ^{31}P NMR spectrum for 2,5-di[(di-*iso*-propyl phosphino)methyl]phenyl palladium benzoate ($^i\text{PrPCP}$)PdOBz

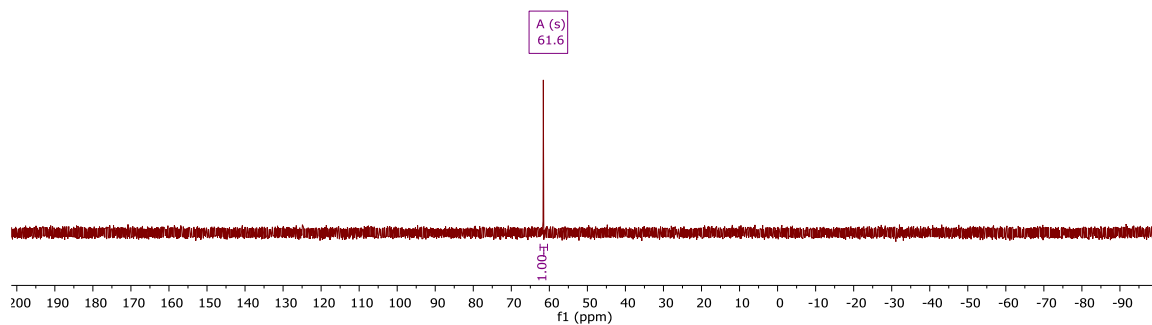
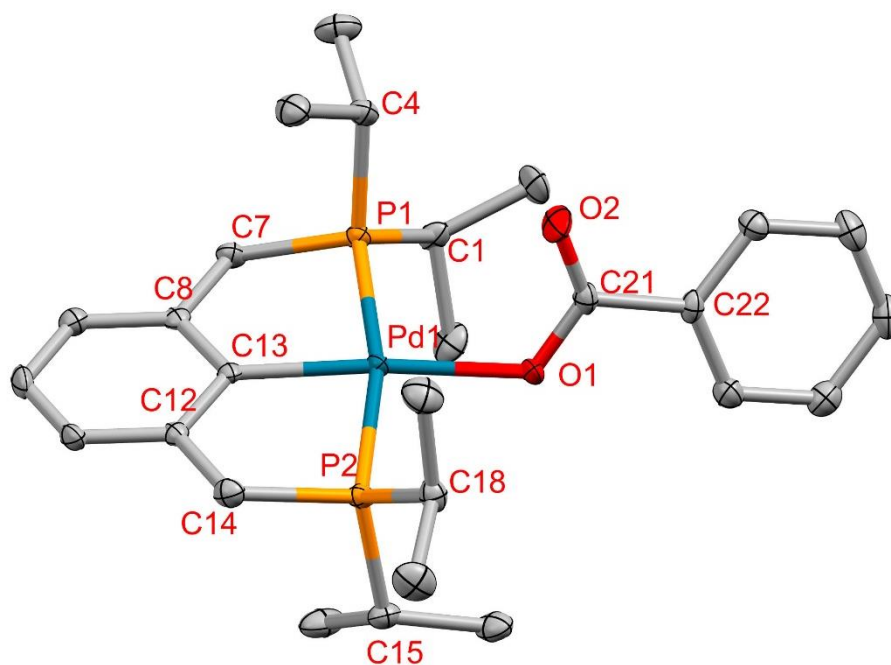


Figure 3.6.23 ORTEP of 2,5-di[(di-*iso*-propyl phosphino)methyl]phenyl palladium benzoate [(^{iPr}PCP)PdOBz]. Ellipsoids are drawn at 50% probability level. Hydrogen atoms are omitted for clarity.

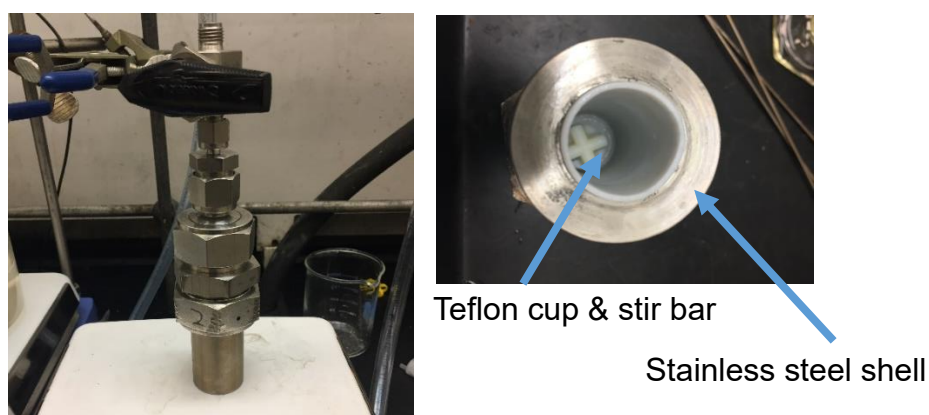


Selected bond lengths for (^{iPr}PCP)PdOBz (Å): Pd1–P1 2.289(1), Pd1–P2 2.268(1), Pd(1)–O1 2.100(3), Pd1–C13 2.010(5), P1–C1 1.842(6), P1–C4 1.837(5), P1–C7 1.838(5), P2–C14 1.837(5), P2–C15 1.837(5), P2–C18 1.827(5), O1–C21 1.281(6), O2–C21 1.232(7), C7–C8 1.507(6), C8–C13 1.410(7), C12–C13 1.416(6), C12–C14 1.509(7), C21–C22 1.516(7). Selected bond angles (deg): P1–Pd1–P2 167.36(5), P1–Pd1–O1 98.32(9), P1–Pd1–C13 83.7(1), P2–Pd1–O1 94.19(9), P2–Pd1–C13 83.6(1), O1–Pd1–C13 174.1(2), Pd1–P1–C1 117.9(2), Pd1–P1–C4 115.8(2), Pd1–P1–C7 102.2(2), C1–P1–C4 107.7(2), C1–P1–C7 105.0(2), C4–P1–C7 107.0(2), Pd1–P2–C14 103.3(2), Pd1–P2–C15 113.4(2), Pd1–P2–C18 117.0(2), C14–P2–C15 107.4(2), C14–P2–C18 108.6(2), C15–P2–C18 106.7(2), Pd1–O1–C21 122.1(3), C7–C8–C13 119.8(4), C13–C12–C14 120.0(4).

General procedures for the condition screening for direct carboxylation of benzene experiments (Table 3.2.1 – Table 3.2.3). All experiments involving CO₂ incorporation were performed in custom-built stainless steel high-pressure reactors (VCO reactors) each fitted with a Teflon cup (**Figure 3.6.24**). Chemicals other than CO₂ were loaded into the Teflon cup and sealed in the VCO reactor in a glovebox under N₂ atmosphere. The reactor was then tightened and pressurized with CO₂ using a custom-built

stainless steel high-pressure line. The high-pressure line was degassed and filled with CO₂ for three cycles before pressurizing. The amount of CO₂ added was measured by recording the weight of each reactor before and after pressurizing. Following heating, the reactors were cooled to room temperature before weights were recorded. After slowly releasing CO₂, the solution was filtered over a frit and washed with 5 mL 37% HCl aqueous solution and 3 mL benzene. The solvent was removed under reduced pressure at 55 °C. The resulting solid was dissolved in benzene, and 1 mL HMB standard solution in benzene (0.0318 M) was added in a 10 mL volumetric flask. The yields of benzoic acid and biphenyl were analyzed by GC-MS.

Figure 3.6.24 Images of high-pressure reaction vessel used (VCO reactor).



General procedures for ¹H NMR scale studies on CO₂ insertion of (ⁱPrPCP)PdPh.

In a Swagelok cap NMR tube, a solution of 3 mg of (ⁱPrPCP)PdPh and a known amount of hexamethyldisiloxane (HMDSO, internal standard) was dissolved in 0.35 mL MeCN-*d*₃ was added. The NMR tube was then charged with a known pressure of CO₂. The solution was heated at a designated temperature for a designated period of time. The concentration of (ⁱPrPCP)PdPh and the CO₂ insertion product (ⁱPrPCP)PdOBz were determined by the integrations of resonances in ¹H NMR compared to the HMDSO internal standard.

General procedures for studies on CO₂ insertion of (ⁱPrPCP)PdPh using VCO reactors. In a VCO reactor, a solution of 10.4 mg (0.02 mmol) (ⁱPrPCP)PdPh and a known amount of hexamethyldisiloxane (HMDSO, internal standard) in 5 mL MeCN was combined. The reactor was then charged with a known pressure of CO₂. The solution was heated at a designated temperature for a designated period of time. 0.5 mL of the reaction solution is transferred into an NMR tube. A capillary loaded with DMSO-*d*₆ is also added to the NMR tube to help locking. The concentration of (ⁱPrPCP)PdPh and the CO₂ insertion product (ⁱPrPCP)PdOBz were determined by the integrations of resonances ($\delta = 8.04$ ppm for (ⁱPrPCP)PdOBz, and $\delta = 7.48$ ppm for (ⁱPrPCP)PdPh) in ¹H NMR with a pre-saturation pulse on the resonance of MeCN ($\delta = 2.21$ ppm) compared to the HMDSO internal standard.

General procedures for studies on (ⁱPrPCP)PdOBz mediated C–H activation of benzene by formation of (ⁱPrPCP)PdPh. In a Swagelok cap NMR tube, 0.3 mL solution of 1.8 mg (0.0053 mmol) (ⁱPrPCP)PdOBz, 10 equivalents (4.1 mg, 4.7 μ L, 0.053 mmol) of benzene, 10 equivalents (0.053 mmol) of base additive, known amount of cyclohexane (internal standard) in solvent (MeCN-*d*₃, benzene-*d*₆, or benzene) were added. The NMR tube was pressurized with 100 psig N₂ to prevent the loss of solvent at raised temperature. The reaction solution was then heated at the designated temperature for 48 hours. The concentration of (ⁱPrPCP)PdPh and (ⁱPrPCP)PdOBz were determined by the integrations of their resonances in ¹H NMR.

General procedures for studies on (ⁱPrPCP)PdOBz mediated C–H activation of benzene by detection of H/D scrambling between C₆H₆ and C₆D₆. In a VCO reactor, a solution of 10 mg (ⁱPrPCP)PdOBz, 1 mL benzene, 1 mL benzene-*d*₆ in 3 mL solvent (MeCN, THF or toluene) were loaded. The solution was pressurized with 100 psig N₂ to prevent the

loss of solvent at raised temperature. The reaction solution was then heated at 150 °C for 48 hours. The H/D scrambling between C₆H₆ and C₆D₆ was determined by the distribution of the benzene molecular ion via GC-MS.

Methods for DFT calculations DFT calculations were performed using the M06 functional. Geometries were calculated using the 6-31+g(d,p) and lanl2dz basis sets. An energy correction was provided using the 6-311+G(2d,2p)³³ and LANL2TZ9(f) basis sets. All structures were optimized in solution phase using the SMD solvation model³⁴ (solvent = benzene) in Gaussian 09.³⁵

3.7 References

- (1) Yang, S.-T. In *Bioprocessing for Value-Added Products from Renewable Resources*, Elsevier, 2007.
- (2) Sang, R.; Kucmierczyk, P.; Dühren, R.; Razzaq, R.; Dong, K.; Liu, J.; Franke, R.; Jackstell, R.; Beller, M. Synthesis of Carboxylic Acids by Palladium-Catalyzed Hydroxycarbonylation. *Angew. Chem. Int. Ed.* **2019**, *58*, 14365-14373.
- (3) Ostermann, T. Building Blocks for the Feed Industry: Oxea Expands Production Capabilities for Butyric Acid and Propionic Acid. *Oxea GmbH: Monheim am Rhein, Germany* **2017**.
- (4) Burdock, G. A. *Fenaroli's Handbook of Flavor Ingredients*; CRC Press, 2009.
- (5) Hoseinifar, S. H.; Sun, Y.-Z.; Caipang, C. M. Short-chain Fatty Acids as Feed Supplements for Sustainable Aquaculture: an Updated View. *Aquaculture Research* **2017**, *48*, 1380-1391.

- (6) Ruiz-Lopez, N.; Haslam, R. P.; Napier, J. A.; Sayanova, O. Successful High-level accumulation of Fish Oil Omega-3 Long-chain Polyunsaturated Fatty Acids in a Transgenic Oilseed Crop. *The Plant Journal* **2014**, *77*, 198-208.
- (7) Polycarpo, G. V.; Andretta, I.; Kipper, M.; Cruz-Polycarpo, V. C.; Dadalt, J. C.; Rodrigues, P. H. M.; Albuquerque, R. Meta-analytic Study of Organic Acids as an Alternative Performance-enhancing Feed Additive to Antibiotics for Broiler Chickens. *Poultry Science* **2017**, *96*, 3645-3653.
- (8) Bagal, V. L.; Khatta, V. K.; Tewatia, B. S.; Sangwan, S. K.; Raut, S. S. Relative Efficacy of Organic Acids and Antibiotics as Growth Promoters in Broiler Chicken. *VETERINARY WORLD* **2016**, *9*, 377-382.
- (9) Arpe, H.-J. r. *Industrielle organische Chemie bedeutende Vor- und Zwischenprodukte*; 2007.
- (10) Vanoye, L.; Aloui, A.; Pablos, M.; Philippe, R.; Percheron, A.; Favre-Réguillon, A.; de Bellefon, C. A Safe and Efficient Flow Oxidation of Aldehydes with O₂. *Org. Lett.* **2013**, *15*, 5978-5981.
- (11) Mozaffari, M.; Nowrouzi, N. Palladium-Catalyzed Synthesis of Symmetrical and Unsymmetrical Ureas Using Chromium Hexacarbonyl as a Convenient and Safe Alternative Carbonyl Source. *Eur. J. Org. Chem.* **2019**, *2019*, 7541-7544.
- (12) Schreiber, A.; Peschel, A.; Hentschel, B.; Zapp, P. Life Cycle Assessment of Power-to-Syngas: Comparing High Temperature Co-Electrolysis and Steam Methane Reforming. *Frontiers in Energy Research* **2020**, *8*.

- (13) Ghiat, I.; Al-Ansari, T. A Review of Carbon Capture and Utilisation as a CO₂ Abatement Opportunity within the EWF Nexus. *Journal of CO₂ Utilization* **2021**, *45*, 101432.
- (14) Boogaerts, I. I. F.; Nolan, S. P. Carboxylation of C–H Bonds Using N-Heterocyclic Carbene Gold(I) Complexes. *J. Am. Chem. Soc.* **2010**, *132*, 8858-8859.
- (15) Boogaerts, I. I. F.; Fortman, G. C.; Furst, M. R. L.; Cazin, C. S. J.; Nolan, S. P. Carboxylation of N-H/C-H Bonds Using N-Heterocyclic Carbene Copper(I) Complexes. *Angew. Chem. Int. Ed.* **2010**, *49*, 8674-8677.
- (16) Suga, T.; Mizuno, H.; Takaya, J.; Iwasawa, N. Direct Carboxylation of Simple Arenes with CO₂ through a Rhodium-catalyzed C–H Bond Activation. *Chem. Commun.* **2014**, *50*, 14360-14363.
- (17) Weast, R. C. *CRC Handbook of Chemistry and Physics*; CRC Press LLC, 1985.
- (18) NIST Chemistry WebBook. 2022. (accessed 2022/07/05).
- (19) Filonenko, G. A.; van Putten, R.; Schulpen, E. N.; Hensen, E. J. M.; Pidko, E. A. Highly Efficient Reversible Hydrogenation of Carbon Dioxide to Formates Using a Ruthenium PNP-Pincer Catalyst. *ChemCatChem* **2014**, *6*, 1526-1530.
- (20) Wang, W.-H.; Himeda, Y.; Muckerman, J. T.; Manbeck, G. F.; Fujita, E. CO₂ Hydrogenation to Formate and Methanol as an Alternative to Photo- and Electrochemical CO₂ Reduction. *Chem. Rev.* **2015**, *115*, 12936-12973.
- (21) Tanaka, R.; Yamashita, M.; Nozaki, K. Catalytic Hydrogenation of Carbon Dioxide Using Ir(III)–Pincer Complexes. *J. Am. Chem. Soc.* **2009**, *131*, 14168-14169.

- (22) Tanaka, R.; Yamashita, M.; Chung, L. W.; Morokuma, K.; Nozaki, K. Mechanistic Studies on the Reversible Hydrogenation of Carbon Dioxide Catalyzed by an Ir-PNP Complex. *Organometallics* **2011**, *30*, 6742-6750.
- (23) Schmeier, T. J.; Dobereiner, G. E.; Crabtree, R. H.; Hazari, N. Secondary Coordination Sphere Interactions Facilitate the Insertion Step in an Iridium(III) CO₂ Reduction Catalyst. *J. Am. Chem. Soc.* **2011**, *133*, 9274-9277.
- (24) Kapdi, A. R. Organometallic aspects of transition-metal catalysed regioselective C–H bond functionalisation of arenes and heteroarenes. *Dalton Trans.* **2014**, *43*, 3021-3034.
- (25) Ryabov, A. D.; Sakodinskaya, I. K.; Yatsimirsky, A. K. Kinetics and mechanism of ortho-palladation of ring-substituted *NN*-dimethylbenzylamines. *J. Chem. Soc., Dalton Trans.* **1985**, 2629-2638.
- (26) Kurzeev, S. A.; Kazankov, G. M.; Ryabov, A. D. Second- and Inverse Order Pathways in the Mechanism of Orthopalladation of Primary Amines. *Inorg. Chim. Acta* **2002**, *340*, 192-196.
- (27) Ackermann, L. Carboxylate-Assisted Transition-Metal-Catalyzed C–H Bond Functionalizations: Mechanism and Scope. *Chem. Rev.* **2011**, *111*, 1315-1345.
- (28) Ackermann, L.; Novák, P.; Vicente, R.; Hofmann, N. Ruthenium-Catalyzed Regioselective Direct Alkylation of Arenes with Unactivated Alkyl Halides through C–H Bond Cleavage. *Angew. Chem. Int. Ed.* **2009**, *48*, 6045-6048.
- (29) O'Reilly, M. E.; Fu, R.; Nielsen, R. J.; Sabat, M.; Goddard, W. A.; Gunnoe, T. B. Long-Range C–H Bond Activation by Rh^{III}-Carboxylates. *J. Am. Chem. Soc.* **2014**, *136*, 14690-14693.

- (30) O'Reilly, M. E.; Pahls, D. R.; Webb, J. R.; Boaz, N. C.; Majumdar, S.; Hoff, C. D.; Groves, J. T.; Cundari, T. R.; Gunnoe, T. B. Reductive Functionalization of a Rhodium(III)–Methyl Bond by Electronic Modification of the Supporting Ligand. *Dalton Trans.* **2014**, *43*, 8273-8281.
- (31) Thompson, W. H.; Sears, C. T. Kinetics of Oxidative Addition to Iridium(I) Complexes. *Inorg. Chem.* **1977**, *16*, 769-774.
- (32) Sugimoto, H.; Kawata, I.; Taniguchi, H.; Fujiwara, Y. Palladium-Catalyzed Carboxylation of Aromatic Compounds with Carbon Dioxide. *J. Organomet. Chem.* **1984**, *266*, c44-c46.
- (33) Martin, J. M. L.; Sundermann, A. Correlation Consistent Valence Basis Sets for Use with the Stuttgart–Dresden–Bonn Relativistic Effective Core Potentials: The Atoms Ga–Kr and In–Xe. *J. Chem. Phys.* **2001**, *114*, 3408-3420.
- (34) Marenich, A. V.; Cramer, C. J.; Truhlar, D. G. Universal Solvation Model Based on Solute Electron Density and on a Continuum Model of the Solvent Defined by the Bulk Dielectric Constant and Atomic Surface Tensions. *J. Phys. Chem. B* **2009**, *113*, 6378-6396.
- (35) M. J. Frisch, G. W. T., H. B. Schlegel, G. E. Scuseria, M. A. Robb, J. R. Cheeseman, G. Scalmani, V. Barone, G. A. Petersson, H. Nakatsuji, X. Li, M. Caricato, A. Marenich, J. Bloino, B. G. Janesko, R. Gomperts, B. Mennucci, H. P. Hratchian, J. V. Ortiz, A. F. Izmaylov, J. L. Sonnenberg, D. Williams-Young, F. Ding, F. Lipparini, F. Egidi, J. Goings, B. Peng, A. Petrone, T. Henderson, D. Ranasinghe, V. G. Zakrzewski, J. Gao, N. Rega, G. Zheng, W. Liang, M. Hada, M. Ehara, K. Toyota, R. Fukuda, J. Hasegawa, M. Ishida, T. Nakajima, Y. Honda, O. Kitao, H. Nakai, T. Vreven, K. Throssell, J. A. Montgomery, Jr., J. E. Peralta, F. Ogliaro, M. Bearpark, J. J. Heyd, E. Brothers, K. N. Kudin, V. N.

Staroverov, T. Keith, R. Kobayashi, J. Normand, K. Raghavachari, A. Rendell, J. C. Burant, S. S. Iyengar, J. Tomasi, M. Cossi, J. M. Millam, M. Klene, C. Adamo, R. Cammi, J. W. Ochterski, R. L. Martin, K. Morokuma, O. Farkas, J. B. Foresman, and D. J. Fox. *Gaussian 09, Revision A.02*; Gaussian, Inc., Wallingford CT, 2016.

(36) Fujiwara, Y.; Asano, R.; Moritani, I.; Teranishi, S. Aromatic Substitution of Olefins. XXV. Reactivity of Benzene, Naphthalene, Ferrocene, and Furan Toward Styrene, and the Substituent Effect on the Reaction of Monosubstituted Benzenes with Styrene. *J. Org. Chem.* **1976**, *41*, 1681-1683.

(37) Stuart, D. R.; Fagnou, K. The Catalytic Cross-Coupling of Unactivated Arenes. *Science* **2007**, *316*, 1172-1175.

(38) Selander, N.; Szabó, K. J. Catalysis by Palladium Pincer Complexes. *Chem. Rev.* **2011**, *111*, 2048-2076.

(39) Takaya, J.; Miyama, K.; Zhu, C.; Iwasawa, N. Metallic Reductant-Free Synthesis of α -Substituted Propionic Acid Derivatives through Hydrocarboxylation of Alkenes with a Formate Salt. *Chem. Commun.* **2017**, *53*, 3982-3985.

(40) Cohen, R.; van der Boom, M. E.; Shimon, L. J. W.; Rozenberg, H.; Milstein, D. The Methylene-Transfer Reaction: Synthetic and Mechanistic Aspects of a Unique C–C Coupling and C–C Bond Activation Sequence. *J. Am. Chem. Soc.* **2000**, *122*, 7723-7734.

(41) Johnson, M. T.; Johansson, R.; Kondrashov, M. V.; Steyl, G.; Ahlquist, M. S. G.; Roodt, A.; Wendt, O. F. Mechanisms of the CO₂ Insertion into (PCP) Palladium Allyl and Methyl σ -Bonds. A Kinetic and Computational Study. *Organometallics* **2010**, *29*, 3521-3529.

- (42) Gusev, D. G.; Madott, M.; Dolgushin, F. M.; Lyssenko, K. A.; Antipin, M. Y. Agostic Bonding in Pincer Complexes of Ruthenium. *Organometallics* **2000**, *19*, 1734-1739.
- (43) Olsson, D.; Nilsson, P.; El Masnaouy, M.; Wendt, O. F. A Catalytic and Mechanistic Investigation of a PCP Pincer Palladium Complex in the Stille Reaction. *Dalton Trans.* **2005**, 1924-1929.
- (44) Shih, W.-C.; Ozerov, O. V. One-Pot Synthesis of 1,3-Bis(phosphinomethyl)arene PCP/PNP Pincer Ligands and Their Nickel Complexes. *Organometallics* **2015**, *34*, 4591-4597.
- (45) Frech, C. M.; Shimon, L. J. W.; Milstein, D. Redox-Induced Collapse and Regeneration of a Pincer-Type Complex Framework: A Nonplanar Coordination Mode of Palladium(II). *Angew. Chem. Int. Ed.* **2005**, *44*, 1709-1711.
- (46) Heredia, D. A.; Larghi, E. L.; Kaufman, T. S. A Straightforward Synthesis of 5-Methylaaptamine from Eugenol, Employing a 6π -Electrocyclization Reaction of a 1-Azatriene. *Eur. J. Org. Chem.* **2016**, *2016*, 1397-1404.
- (47) Kraatz, H. B. v. d. B., M.E.; Ben-David, Y.; Milstein, D. Reaction of Aryl Iodides with (PCP)Pd(II)-Alkyl and Aryl Complexes: Mechanistic Aspects of Carbon-Carbon Bond Formation. *Isr. J. Chem.* **2001**, *41*, 163-171.
- (48) Armarego, W. L. F.; Chai, C. L. L. *Purification of Laboratory Chemicals*; Elsevier Inc., 2009.
- (49) Fulmer, G. R.; Miller, A. J. M.; Sherden, N. H.; Gottlieb, H. E.; Nudelman, A.; Stoltz, B. M.; Bercaw, J. E.; Goldberg, K. I. NMR Chemical Shifts of Trace Impurities: Common Laboratory Solvents, Organics, and Gases in Deuterated Solvents Relevant to the Organometallic Chemist. *Organometallics* **2010**, *29*, 2176-2179.

(50) Rossin, A.; Bottari, G.; Lozano-Vila, A. M.; Paneque, M.; Peruzzini, M.; Rossi, A.; Zanolini, F. Catalytic Amine-Borane Dehydrogenation by a PCP-Pincer Palladium Complex: A Combined Experimental and DFT Analysis of the Reaction Mechanism. *Dalton Trans.* **2013**, *42*, 3533-3541.

(51) Martínez-Prieto, L. M.; Melero, C.; del Río, D.; Palma, P.; Cámpora, J.; Álvarez, E. Synthesis and Reactivity of Nickel and Palladium Fluoride Complexes with PCP Pincer Ligands. NMR-Based Assessment of Electron-Donating Properties of Fluoride and Other Monoanionic Ligands. *Organometallics* **2012**, *31*, 1425-1438.

4 Catalytic methanol carbonylation using rhodium or iridium catalysts ligated by “capping arene” ligands

4.1 Introduction

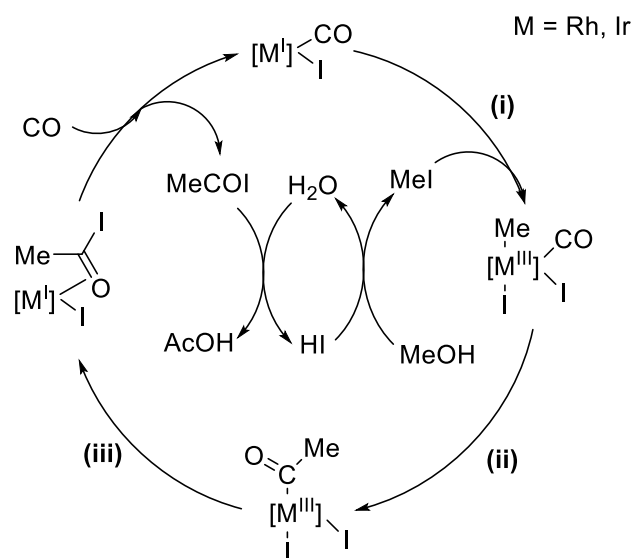
Acetic acid is an industrially important chemical with the global annual production reaching 13 million tons in 2015, and the production of acetic acid was estimated to reach 18 million tons in 2020.¹ One of the major applications of acetic acid is to produce polymers such as poly(vinyl acetate) and cellulose acetate (acetate fibers).^{2,3}

During the last 50 years, the industrial methanol carbonylation process has been developed for the synthesis of acetic acid. An early example of catalytic methanol carbonylation was reported in the 1950s, in which Reppe and coworkers at BASF used cobalt iodide to catalyze the production of acetic acid (AcOH) or its derivatives from methanol (MeOH) and carbon monoxide (CO) under relatively harsh conditions (*c.a.* 250 °C, 600 bar).^{4,5} In the 1970s, Paulik and Roth at Monsanto developed a rhodium catalyzed methanol carbonylation method (Monsanto process) using methyl iodide and iodide salts as promoters under milder conditions (*c.a.* 175 °C, 30 bar).⁶ The Monsanto process was able to improve the selectivity of the reaction from 90% to > 99% based on methanol, and from 70% to 85% based on CO, compared with the cobalt catalyzed methanol carbonylation described above. In 1996, BP Chemicals announced the Cativa™ process, an iodide promoted iridium-catalyzed methanol carbonylation system, which exhibits greater stability than the Rh-based processes.⁷⁻⁹

The mechanism for the iodide-promoted Rh- and Ir-catalyzed methanol carbonylation has been studied extensively in the past few decades.¹⁰⁻¹² In methanol carbonylation chemistry, the oxidative addition of methyl iodide (MeI) to Rh(I) or Ir(I) is proposed to

play an important role in the catalytic reaction (**Scheme 4.1.1**). Through the oxidative addition of MeI to the Rh(I) or Ir(I) catalyst, the Rh(III) or Ir(III) intermediate is formed (Step i). Then, the migratory insertion of CO into the M–Me (M = Rh or Ir) bond leads to the formation of a M(III)-acetyl complex (Step ii), reductive coupling to form a M(I)- η^2 -acetyl iodide complex follows (Step iii). Finally, acetyl iodide exchanges with free CO and free acetyl iodide is hydrolyzed to acetic acid. MeI is regenerated by the reaction of methanol with HI.

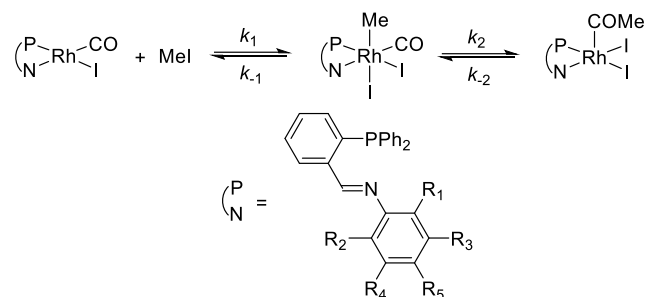
Scheme 4.1.1 Proposed mechanism for rhodium or iridium catalyzed methanol carbonylation



Haynes and coworkers have studied the reactivity of a series of Rh(I)-iminophosphine complexes with MeI.¹³ It was suggested that the reactivity toward MeI significantly increases when a methoxy group is present on the ortho position of the phenyl group connected to the imine nitrogen (**Table 4.1.1**, entry e). It was rationalized that the methoxy group could coordinate to the axial position of the PN–Rh–CO plane, forming a cationic

Rh(III) intermediate after oxidative addition of MeI. This neighboring group effect is proposed to explain the faster oxidative addition.¹⁴⁻¹⁸

Table 4.1.1 Second-order rate constants (k_1 , 25 °C) for the oxidative addition of MeI to PN–Rh(I) complexes

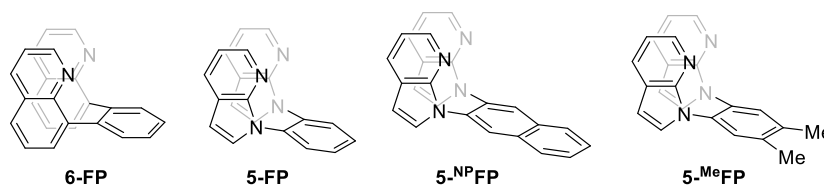


	R₁	R₂	R₃	R₄	R₅	k_1 (L·mol⁻¹·s⁻¹)
a	H	H	H	H	H	3.60
b	Me	Me	H	H	H	7.50
c	ⁱ Pr	ⁱ Pr	H	H	H	9.10
d	Et	H	H	H	H	7.71
e	OMe	H	H	H	H	31.4
f	H	H	H	H	OMe	2.61
g	H	H	CF ₃	CF ₃	H	0.78

Recently, our group has studied a series of bidentate “capping arene” ligands (FP) coordinated to Rh or Ir⁺ complexes.¹⁹⁻²⁴ The capping arene ligands are a series of nitrogen-based bidentate ligands linked by arene groups. The most typical “capping arene” ligands include 6-FP (8,8'-(1,2-phenylene)diquinoline) and 5-FP (1,2-bis(*N*-7-azaindoly)benzene) (**Figure 4.1.1**). Recent studies revealed that the arene moiety can be positioned at the axial position of the square plane for 6-FP and 5-FP ligated Rh(I) or Ir(I) complexes. Due to the structure of the ligand backbones, Rh(I) or Ir(I) complexes with 6-FP and 5-FP have a significant difference (~0.5 Å) in the distance from the metal center to the arene moiety,

which could influence the stability and reactivity of the “capping arene” Rh and Ir complexes.^{19,20} Furthermore, the electronic properties of the capping arene complexes can be tuned by changing the substituents on the arene groups. For example, 5-MeFP (1,2-bis(*N*-7-azaindoly)-4,5-dimethylbenzene) or 5-NPFP (2,3-bis(*N*-7-azaindoly)naphthalene) can be used as the ligand instead of 5-FP (**Figure 4.1.1**).

Figure 4.1.1 Examples of “capping arene” ligands

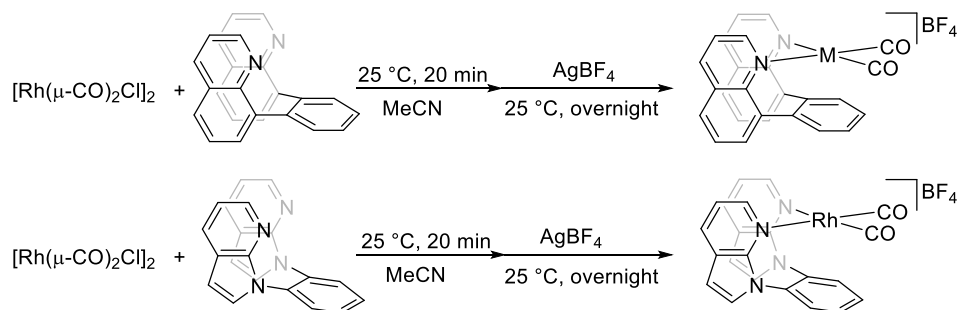


Inspired by the neighboring group effect on MeI oxidative addition of Ir(I) and Rh(I) complexes described above, we speculated that oxidative addition to capping arene M(I) (M = Rh or Ir) complexes might also favor the formation of a cationic M(III) product, which could lead to a faster oxidative addition of MeI, and thus possibly faster catalytic methanol carbonylation. In this work, a series of [(FP)M(CO)₂]BF₄ (FP = 5-FP or 6-FP, M = Rh or Ir) complexes were synthesized, and their catalytic performance for methanol carbonylation was evaluated under an optimized condition. Unfortunately, the experimental results suggest that the rate of methanol carbonylation is not dependent on the ligated capping arene ligands. Further mechanistic studies provide evidence that the capping arene could react with the MeI additive, resulting in dissociation of the capping arene ligands.

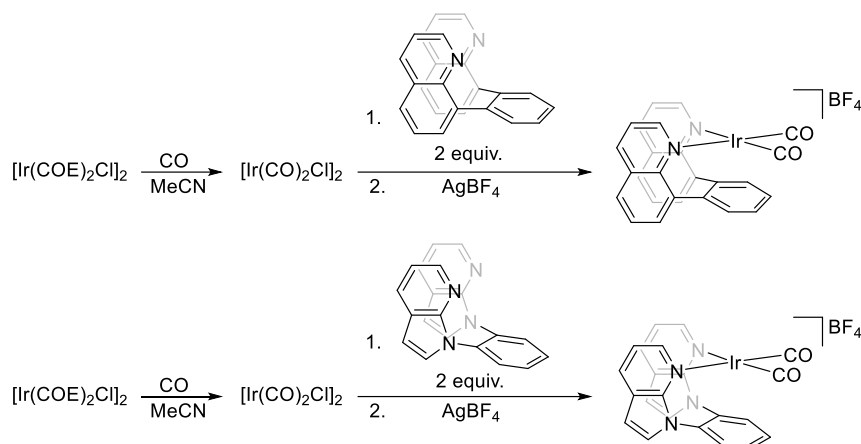
4.2 Synthesis and characterization of [(FP)M^I(CO)₂]BF₄ (FP = 5-FP or 6-FP, M = Rh or Ir) complexes

The syntheses of [(5-FP)Rh(CO)₂]BF₄ and [(6-FP)Rh(CO)₂]BF₄ follow similar one-pot procedures. The precursor [Rh(CO)₂(μ-Cl)]₂ is mixed with 2 equivalents of capping arene ligand (5-FP or 6-FP) in acetonitrile followed by the addition of 2 equivalents of silver tetrafluoroborate. The detailed procedures and characterizations for [(5-FP)Rh(CO)₂]BF₄ and [(6-FP)Rh(CO)₂]BF₄ are described in the **Experimental section**.

Figure 4.2.1 Procedures for the syntheses of [(5-FP)Rh(CO)₂]BF₄ and [(6-FP)Rh(CO)₂]BF₄



The syntheses of [(5-FP)Ir(CO)₂]BF₄ and [(6-FP)Ir(CO)₂]BF₄ follow the procedures reported by a former group member.²⁵ The [Ir(CO)₂(μ-Cl)]₂ precursor is formed *in situ* by substituting cyclooctene ligands of [Ir(η²-COE)₂(μ-Cl)]₂ with CO. The addition of 2 equivalents of capping arene ligand (5-FP or 6-FP) and 2 equivalents of silver(I) tetrafluoroborate produces the capping arene ligated Ir complexes.

Figure 4.2.2 Procedures for the syntheses of [(5-FP)Ir(CO)₂]BF₄ and [(6-FP)Ir(CO)₂]BF₄

The ^1H NMR and ^{13}C NMR spectra for $[(\text{FP})\text{M}^{\text{I}}(\text{CO})_2]\text{BF}_4$ (FP = 5-FP or 6-FP, M = Rh or Ir) complexes suggest that the complexes possess mirror symmetry (**Figure 4.6.3** – **Figure 4.6.13**). Only one coordinated CO resonance is observed for each of the $[(\text{FP})\text{M}^{\text{I}}(\text{CO})_2]\text{BF}_4$ complexes, for which the chemical shift, multiplicity and the frequencies for the C–O stretch are summarized in **Table 4.2.1**.

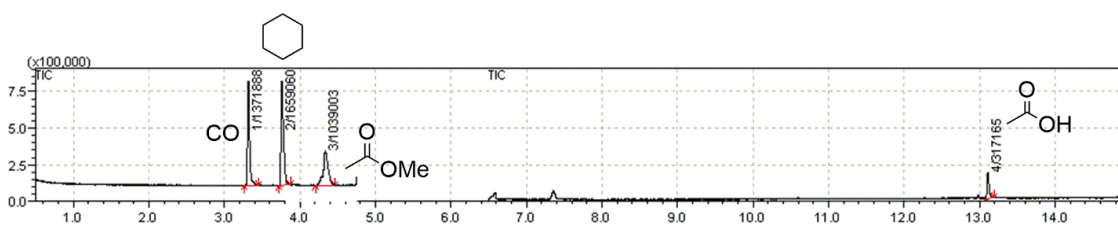
Table 4.2.1 ^{13}C NMR resonances of coordinated CO in $[(\text{FP})\text{M}^{\text{I}}(\text{CO})_2]\text{BF}_4$ (FP = 5-FP or 6-FP, M = Rh or Ir)

Complex	δ (ppm) for $\text{M}-\underline{\text{C}}\text{O}$	Multiplicity	J (Hz)	ν_{CO} (KBr, cm^{-1})
$[(5\text{-FP})\text{Rh}(\text{CO})_2]\text{BF}_4$	182.1	d	70	2037, 2098
$[(6\text{-FP})\text{Rh}(\text{CO})_2]\text{BF}_4$	183.4	d	72	2026, 2088
$[(5\text{-FP})\text{Ir}(\text{CO})_2]\text{BF}_4$	169.3	s	N.A.	2019, 2084
$[(6\text{-FP})\text{Ir}(\text{CO})_2]\text{BF}_4$	170.0	s	N.A.	2011, 2082

4.3 Methanol carbonylation catalyzed by [(FP)M^I(CO)₂]BF₄ (FP = 5-FP or 6-FP, M = Rh or Ir) complexes

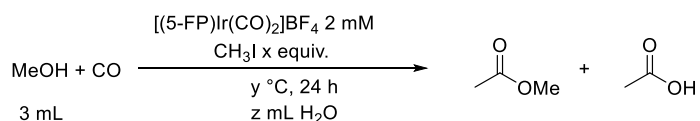
Methanol carbonylation catalyzed by capping arene ligated Rh(I) or Ir(I) complexes promoted by MeI was attempted. The major products for the catalytic methanol carbonylation are methyl acetate (MeOAc) and acetic acid (HOAc). The yields of MeOAc and HOAc were quantified by GC-MS using cyclohexane as the standard (Figure 4.3.1).

Figure 4.3.1 Example of GC-MS chromatogram for the quantification of methyl acetate (MeOAc) and acetic acid (HOAc) using cyclohexane as the standard.



The optimization of MeI promoted methanol carbonylation condition was performed using [(5-FP)Ir(CO)₂]BF₄ as the catalyst, which is summarized in (Table 4.3.1). It can be concluded that the production of MeOAc is enhanced with increased concentration of MeI. Moreover, the presence of water likely inhibits the carbonylation of methanol.

Table 4.3.1 Condition optimization of MeI promoted methanol carbonylation catalyzed by [(5-FP)Ir(CO)₂]BF₄

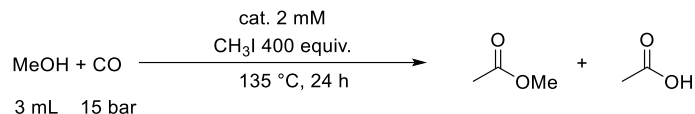


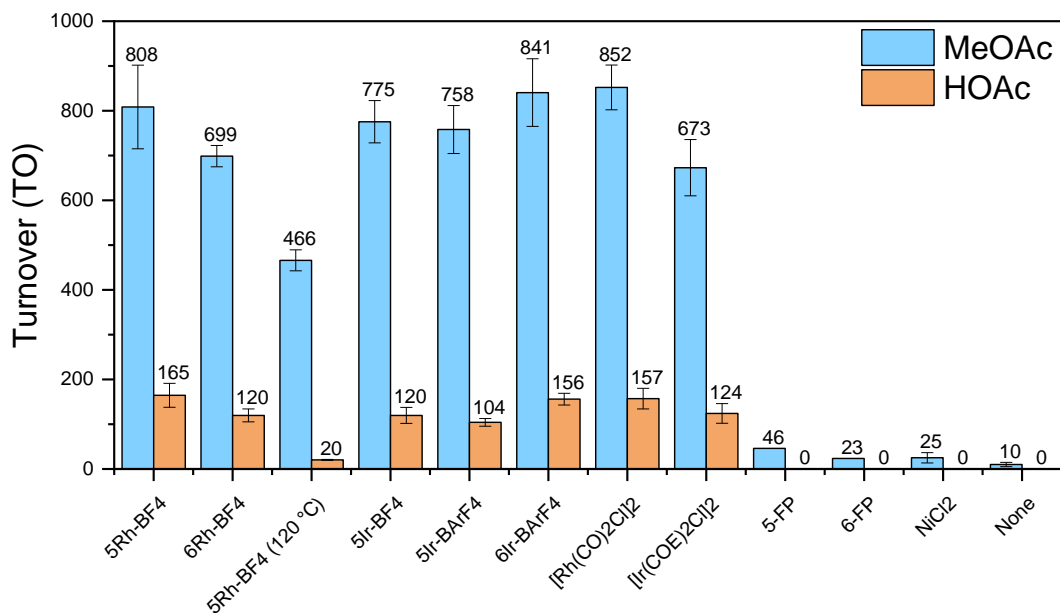
CO (bar)	MeI (equiv.)	H ₂ O (mL)	Temp. (°C)	MeOAc (TO)	HOAc (TO)
10	1	0	80	Trace	N.D.
15	20	0	80	15	0
15	50	0	80	18	0

15	100	0	80	43	0
15	1	0	150	8	0
15	400	0	135	791	96
15	400	0.3	135	385	42
15	400	0.6	135	201	21

With the optimized conditions (2 mM catalyst, 400 equiv. MeI, 15 bar CO at 135 °C), the performance of catalysts was evaluated. The yields of MeOAc and HOAc for methanol carbonylation catalyzed by $[(FP)M^I(CO)_2]BF_4$ (FP = 5-FP or 6-FP, M = Rh or Ir) or $[(FP)Ir^I(CO)_2]BAr^F_4$ are reported in **Figure 4.3.2**. Comparing $[(FP)Rh^I(CO)_2]BF_4$ (FP = 5-FP or 6-FP) with $[Rh(CO)_2(\mu-Cl)]_2$, the yields are statistically identical. Similarly, $[(FP)Ir^I(CO)_2]BF_4$ versus $[(FP)Ir^I(CO)_2]BAr^F_4$ (FP = 5-FP or 6-FP) does not show a significant difference compared with $[Ir(COE)_2(\mu-Cl)]_2$. The complex $[Ir(COE)_2(\mu-Cl)]_2$ can rapidly form $[Ir(CO)_2(\mu-Cl)]_2$ *in situ* under a CO atmosphere. When the catalyst is replaced by 5-FP ligand, 6-FP ligand, nickel(II) chloride or no catalyst, the yield of MeOAc is sharply decreased.

Figure 4.3.2 Comparison of methanol carbonylation catalyzed by “capping arene” ligated Ir or Rh complexes.





4.4 Mechanistic studies on methanol carbonylation catalyzed by [(FP)Rh(CO)₂]BF₄ complexes

To investigate the reason for the similar catalyst performance of “capping arene” ligated Rh and Ir complexes with $[\text{M}(\text{CO})_2\mu\text{-Cl}]_2$ ($\text{M} = \text{Rh}$ or Ir), a series of mechanistic studies were performed. One possible explanation is that the active catalyst for both “capping arene” ligated and unligated Rh/Ir complexes are identical, which means the “capping arene” ligated Rh/Ir complexes likely undergo a ligand dissociation pathway before the methanol carbonylation catalysis occurs.

It is proposed that the $[(\text{FP})\text{M}^{\text{I}}(\text{CO})_2]\text{BF}_4$ ($\text{FP} = 5\text{-FP}$ or 6-FP , $\text{M} = \text{Rh}$ or Ir) could decompose under increased temperature. To test this hypothesis, the stability of $[(\text{FP})\text{M}^{\text{I}}(\text{CO})_2]\text{BF}_4$ at 135 °C in $\text{MeOH-}d_4$ was studied using ^1H NMR spectroscopy (**Figure 4.4.1–Figure 4.4.4**). Among the four complexes, $[(6\text{-FP})\text{Rh}(\text{CO})_2]\text{BF}_4$ exhibited the fastest decomposition (**Figure 4.4.2**). The decomposition of $[(5\text{-FP})\text{Rh}(\text{CO})_2]\text{BF}_4$ and $[(6\text{-FP})\text{Ir}(\text{CO})_2]\text{BF}_4$, although not as rapid as $[(6\text{-FP})\text{Rh}(\text{CO})_2]\text{BF}_4$, could be observed after

4 hours at 135 °C in MeOH- d_4 (**Figure 4.4.1** and **Figure 4.4.3**). However, the decomposition of [(6-FP)Ir(CO) $_2$]BF $_4$ was not observed under the same conditions (**Figure 4.4.4**). It was also demonstrated that both 5-FP ligand and 6-FP ligand are stable at 135 °C (**Figure 4.4.5** and **Figure 4.4.6**). Interestingly, none of the ^1H NMR resonances of the decomposition product for [(FP)M I (CO) $_2$]BF $_4$ are consistent with 5-FP or 6-FP ligands.

Figure 4.4.1 Stacked ^1H NMR spectra for the stability of [(5-FP)Rh(CO) $_2$]BF $_4$ at 135 °C in MeOH- d_4 . The top spectrum is the ^1H NMR spectrum of 5-FP ligand for comparison.

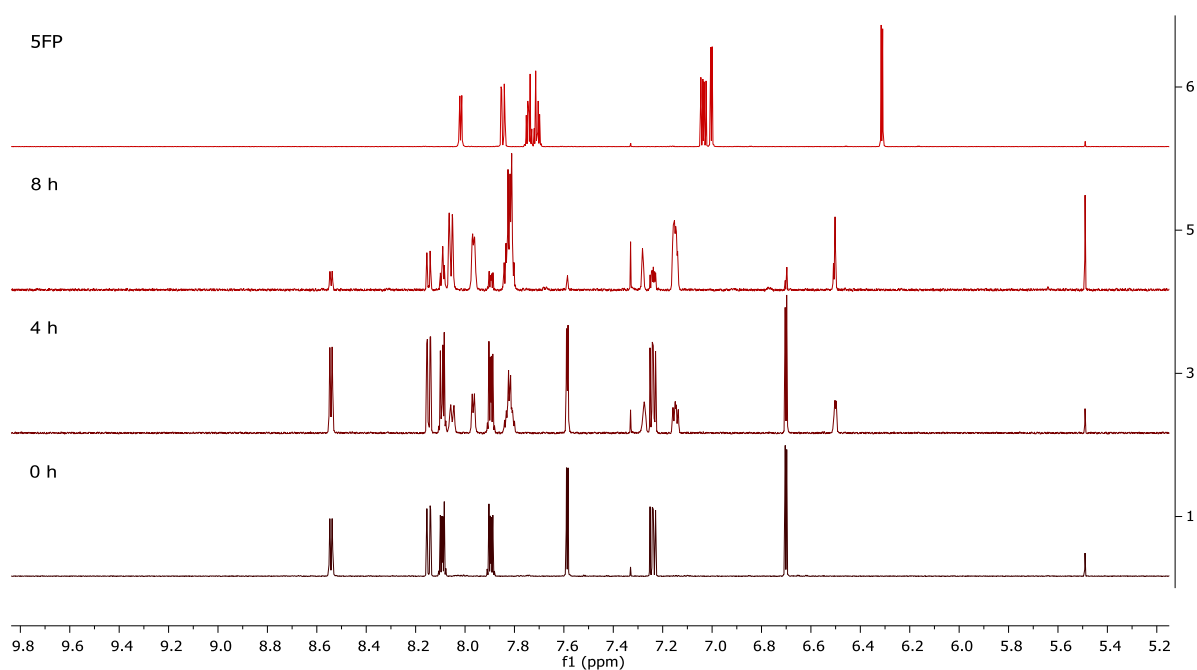


Figure 4.4.2 Stacked ^1H NMR spectra for the stability of $[(6\text{-FP})\text{Rh}(\text{CO})_2]\text{BF}_4$ at $135\text{ }^\circ\text{C}$ in $\text{MeOH-}d_4$. The top spectrum is the ^1H NMR spectrum of 6-FP ligand for comparison.

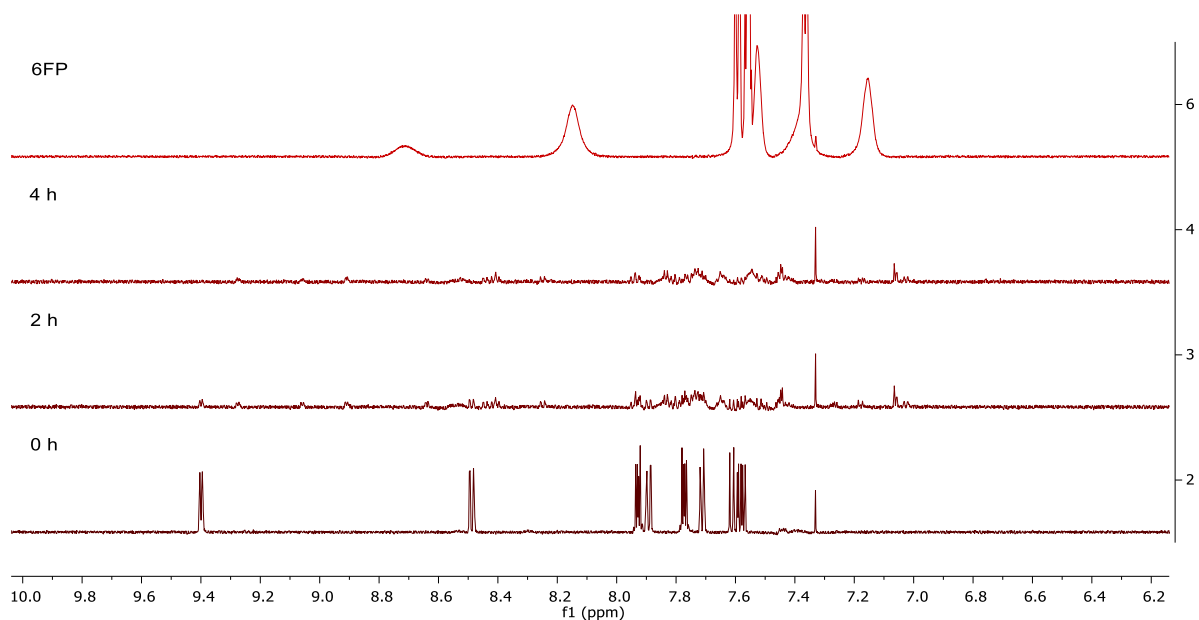


Figure 4.4.3 Stacked ^1H NMR spectra for the stability of $[(5\text{-FP})\text{Ir}(\text{CO})_2]\text{BF}_4$ at $135\text{ }^\circ\text{C}$ in $\text{MeOH-}d_4$. The top spectrum is the ^1H NMR spectrum of 5-FP ligand for comparison.

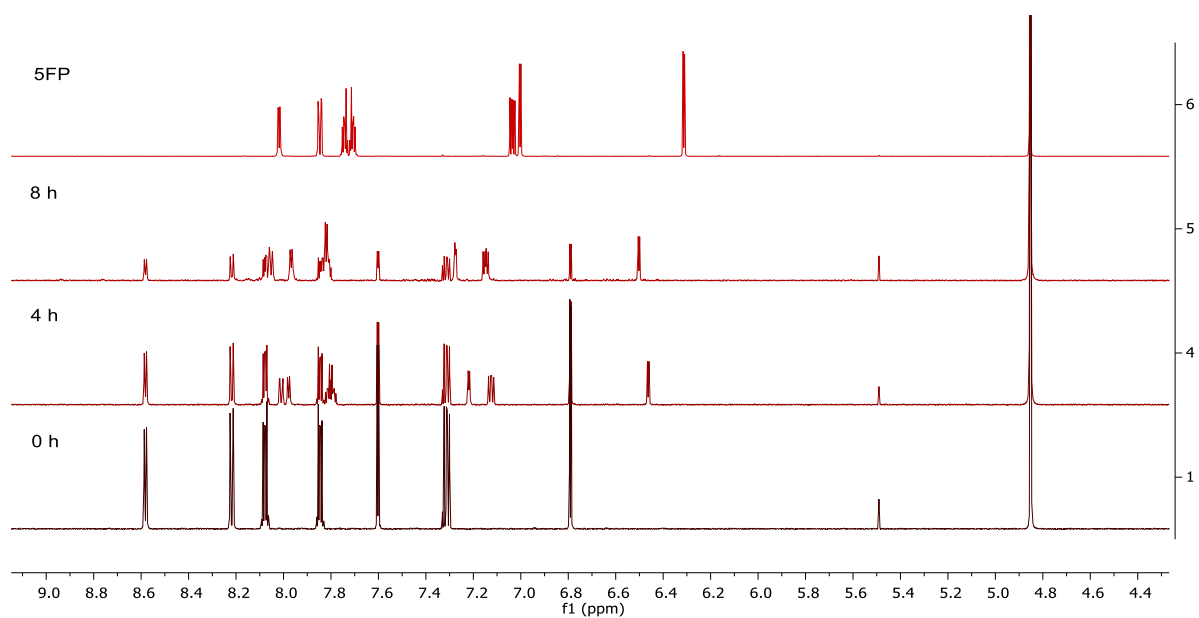


Figure 4.4.4 Stacked ^1H NMR spectra for the stability of $[(6\text{-FP})\text{Ir}(\text{CO})_2]\text{BF}_4$ at $135\text{ }^\circ\text{C}$ in $\text{MeOH-}d_4$. The top spectrum is the ^1H NMR spectrum of 6-FP ligand for comparison.

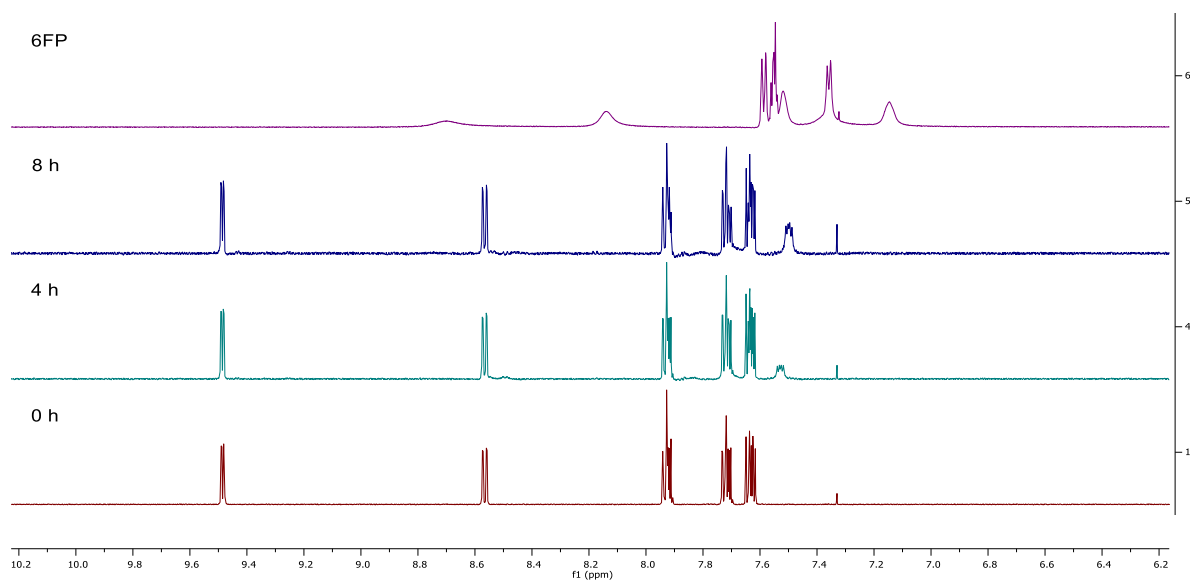


Figure 4.4.5 Stacked ^1H NMR spectra for the stability of 6-FP ligand at $135\text{ }^\circ\text{C}$ in $\text{MeOH-}d_4$.

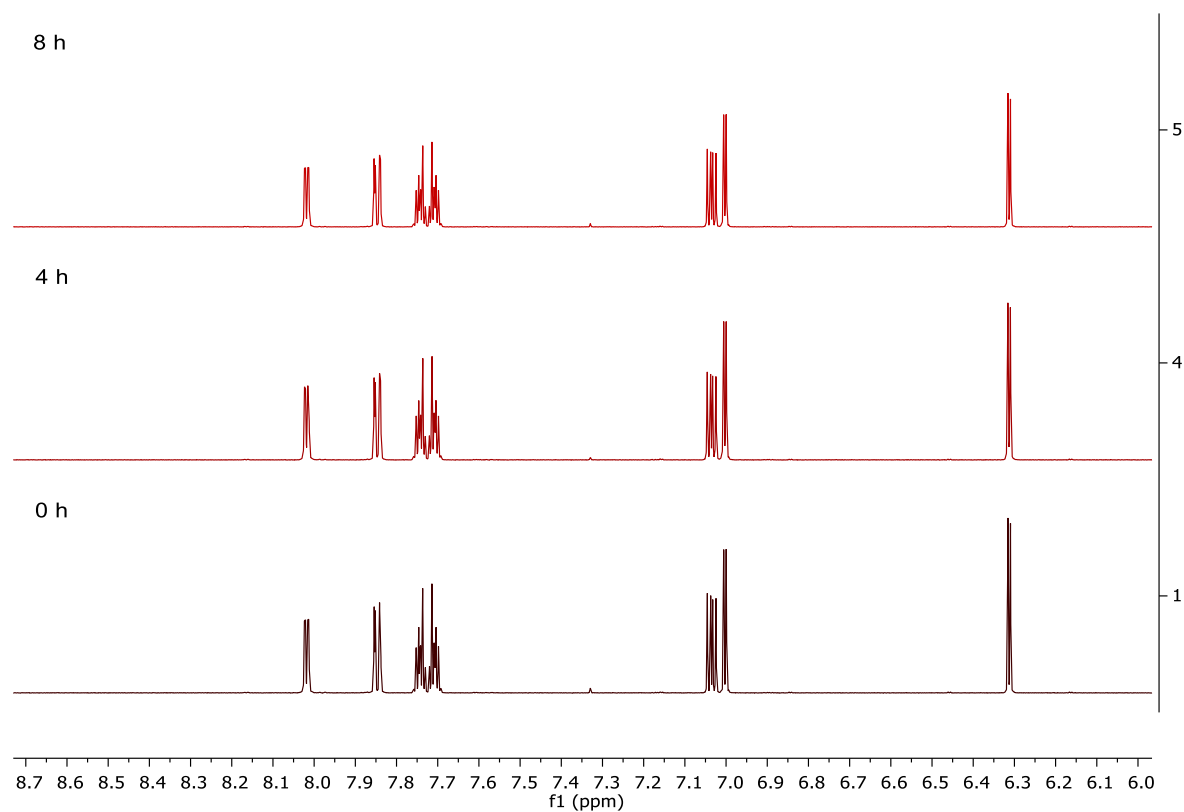
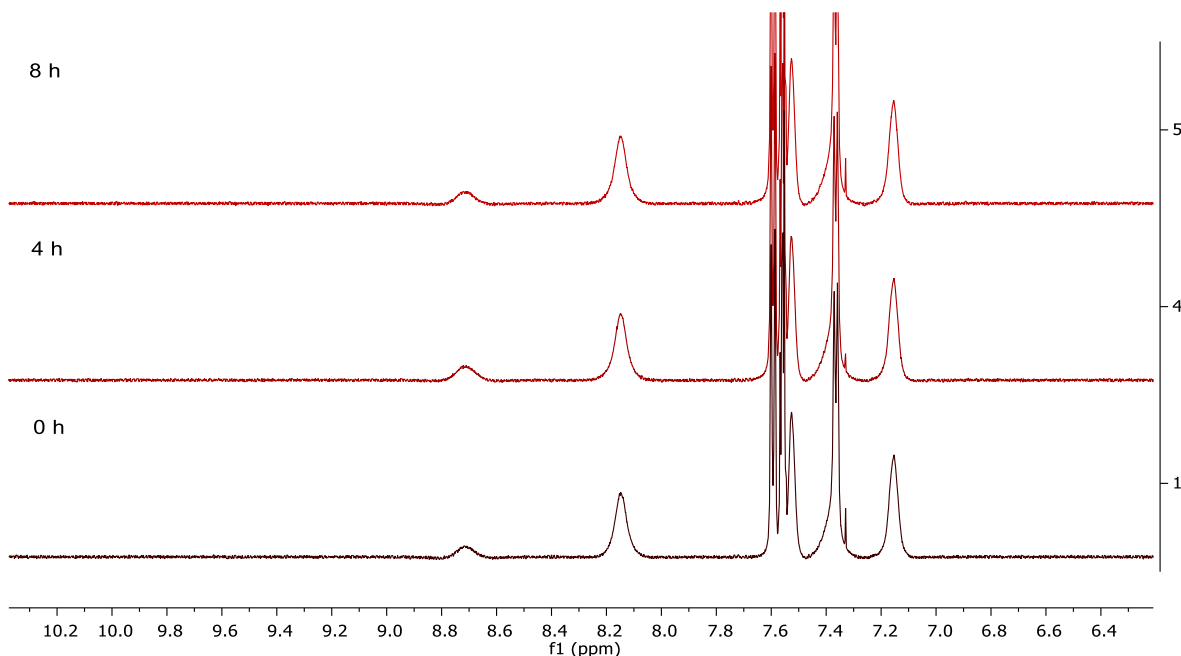


Figure 4.4.6 Stacked ^1H NMR spectra for the stability of 5-FP ligand at 135 °C in $\text{MeOH-}d_4$.



The reaction of methyl iodide with $[(\text{FP})\text{M}^{\text{I}}(\text{CO})_2]\text{BF}_4$ (FP = 5-FP or 6-FP, M = Rh or Ir) was also studied (**Figure 4.4.7–Figure 4.4.12**). All four capping arene complexes showed a rapid reaction at 135 °C in the presence of methyl iodide (**Figure 4.4.7–Figure 4.4.10**). Interestingly, the 5-FP ligand and 6-FP ligand also exhibited reactions with methyl iodide at raised temperature (**Figure 4.4.11** and **Figure 4.4.12**). A comparison of the products from the reactions of $[(\text{FP})\text{M}^{\text{I}}(\text{CO})_2]\text{BF}_4$ (FP = 5-FP or 6-FP, M = Rh or Ir) or the 5-FP and 6-FP free ligands with MeI at 135 °C are shown in **Figure 4.4.13** and **Figure 4.4.14**. Based on the comparison of ^1H NMR resonances, it can be concluded that the products for $[(5\text{-FP})\text{Rh}(\text{CO})_2]\text{BF}_4$ and $[(5\text{-FP})\text{Ir}(\text{CO})_2]\text{BF}_4$ are identical to the product when using 5-FP ligand with MeI at 135 °C (**Figure 4.4.13**). Similarly, the products for $[(6\text{-FP})\text{Rh}(\text{CO})_2]\text{BF}_4$ and $[(6\text{-FP})\text{Ir}(\text{CO})_2]\text{BF}_4$ with MeI are likely identical to the product for 6-FP ligand with MeI at 135 °C (**Figure 4.4.14**). This observation suggests that in the presence of MeI, the capping arene ligand on $[(\text{FP})\text{M}^{\text{I}}(\text{CO})_2]\text{BF}_4$ complexes might

dissociate from the metal center, followed by conversion into the decomposition product. It has been reported that both 7-azaindole and quinoline can react with methyl iodide, forming the 7-methyl-1*H*-pyrrolo [2,3-*b*]-pyridinium iodide and 1-methylquinolin-1-ium iodide respectively (**Scheme 4.4.1**).^{26, 27} Therefore, it is speculated that the the capping arene ligands undergo a similar methylation process with methyl iodide, which causes an irreversible ligand dissociation for the [(FP)M^I(CO)₂]BF₄ (FP = 5-FP or 6-FP, M = Rh or Ir) complexes. Thus, we conclude that Rh or Ir complexes without the ligation of the capping arene are likely the active catalysts for the MeI promoted methanol carbonylation, which exhibit similar reactivity to the [Rh(CO)₂(μ-Cl)]₂ or [Ir(COE)₂(μ-Cl)]₂, respectively.

Figure 4.4.7 Stacked ¹H NMR spectra for the reaction [(5-FP)Rh(CO)₂]BF₄ in the presence of MeI at 135 °C.

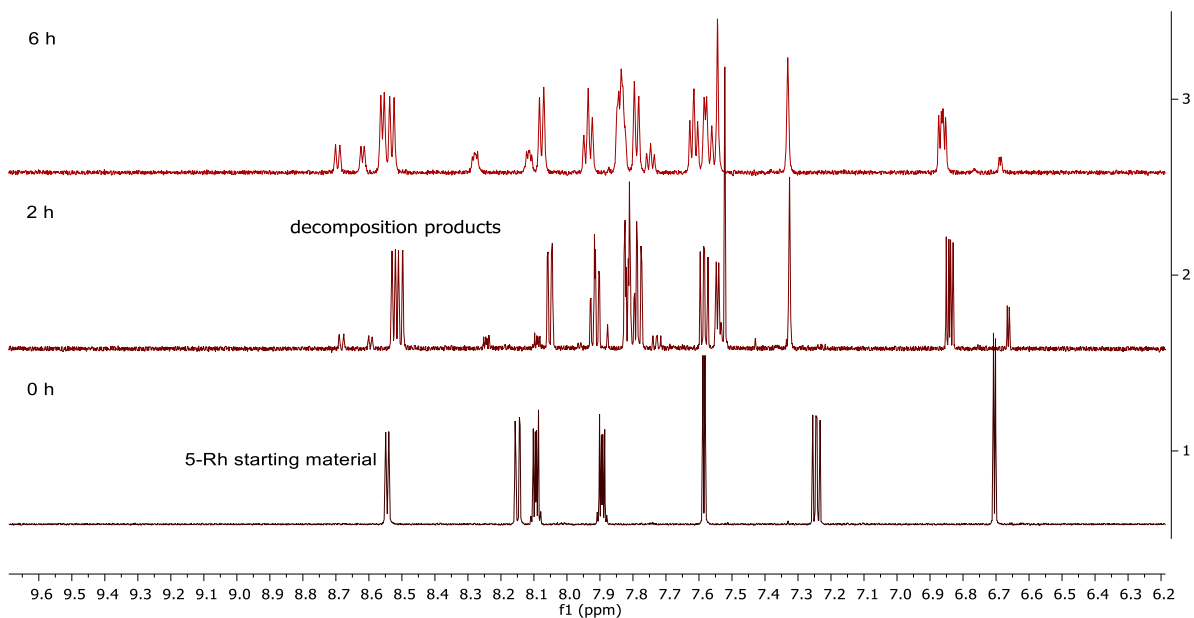


Figure 4.4.8 Stacked ^1H NMR spectra for the reaction $[(6\text{-FP})\text{Rh}(\text{CO})_2]\text{BF}_4$ in the presence of MeI at $135\text{ }^\circ\text{C}$.

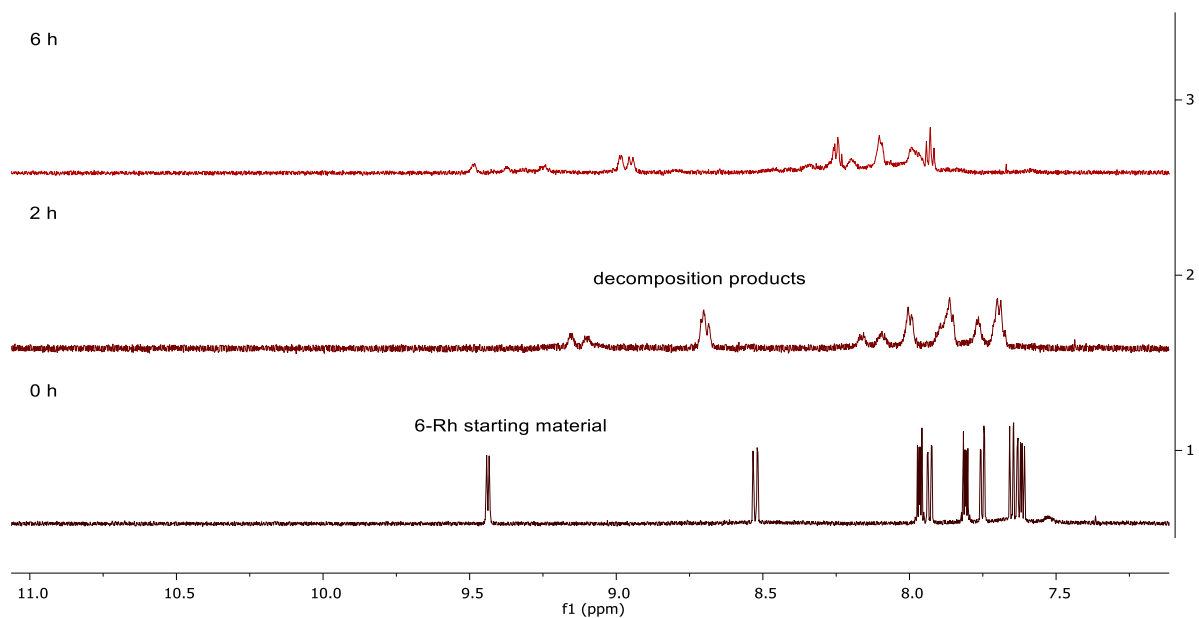


Figure 4.4.9 Stacked ^1H NMR spectra for the reaction $[(5\text{-FP})\text{Ir}(\text{CO})_2]\text{BF}_4$ in the presence of MeI at $135\text{ }^\circ\text{C}$.

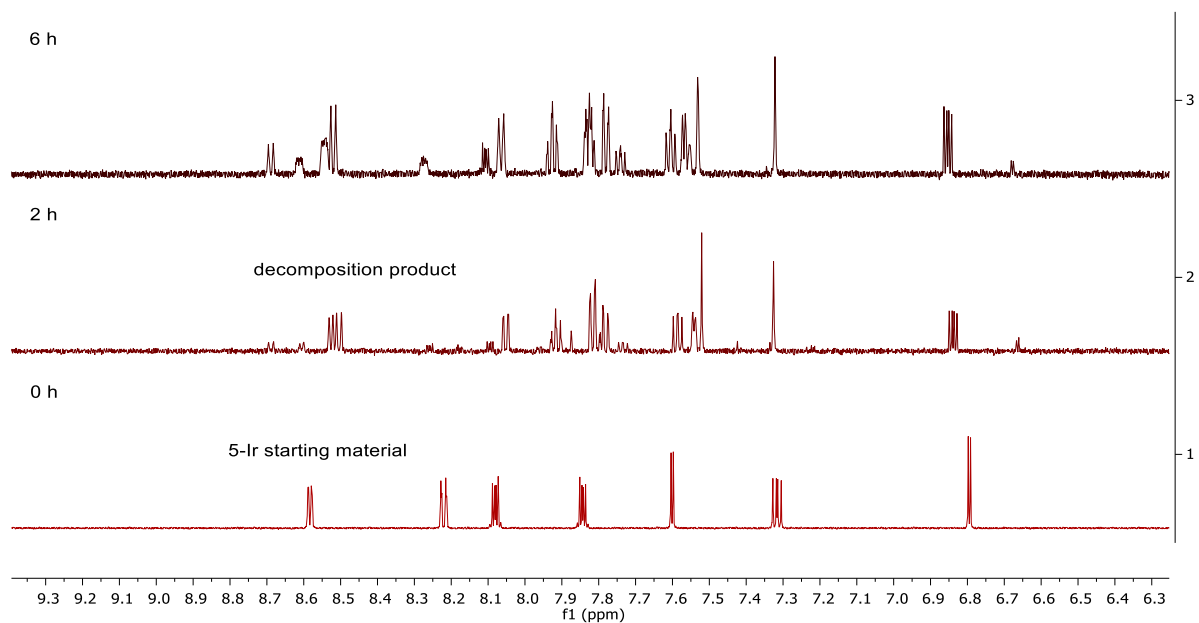


Figure 4.4.10 Stacked ^1H NMR spectra for the reaction $[(6\text{-FP})\text{Ir}(\text{CO})_2]\text{BF}_4$ in the presence of MeI at $135\text{ }^\circ\text{C}$.

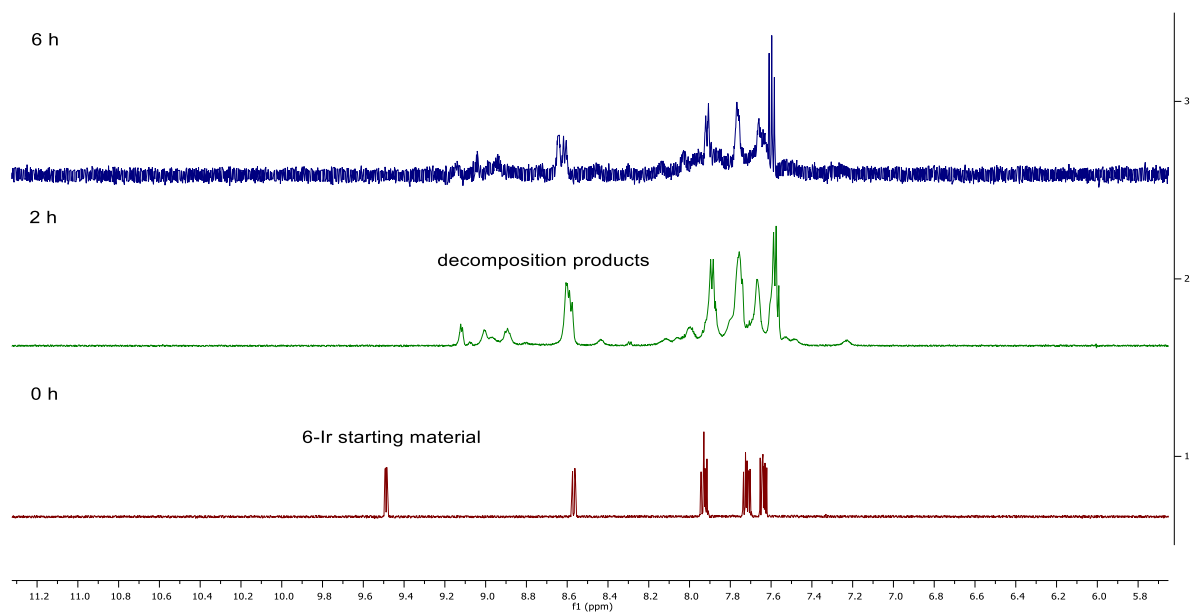


Figure 4.4.11 Stacked ^1H NMR spectra for the reaction 6-FP ligand in the presence of MeI at $135\text{ }^\circ\text{C}$.

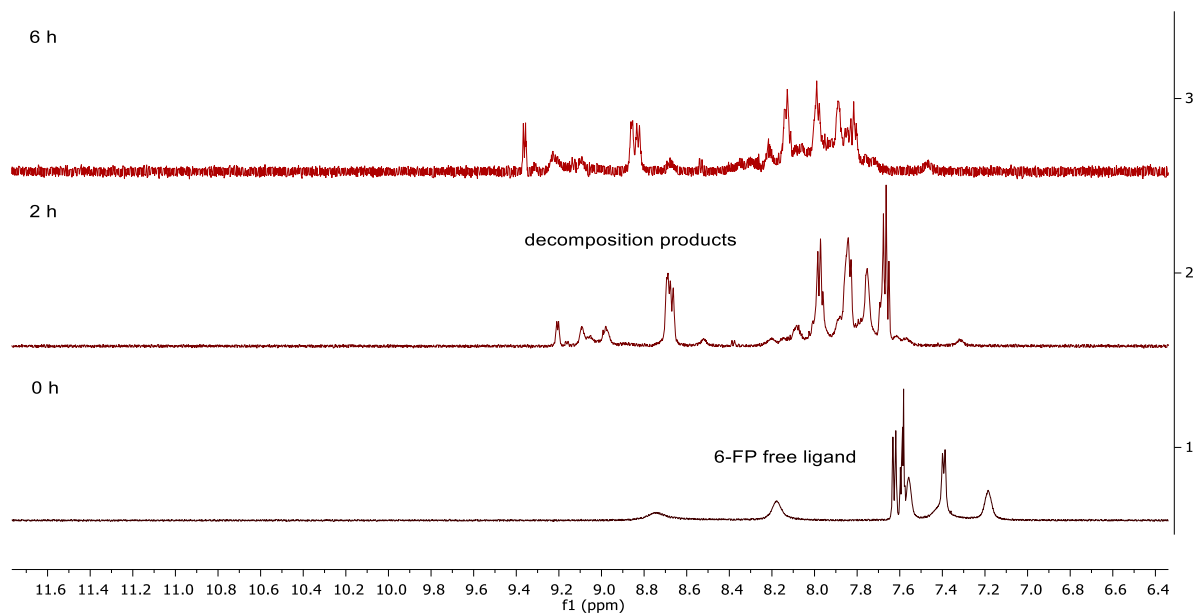


Figure 4.4.12 Stacked ^1H NMR spectra for the reaction 5-FP ligand in the presence of MeI at 135 °C.

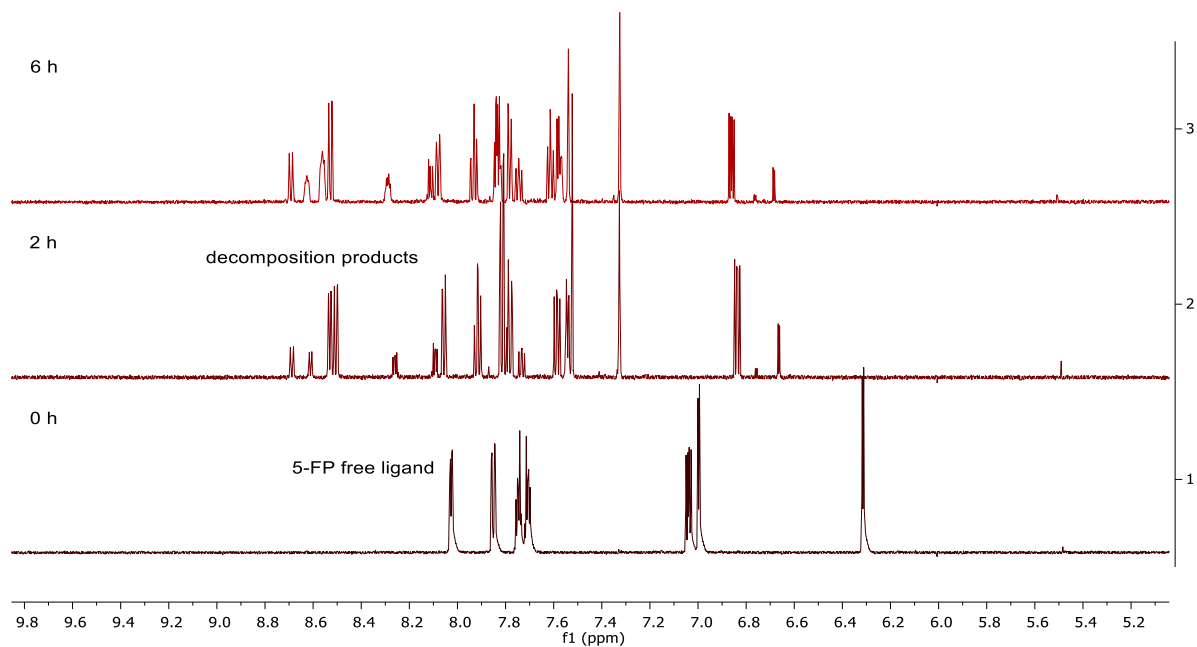


Figure 4.4.13 Comparison of the products for the reaction of $[(5\text{-FP})\text{Ir}(\text{CO})_2]\text{BF}_4$, $[(5\text{-FP})\text{Rh}(\text{CO})_2]\text{BF}_4$ or 5-FP ligand with methyl iodide at 135 °C after 6 hours. The decomposition products show identical ^1H NMR resonances for the three samples.

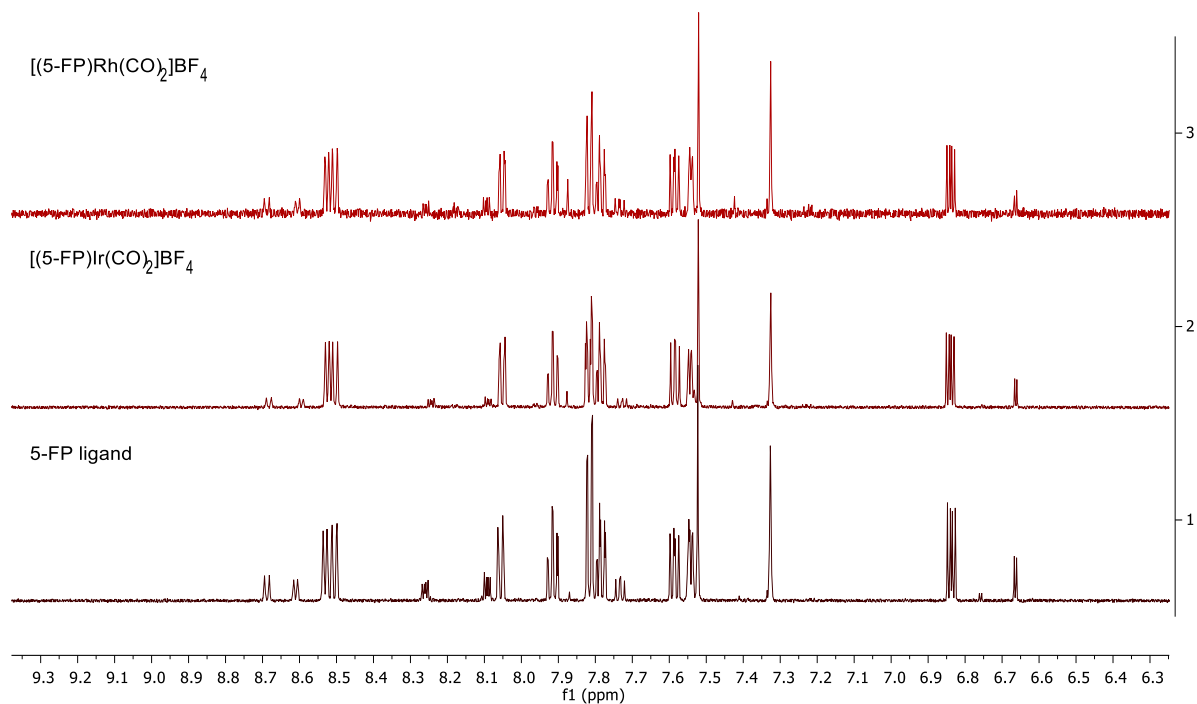
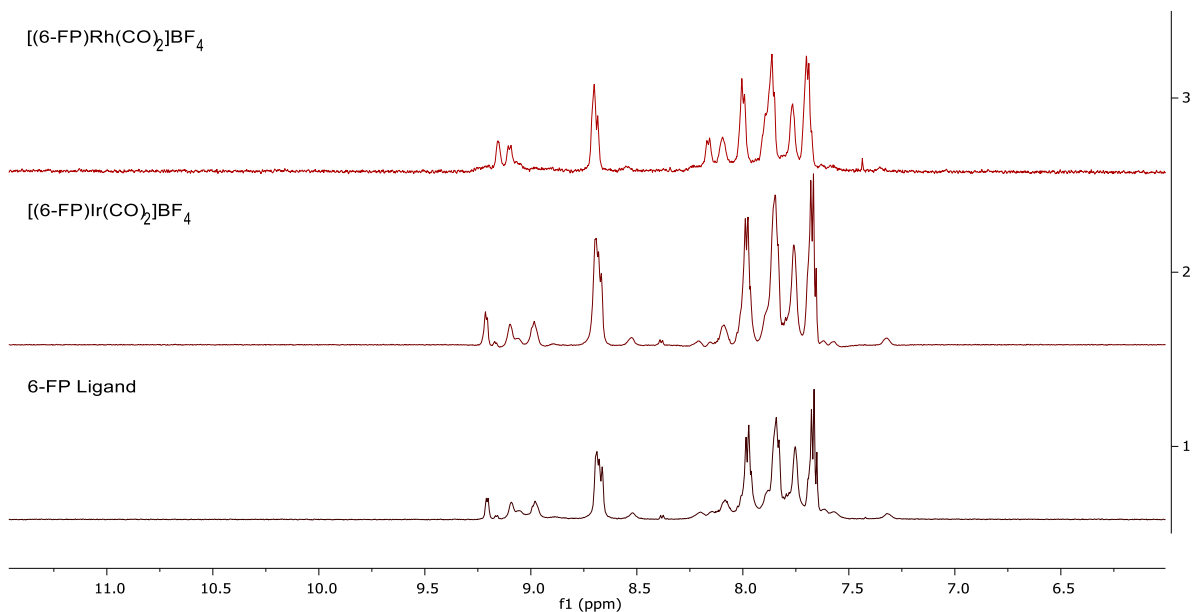
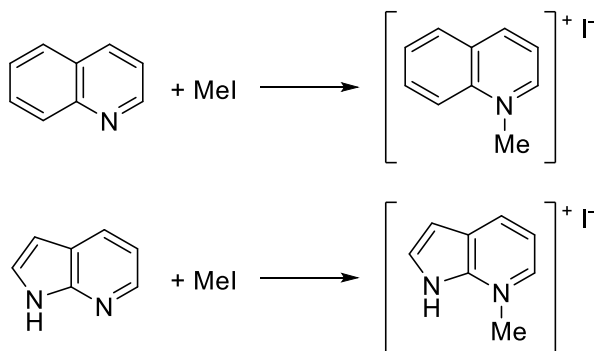


Figure 4.4.14 Comparison of the products for the reaction of [(6-FP)Ir(CO)₂]BF₄, [(6-FP)Rh(CO)₂]BF₄ or 6-FP ligand with methyl iodide at 135 °C after 6 hours. The decomposition products show identical ¹H NMR resonances for the three samples.



Scheme 4.4.1 Reported reaction between quinoline or 7-azaindole and methyl iodide.^{26, 27}



4.5 Summary and Conclusion

A series of capping arene ligated Rh or Ir carbonyl complexes with the general formula [(FP)M^I(CO)₂]BF₄ (FP = 5-FP or 6-FP, M = Rh or Ir) were synthesized. The performances of these complexes on MeI promoted methanol carbonylation were examined. The turnover frequency using [(FP)M^I(CO)₂]BF₄ (FP = 5-FP or 6-FP, M = Rh or Ir) as the catalyst was not improved when compared to catalysis using [Rh(CO)₂(μ-Cl)]₂ or [Ir(COE)₂(μ-Cl)]₂.

Mechanistic studies revealed that the [(5-FP)Rh(CO)₂]BF₄, [(5-FP)Ir(CO)₂]BF₄ and [(6-FP)Rh(CO)₂]BF₄ are unstable at 135 °C without MeI. When MeI is present, all four [(FP)M^I(CO)₂]BF₄ complexes as well as the 5-FP and 6-FP ligands show reactivity with MeI at 135 °C. One of the decomposition products for [(5-FP)Rh(CO)₂]BF₄ or [(5-FP)Ir(CO)₂]BF₄ with MeI at 135 °C are identical to the decomposition product of 5-FP ligand reacting with MeI. Similarly, one of the decomposition products for [(6-FP)Rh(CO)₂]BF₄ or [(6-FP)Ir(CO)₂]BF₄ with MeI at 135 °C are identical to the decomposition product of 6-FP ligand reacting with MeI. The identical decomposition products could suggest that the capping arene ligand dissociates from the Rh and Ir complexes. Thus, the active catalyst for the methanol carbonylation using [(FP)M^I(CO)₂]BF₄ and MeI is likely a metal complex without the capping arene ligand, which explains why no ligand effect is observed for the methanol carbonylation with MeI promoter.

4.6 Experimental section

General Procedures. All experiments with metal complexes and capping arene ligands were performed under an atmosphere of nitrogen in a glovebox, or using standard Schlenk techniques. All solvents were reagent grade or better. Solvents in the glovebox were distilled from a mixture of solvent and potassium/benzophenone (for Et₂O and THF) or CaH₂ (for MeCN), or obtained from an MBraun solvent purification system (for DCM, benzene, pentane) and purged under nitrogen flow, and then stored with molecular sieves.²⁸ Deuterated solvents were kept in the glovebox with molecular sieves (3Å or 4Å, depending on the type of solvents²⁸). Molecular sieves were dried in a vacuum oven at 150 °C overnight before transferring into the glovebox. All celite used in this chapter was Celite™

545 purchased from Fisher Chemical (LOT 225266). Commercially available reagents were used as received.

^1H NMR spectra were obtained at 600 MHz by a Varian NMRS 600 with multiple probes, or at 800 MHz by a Bruker Advance III 800 MHz spectrometer. ^{13}C NMR spectra were obtained at 201 MHz by a Bruker Advance III 800 MHz spectrometer. ^1H NMR and ^{13}C NMR were referenced against residual proton or ^{13}C signals of the deuterated solvent, respectively.²⁹

GC-MS data were collected by a Shimadzu GCMS-QP 2010 gas chromatograph mass spectrometer with a DB-FFAP capillary column (60 m \times 0.250 mm \times 0.25 μm). The temperature of the oven was set to start at 50 $^\circ\text{C}$ and hold for 5 min, then heat up by a 15 $^\circ\text{C}/\text{min}$ increment until the temperature reached 200 $^\circ\text{C}$. The retention time of cyclohexane (internal standard), methyl acetate, and acetic acid were 3.76 min, 4.34 min, and 13.12 min respectively. The calibration curves for methyl acetate, and acetic acid were recorded for quantitative measurements (**Figure 4.6.1** and **Figure 4.6.2**).

Figure 4.6.1 Calibration curve for the quantification of methyl acetate (MeOAc) versus cyclohexane (internal standard, CyH).

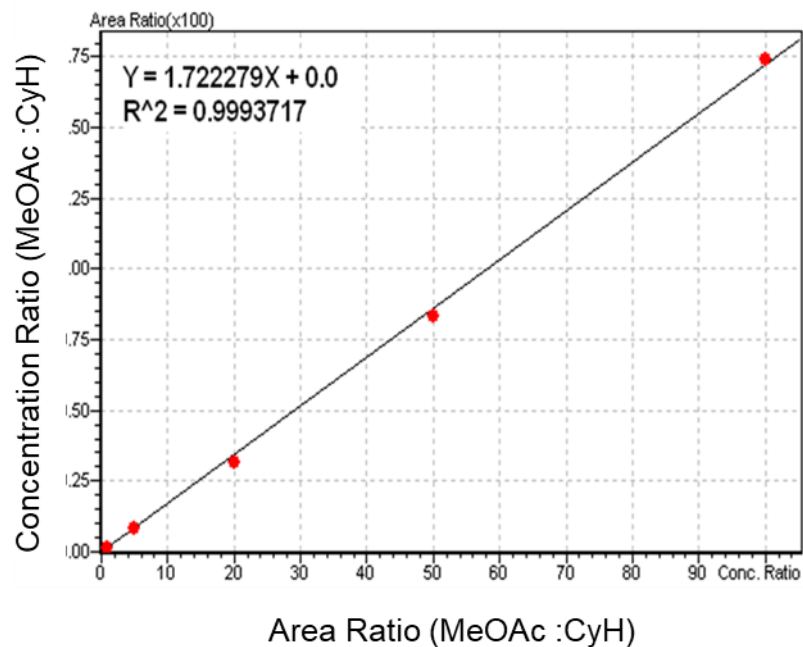
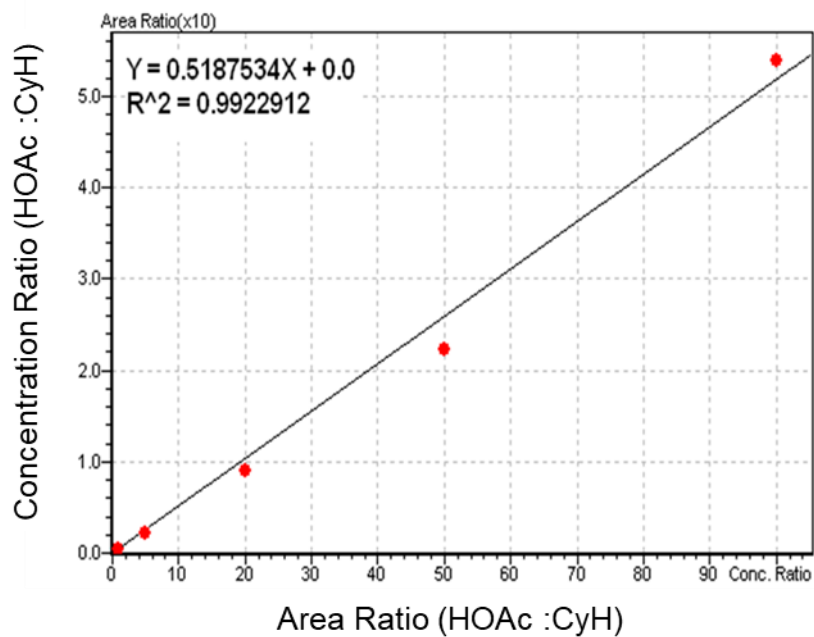


Figure 4.6.2 Calibration curve for the quantification of acetic acid (HOAc) versus cyclohexane (internal standard, CyH).



Synthesis of [(5-FP)Rh(CO)₂]BF₄. In a glovebox, 40.0 mg (0.103 mmol) of [Rh(CO)₂(μ-Cl)]₂ was mixed with 63.9 mg (0.206 mmol) of 5-FP ligand to create a 15 mL suspension in MeCN. The solution was allowed to stir for 20 minutes at room temperature, then 40.1 mg (0.206 mmol) of AgBF₄ were added to the mixture and reacted overnight. The reaction mixture was filtered through a plug of Celite. Then, the filtrate was dried *in vacuo*, and the resulting solid was dissolved in a minimal amount of THF (*c.a.* 3 mL), followed by the addition of 100 mL of pentanes, and the orange product precipitated out from the solution. The mixture was filtered through a Büchner funnel with a fine fritted disc, and the product was collected and dried *in vacuo* as an orange solid (0.0934 g, 0.168 mmol, 81.5% yield). The product was characterized by ¹H NMR, ¹³C NMR, single crystal X-ray diffraction and IR spectroscopy. ¹H NMR (600 MHz, methylene chloride-*d*₂) δ 8.42 (d, ³J_{HH} = 5 Hz, 1H), 8.07 (dd, ³J_{HH} = 8 Hz, 1H), 8.04 (dd, ³J_{HH} = 6, 4 Hz, 1H), 7.73 (dd, ³J_{HH} = 6, 4 Hz, 1H), 7.39 (d, ³J_{HH} = 4 Hz, 1H), 7.23 (dd, ³J_{HH} = 8, 6 Hz, 1H), 6.68 (d, ³J_{HH} = 4 Hz, 1H). ¹³C NMR (201 MHz, methylene chloride-*d*₂) δ 182.1 (d, ¹J_{Rh-C} = 69 Hz, Rh-CO), 148.7, 144.3, 135.3, 134.2, 133.1, 132.4, 132.1, 124.7, 118.5, 104.4. IR(KBr): ν_{CO} (cm⁻¹) = 2037, 2098.

Figure 4.6.3 ¹H NMR spectrum for [(5-FP)Rh(CO)₂]BF₄ in methylene chloride-*d*₂.

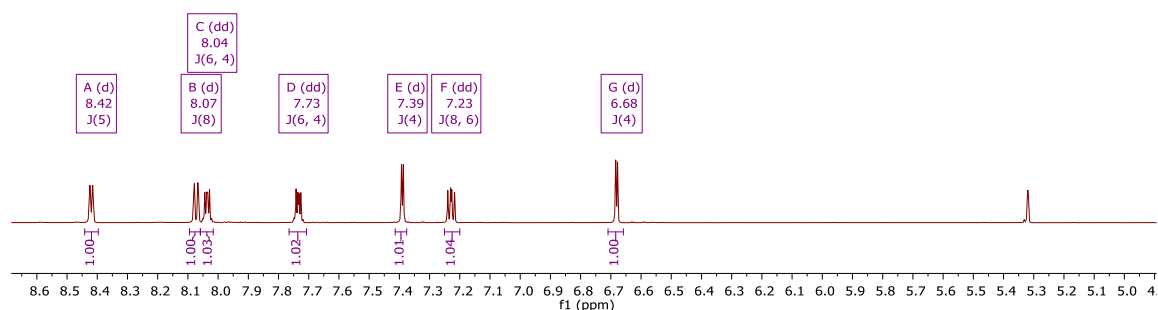


Figure 4.6.4 ^{13}C NMR spectrum for $[(5\text{-FP})\text{Rh}(\text{CO})_2]\text{BF}_4$ in methylene chloride- d_2 .

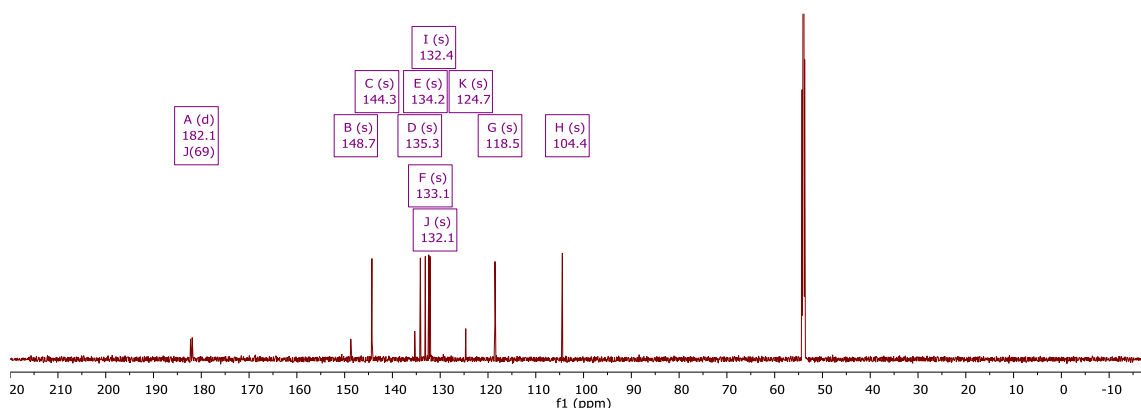
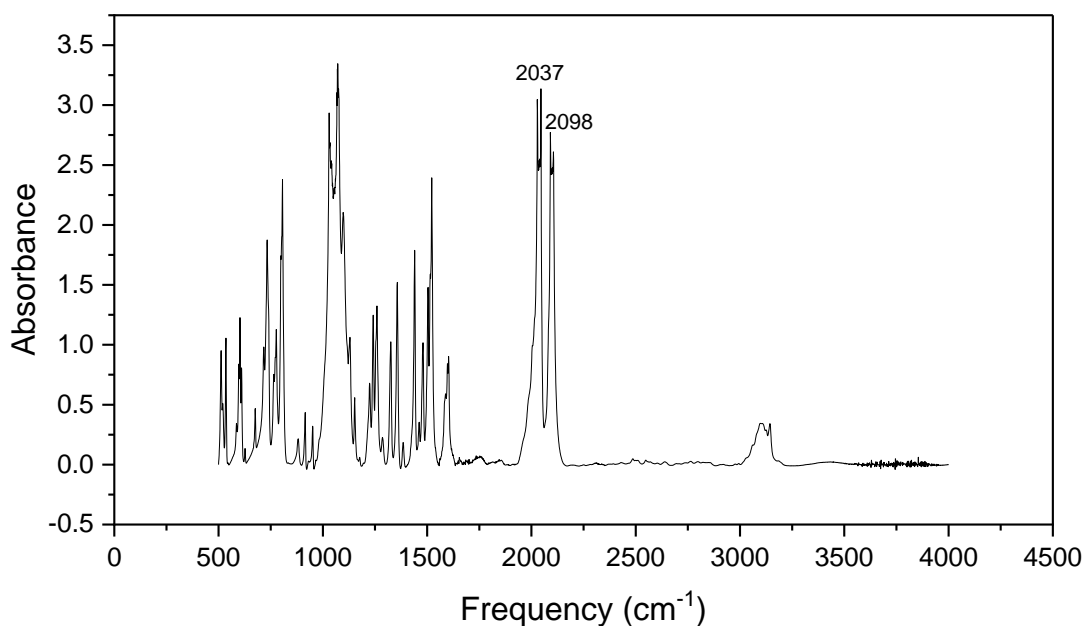


Figure 4.6.5 FTIR spectrum of $[(5\text{-FP})\text{Rh}(\text{CO})_2]\text{BF}_4$



Synthesis of $[(6\text{-FP})\text{Rh}(\text{CO})_2]$ In a glovebox, 50.0 mg (0.129 mmol) of $[\text{Rh}(\text{CO})_2(\mu\text{-Cl})_2]$ were mixed with 82.9 mg (0.257 mmol) of 6-FP ligand in 15 mL of MeCN. The solution was allowed to stir for 20 minutes at room temperature, and 50.1 mg (0.257 mmol) of AgBF_4 were added to the mixture to react overnight. The reaction mixture was then filtered through a plug of Celite. Then, the filtrate was dried *in vacuo*, and the resulting solid was dissolved in a minimal amount of THF (*c.a.* 3 mL), followed by the addition of

100 mL of pentanes, and the orange colored product precipitated out from the solution. The mixture was filtered through a Buchner funnel with fine fritted disc, and the product was collected and dried *in vacuo* as an orange colored solid (0.131 g, 0.227 mmol, 88.3% yield). The product was characterized by ^1H NMR, ^{13}C NMR and IR spectroscopy. ^1H NMR (800 MHz, methylene chloride- d_2) δ 9.30 (d, $^3J_{\text{HH}} = 5$ Hz, 1H), 8.33 (d, $^3J_{\text{HH}} = 8$ Hz, 1H), 7.90 – 7.86 (m, 1H), 7.80 (d, $^3J_{\text{HH}} = 8$ Hz, 1H), 7.71 – 7.66 (m, 1H), 7.63 (d, $^3J_{\text{HH}} = 8$ Hz, 1H), 7.60 – 7.54 (m, 2H). ^{13}C NMR (201 MHz, methylene chloride- d_2) δ 183.4 (d, $^1J_{\text{Rh-C}} = 71$ Hz, Rh–CO), 155.5, 146.4, 141.6, 136.9, 135.3, 133.6, 130.3, 130.1, 130.0, 123.0. IR(KBr): ν_{CO} (cm^{-1}) = 2026, 2088.

Figure 4.6.6 ^1H NMR spectrum for $[(6\text{-FP})\text{Rh}(\text{CO})_2]\text{BF}_4$ in methylene chloride- d_2 .

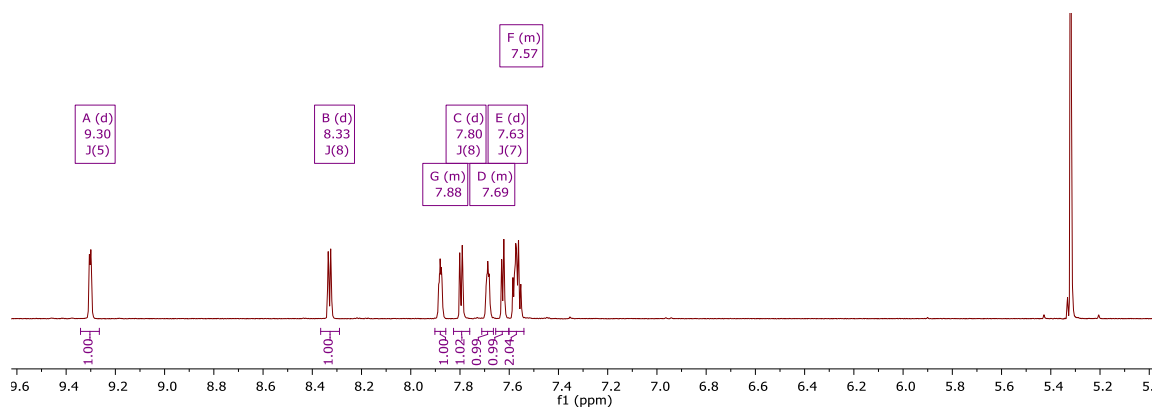


Figure 4.6.7 ^{13}C NMR spectrum for $[(6\text{-FP})\text{Rh}(\text{CO})_2]\text{BF}_4$ in methylene chloride- d_2 .

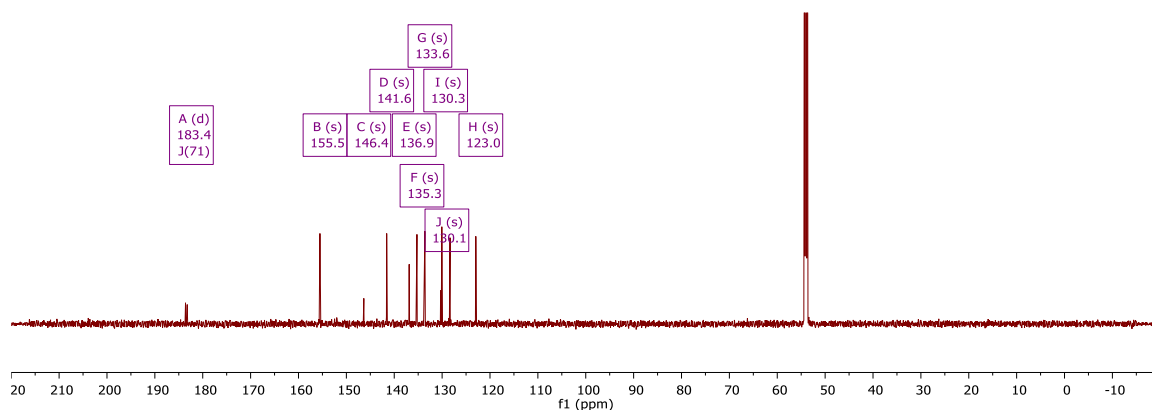
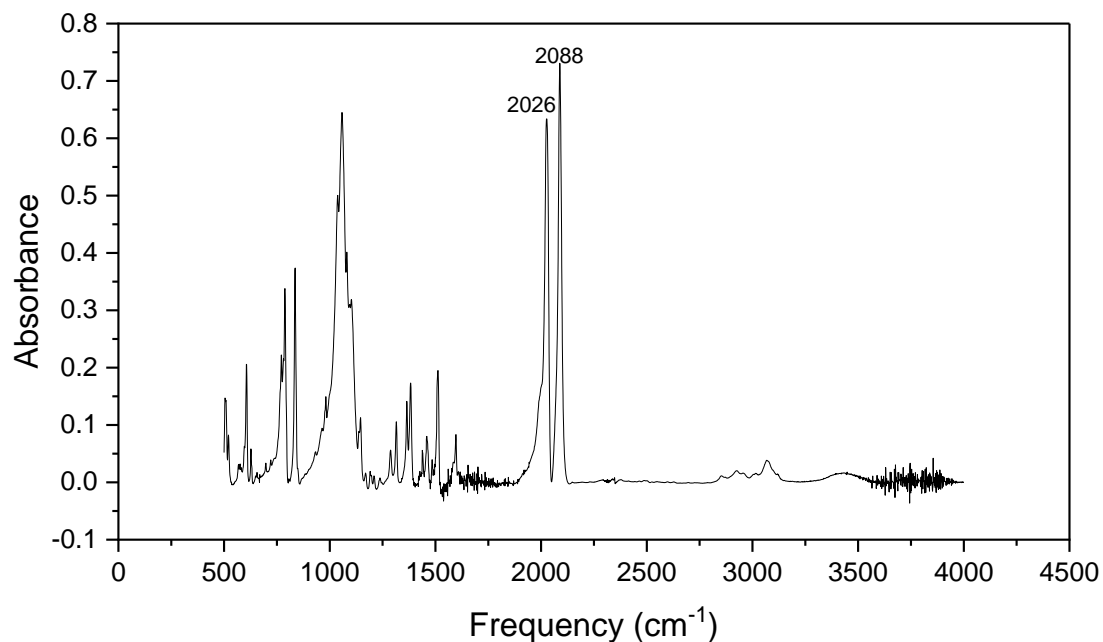


Figure 4.6.8 FTIR spectrum of $[(6\text{-FP})\text{Rh}(\text{CO})_2]\text{BF}_4$ 

Synthesis of $[(5\text{-FP})\text{Ir}(\text{CO})_2]\text{BF}_4$ The synthesis of $[(5\text{-FP})\text{Ir}(\text{CO})_2]\text{BF}_4$ followed a previously reported procedure.²⁵ In a 100 mL Schlenk flask, 43.3 mg (0.0483 mmol) of $[\text{Ir}(\text{COE})_2(\mu\text{-Cl})]_2$ and 30 mL of acetonitrile were added under dinitrogen. Gaseous carbon monoxide was allowed to bubble through the suspension for *c.a.* 5 minutes, resulting in the formation of a green solution. A solution of 30.0 mg (0.0967 mmol) of 5-FP ligand in 10 mL of acetonitrile was added to the solution via a syringe. The flask was transferred into a glovebox, and 18.8 mg (0.0967 mmol) of AgBF_4 were added. The mixture was allowed to react in the dark overnight, and the reaction mixture was then filtered through a plug of Celite. The filtrate was dried *in vacuo* and the resulting solid was dissolved in a minimal amount of THF (*c.a.* 3 mL), followed by the addition of 100 mL of pentanes, and the yellow product precipitated from the solution. The mixture was filtered through a Buchner funnel with fine fritted disc, and the product was collected and dried *in vacuo*, as a yellow solid (48 mg, 0.074 mmol, 77% yield). The product was characterized by ¹H NMR, ¹³C NMR

and IR spectroscopy. ^1H NMR (800 MHz, methylene chloride- d_2) δ 8.44 (d, $^3J_{\text{HH}} = 5$ Hz, 1H), 8.18 – 8.10 (m, 1H), 8.07 – 7.99 (m, 1H), 7.68 (dt, $^3J_{\text{HH}} = 6$, 3 Hz, 1H), 7.40 (d, $^3J_{\text{HH}} = 4$ Hz, 1H), 7.34 – 7.26 (m, 1H), 6.77 (d, $^3J_{\text{HH}} = 3$ Hz, 1H). ^{13}C NMR (201 MHz, methylene chloride- d_2) δ 168.8 (s, Ir-CO), 148.3, 143.9, 135.3, 134.3, 132.7, 131.9, 131.4, 125.1, 118.2, 104.3. IR(KBr): ν_{CO} (cm^{-1}) = 2019, 2084.

Figure 4.6.9 ^1H NMR spectrum for $[(5\text{-FP})\text{Ir}(\text{CO})_2]\text{BF}_4$ in methylene chloride- d_2 .

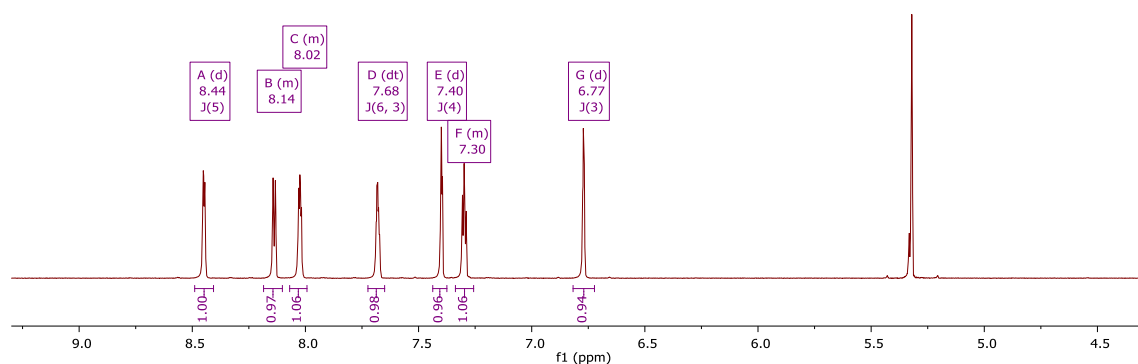


Figure 4.6.10 ^{13}C NMR spectrum for $[(5\text{-FP})\text{Ir}(\text{CO})_2]\text{BF}_4$ in methylene chloride- d_2 .

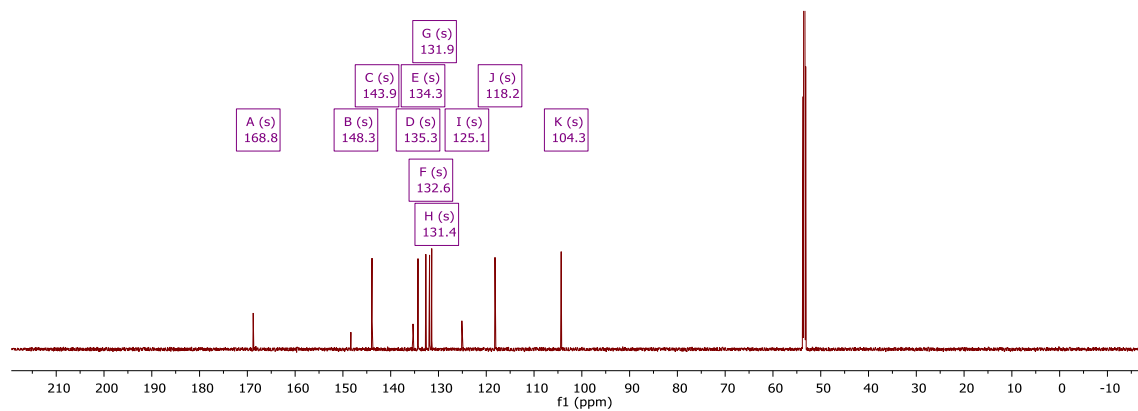
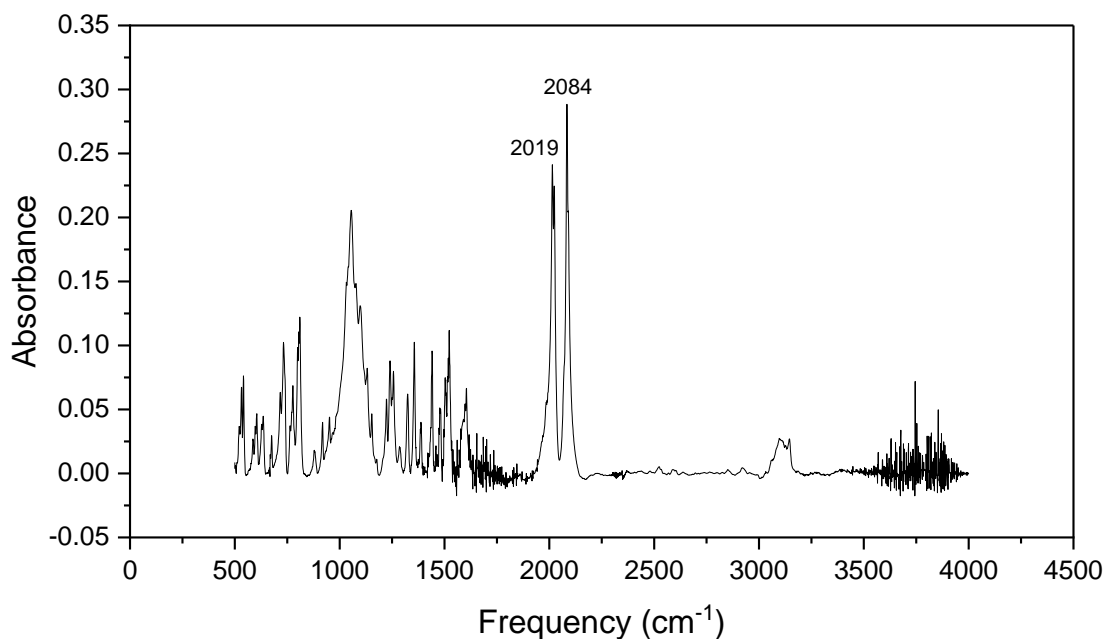


Figure 4.6.11 FTIR spectrum of [(5-FP)Ir(CO)₂]BF₄.

Synthesis of [(6-FP)Ir(CO)₂]BF₄. The synthesis of [(6-FP)Ir(CO)₂]BF₄ followed a previously reported procedure.²⁵ In a 250 mL Schlenk flask, 107.5 mg (0.120 mmol) of [Ir(COE)₂(μ-Cl)]₂ and 60 mL of acetonitrile were added under dinitrogen. Gaseous carbon monoxide was allowed to bubble through the suspension for *c.a.* 5 minutes, resulting in the formation of a green solution. A solution of 80.0 mg (0.241 mmol) of 6-FP ligand in 20 mL of acetonitrile was added to the solution via a syringe. The flask was transferred into a glovebox, and 46.7 mg (0.240 mmol) of AgBF₄ were added. The mixture was allowed to react in the dark overnight, and the reaction mixture was then filtered through a plug of Celite. The filtrate was dried *in vacuo*, and the resulting solid was dissolved in a minimal amount of THF (*c.a.* 5 mL), followed by the addition of 100 mL of pentanes, and the yellow product precipitated from the solution. The mixture was filtered through a Buchner funnel with fine fritted disc, and the product was collected and dried *in vacuo* as a yellow solid (127.0 mg, 0.190 mmol, 79.3% yield). The product was characterized by ¹H NMR, ¹³C

NMR and IR spectroscopy. ^1H NMR (600 MHz, methylene chloride- d_2) δ 9.39 (dd, $^3J_{\text{HH}} = 5, 2$ Hz, 1H), 8.40 (d, $^3J_{\text{HH}} = 8, 2$ Hz, 1H), 8.40 (dd, $^3J_{\text{HH}} = 8, 2$ Hz, 1H), 7.89 – 7.86 (m, 1H), 7.83 (dd, $^3J_{\text{HH}} = 8, 2$ Hz, 1H), 7.83 (dd, $^3J_{\text{HH}} = 8, 2$ Hz, 1H), 7.65 – 7.57 (m, 4H). ^{13}C NMR (201 MHz, methylene chloride- d_2) δ 170.0 (s, Ir- $\underline{\text{CO}}$), 156.7, 147.4, 142.3, 137.9, 136.2, 136.0, 133.4, 131.1, 130.3, 130.2, 123.2. IR(KBr): ν_{CO} (cm^{-1}) = 2011, 2082.

Figure 4.6.12 ^1H NMR spectrum for $[(6\text{-FP})\text{Ir}(\text{CO})_2]\text{BF}_4$ in methylene chloride- d_2 .

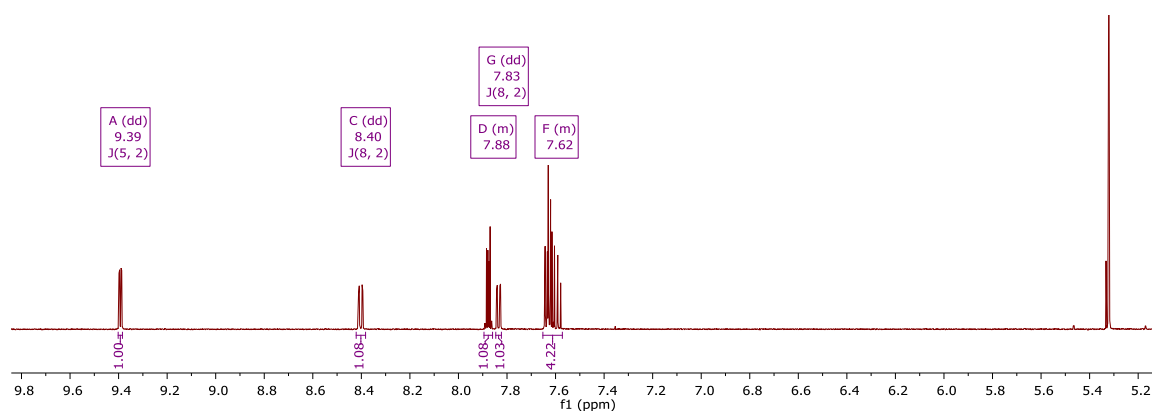


Figure 4.6.13 ^{13}C NMR spectrum for $[(6\text{-FP})\text{Ir}(\text{CO})_2]\text{BF}_4$ in methylene chloride- d_2 .

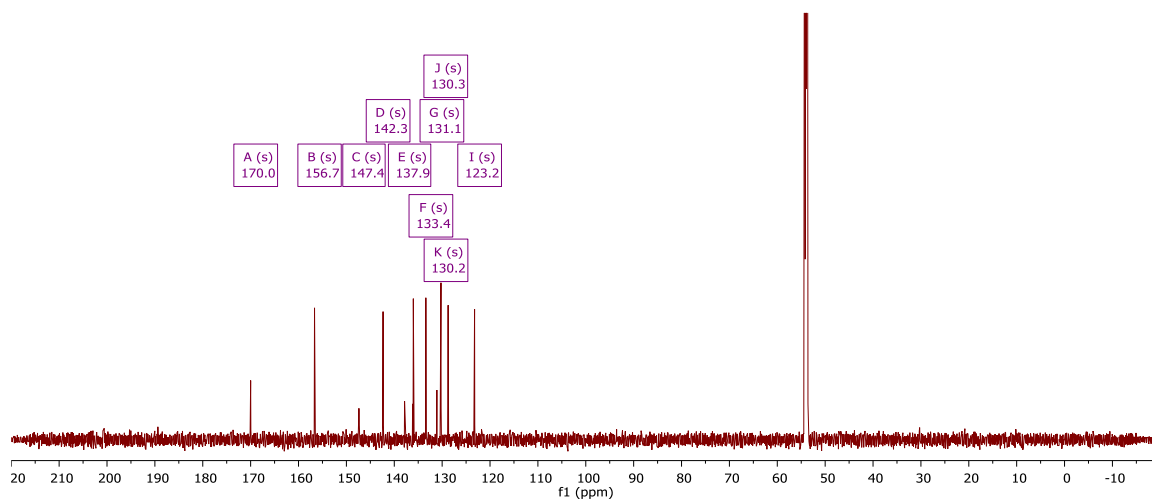
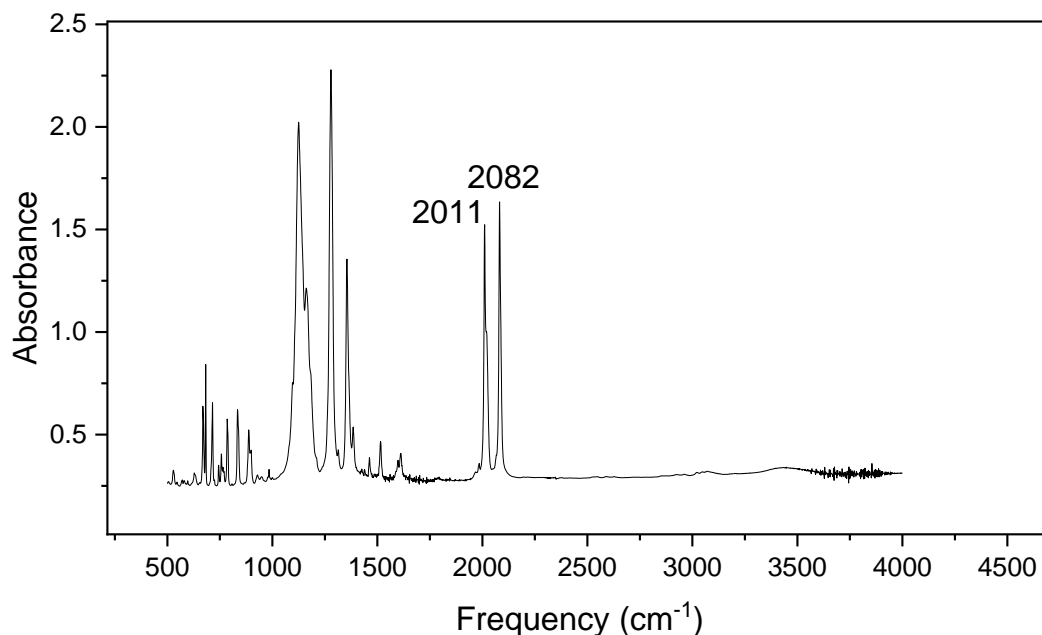
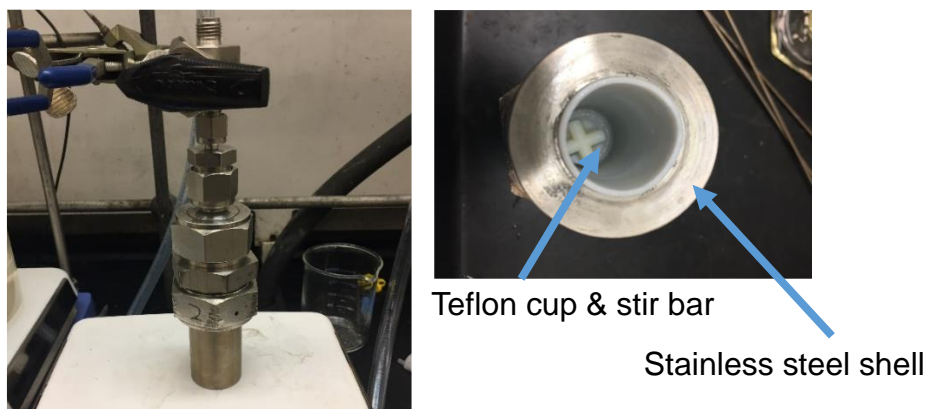


Figure 4.6.14 FTIR spectrum of [(6-FP)Ir(CO)₂]BF₄

General procedure for catalytic methanol carbonylation experiments. In a glovebox, 2 mM of Rh or Ir catalyst, designated amount of CH₃I and deionized H₂O were added to 3 mL of methanol and loaded into a custom made VCO reactor (**Figure 4.6.15**). Designated pressure of CO was then charged into the sealed reactor, and the reactor was heated to a designated temperature for 24 hours or 48 hours. After the reaction, CO was released and the reaction solution was diluted by 10 mL of methanol. 0.1 mL of cyclohexane stock solution in methanol (64.8 mL/L in MeOH) was added to the diluted reaction solution. The resulting solution was analyzed by GC-MS. Further dilution of the analyte by methanol may have been performed to avoid over saturation of signals on the GC-MS spectrum.

Figure 4.6.15 Images of high-pressure reaction vessel used (VCO reactor).



4.7 References

- (1) Kalck, P.; Le Berre, C.; Serp, P. Recent Advances in the Methanol Carbonylation Reaction into Acetic Acid. *Coord. Chem. Rev.* **2020**, *402*, 213078.
- (2) Le Berre, C.; Serp, P.; Kalck, P.; Torrence, G. P. Acetic Acid. *Ullmann's Encyclopedia of Industrial Chemistry* **2014**, 1-34.
- (3) Roscher, G. Vinyl Esters. *Ullmann's Encyclopedia of Industrial Chemistry* **2000**.
- (4) Walter, R. H., F.; Walter, M. Process for the Production of Aliphatic Oxygen Compounds by Carbonylation of Acohols, Ethers, and Esters. US2729651A, 1956.
- (5) Walter, R. H., F. Acetic Acid Anhydride. 1957.
- (6) Paulik, F. E.; Roth, J. F. Novel Catalysts for the Low-Pressure Carbonylation of Methanol to Acetic Acid. *Chemical Communications (London)* **1968**, 1578a-1578a.
- (7) Haynes, A.; Maitlis, P. M.; Morris, G. E.; Sunley, G. J.; Adams, H.; Badger, P. W.; Bowers, C. M.; Cook, D. B.; Elliott, P. I. P.; Ghaffar, T.; et al. Promotion of Iridium-Catalyzed Methanol Carbonylation: Mechanistic Studies of the Cativa Process. *J. Am. Chem. Soc.* **2004**, *126*, 2847-2861.

- (8) Howard, M. J. S., G.J.; Poole, A.D.; Watt, R.J.; Sharma, B.K. New Acetyls Technologies from BP Chemicals. *Stud. Surf. Sci. Catal.* **1999**, *121*, 61-68.
- (9) Sunley, G. J.; Watson, D. J. High Productivity Methanol Carbonylation Catalysis Using Iridium: The Cativa™ Process for the Manufacture of Acetic Acid. *Catal. Today* **2000**, *58*, 293-307.
- (10) Haynes, A. Chapter 1 - Catalytic Methanol Carbonylation. In *Advances in Catalysis*, Gates, B. C., Knözinger, H. Eds.; Vol. 53; Academic Press, 2010; pp 1-45.
- (11) Forster, D. Mechanistic Pathways in the Catalytic Carbonylation of Methanol by Rhodium and Iridium Complexes. In *Advances in Organometallic Chemistry*, Stone, F. G. A., West, R. Eds.; Vol. 17; Academic Press, 1979; pp 255-267.
- (12) Yoneda, N.; Kusano, S.; Yasui, M.; Pujado, P.; Wilcher, S. Recent Advances in Processes and Catalysts for the Production of Acetic Acid. *Applied Catalysis A: General* **2001**, *221*, 253-265.
- (13) Best, J.; Wilson, J. M.; Adams, H.; Gonsalvi, L.; Peruzzini, M.; Haynes, A. Reactivity of Rhodium(I) Iminophosphine Carbonyl Complexes with Methyl Iodide. *Organometallics* **2007**, *26*, 1960-1965.
- (14) Miller, E. M.; Shaw, B. L. Kinetic and Other Studies on Oxidative Addition Reactions of Iridium Phosphine Complexes of the Type *trans*-[IrCl(CO)(PMe₂R)₂](R = Ph, *o*-MeO·C₆H₄, or *p*-MeO·C₆H₄). *Dalton Trans.* **1974**, 480-485.
- (15) Verspui, G.; Schanssema, F.; Sheldon, R. A. A Stable, Conspicuously Active, Water-Soluble Pd Catalyst for the Alternating Copolymerization of Ethene and CO in Water. *Angew. Chem. Int. Ed.* **2000**, *39*, 804-806.

- (16) Carter, A.; Cohen, S. A.; Cooley, N. A.; Murphy, A.; Scutt, J.; Wass, D. F. High Activity Ethylene Trimerisation Catalysts Based on Diphosphine Ligands. *Chem. Commun.* **2002**, 858-859.
- (17) Knowles, W. S. Asymmetric hydrogenation. *Acc. Chem. Res.* **1983**, *16*, 106-112.
- (18) Drexler, H.-J.; Baumann, W.; Schmidt, T.; Zhang, S.; Sun, A.; Spannenberg, A.; Fischer, C.; Buschmann, H.; Heller, D. Are β -Acylaminoacrylates Hydrogenated in the Same Way as α -Acylaminoacrylates? *Angew. Chem. Int. Ed.* **2005**, *44*, 1184-1188.
- (19) Gu, S.; Chen, J.; Musgrave, C. B.; Gehman, Z. M.; Habgood, L. G.; Jia, X.; Dickie, D. A.; Goddard, W. A.; Gunnoe, T. B. Functionalization of Rh^{III}-Me Bonds: Use of “Capping Arene” Ligands to Facilitate Me-X Reductive Elimination. *Organometallics* **2021**, *40*, 1889-1906.
- (20) Gu, S.; Musgrave, C. B.; Gehman, Z. M.; Zhang, K.; Dickie, D. A.; Goddard, W. A.; Gunnoe, T. B. Rhodium and Iridium Complexes Bearing “Capping Arene” Ligands: Synthesis and Characterization. *Organometallics* **2021**, *40*, 2808-2825.
- (21) O'Reilly, M. E.; Fu, R.; Nielsen, R. J.; Sabat, M.; Goddard, W. A.; Gunnoe, T. B. Long-Range C-H Bond Activation by Rh^{III}-Carboxylates. *J. Am. Chem. Soc.* **2014**, *136*, 14690-14693.
- (22) O'Reilly, M. E.; Johnson, S. I.; Nielsen, R. J.; Goddard, W. A.; Gunnoe, T. B. Transition-Metal-Mediated Nucleophilic Aromatic Substitution with Acids. *Organometallics* **2016**, *35*, 2053-2056.
- (23) Fu, R.; O'Reilly, M. E.; Nielsen, R. J.; Goddard, W. A.; Gunnoe, T. B. Rhodium Bis(quinolinyl)benzene Complexes for Methane Activation and Functionalization. *Chemistry – A European Journal* **2015**, *21*, 1286-1293.

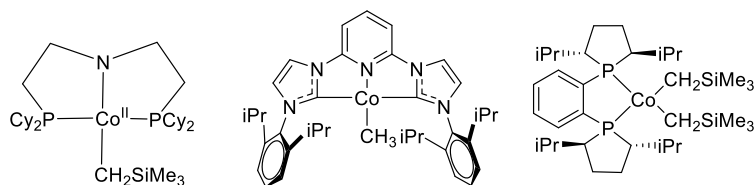
- (24) Chen, J.; Nielsen, R. J.; Goddard, W. A.; McKeown, B. A.; Dickie, D. A.; Gunnoe, T. B. Catalytic Synthesis of Superlinear Alkenyl Arenes Using a Rh(I) Catalyst Supported by a “Capping Arene” Ligand: Access to Aerobic Catalysis. *J. Am. Chem. Soc.* **2018**, *140*, 17007-17018.
- (25) Gu, S. Studies of Rh and Ir Complexes Relevant to Catalytic Functionalization of Hydrocarbons and Alcohols. Dissertation, University of Virginia, 2020.
- (26) Stockman, R. The Physiological Action of Quinoline, Isoquinoline and Some of Their Derivatives. *The Journal of physiology* **1893**, *15*, 245-248.
- (27) Robison, M. M.; Robison, B. L. 7-Azaindole. II. Conversion to 7-Methyl-7H-pyrrolo [2,3-b]pyridine and Related Compounds^{1,2}. *J. Am. Chem. Soc.* **1955**, *77*, 6554-6559.
- (28) Armarego, W. L. F.; Chai, C. L. L. *Purification of Laboratory Chemicals*; Elsevier Inc., 2009.
- (29) Fulmer, G. R.; Miller, A. J. M.; Sherden, N. H.; Gottlieb, H. E.; Nudelman, A.; Stoltz, B. M.; Bercaw, J. E.; Goldberg, K. I. NMR Chemical Shifts of Trace Impurities: Common Laboratory Solvents, Organics, and Gases in Deuterated Solvents Relevant to the Organometallic Chemist. *Organometallics* **2010**, *29*, 2176-2179.

5 Catalytic hydrogenation of styrene catalyzed by a “capping arene” ligated cobalt complex

5.1 Introduction

The homogeneous catalytic hydrogenation of olefins has been well studied since the 1960s. The most successful homogeneous olefin hydrogenation processes usually feature Rh or Ir catalysts, such as Wilkinson’s catalyst ($\text{Rh}(\text{PPh}_3)_3\text{Cl}$), the Schrock-Osborn catalyst $\{[\text{Rh}(\text{L})_2(\text{diene})]^+\}$ (L = phosphine ligand) or Crabtree’s catalyst $\{([\text{Ir}(\text{COD})(\text{py})(\text{PR}_3)]^+\}$ (py = pyridine; R = cyclohexyl or isopropyl).¹⁻¹¹ Also, in the last century, there have been a few reported examples of first-row transition metal catalyzed olefin hydrogenation.^{12, 13} However, the catalytic olefin hydrogenation processes involving first-row transition metals have not been developed to the same extent as the Rh and Ir-catalyzed processes due to limited understanding of the mechanisms.¹⁴ In the past two decades, more examples of first-row transition metals catalyzing olefin hydrogenation reactions were reported. **Figure 5.1.1** shows a few examples of cobalt catalysts that have been reported for catalytic olefin hydrogenation.¹⁵⁻¹⁷

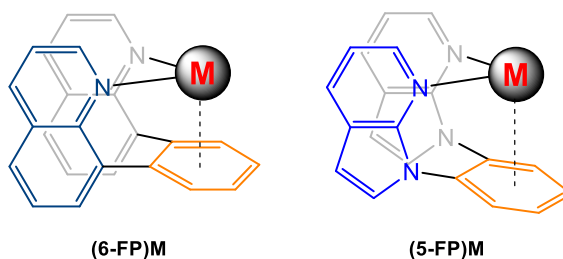
Figure 5.1.1 Examples of cobalt catalysts for olefin hydrogenation.



Recently, our group has studied a series of capping arene ligands and corresponding complexes.¹⁸⁻²⁴ The capping arene ligands consist of two quinoline (for 6-FP, 8,8'-(1,2-phenylene)diquinoline) or two 7-azaindole (for 5-FP, 1,2-bis(*N*-7-azaindoly)benzene) groups to ligate the metal as well as an arene moiety (benzene or naphthalene or their

derivatives) (**Figure 5.1.2**). It has been proposed that the arene moiety can serve as a ligand with η^2 coordination or a sterically bulky substituent, creating a unique environment for redox chemistry on the metal center (see more details in Chapter 2 and Chapter 4).²¹ In this work, (5-FP)CoCl₂ (**1**) has been synthesized. Styrene hydrogenation catalyzed by **1** reached 5.6 ± 2.4 turnovers under optimized conditions.

Figure 5.1.2 Generic examples of capping arene ligated metal complexes.



5.2 Synthesis and characterization of (5-FP)CoCl₂

Complex **1** was synthesized by mixing anhydrous CoCl₂ with 5-FP ligand in MeCN for 24 hours at room temperature under dinitrogen atmosphere (**Scheme 5.2.1**). DCM was also added to the solution to improve the solubility of the 5-FP ligand. X-ray quality crystals were obtained after purification and crystallization (see **Experimental section** for detailed procedures). The crystal structure of **1** is shown in **Figure 5.2.1**. Unlike the square planar or trigonal bipyramidal capping arene-Rh(I) complexes, **1** exhibits a tetrahedral geometry.

Scheme 5.2.1 Synthesis of (5-FP)CoCl₂ (**1**).

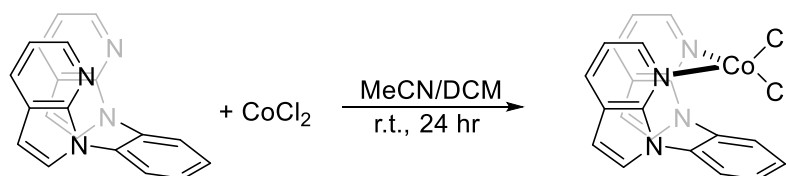
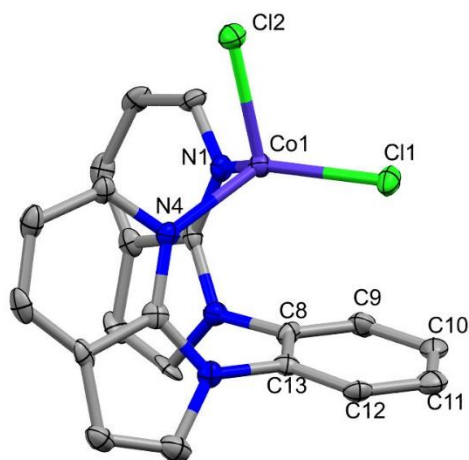


Figure 5.2.1 ORTEP of (5-FP)CoCl₂ (**1**). Ellipsoids are drawn at 50% probability level. Hydrogen atoms are omitted for clarity. Selected bond lengths for (5-FP)CoCl₂ (Å): Co1–

Cl1 2.229(3), Co1–Cl2 2.272(2), Co1–N1 2.046(7), Co1–N4 2.070(7). Selected bond angles for (5-FP)CoCl₂ (deg): Cl1–Co1–Cl2 102.94(9), Cl1–Co1–N1 123.9(2), Cl1–Co1–N4 121.9(2), Cl2–Co1–N1 104.0(2), Cl2–Co1–N4 104.7, N1–Co1–N4 96.9(3).



The peaks in the ¹H NMR spectrum of **1** (**Figure 5.2.2**) are broadened and distributed between 100 ppm and -2 ppm, which is consistent with the paramagnetic properties of a tetrahedral *d*⁷ complex. Seven resonances were observed in the ¹H NMR spectrum, indicating that the complex is probably σ -symmetric. In the ¹³C NMR spectrum of **1** (**Figure 5.2.3**), ten peaks are observed in the range of 120-380 ppm, which is also consistent with the paramagnetic property and σ -symmetric structure for **1**.

Figure 5.2.2 ^1H NMR spectrum of (5-FP)CoCl₂ (**1**) in DCM-*d*₂.

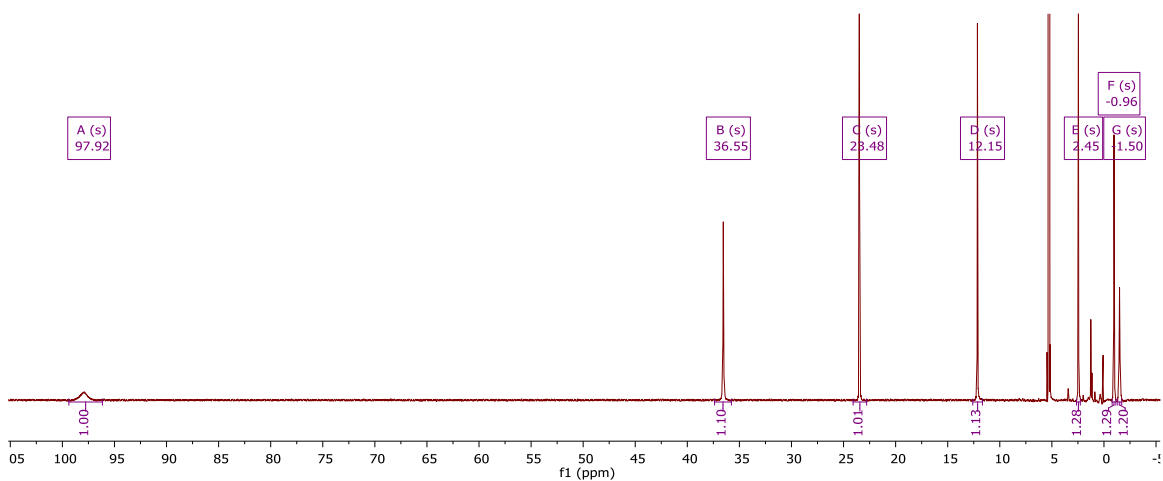
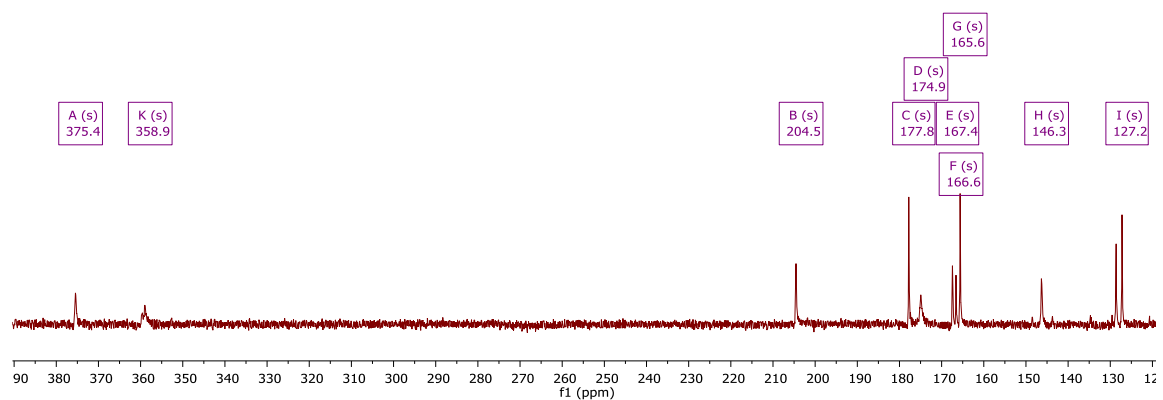


Figure 5.2.3 ^{13}C NMR spectrum of (5-FP)CoCl₂ (**1**) in DCM-*d*₂.



5.3 Preliminary NMR-scale studies for (5-FP)CoCl₂-catalyzed styrene hydrogenation

The ability of **1** to catalyze styrene hydrogenation was tested on the NMR scale. As **Figure 5.3.1** shows, *c.a.* 0.5% of the initial styrene (0.002 turnover) was converted to ethylbenzene based on the peak integration after 100 hours. The activity for styrene hydrogenation with **1** and additives was also tested (**Table 5.3.1**). When elemental zinc was added to the reaction, the turnovers significantly increased. However, the addition of

stronger reducing agent Mg(0) or Mn(0) inhibited the styrene hydrogenation. Instead, the color of the reaction turned from blue to colorless immediately after the addition of Mg(0) or Mn(0) powder, indicating that the (5-FP)CoCl₂ catalyst most likely decomposed. The addition of CuI also did not improve the catalytic efficiency.

Figure 5.3.1 ¹H NMR spectrum of styrene hydrogenation catalyzed by (5-FP)CoCl₂. Conditions: (5-FP)CoCl₂ (4 mg, 0.009 mmol), styrene (5.0 μL, 4.5 mg, 0.043 mmol), H₂ (50 psig), DCM-*d*₂ (0.4 mL), 45 °C, 100 hours.

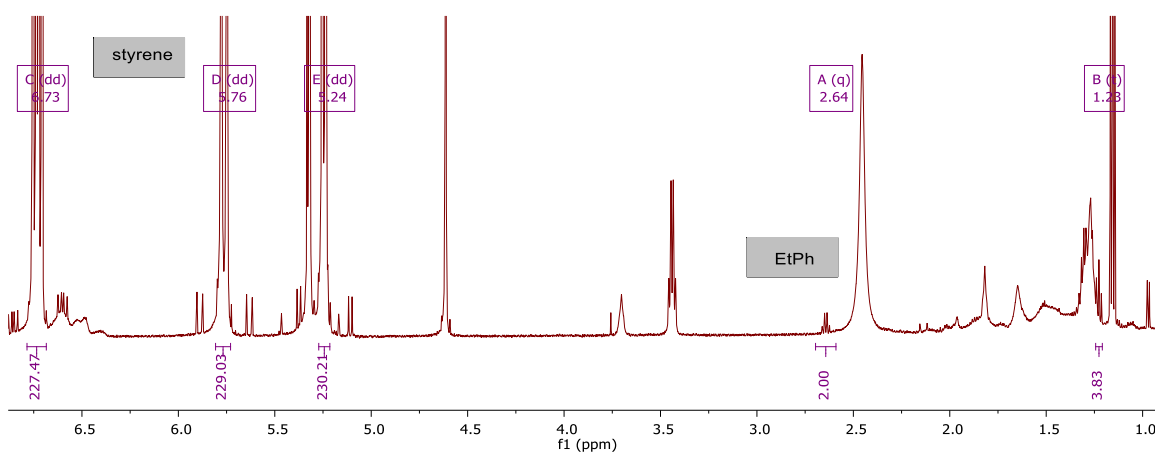
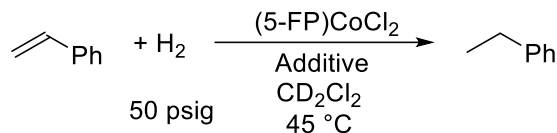


Table 5.3.1 Turnovers of ethylbenzene from (5-FP)CoCl₂ catalyzed styrene hydrogenation with additives.^a



Additive	Turnovers (TO)
Zn	0.42
Mg ^b	0
Mn ^b	0
CuI	0
Zn (no Co catalyst)	0

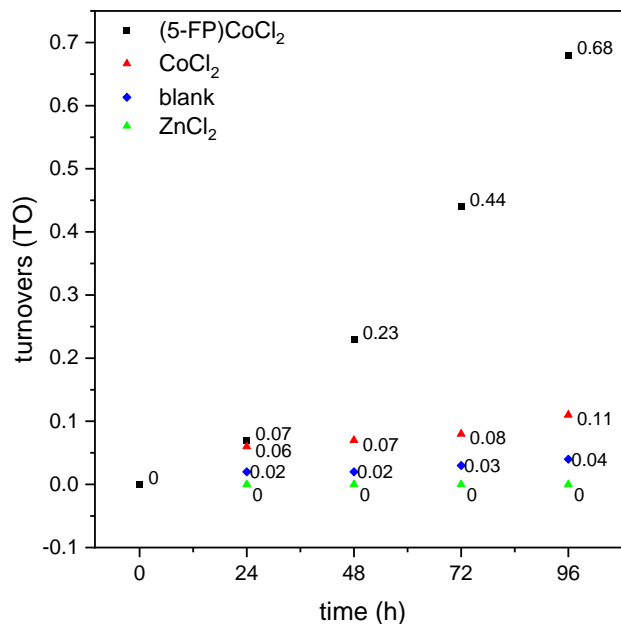
^a Reaction conditions: (5-FP)CoCl₂ (4 mg, 0.009 mmol), styrene (5.0 μL, 4.5 mg, 0.043 mmol), 10 equivalents of additive, H₂ (50 psig), DCM-*d*₂ (0.4 mL), 45 °C, 24 hours, 1 trial.

^b The reaction solution turned from blue to colorless after the addition of Mg or Mn.

5.4 Condition optimization for (5-FP)CoCl₂ catalyzed styrene hydrogenation

With the encouraging preliminary results of **1**-catalyzed styrene hydrogenation on an NMR scale, the styrene hydrogenation reaction was further studied on a larger scale. Styrene hydrogenation was performed in a Fisher-Porter reactor under the conditions indicated in **Figure 5.4.1**. The turnovers of ethylbenzene from the **1**-catalyzed styrene hydrogenation reaction reached 0.67 after 96 hours at 50 °C with 50 psig of H₂. A series of control experiments suggest that CoCl₂ and ZnCl₂ can catalyze styrene hydrogenation, but the turnovers are much lower than that for **1**. When only elemental zinc is presented, no hydrogenation was observed.

Figure 5.4.1 Turnovers of ethylbenzene vs. time (h) plot for catalytic styrene hydrogenation. Conditions: styrene (50 μ L, 45 mg, 0.44 mmol), catalyst (5 mol% relative to styrene, 0.022 mmol), Zn (40 mol% relative to styrene, 0.17 mmol; 0 mmol for ZnCl₂ entry), 50 psig H₂, DCM (10 mL), 50 °C, 1 trial.



The styrene hydrogenation reactions were performed in a custom-made high-pressure reactor (VCO reactor, **Figure 3.6.24**) so that the pressure of H₂ could be raised to 500 psig. Although the standard deviation of the 96-hour time point in **Figure 5.4.3** is large, the ethylbenzene turnovers under 500 psig H₂ (5.6 ± 2.4) was significantly increased compared to turnovers under 50 psig H₂ (0.68). However, increasing the reaction temperature from 50 °C to 90 °C under 500 psig H₂ does not improve the ethylbenzene turnovers (3.8 ± 1.7) (**Figure 5.4.4**).

Figure 5.4.2 Images of a VCO reactor.

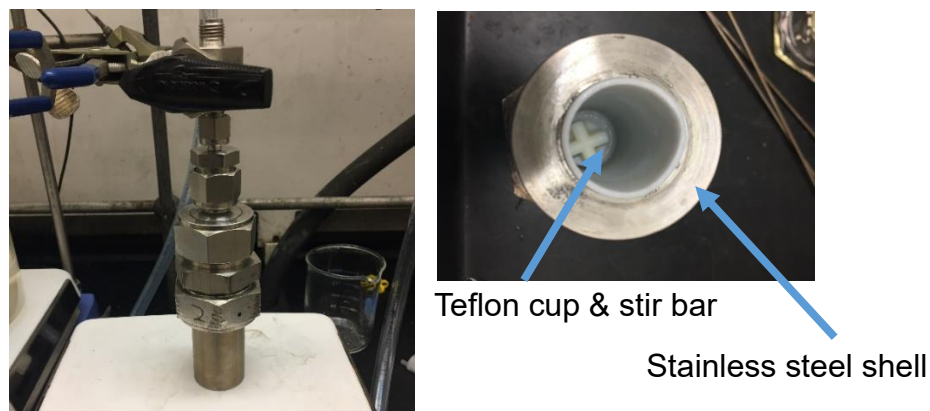


Figure 5.4.3 Turnovers of ethylbenzene vs. time (h) plot for (5-FP)CoCl₂ catalyzed styrene hydrogenation. Conditions: styrene (50 μ L, 45 mg, 0.44 mmol), (5-FP)CoCl₂ (5 mol%, 0.022 mmol), Zn (40 mol%, 0.17 mmol), 500 psig H₂, DCM (5 mL), 50 °C. All data points and standard deviations are based on at least three independent experiments.

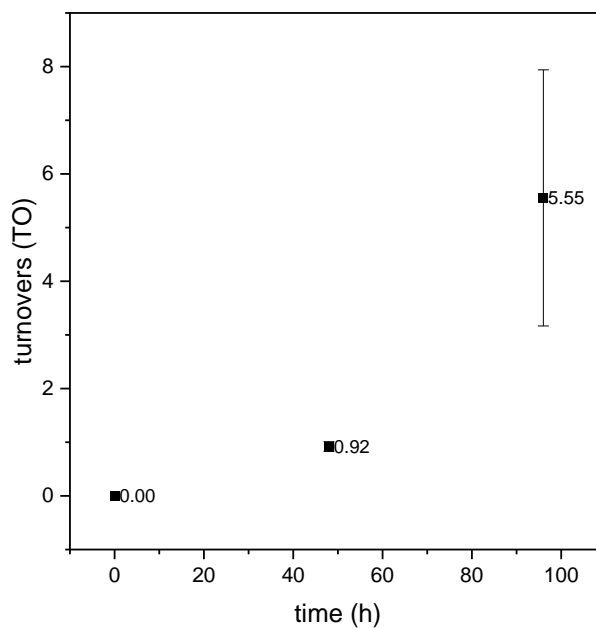


Figure 5.4.4 Turnovers of ethylbenzene vs. time (h) plot for (5-FP)CoCl₂ catalyzed styrene hydrogenation. Conditions: styrene (50 μ L, 45 mg, 0.44 mmol), (5-FP)CoCl₂ (5 mol% relative to styrene, 0.022 mmol), Zn (40 mol% relative to styrene, 0.17 mmol), 500 psig H₂, DCM (5 mL), 90 °C. All data points and standard deviations are based on at least three independent experiments.

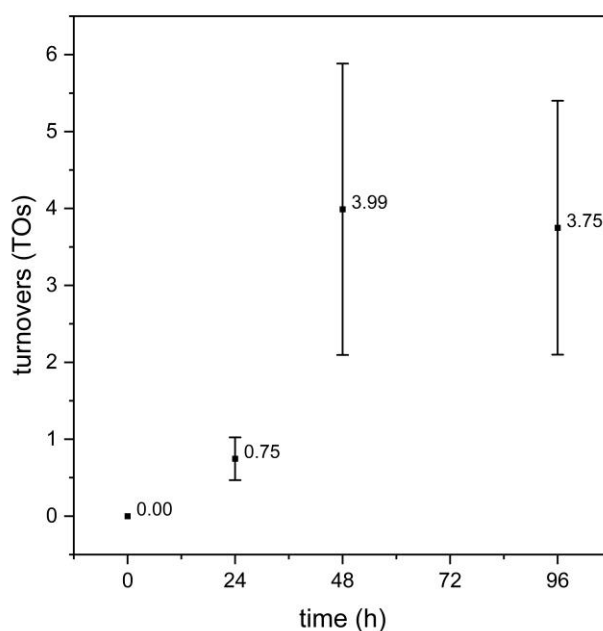
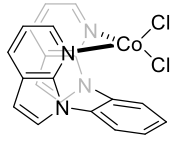
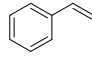
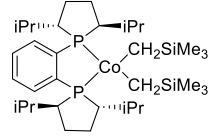
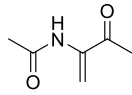
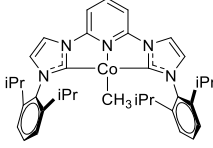
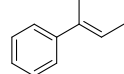
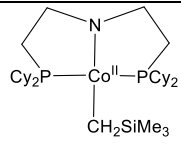
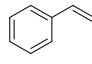


Table 5.4.1 shows a comparison of the activity of complex **1** for olefin hydrogenation with some recently reported Co-catalyzed olefin hydrogenation reactions.¹⁵⁻¹⁷ As **Table 5.4.1** shows, catalytic olefin hydrogenation using **1** has the harshest conditions (50 °C, 500 psig H₂, 96 hours) among the four catalytic olefin hydrogenation reactions. However, turnovers for olefin hydrogenation using **1** are the lowest. However, at this point in our studies, it is impossible to know how much active Co catalyst is formed using **1** as the precursors, and, thus, we are unable at this time to draw any conclusions about relative activity compared to other molecular Co catalysts.

Table 5.4.1 Comparison of the turnovers for (5-FP)CoCl₂ catalyzed olefin hydrogenation with reported cobalt catalyzed olefin hydrogenation reactions.¹⁵⁻¹⁷

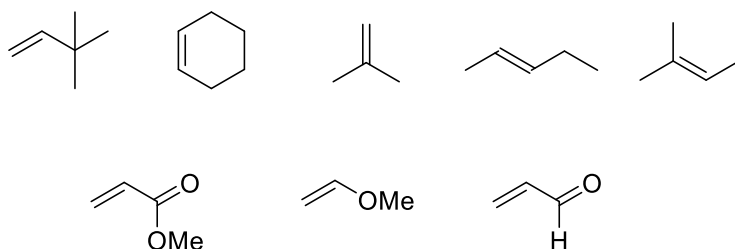
Catalyst	Cat. Conc. (mol %)	Temp. (°C)	<i>p</i> (H ₂) (psig)	substrate	Time (h)	Turnover
	5	50	500		96	5.6 ± 2.4
	5	22	500		12	> 19.8
	5	22	60		5	> 19
	2	25	15		24	50

5.5 Summary and future directions

A capping arene ligated Co(II) complex (5-FP)CoCl₂ (**1**) was successfully synthesized and characterized. The styrene hydrogenation catalyzed by **1** shows a promising preliminary result with 5.6 ± 2.4 turnover for the best condition (0.44 mmol styrene, 5 mol% catalyst, 40 mol% Zn, 50 °C, 500 psig H₂, 96 hours) and the yield of hydrogenated product may be further improved by optimizing the reaction conditions.

In the future, the catalytic activity of **1** on the hydrogenation of other olefin species can be tested. **Figure 5.5.1** shows some possible substrates to be studied for **1** catalyzed olefin hydrogenation. The target olefins include 3,3-dimethyl-1-butene (primary), cyclohexene, 2-methyl-1-propene, 2-pentene (secondary), 2-methyl-2-butene (tertiary), methyl acrylate, methoxyethene and acrylaldehyde (with functional groups). Although **1** may not be able to catalyze the hydrogenation for all of the substrates, especially the more substituted olefins such as 2-methyl-2-butene, the selectivity of **1** catalyzed olefin hydrogenation on substrates can be interesting because the regioselective hydrogenation of multi-alkenes can be useful.

Figure 5.5.1 Possible substrates for (5-FP)CoCl₂ (**1**) catalyzed olefin hydrogenation



Furthermore, understanding the mechanism of **1** catalyzed olefin hydrogenation is also important. The initial efforts could be made on kinetic studies to figure out the dependence of H₂, Co catalyst, zinc additive and styrene on the reaction rates. The kinetic isotope effects (KIE) and Eyring equation can also provide useful information for understanding the mechanism. Moreover, the isolation of the active catalyst and key intermediates, especially the reduced cobalt species by Zn(0), will provide more direct evidence for the catalytic process.

5.6 Experimental section

General Procedures. All experiments with cobalt complexes were performed under air-free environments using a glovebox. All solvents were reagent grade or better. Solvents

in the glovebox were distilled from a mixture of solvent and potassium/benzophenone (for Et₂O), or obtained from an MBraun solvent purification system (for DCM and MeCN) and purged under nitrogen flow, and then stored with molecular sieves.²⁵ Deuterated solvents were kept in the glovebox with molecular sieves (3Å or 4 Å, depending on the type of solvents²⁵). Molecular sieves were dried in a vacuum oven at 150 °C overnight before transferring into the glovebox. All celite used in this chapter was Celite™ 545 purchased from Fisher Chemical (LOT 225266). Commercially available reagents were used as received.

¹H NMR spectra were performed at 600 MHz using a Varian NMRS 600 MHz spectrometer. ¹³C NMR spectra were obtained at 201 MHz by a Bruker Advance III 800 MHz spectrometer. ¹H NMR and ¹³C NMR spectra are referenced against residual proton signals of the deuterated solvent.²⁶

GC-MS data were collected using a Shimadzu GC-2014 gas chromatograph with a DB-5MS capillary column (30 m × 0.32 mm × 0.25 μm) and flame ionization detector (FID) detector. The temperature of the oven was set to start of 50 °C, hold for 2.5 min, and then increase temperature with a 20 °C/min increment until the temperature reached 240 °C, and finally held at 240 °C for 2 min. The retention times of hexamethylbenzene (HMB, internal standard), ethylbenzene, and styrene were 12.59 min, 13.32 min, and 17.44 min, respectively. The calibration curves for ethylbenzene and styrene were determined for quantitative measurements (**Figure 5.6.1** and **Figure 5.6.2**).

Figure 5.6.1 Calibration curve for the quantification of ethylbenzene (EtPh) against hexamethylbenzene (internal standard, HMB).

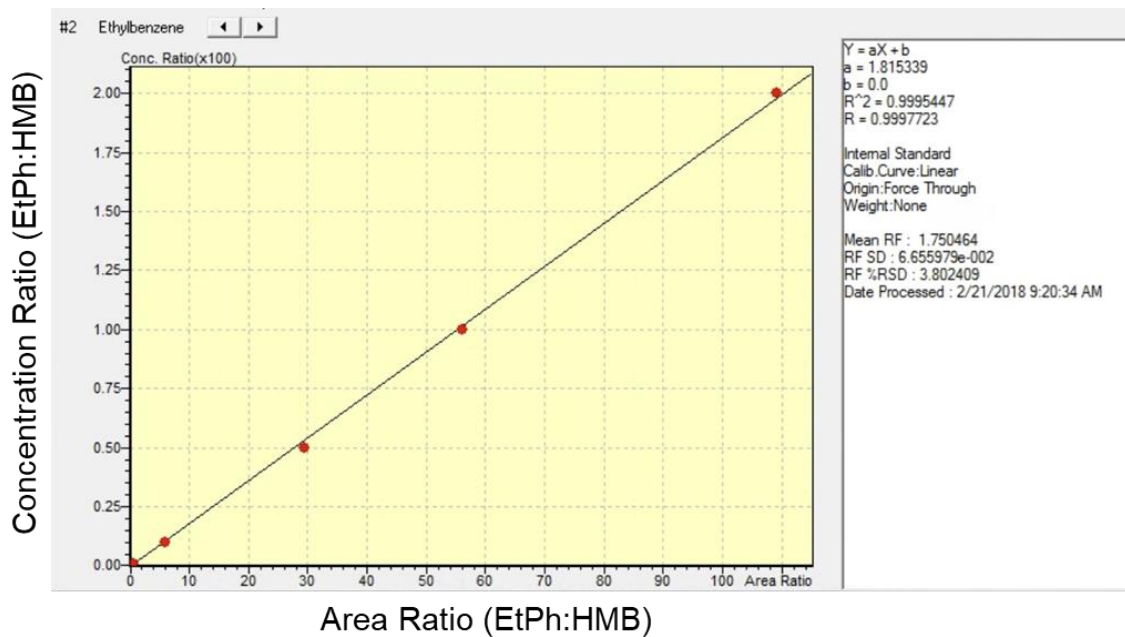
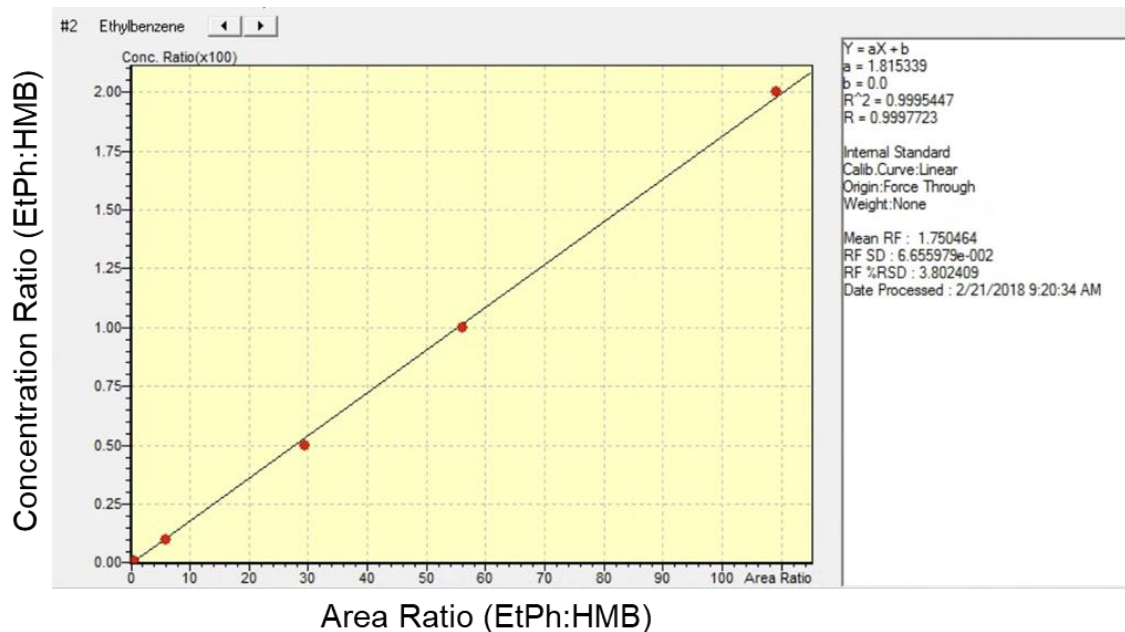


Figure 5.6.2 Calibration curve for the quantification of styrene against hexamethylbenzene (internal standard, HMB).



Synthesis of (5-FP)CoCl₂ (1) In a glovebox, anhydrous CoCl₂ (42.3 mg, 0.326 mmol) was dissolved in 10 mL of MeCN (solution A) in a 50 mL round bottom flask. In a second container (25 mL glass vial), 5-FP (101.3 mg, 0.326 mmol) was dissolved in 2 mL of DCM, and then diluted to 10 mL by MeCN (solution B). Solution B was dropwise added into solution A with stirring. The mixture was stirred for 24 hours at room temperature. The solvent was removed *in vacuo*, and the crude blue product was dissolved in 5 mL of DCM. The DCM solution was filtered by a plug of Celite to remove remaining CoCl₂. The filtrate was collected, and the solvent was removed *in vacuo*. The blue solid was dissolved in a minimal amount of DCM, and X-ray quality crystal was obtained by solvent diffusion of Et₂O into DCM. The deep blue product (97.8 mg, 0.222 mmol, 68.1 % yield) was characterized by ¹H NMR, ¹³C NMR, X-ray diffraction and elemental analysis. ¹H NMR (600 MHz, DCM-*d*₂) δ 97.9 (s, 1H), 36.6 (s, 1H), 23.5 (s, 1H), 12.2 (s, 1H), 2.5 (s, 1H), -1.0 (s, 1H), -1.5 (s, 1H). ¹³C NMR (201 MHz, DCM-*d*₂) δ 375.4, 358.9, 204.5, 177.8, 174.9, 167.4, 166.6, 165.6, 146.3, 127.2. Anal. Calcd. For C₂₀H₁₄Cl₂CoN₄: C, 54.57; H, 3.21; N, 12.73. Found: C, 54.55; H, 3.15; N, 12.63.

Figure 5.6.3 ¹H NMR spectrum for (5-FP)CoCl₂ (1) in DCM-*d*₂

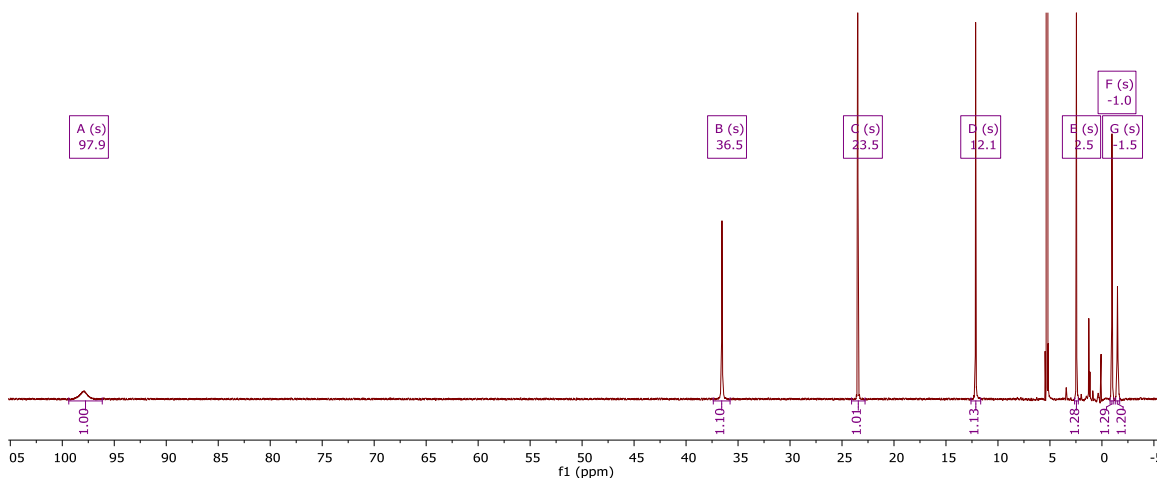


Figure 5.6.4 ^{13}C NMR spectrum for (5-FP)CoCl₂ (**1**) in DCM-*d*₂.

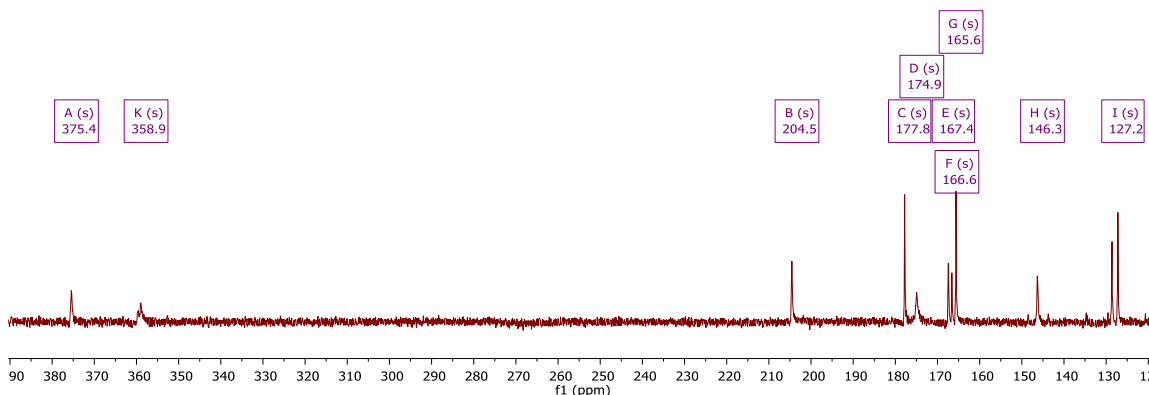
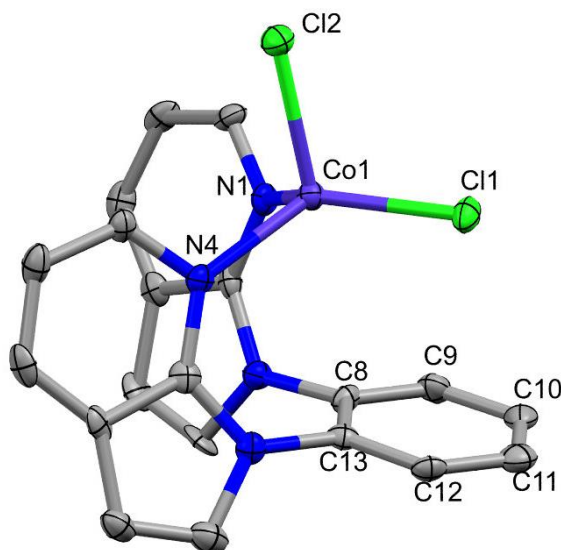


Figure 5.6.5 ORTEP of (5-FP)CoCl₂(**1**). Ellipsoids are drawn at 50% probability level. Hydrogen atoms are omitted for clarity. Selected bond lengths for (5-FP)CoCl₂ (Å): Co1–Cl1 2.229(3), Co1–Cl2 2.272(2), Co1–N1 2.046(7), Co1–N4 2.070(7). Selected bond angles for (5-FP)CoCl₂ (deg): Cl1–Co1–Cl2 102.94(9), Cl1–Co1–N1 123.9(2), Cl1–Co1–N4 121.9(2), Cl2–Co1–N1 104.0(2), Cl2–Co1–N4 104.7, N1–Co1–N4 96.9(3).



General procedures for NMR scale styrene hydrogenation experiment. In a J. Young NMR tube, a designated amount of styrene, catalyst, additive, hexamethylbenzene (internal standard) and DCM-*d*₂ were loaded under dinitrogen atmosphere. Dihydrogen (50 psig) was then added into the tube. The reaction was heated in an oil bath at 50 °C. The ^1H

NMR spectra were recorded, and the concentration of styrene and ethylbenzene was quantified based on the integrations of their ^1H NMR peaks.

General procedures for styrene hydrogenation experiments using Fisher-porter reactor. In a Fisher-porter reactor, the designated amount of styrene, catalyst, additive, hexamethylbenzene (internal standard) and DCM were loaded under a dinitrogen atmosphere. Dihydrogen (50 psig) was then added to the reactor. The reaction was heated in an oil bath at 50 °C. The sample (*c.a.* 0.2 mL) was obtained using a 1 mL syringe with an 18-inch stainless steel needle under N_2 flow and transferred into a GC vial. The concentrations of styrene and ethylbenzene were determined based on their peak integrations from the GC chromatogram.

General procedures for styrene hydrogenation experiments using VCO reactor. In a custom-made high-pressure reactor (VCO reactor, **Figure 3.6.24**), the designated amount of styrene, catalyst, additive, hexamethylbenzene (internal standard) and DCM were loaded under a dinitrogen atmosphere. 500 psig of H_2 was then added to the reactor. The reaction was heated in an aluminum metal block at 50 or 90 °C. The sample (*c.a.* 0.2 mL) was obtained using a 1 mL syringe with an 18-inch stainless steel needle under N_2 flow and transferred into a GC vial. The concentration of styrene and ethylbenzene was determined based on their peak integrations on the GC chromatogram.

5.7 References

- (1) Young, J. F.; Osborn, J. A.; Jardine, F. H.; Wilkinson, G. Hydride Intermediates in Homogeneous Hydrogenation Reactions of Olefins and Acetylenes Using Rhodium Catalysts. *Chem. Commun.* **1965**, 131-132.
- (2) Evans, D.; Osborn, J. A.; Jardine, F. H.; Wilkinson, G. Homogeneous Hydrogenation and Hydroformylation using Ruthenium Complexes. *Nature* **1965**, 208, 1203-1204.
- (3) Osborn, J. A.; Jardine, F. H.; Young, J. F.; Wilkinson, G. The Preparation and Properties of Tris(Triphenylphosphine)halogenorhodium(I) and Some Reactions Thereof Including Catalytic Homogeneous Hydrogenation of Olefins and Acetylenes and their Derivatives. *J. Chem. Soc. A* **1966**, 1711-1732.
- (4) Baird, M. C.; Mague, J. T.; Osborn, J. A.; Wilkinson, G. Addition Reactions of Tris(triphenylphosphine)chlororhodium(I); Hydrido-, Alkyl, and Acyl Complexes; Carbon Monoxide Insertion and Decarbonylation Reactions. *J. Chem. Soc. A* **1967**, 1347.
- (5) Hallman, P. S.; Evans, D.; Osborn, J. A.; Wilkinson, G. Selective Catalytic Homogeneous Hydrogenation of Terminal Olefins Using Tris(Triphenylphosphine)Hydridochlororuthenium(II); Hydrogen Transfer in Exchange and Isomerisation Reactions of Olefins. *Chem. Commun.* **1967**, 305.
- (6) Schrock, R. R.; Osborn, J. A. Catalytic Hydrogenation Using Cationic Rhodium Complexes. I. Evolution of The Catalytic System and the Hydrogenation of Olefins. *J. Am. Chem. Soc.* **1976**, 98, 2134-2143.
- (7) Schrock, R. R.; Osborn, J. A. Catalytic Hydrogenation Using Cationic Rhodium Complexes. II. The Selective Hydrogenation of Alkynes to *Cis* Olefins. *J. Am. Chem. Soc.* **1976**, 98, 2143-2147.

- (8) Schrock, R. R.; Osborn, J. A. Catalytic Hydrogenation Using Cationic Rhodium Complexes. 3. The Selective Hydrogenation of Dienes to Monoenes. *J. Am. Chem. Soc.* **1976**, *98*, 4450-4455.
- (9) Crabtree, R. Iridium Compounds in Catalysis. *Acc. Chem. Res.* **1979**, *12*, 331-337.
- (10) Crabtree, R. H.; Hlatky, G. G.; Parnell, C. A.; Segmueller, B. E.; Uriarte, R. J. Solvento Complexes of Tungsten, Rhenium, Osmium, and Iridium and The X-Ray Crystal Structure of $[\text{IrH}_2(\text{Me}_2\text{CO})_2(\text{PPh}_3)_2]\text{BF}_4$. *Inorg. Chem.* **1984**, *23*, 354-358.
- (11) Suggs, J. W.; Cox, S. D.; Crabtree, R. H.; Quirk, J. M. Facile Homogeneous Hydrogenations of Hindered Olefins with $[\text{Ir}(\text{cod})\text{py}(\text{PCy}_3)]\text{PF}_6$. *Tetrahedron Lett.* **1981**, *22*, 303-306.
- (12) Funabiki, T.; Tarama, K. A Novel Solvent Effect on the Selectivity of the Hydrogenation Of Butadiene Catalyzed By Pentacyanocobaltate(II). *Tetrahedron Lett.* **1971**, *12*, 1111-1114.
- (13) Ohgo, Y.; Takeuchi, S.; Yoshimura, J. Asymmetric Reactions. V. Homogeneous Hydrogenation of Unsaturated Compounds Catalyzed by Bis(dimethylglyoximato)cobalt(II). *Bull. Chem. Soc. Jpn.* **1971**, *44*, 283-285.
- (14) Wen, J.; Wang, F.; Zhang, X. Asymmetric Hydrogenation Catalyzed by First-Row Transition Metal Complexes. *Chem. Soc. Rev.* **2021**, *50*, 3211-3237.
- (15) Zhang, G.; Scott, B. L.; Hanson, S. K. Mild and Homogeneous Cobalt-Catalyzed Hydrogenation of C–C, C–O, and C–N Bonds. *Angew. Chem. Int. Ed.* **2012**, *51*, 12102-12106.
- (16) Yu, R. P.; Darmon, J. M.; Milsman, C.; Margulieux, G. W.; Stieber, S. C. E.; Debeer, S.; Chirik, P. J. Catalytic Hydrogenation Activity and Electronic Structure Determination

of Bis(arylimidazol-2-ylidene)pyridine Cobalt Alkyl and Hydride Complexes. *J. Am. Chem. Soc.* **2013**, *135*, 13168-13184.

(17) Friedfeld, M. R.; Shevlin, M.; Hoyt, J. M.; Krska, S. W.; Tudge, M. T.; Chirik, P. J. Cobalt Precursors for High-Throughput Discovery of Base Metal Asymmetric Alkene Hydrogenation Catalysts. *Science* **2013**, *342*, 1076-1080.

(18) O'Reilly, M. E.; Johnson, S. I.; Nielsen, R. J.; Goddard, W. A.; Gunnoe, T. B. Transition-Metal-Mediated Nucleophilic Aromatic Substitution with Acids. *Organometallics* **2016**, *35*, 2053-2056.

(19) O'Reilly, M. E.; Fu, R.; Nielsen, R. J.; Sabat, M.; Goddard, W. A.; Gunnoe, T. B. Long-Range C–H Bond Activation by Rh^{III}-Carboxylates. *J. Am. Chem. Soc.* **2014**, *136*, 14690-14693.

(20) Fu, R.; O'Reilly, M. E.; Nielsen, R. J.; Goddard, W. A.; Gunnoe, T. B. Rhodium Bis(quinolinyl)benzene Complexes for Methane Activation and Functionalization. *Eur. J. Chem.* **2015**, *21*, 1286-1293.

(21) Gu, S.; Chen, J.; Musgrave, C. B.; Gehman, Z. M.; Habgood, L. G.; Jia, X.; Dickie, D. A.; Goddard, W. A.; Gunnoe, T. B. Functionalization of Rh^{III}–Me Bonds: Use of “Capping Arene” Ligands to Facilitate Me–X Reductive Elimination. *Organometallics* **2021**, *40*, 1889-1906.

(22) Gu, S.; Musgrave, C. B.; Gehman, Z. M.; Zhang, K.; Dickie, D. A.; Goddard, W. A.; Gunnoe, T. B. Rhodium and Iridium Complexes Bearing “Capping Arene” Ligands: Synthesis and Characterization. *Organometallics* **2021**, *40*, 2808–2825.

(23) Liu, C.; Geer, A. M.; Webber, C.; Musgrave, C. B.; Gu, S.; Johnson, G.; Dickie, D. A.; Chhabra, S.; Schnegg, A.; Zhou, H.; et al. Immobilization of “Capping Arene”

Cobalt(II) Complexes on Ordered Mesoporous Carbon for Electrocatalytic Water Oxidation. *ACS Catal.* **2021**, *11*, 15068-15082.

(24) Chen, J.; Nielsen, R. J.; Goddard, W. A.; McKeown, B. A.; Dickie, D. A.; Gunnoe, T. B. Catalytic Synthesis of Superlinear Alkenyl Arenes Using a Rh(I) Catalyst Supported by a “Capping Arene” Ligand: Access to Aerobic Catalysis. *J. Am. Chem. Soc.* **2018**, *140*, 17007-17018.

(25) Armarego, W. L. F.; Chai, C. L. L. *Purification of Laboratory Chemicals*; Elsevier Inc., 2009.

(26) Fulmer, G. R.; Miller, A. J. M.; Sherden, N. H.; Gottlieb, H. E.; Nudelman, A.; Stoltz, B. M.; Bercaw, J. E.; Goldberg, K. I. NMR Chemical Shifts of Trace Impurities: Common Laboratory Solvents, Organics, and Gases in Deuterated Solvents Relevant to the Organometallic Chemist. *Organometallics* **2010**, *29*, 2176-2179.

6 Summary and Future Directions

6.1 Summary

In summary, catalytic olefin hydrogenation reactions using capping arene ligated Rh complexes were studied as a model study of a catalytic reaction that involves formal oxidation state changes at the transition metal catalyst. The reaction rates for the olefin hydrogenation is dependent on the capping arene ligand coordinates to the Rh catalyst, for which the trend is: $(5\text{-}^{\text{NPF}}\text{FP})\text{Rh}(\eta^2\text{-C}_2\text{H}_4)\text{Cl} > (6\text{-FP})\text{Rh}(\eta^2\text{-C}_2\text{H}_4)\text{Cl} > (5\text{-FP})\text{Rh}(\eta^2\text{-C}_2\text{H}_4)\text{Cl}$, while the $(6\text{-}^{\text{NPF}}\text{FP})\text{Rh}(\eta^2\text{-C}_2\text{H}_4)\text{Cl}$ decomposes rapidly during the catalysis. The kinetic and computational modeling studies suggest an “olefin first” mechanism for the catalytic hydrogenation. Based on the computational modeling, the rate-determining step is likely oxidative addition of dihydrogen, and the calculated activation energy for oxidative addition of dihydrogen on $(6\text{-FP})\text{Rh}(\eta^2\text{-styrene})\text{Cl}$ is 1.2 kcal/mol lower than that on $(5\text{-FP})\text{Rh}(\eta^2\text{-styrene})\text{Cl}$, which is consistent with our experimental results.

Moreover, although a catalytic process for the direct carboxylation using Pd catalysts was not successfully developed, CO_2 insertion into the Pd–Ph bond of $(i^{\text{Pr}}\text{PCP})\text{PdPh}$ complex and C–H activation of benzene by $(i^{\text{Pr}}\text{PCP})\text{PdOBz}$ (OBz = benzoate) were both investigated. The insertion of CO_2 into the Pd–Ph bond of $(i^{\text{Pr}}\text{PCP})\text{PdPh}$ complex shows a dependence on the solvent, and the reaction is favored in MeCN and DMF compared with THF and benzene. However, there is no evidence that $(i^{\text{Pr}}\text{PCP})\text{PdOBz}$ can facilitate the C–H activation of benzene to complete a catalytic cycle.

The performance of MeI promoted methanol carbonylation using a series of capping arene ligated Rh and Ir carbonyl complexes were compared. However, no improvement on

the turnover frequency was observed compared to catalysis using $[\text{Rh}(\text{CO})_2(\mu\text{-Cl})]_2$ or $[\text{Ir}(\text{COE})_2(\mu\text{-Cl})]_2$. Mechanistic studies suggests that the capping arene ligated Rh or Ir carbonyl complexes likely undergo a decomposition pathway when MeI is present, resulting in the formation of an active catalyst without the coordination of capping arene ligands.

Last, a capping arene ligated Co(II) complex, $(5\text{-FP})\text{CoCl}_2$, was synthesized and characterized. Preliminary result for the styrene hydrogenation catalyzed by $(5\text{-FP})\text{CoCl}_2$ produced 5.6 ± 2.4 equivalents (based on $(5\text{-FP})\text{CoCl}_2$) of ethylbenzene for the best condition.

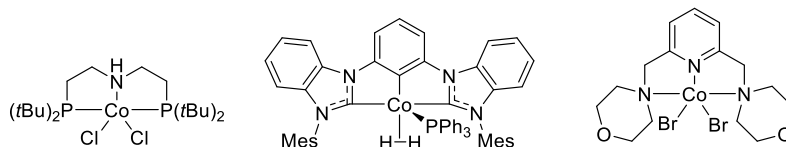
6.2 Future Directions

6.2.1 Co-catalyzed alkyne partial hydrogenation to produce alkene

Although $(5\text{-FP})\text{CoCl}_2$ is speculated to be a less active catalyst for olefin hydrogenation than the capping arene Rh(I) catalysts based on the current results, this advantage can be utilized by using $(5\text{-FP})\text{CoCl}_2$ to catalyze the partial hydrogenation of alkyne to produce alkene.

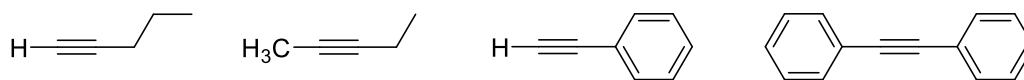
One of the early reports for partial reduction of alkynes is catalyzed by the Lindlar catalyst, a heterogenous Pd based catalyst that is treated with calcium carbonate and lead acetate.¹ Catalytic alkyne partial hydrogenation reactions have been further developed by using Ru, Ir and Pd catalysts.²⁻⁷ Recently, a few examples of Co-catalyzed alkyne partial hydrogenation have been reported, which has been mainly focused on Co catalysts with pincer ligands (**Figure 6.2.1**).⁸⁻¹¹ However, these Co-catalyzed alkyne partial hydrogenation reactions usually require either NH_3BH_3 as the hydrogen source^{9, 10} or highly reactive reducing agent (such as NaBH_4)⁸ or catalyst (Co^{I} catalyst).¹¹

Figure 6.2.1 Reported cobalt catalysts for alkyne partial hydrogenation.⁸⁻¹¹



We speculate that the (5-FP)CoCl₂ can also catalyze alkyne partial hydrogenation without NH₃BH₃ or strong reducing agents such as NaBH₄. The capping arene ligand might destabilize the high valent intermediate (likely Co^{III}) by preventing the formation of an octahedral complex due to the steric effect. The destabilized high valent intermediate could potentially lead to a faster reductive elimination of the olefin product. The preliminary studies could be performed on some liquid phase alkynes shown in **Figure 6.2.2**, which includes terminal alkyne, internal alkyne, and conjugated alkynes.

Figure 6.2.2 Proposed target substrates for the studies on Co catalyzed alkyne partial hydrogenation

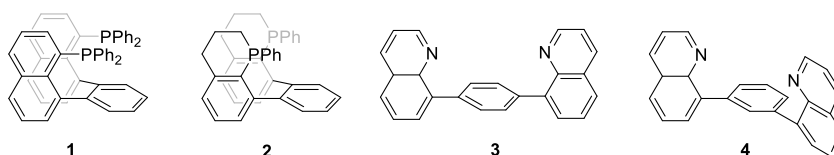


6.2.2 Development of "capping arene" ligands

Despite the reactivity of capping arene catalyst observed in this work and previous works, there are some improvements can be made by designing the new capping arene ligands. The new features for the new "capping arene" ligated complexes may include: (1) higher thermal stability; (2) better tolerance toward additives or solvents. For example, in Chapter 4, it is demonstrated that the capping arene Rh or Ir complexes are unstable with MeI at high temperature; (3) faster oxidative addition or reductive elimination reaction for "new capping arene" ligated complexes.

Figure 6.2.3 shows some examples for the new designs for the capping arene ligands. We speculate that the new capping arene ligands can form more stable metal complexes against ligand dissociation due to the π -back bonding between phosphine and the metal center. Additionally, there are many examples for catalytic methanol carbonylation promoted by MeI using rhodium complexes with phosphine ligands, which suggests that the phosphine-based ligands are tolerant to MeI.¹²⁻¹⁴ Thus, the phosphine-based capping arene Rh or Ir complexes should also be tolerant for environment with MeI, which might be used to catalyze the methanol carbonylation with MeI promoter.

Figure 6.2.3 Proposed new capping arene ligands.



Moreover, the capping arene complex with the two quinolyl groups in *para* or *meta* positions on the benzene moiety might create a larger bite angle when coordinated to the metal (**Figure 6.2.3**, ligand **3** and **4**). It has been concluded that the bite angle of biphosphine ligands on transition metal complexes can affect the rate of the oxidative addition and reductive elimination reactions.¹⁵ Since the oxidative addition and reductive elimination reactions can often be the rate determining step of catalytic reactions,¹⁶⁻²⁷ enhancing the rate of oxidative addition and reductive elimination reactions would improve the rate of the catalytic processes. Hence, it will be an interesting topic to study the effect of bite angle of these capping arenes on oxidative addition and reductive elimination reactions.

6.3 References

- (1) Chen, C.; Huang, Y.; Zhang, Z.; Dong, X.-Q.; Zhang, X. Cobalt-catalyzed (*Z*)-Selective Semihydrogenation of Alkynes with Molecular Hydrogen. *Chem. Commun.* **2017**, 53, 4612-4615.
- (2) Landge, V. G.; Pitchaimani, J.; Midya, S. P.; Subaramanian, M.; Madhu, V.; Balaraman, E. Phosphine-free Cobalt Pincer Complex Catalyzed *Z*-selective Semi-Hydrogenation of Unbiased Alkynes. *Catal. Sci. Technol.* **2018**, 8, 428-433.
- (3) Fu, S.; Chen, N.-Y.; Liu, X.; Shao, Z.; Luo, S.-P.; Liu, Q. Ligand-Controlled Cobalt-Catalyzed Transfer Hydrogenation of Alkynes: Stereodivergent Synthesis of *Z*- and *E*-Alkenes. *J. Am. Chem. Soc.* **2016**, 138, 8588-8594.
- (4) Tokmic, K.; Fout, A. R. Alkyne Semihydrogenation with a Well-Defined Nonclassical Co-H₂ Catalyst: A H₂ Spin on Isomerization and *E*-Selectivity. *J. Am. Chem. Soc.* **2016**, 138, 13700-13705.
- (5) Baker, M. J.; Giles, M. F.; Orpen, A. G.; Taylor, M. J.; Watt, R. J. Cis-[RhI(CO)(Ph₂PCH₂P(S)Ph₂)]: a New Catalyst for Methanol Carbonylation. *J. Chem. Soc., Chem. Commun.* **1995**, 197.
- (6) Carraz, C.-A.; Orpen, A. G.; Ellis, D. D.; Pringle, P. G.; Ditzel, E. J.; Sunley, G. J. Rhodium(I) Complexes of Unsymmetrical Diphosphines: Efficient and Stable Methanol Carbonylation Catalysts. *Chem. Commun.* **2000**, 1277-1278.
- (7) Deb, B.; Dutta, D. K. Influence of Phosphorus and Oxygen Donor Diphosphine Ligands on the Reactivity of Rhodium(I) Carbonyl Complexes. *J. Mol. Catal. A: Chem.* **2010**, 326, 21-28.

- (8) Dierkes, P.; Van Leeuwen, P. W. N. M. The Bite Angle Makes the Difference: a Practical Ligand Parameter for Diphosphine Ligands. *J. Chem. Soc., Dalton Trans.* **1999**, 1519-1530.
- (9) Niu, S.; Hall, M. B. Theoretical Studies on Reactions of Transition-Metal Complexes. *Chem. Rev.* **2000**, *100*, 353-406.
- (10) Thompson, W. H.; Sears, C. T. Kinetics of Oxidative Addition to Iridium(I) Complexes. *Inorg. Chem.* **1977**, *16*, 769-774.
- (11) Kubota, M.; Kiefer, G. W.; Ishikawa, R. M.; Bencala, K. E. Kinetics of Reactions of Methyl Iodide with Four-Coordinated Iridium(I) Complexes. *Inorg. Chim. Acta* **1973**, *7*, 195-202.
- (12) Gu, S.; Nielsen, R. J.; Taylor, K. H.; Fortman, G. C.; Chen, J.; Dickie, D. A.; Goddard, W. A.; Gunnoe, T. B. Use of Ligand Steric Properties to Control the Thermodynamics and Kinetics of Oxidative Addition and Reductive Elimination with Pincer-Ligated Rh Complexes. *Organometallics* **2020**, *39*, 1917-1933.
- (13) Feller, M.; Iron, M. A.; Shimon, L. J. W.; Diskin-Posner, Y.; Leitius, G.; Milstein, D. Competitive C-I versus C-CN Reductive Elimination from a RhIII Complex. Selectivity is Controlled by the Solvent. *J. Am. Chem. Soc.* **2008**, *130*, 14374-14375.
- (14) Feller, M.; Diskin-Posner, Y.; Leitius, G.; Shimon, L. J. W.; Milstein, D. Direct Observation of Reductive Elimination of MeX (X = Cl, Br, I) from Rh^{III} Complexes: Mechanistic Insight and the Importance of Sterics. *J. Am. Chem. Soc.* **2013**, *135*, 11040-11047.
- (15) O'Reilly, M. E.; Pahls, D. R.; Webb, J. R.; Boaz, N. C.; Majumdar, S.; Hoff, C. D.; Groves, J. T.; Cundari, T. R.; Gunnoe, T. B. Reductive Functionalization of a

Rhodium(III)–Methyl Bond by Electronic Modification of the Supporting Ligand. *Dalton Trans.* **2014**, *43*, 8273-8281.

(16) O'Reilly, M. E.; Fu, R.; Nielsen, R. J.; Sabat, M.; Goddard, W. A.; Gunnoe, T. B. Long-Range C–H Bond Activation by Rh^{III}-Carboxylates. *J. Am. Chem. Soc.* **2014**, *136*, 14690-14693.

(17) Albrecht, M.; van Koten, G. Platinum Group Organometallics Based on “Pincer” Complexes: Sensors, Switches, and Catalysts. *Angew. Chem. Int. Ed.* **2001**, *40*, 3750-3781.

(18) Choi, J.; MacArthur, A. H. R.; Brookhart, M.; Goldman, A. S. Dehydrogenation and Related Reactions Catalyzed by Iridium Pincer Complexes. *Chem. Rev.* **2011**, *111*, 1761-1779.

(19) Goldberg, J. M.; Wong, G. W.; Brastow, K. E.; Kaminsky, W.; Goldberg, K. I.; Heinekey, D. M. The Importance of Steric Factors in Iridium Pincer Complexes. *Organometallics* **2015**, *34*, 753-762.

(20) Goldberg, J. M.; Cherry, S. D. T.; Guard, L. M.; Kaminsky, W.; Goldberg, K. I.; Heinekey, D. M. Hydrogen Addition to (pincer)Ir^I(CO) Complexes: The Importance of Steric and Electronic Factors. *Organometallics* **2016**, *35*, 3546-3556.